Computational Analysis of the Flow Fields Induced by a DBD Plasma Actuator toward Separated-Flow Control

(プラズマアクチュエータによる剥離流れ制御の数値解析に関する研究)

Department of Aeronautics and Astronautics, University of Tokyo

Kengo Asada

浅田　健吾

March, 2014

Abstract

For aircrafts, flow separation is a critical phenomenon that leads to an increase in drag and a decrease in lift. In the current aircraft design, shapes of wing surface are changed using devices, e.g. vortex generators and flaps, and the flow separation is passively avoided. However this approach is effective only for the design points and encompasses limitation in a range of aerodynamic body design. In this context, active flow control using micro-scale devices are getting much attention in various fields. Especially in the aerospace engineering field, a "dielectric barrier discharge (DBD) plasma actuator" is well investigated in several devices for separated-flow control around airfoils. This device can control the global flow fields by adding the fluctuation to the local flow field with inducing weak flow (of a few meters per second). When a DBD plasma actuator is installed near the leading edge of an airfoil at a stall angle, and is operated, the separated flow is suppressed. Dielectric barrier discharge plasma actuators have a lot of advantages such as simplicity, active control capability and low energy consumption compared to conventional flow control devices (e.g. steady jets). Although the availability of a DBD plasma actuator for separated-flow control is mainly verified by experimental studies, there are no clear guides for operation of the DBD plasma actuator because most of these studies are conducted by trial and error approaches, and understanding the mechanism of separated-flow control is insufficient. On the other hand, some studies in recent years show that use of unsteady input voltage which is called a "duty cycle" or a "burst wave" gives higher capability of separated-flow control with less input energy. The burst wave is the unsteady alternative current switched on and off periodically. The separated-flow control by the DBD plasma actuator operated with this bust wave might have the key phenomena for separated-flow control. (In the present study, the operating condition when the DBD actuator operated with a burst wave, is called as a "bust mode" while the operating condition when the DBD actuator operated with a basic sinusoidal wave, is called as a "normal mode".)

Therefore, the objectives of this study are to clarify the mechanism of separated-flow control and to show guides for use of DBD plasma actuators, toward the practical use of

DBD plasma actuators for separated-flow control. In this study, flow fields controlled by a DBD plasma actuator around NACA0015 at a low Reynolds number ($Re_c = 63,000$ based on chord length and free stream velocity) are analyzed with computational fluid dynamics (CFD) . Large-eddy simulations (LES) using compact difference scheme are conducted to resolve small fluctuations induced by DBD plasma actuators and unsteady phenomena like flow separation and turbulent transition.

This thesis comprises seven chapters. In chapter 1, backgrounds and previous studies are introduced. In chapter 2, problem settings are described. In chapter 3, governing equations, numerical methods, and the numerical modeling of a DBD plasma actuator utilized in the present study are explained. In chapter 4, validation and verification of the numerical methods and the modeling explained in chapter 3 are described.

In chapter 5, we analyze seven cases in which the operating conditions (normal and burst modes), the locations of the actuator, and the power of DBD plasma actuators, are changed. In the first half of this chapter, the relations between aerodynamic characteristics and the effectiveness of separated-flow control with a DBD plasma actuator over the airfoil are discussed. The results show that even if lift coefficients are comparable values on two different controlled-flow fields, lift-drag ratios could be different. Thus, the appropriate criteria should be chosen for any purpose. In the second half of this chapter, first, differences between the burst mode and the normal mode cases are discussed. For the normal mode, direct momentum addition into separated boundary layer plays an important role in separated-flow control. On the other hand, for the burst mode, vortices generated by the DBD plasma actuator enhance fluid mixing, and free stream momentum is induced into the separated flow. This indirect momentum induction plays an important role for the burst mode.

Second, the burst frequency effect of the DBD plasma actuator on the control of separated flow over the airfoil is discussed. For the burst mode, non-dimensional burst frequency F^+ based on a chord length and a free stream velocity is often discussed as an important parameter when the effectiveness of burst waves is considered. In this study, F^+ is set to one and six. In the conditions of the present analysis, $F^+ = 6$ achieves better aerodynamic characteristics and robustness against the installed locations than $F^+ = 1$. This is because the dominant mechanism of the separated-flow control is different between the $F^+ = 1$ and $F^+ = 6$. The $F^+ = 1$ enhances the vortex shedding from the separated shear layer, and the flow field has the unsteady large separated region near the leading edge although the massive separation from the leading edge is avoided. In addition, this mechanism associated with the large fluctuation of lift. The $F^+ = 6$ suppresses the separated flow mainly by promoting the turbulent mixing.

In chapter 6, transient states in which separated flows are controlled and separated regions are gradually suppressed, are discussed. The results show the transient states consist of following three stages: 1) the large lift and drag decreasing temporally occur. 2) the peak of negative pressure near the leading edge gradually recovers. 3) the fluid mixing region moves upstream gradually, and the flow goes to the quasi-steady state. In particular, on the stage 1), the large lift and drag decreasing which are temporary observed , are caused by advections of the spanwise vortices which involve the free stream to the airfoil surface. This vortex advection plays an important role in the initial stage of separated-flow control.

Finally, in chapter 7, the results of the present analysis are concluded, and guides for the practical use of the DBD plasma actuator are proposed. the conclusions gathered from this study are as follows: There are three mechanisms of separated flow control. The first one is a direct momentum addition into the separated boundary layer (Normal mode), the second one is a spanwise vortex advection to downstream ($F^+ = 1$) and the third one is a mixing enhancement ($F^+ = 6$). At low Reynolds number like this study, the third mechanism is most preferable for separated-flow control because the robustness to the location of the DBD plasma actuators and stable aerodynamic characteristics.

Acknowledgements

I would like to express my deepest gratitude to my advisor, Professor Kozo Fujii of Institute of Space and Astronautical Science/Japan Aerospace Exploration Agency (ISAS/JAXA). His delight personality and wisdom has guided me along the way. Without his invaluable advice, suggestions and encouragement, this work would not have been possible.

I would also like to thank Professor Kenichi Rinoie, Professor Kojiro Suzuki and associate Professor Taro Imamura of Department of Aeronautics and Astronautics at the University of Tokyo and Associate Professor Ryoji Takaki at ISAS/JAXA. I am thankful to them for accepting me to become the thesis committee and their excellent advice and suggestions.

Additional thanks are due to Associate Professor Akira Oyama, Associate Researcher Taku Nonomura, and International Top Young Fellow Soshi Kawai of ISAS/JAXA for their enlightening discussions and constructive comments.

I am also grateful to project members of the K supercomputer. Especially I would like to thank Dr. Hikaru Aono and Dr. Makoto Sato of ISAS/JAXA for their constructive comments.

Special thanks to the present and former members in Professor Fujii's High Speed Aerodynamics Laboratory for their friendship and supporting my research.

This work is partially supported by Global Center of Excellence (GCOE) program "GCOE Mechanical System Innovation (GMSI)."

Finally, I would like to express my sincere thankfulness to my parents and friends. Without their encouragement, this work could not have been completed.

February 2013

Kengo Asada

Contents

List of Figures

List of Tables

Nomenclature

Roman Symbols

a	speed of sound
A	amplitude of oscillation
$a_{cmpt}, b_{cmpt}, c_{cmpt}$	coefficients for compact scheme
BR	burst ratio, BR=$\dfrac{T_{on}}{T_{BST}}$
c	chord length
C_D	drag coefficient
C_L	lift coefficient
C_p	pressure coefficient
D_c	ratio between electrostatic energy added
	from plasma actuator and dynamical pressure
e	total energy per unit volume
E, F, G	fluxes in Navier-Stokes equations
E_i, E_k	electric field vector induced by plasma actuator, $i, k = 1, 2, 3$
f	frequency
f_{base}	input voltage sine wave frequency
f^+	burst frequency, $f^+ = \dfrac{f_{base}\ BR}{n} = \dfrac{1}{T_{BST}}$
F^+	non-dimensional burst frequency, $F^+ = \dfrac{f^+\ c}{U_\infty}$
f_e^+	excitation frequency by active flow control device
F_e^+	non-dimensional excitation frequency, $F_e^+ = \dfrac{f_e^+\ X_{te}}{U_\infty}$
M	Mach number
M_∞	free stream Mach number
n	wavenumber for one burst wave cycle
p	pressure
Pr	Prandtl number
q_c	electric charge

q_i	heat flux vector, $i = 1, 2, 3$
Q	conservative variables in Navier-Stokes equations
Re	Reynolds number based on chord length
S_i	body force vector, $S_i = q_c E_i$, $i = 1, 2, 3$
$S_{max,i}$	maximum magnitude body force vector , $i = 1, 2, 3$
St	Strouhal number
t	time
T	temperature
T_{BST}	burst wave period
T_{on}	period of sine wave switch on in a burst wave period
u, v, w	velocity components in Cartesian coordinate (x, y, z); also u_i, u_k, $i, k = 1, 2, 3$
u', v', w'	velocity fluctuations in Cartesian coordinate (x, y, z)
U, V, W	contravariant velocity components in curvilinear coordinate
U_∞	free stream velocity
x, y, z	Cartesian coordinates; also x_k, $k = 1, 2, 3$
X_{te}	distance between the location of excitation by active flow control device and trailing edge

Greek Symbols

α	angle of attack
$\alpha_{cmpt}, \beta_{cmpt}$	coefficient of compact scheme
α_f	coefficient of filter
γ	specific heat ratio
δ_{ik}	Kronecker's delta, $i, k = 1, 2, 3$
Δ	discretized step size
κ	coefficient of heat conductivity
μ	coefficient of viscosity
ω	circular frequency
ρ	density
$\tau_{i,j}$	viscous stress tensor, $i, j = 1, 2, 3$
ξ, η, ζ	curvilinear coordinates
ζ_w	wall-normal distance

Subscripts

ref	reference value
∞	ambient (free stream) condition

Superscripts

$\acute{}$	filtered quantity
$'$	fluctuation quantity
*	dimensional quantity

Symbols

$\langle Q \rangle$	mean or ensemble average of Q
$\langle Q \rangle_{\mathrm{rms}}$	root mean square of Q
$\lfloor Q \rfloor$	the largest integer less than or equal to Q

Abbreviations

CFD	computational fluid dynamics
CFL	Courant-Friedrichs-Lewy
DBD	dielectric barrier discharge
DES	detached eddy simulation
DNS	direct numerical simulation
GCL	geometric conservation law
ILES	implicit large-eddy simulation
LDV	laser Doppler velocimeter
LES	large-eddy simulation
MILES	monotonically integrated large-eddy simulation
MUSCL	monotonic upstream scheme for conservation laws
PSD	power spectrum density
PIV	particle image velocimetry
RANS	reynolds-averaged Navier-Stokes
RMS	root mean square
TKE	turbulence kinetic energy
TVD	total-variation diminishing
WCNS	weighted compact non-linear scheme

Chapter 1

Introduction

In this chapter, background, related previous studies, studies on flow control in our laboratory and necessity of unsteady computational analysis are described. Then, the objective and outline of this thesis are presented.

1.1 Progress of Separated Flow Control

Separated flows are observed in a variety of applications in aeronautical and mechanical engineering, and they have negative impacts on performance of their applications. Therefore, the control of separated flow has being continuously and extensively investigated because of its large potential payoff and its numerous applications. Especially, in modern design of various aircrafts and rotorcrafts, separated flow control is vital to improving the flight characteristics of airfoils whether the application is highly maneuverable fighters, or micro air vehicles. When flow separates from a wing in flight, the result is loss of lift and increase in drag that threatens the stability of the aircraft and the safety of the pilot.

The control of separated flow is a challenging topic in both industrial and academic research. From the industrial viewpoints, flow control is a way to increase the performance of a given vehicle (aeronautics, car manufacturer and naval industry) or of the production apparatus (chemical industry and energy production). Peculiarly, this technology decreases runway distance, aerodynamic noise of flap, and fuel consumption, while it increases climb rate in aerospace engineering field. This technology also decrease a base drag of automobile and track, energy loss in turbomachinery, noise and vibration of separation flow in internal flow, and aerodynamic noise from wind turbine in mechanical engineering field. From the academic viewpoint, it is exciting theoretical, experimental and computational problem for us to research good knowledge and

evaluation-index about control mechanism of separated flow, in order to find that of the optimal condition. The research on flow control has been one of the major topics in fluid mechanics in the past couple of decades.[7,8,9,10,11,12,13,14,15]

To begin with, separation is typically avoided by geometric changes and by flying the aircraft within the flight envelope. Though giving a fluid-dynamically good design (e.g. low drag configuration and high lift-to-drag ratio airfoil) is a kind of passive flow control, the drastically performance improvement is limited because of limitation in empirical design and constraints in non-aerodynamic issues such as material property and manufacturability.

Most flow control techniques have been focused on control of separation, which has been achieved by either passive or active techniques. The passive separated flow control devises are comparatively simple methods, For example, Figure 1.1 shows vortex generators.[16] Vortex generators consist of small vanes or bumps that create vortices, and delay flow separation and aerodynamic stalling by promoting turbulent transition. However, it induces a drag and weight penalty when the flow does not separate under a cruise condition. Figure 1.2 show a leading edge slat. The slat is aerodynamic surfaces on the leading edge of the wings of fixed-wing aircraft which, allow the wing to operate at a higher angle of attack, avoiding leading-edge separation. The slat can be extended only when it is needed (e.g. takeoff and landing) but it takes several seconds to extend it. Thus it can not respond to sudden change of airstream such as a gust. In addition, the mechanism of extension makes the wing complex.

In order to overcome these weaknesses, active flow control approaches have been researched over the years as an alternative technology of passive separated flow control devises, because the control conditions can be changed for various flight or flow conditions, i.e. on/off design point. Over the past several decades various active flow control concepts have been proposed and evaluated to improve the efficiency and stability of lift systems by controlling flow separation. The flow field is changed globally by locally acting on the flow. The basic idea of active separated flow control have been initiated by Prandtl[17] adding or removing momentum from boundary layer. This may be achieved by arrays of actuators that energize the boundary layer with steady momentum through the wing surface. These types of controlled actuation change the velocity, pressure, and vorticity field around the wing to achieve the desired objectives. Active flow control devises using continuous blowing or suction[18,19,20,21,22] have been investigated due to the effectiveness for controlling or preventing separated flow. However, it are most steady blowing in extremely limited applications (e.g. F-104 Star Fighter and F-4 Phantom of fighter aircraft and US-2 flying boat) because of their drawbacks such as need of

air-supplier systems, heavyweight and the complexity of the systems as shown Fig. 1.3. Figure 1.3 shows US-2 Flying boat and its steady jet blowing systems. The aircraft has additional engine for steady blowing. Furthermore, the steady blowing may also cause a thickening of both the boundary layer and the wake behind the airfoil which leads to increased drag.

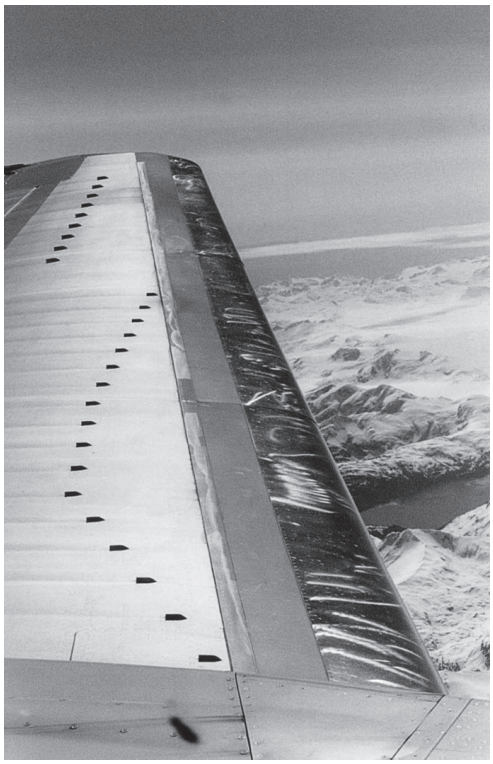

Figure 1.1: Vortex generator on the Boeing 737 (http://www.microaero.com/pages/v_answer.html).

Figure 1.2: Slat of A319 during landing (http://en.wikipedia.org/wiki/File:Voilure_A319.jpg).

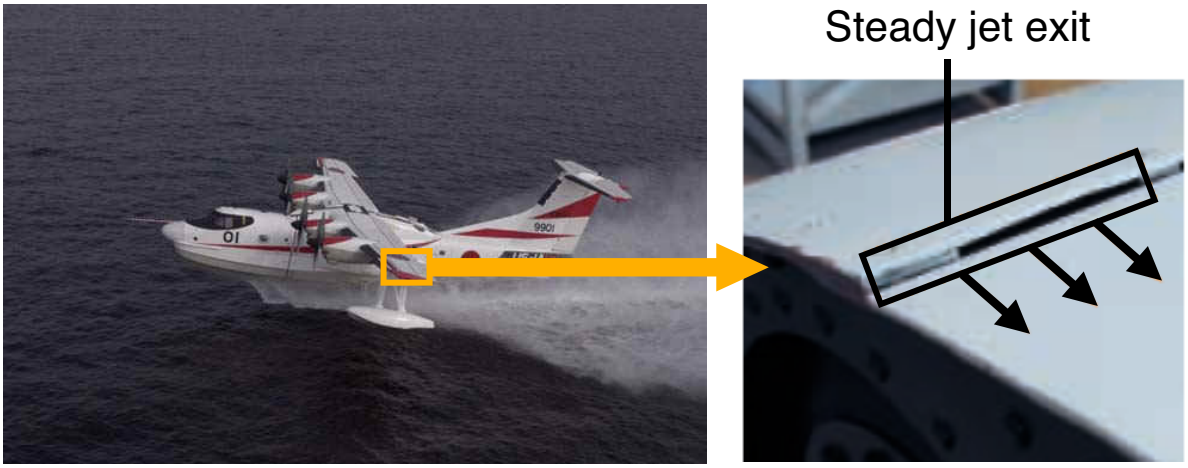

Figure 1.3: Steady jet of US-2 Flying boat (http://www.shinmaywa.co.jp/english/).

1.2 Dielectric Barrier Discharge (DBD) Plasma Actuator

Active flow control using micro-scale devices are getting much attention in various fields. In the aerospace field, "dielectric barrier discharge (DBD) plasma actuator"[23,24,25,26] and "synthetic jet"[27,28] are well investigated within several devices for separation control around airfoil. These devices can control the flow-field by adding the fluctuation to the local flow-field with inducing weak flow (several meters per second). In particular, DBD plasma actuator has a lot of advantages such as simplicity, active control capability, high-speed responsivity and low energy consumption compared to conventional flow control devices.

The most basic DBD plasma actuator which is sometimes called as "single DBD (SDBD) plasma actuator" , is mainly composed of two electrodes and a dielectric as shown in Fig. 1.4. Although it is not clarify in detail how DBD plasma actuator induces the flow, the mechanism is explained briefly as follows.[25] The plasma is generated with the dielectric barrier discharge in the area between the exposed electrode and the dielectric when high alternative-current voltage is applied to the exposed electrode. The ions of the plasma are accelerated by electric field and collide with molecules of atmosphere. As a result, the time averaged flow from the exposed electrode to the insulated electrode is induced. When the DBD plasma actuator is installed near the leading edge of an airfoil and actuated, the flow over the airfoil does not separate and passes along the airfoil surface at the angle of attack at which the flow is naturally separated from the leading edge 1.6. DBD plasma actuator does not require holes and moving part, which are significant from a maintenance viewpoint. Additionally, the actuators can be manufactured to be very thin; meaning that retrofit on existing aircraft skins is possible without major structural redesign. Furthermore, they are flexible, so that they can be formed to various shapes and located on the air vehicles with relative ease. There are no other known actuators that have such flexibility.[29] In the aerospace engineering field, the DBD plasma actuator has been expected as a powerful device to control separated flows and has been studied in the past decade worldwide. In Japan, the studies on the DBD Plasma actuator have been also held widely, which is well introduced in the news letter of JSME Fluids Engineering Division by Prof. Kozo Fujii.[30]

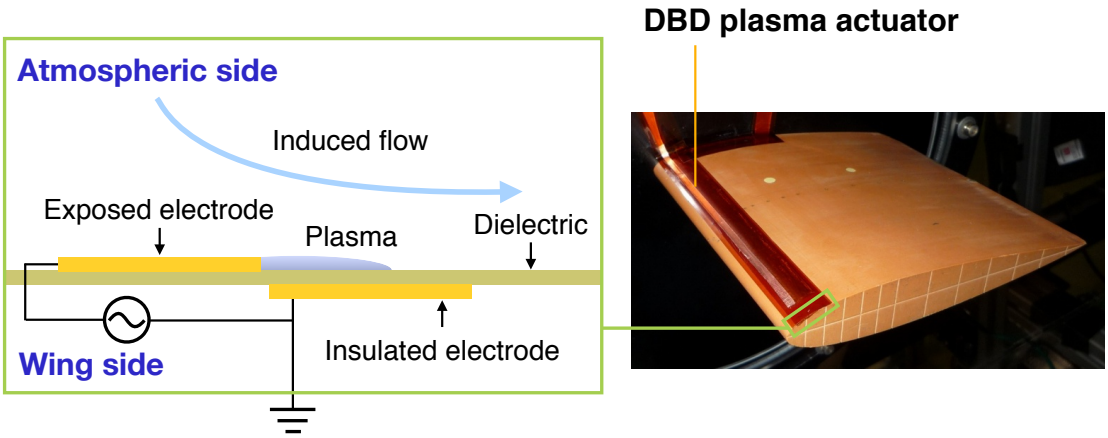

Figure 1.4: Schematic of DBD plasma actuator and an actual DBD plasma actuator installed on a NACA0015 wing.

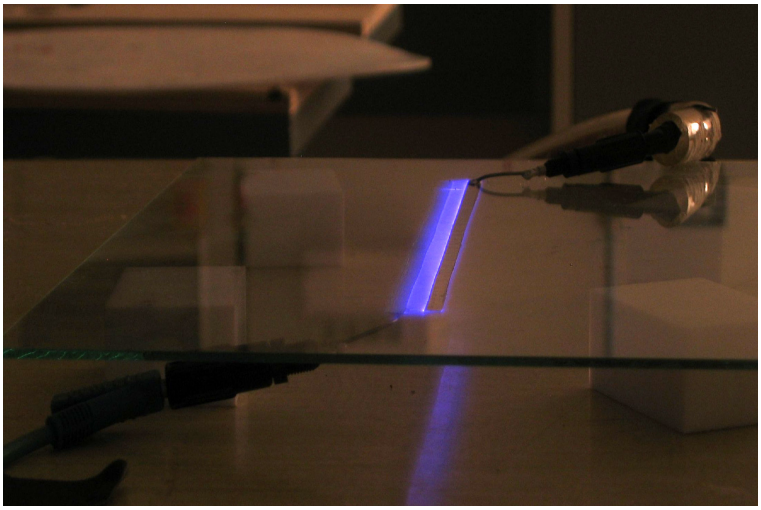

Figure 1.5: Photography of discharge of a DBD plasma actuator (on a glass plate)[1].

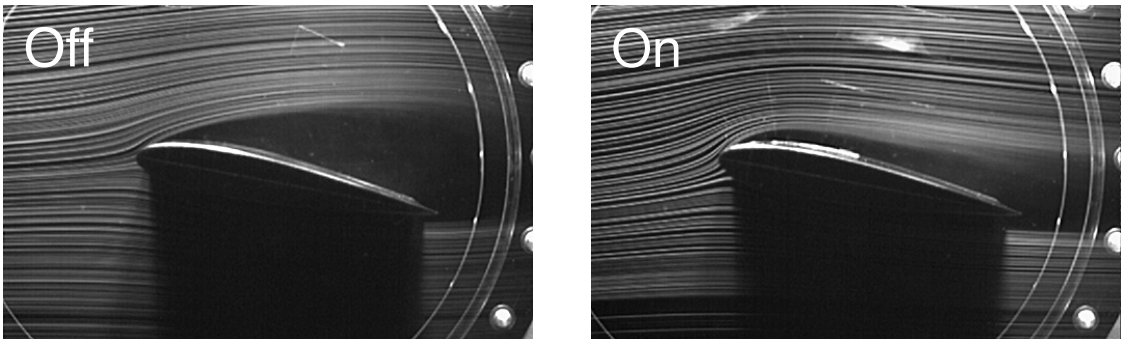

Figure 1.6: Flow fields controlled by DBD plasma actuator.

1.3 Previous Studies of DBD Plasma Actuator

In aerospace engineering fields, the DBD plasma actuator has been introduced by Roth et al.[31] They show that the device changes the boundary layer velocity profile and reduces the friction drag on a flat plate. Corke et al. extend the range of application of the device and show the capability to control separated flows.[32] From this point forward, studies on the DBD plasma actuator has been done actively.

There are many studies about DBD plasma actuator in recent years. Concerning fundamental studies, Corke et al. has presented the suitable electrodes shape of plasma actuator for flow control on airfoil.[32,33,34] Benard et al.[35] demonstrate the versatility of surface discharges for airflow control in real flight atmospheric conditions, and show that the mass flow rate and the induced electric wind velocity exhibit different behaviours when the pressure is decreased. Gregory et al.[36] show that the force production is independent of the density of the neutral particles, but is governed by ion density, volume of the plasma, and the applied electric field. They also show a linear relationship between force production and air pressure, with the force going to zero at vacuum conditions. Abe et al. investigate the effect of applied-voltage wave forms[37] and ambient gas species[2] on the momentum transfer performance. The results show that the wave form of the high voltage has a significant effect; 1) the steeper the up-going part of the high voltage wave is, the larger the momentum transfer is, 2) both negative and positive part of the sinusoidal wave equivalently are fundamental for the net momentum transfer and have a significant contribution to the momentum transfer, and show that the momentum transfer in air is greater than that in nitrogen gas at pressures of less than 1 atm, which suggests a considerable contribution of oxygen molecules in the air. Forte et al.[1] investigate that the effect of frequency and applied voltage on the induced velocity and,

show the effects increases with applied voltage but reduces as flow velocity increase. Enloe et al.[38] show that the presence of oxygen in the Earth's atmosphere plays a substantial role in the efficiency of the actuator.

In a sinusoidal wave cycle, it is known the discharge occors two times (Fig. 1.7). With regard to provided momentum by the DBD plasma actuator in this discharges, there are two main theories: "push—push"[39] and "push—pull"[40] theories. In the former theory, the DBD plasma actuator provides the momentum in a definite direction (from exposed electrode to insulated electrode) on both positive and negative phase of the base sinusoidal wave. Where the positive phase denote the phase when a potential of the exposed electrode is positive. In the later theory, the DBD plasma actuator provides the momentum in the opposite direction on the negative phase to the direction on the positive phase. However, the "push-push" theory has become widely-accepted theory in the recent years by many researcher's efforts. For example, Font et al.[41] show DBD plasma actuator produces two positive (accelerating) forces per AC cycle by temporal force measurements. Font et al.[42] also show that oxygen plays an important roll on the negative phase, and the results support the "push-push" theory through computer simulations using particle-in-cell Monte Carlo methods. Nishida and Abe[43] propose a simple fluidic plasma model and validated comparing with experimental results. The results of study show the same trends as the Font's results.[41]

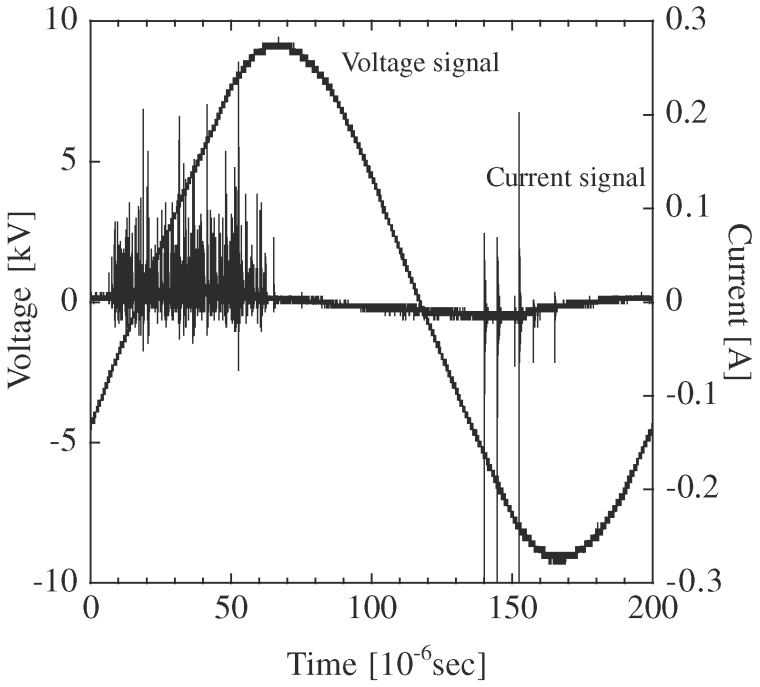

Figure 1.7: Typical behavior for a high voltage and electric current[2].

1.3.1 Experimental Studies of Separated-Flow Control

Especially, in the separation control field, the objectives of a lot of studies are application and almost all the studies are conducted with experimental approach. First, Corke et al. apply DBD plasma actuator to suppressing trailing-edge separation over NACA009.[32] They also apply the device to suppressing massive separation from a leading-edge over NACA66$_3$-018,[34] and show that use of unsteady input voltage that is called a "duty cycle" or a "burst wave" gives higher separation control capability with less input energy.[44,45,46] The burst wave is the unsteady alternative current switched on and off periodically as shown in Fig. 1.8. In the present study, the operating condition when the DBD actuator operated with burst wave, is called as a "bust mode" while the operating condition when the DBD actuator operated with basic sinusoidal wave, is called as a "normal mode". Non-dimensional burst frequency F^+ (which is normalized by chord length and free stream velocity) is often discussed as an important parameter when the effectiveness of burst wave is considered. Many researchers investigate the optimum F^+ value for separation control over an airfoil, and there are two assertions: 1) $F^+ \approx 1$ is the optimum frequency[44,45,47] and 2) $F^+ \approx 10$ is the optimum frequency.[46,3] Figure 1.9 shows lift coefficients of the controlled flow over NACA0015 aifoil versus dimensional burst frequency, obtained by Asada et al.. In this figure, 100 [Hz] and 600 [Hz] correspond to $F^+ = 1$ and $F^+ = 6$ respectively. Blue and red color plots denote results of burst mode operations and green line denote a result of normal mode. The figure shows the burst mode is clearly effective and especially $F^+ = 6$ is more effective than $F^+ = 1$ for lift enhancement.

The similar topic is more discussed in the studies of separation control with other devices. Greenblatt and Wygnanski[48] reviewed the previous studies in terms of nondimensional excitation frequency. They summarize that $F^+ \approx 1$ is the most effective on the control of massively separated flow around airfoil. Glezer and Amitay[49] who use the synthetic jet as an excitation device discuss the difference in the response of the separated flow to actuation at two distinct frequency bands ($F^+ \approx 1$ and $F^+ \approx 10$). They show that the first band includes the unstable frequencies of the separating shear layer, and the actuator makes a Coanda-like deflection by modifying the evolution of large vortical structures that are shed from the separation line into the wake, whereas the second frequency band is well above the receptivity range, and there is a different control strategy that emphasizes full or partial suppression of separation by fluidic modification of the apparent aerodynamic shape of the surface. In the study of DBD plasma actuator, it is not known whether there is different control strategy or not.

As mentioned above, one of the advantage of the DBD plasma actuator is high-speed responsivity. Therefore, DBD actuator is expected as a device which can respond sudden change of airstream. This advantage is particularly useful for micro air vehicle (MAV) application. Concerning quasi-steady flow, many studies has done as shown above. However the short term transient flows are not as widely discussed, though there are some studies on other micro devices.[50]

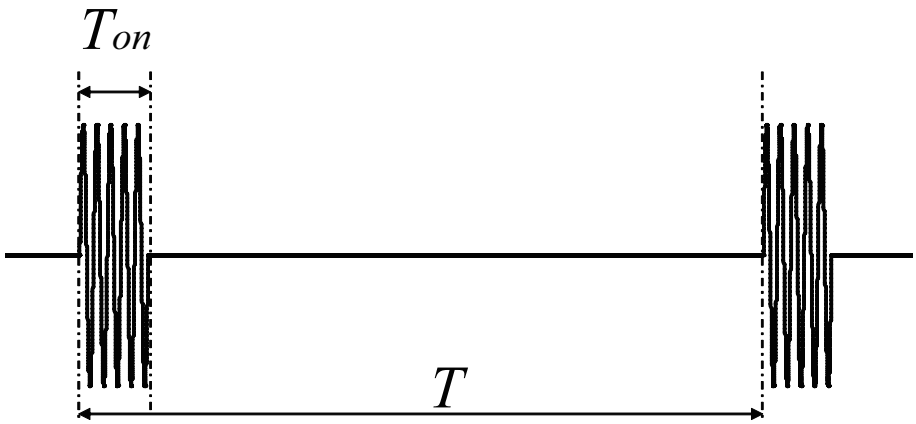

Figure 1.8: Schematic of burst wave

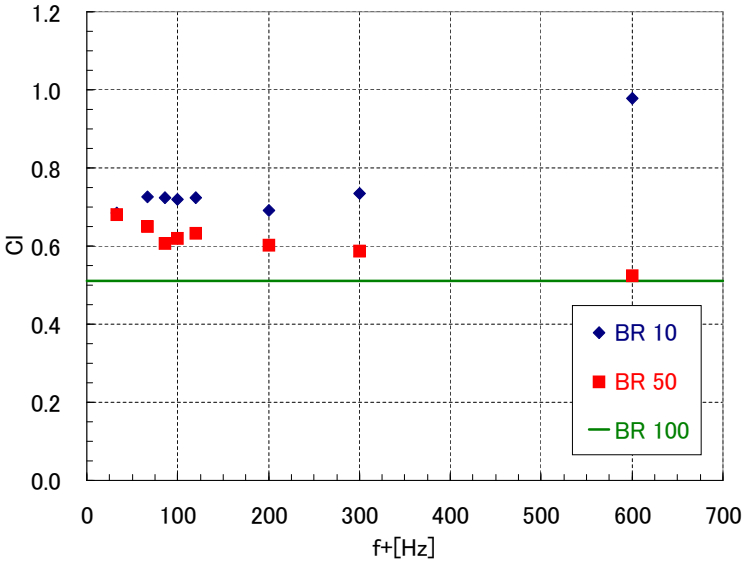

Figure 1.9: C_L vs. f^+ on $Re_c = 6.3 \times 10^4$ (BR = 10, 50, 100%)[3].

1.3.2 Computational Studies of Separated-Flow Control

The computational approaches are attractive for understanding the unsteady flow fields. So far, computational fluid dynamics (CFD) has been taking a role for understanding

the flow fields in engineering or scientific research.

The previous studies[47,51] indicate that turbulent transition and excitation of unsteadiness are important for separation control using DBD plasma actuator. Therefore it is necessary to utilize approach which can treat unsteady flows including turbulence. There are mostly three ways to simulate turbulence flow.

First, one of the most accurate ways is a direct numerical simulation (DNS). DNS resolves the Kolmogorov vortex scale[52] which is the minimum vortex scale in the turbulent flow. (In general, DNS is computed with central difference schemes where the flow fields are stabilized by the physical viscosity without numerical viscosity or dissipation.) In this way, enormous grid points are required to resolve the vortices and the applicable range of this approach is only limited to simple and moderate Reynolds number flows (e.g. attached turbulence boundary layer).

Second way is the method to solve the Reynolds averaged Navier-Stokes equations (RANS). RANS simulation is the most modeled method and only produces time (ensemble) averaged flow and turbulence data (where obtained turbulence data, e.g. turbulence kinetic energy and Rynolds stress, depends on the RANS methods). Therefore RANS simulation needs only steady computation and low resolution of scheme and grids. As a result, it takes very low computational cost. Tsubakino et al. *et al.*[4] show that the effect of locations of dielectric barrier discharge (DBD) plasma actuators is computationally investigated with two-dimensional RANS computation in order to control the flow separations around NACA 0012 airfoil. The difference in the layout is not observed when the induced velocity is low with a low input voltage. Whereas, the difference appears when the induced velocity is enough high. Totally, to induce higher velocity at the leading edge is the most effective way to control the flow separation in this condition (Fig.1.10). Besides, the use of multiple actuators is discussed. The multiple actuators can reduce the input energy.

However as mentioned above, RANS simulation only can obtain ensemble-averaged flow data, and has limited accuracy for especially unsteady massively separated flow or shear flow as shown by the results of base flow by Kawai.[53] Therefore this method does not suitable for unsteady flows which involve separation or transition when detailed analysis is required.

Third way is large-eddy simulation (LES) or monotonically integrated LES (MILES) which resolves only large vortex with grid scale where the effect of small vortices are evaluated in sub-grid scale model or numerical dissipation. The resolved range of the LES and DNS are shown in the left side of Fig. 1.11 and instantaneous spatial distribution of fluid quantity are shown in the right side of Fig. 1.11. Spatial distribution of LES

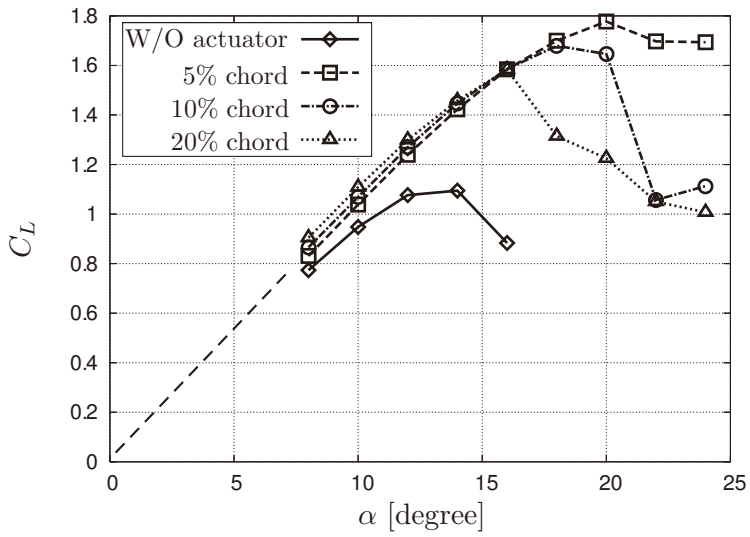

Figure 1.10: Controlled lift coefficients versus α ($Dc = 50$)[4].

becomes filtered one of DNS. In LES approach, coarser resolution is required than in DNS, while much finer resolution is needed than in RANS. Therefore it was difficult to compute flow fields with LES approach due to its computational costs. Recently the high performance computers, however, has been developed whose computing ability is order of peta FLOPS. (e.g. K computer has a computational speed of 10 peta FLOPS). In addition, the high resolution schemes, such as a compact scheme[54] and weighted compact non-linear scheme(WCNS),[55,56] which reduce the computational costs by the factor 10 - 100 times compared with conventional second order schemes, are developed. Thanks to the high performance computers and the high resolution schemes, LES-like computation is becoming capable. Recently some researchers has worked on studies using LES. Visbal et al.[47,51] show that three-dimensional vortices are induced by the DBD plasma actuator in burst mode. Rizzetta and Visbal,[57,58] and Asada et al.[59,60] show a possibility that inducing three-dimensional vortices in design by spatially inhomogeneous DBD plasma actuator are more effective for separation control than homogeneous one.

Although these results show the importance of three-dimensional vortices and unsteady actuation like burst mode, detailed phenomena and mechanism of separated-flow control are not discussed well. In addition, transient flows are not as widely documented as well as experimental study although Riherd et al.[61] discussed that the transient effects of the flow which is controlled by DBD plasma actuator at a trailing edge, by conducting LES trailing edge.

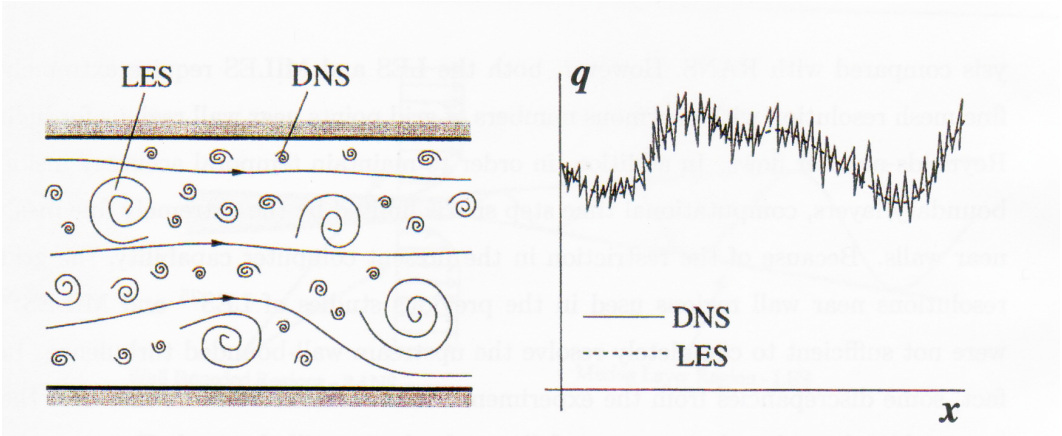

Figure 1.11: Schematic representation of turbulent motion (left) and the distribution of spatially filtered quantity (right)[5].

1.4 Objectives

As discussed before, although the availability of a DBD plasma actuator for separated-flow control is verified by experimental studies, there are no clear guides for operation of the DBD plasma actuator, and detailed phenomena and mechanisms of separated-flow control do not discussed enough because most of these studies are conducted by trial-and-error approaches. This lack of understanding of the separation-control mechanism keeps the DBD plasma actuator away from practical use. Therefore, final purpose of the present study is to clarify the mechanism of separated-flow control of the DBD plasma actuator, and to provide guidelines for practical use of DBD plasma actuator.

Especially following terms are investigated with numerical simulations.

Relationships between evaluation-index and aerodynamic characteristics

First objective is to make clear means of evaluation-index (e.g. lift coefficients C_L). In the almost previous studies discussed above, C_L is utilize as a criterion for effect of separated flow control. However, the relation between flow fields such as attached regions and C_L value is not clear. Thus first of all, we discuss the relations between the aerodynamic characteristics of an airfoil which is improved by the DBD plasma actuator and the evaluation-index of separation control.

Effects of burst actuations

With regard to the separated flow control by DBD plasma actuator on the burst mode, we found variability in optimum value of non-dimensional bust frequencies F^+ among the previous studies. Second objective of the present study is to clarify the effect of burst actuation. Especially, burst mode effect and burst frequency effect to understand the reason behind the variability by discussion of detailed quasi-steady flow fields.

Transient states of controlled flows

Concerning quasi-steady flows, many studies have done. However the transient process in which separated flows gradually introduced to attached flows, has not discussed enough. Third objective is to discuss the transient state, and to clarify the mechanism of separation control.

In order to perform these objectives, the flow fields controlled by DBD plasma actuator is analyzed with large-eddy simulation (LES) using compact difference scheme, because the present computational resources are not sufficient for DNS, and the analysis of vortex structure that can be resolved using LES is sufficient for understanding the flow control mechanism.

In this study, implicit LES (ILES) is utilized instead of LES with SGS model. The ILES approach which any explicit sub-grid scale terms are not used while numerical viscosity (dissipation and dispersion) of upwinding scheme[62,63,64] or high-order filtering procedure[65,66,67] are used to dissipate the small waves compared with grid size. As a result, reasonable energy spectra are obtained with the ILES approaches. Moreover, ILES is sufficient stable.

1.5 Outline of This Thesis

In chapter 2, problem settings are presented. First, is Target flow for Separation Control is presented. Then, the parameters of DBD plasma actuator and Non-dimensionalization of the parameters are explained. Finally, the case names are noted.

In chapter 3, numerical methods employed in this study are described. CFD methodology, which is employed in the computation of fluid is explained. Then, the DBD plasma actuator model which is introduced to the fluid computation.

In chapter 4 validation results of this study are described. First, for the section 5.2 mean pressure values and grid resolutions are discussed. Second, for the section 5.3 mean statistics and a grid convergence and grid resolutions are discussed.

In chapter 5 quasi-steady flows which are controlled by the DBD plasma actuator are discussed. First, the relationship between aerodynamics characteristics and the effect of separation control is discussed. Second, the burst frequency effect is discussed.

In chapter 6, the transient processes in which the separated flow is controlled and the separated region is suppressed gradually are discussed.

In chapter chapter 7 the results of this thesis are summarized with the conclusions.

Chapter 2

Problem Settings

2.1 Target Flow for Separation Control

In this study, the flow-field controlled by a DBD plasma actuator around NACA0015 at a moderate Reynolds number is analyzed with computational fluid dynamics (CFD) because the flow around this airfoil is well investigated in previous studies.

2.2 Free Stream Conditions

Free stream conditions are decided by considering the previous experimental study.[3] Figure 2.1 shows lift curves of the NACA0015 at moderate Reynolds numbers (Re_c = 44,000, 63,000, 100,000, Re_c is the Reynolds number based on chord length and free-stream velocity). These curves C_L values are calculated from the measured pressure values. In this study, massively separated-flow from the leading edge is targeted for separated-flow control. At each Reynolds number, the flows are regarded as stalled at α=14 degs. At Reynolds number 63,000 and 44,000, the flows also are regarded as stalled at α=12 degs. In the previous study,[3] wealth of experiments have done at Reynolds number 63,000. Thus, Reynolds number $Re_c = 63,000$ is chosen. With regard to angle of attack, α=12 degs in chapter 5 and α=12 degs in chapter 6 is chosen respectively. Details are explained in chapter 4.

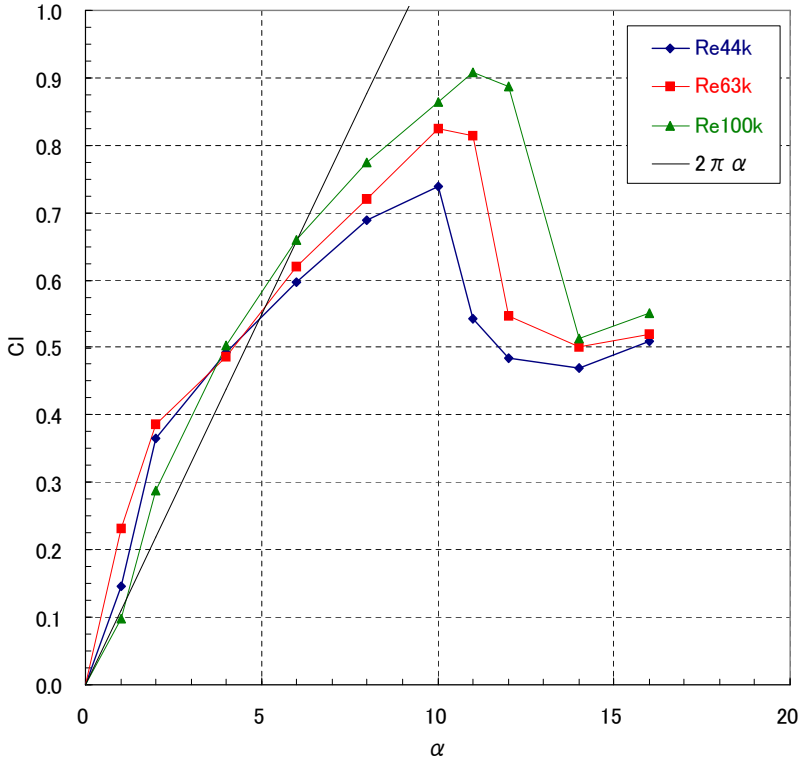

Figure 2.1: NACA0015 lift curves obtained by pressure measurements[3] ($Re_c = 4.4 \times 10^4, 6.3 \times 10^4, 10.0 \times 10^4$).

2.3 DBD Plasma Actuator Parameters

2.3.1 Parameters of Burst Wave

Burst waves consist of sinusoidal waves can be represented with four parameters (A^*, f^*_{base}, T^*_{BST}, and T^*_{on}) as flow:

$$V(t)^* = \begin{cases} A^* \sin(2\pi f^*_{base} t^*) & mT^*_{BST} \leq t^* \leq T^*_{on} + mT^*_{BST} \\ 0 & T^*_{on} + mT^*_{BST} \leq t^* \leq (m+1)T^*_{BST} \end{cases} \quad (m = 0, 1, 2 \ldots), \quad (2.1)$$

where m is an integer, A^* is an amplitude of the base sinusoidal wave, f^*_{base} is a frequency of the base sinusoidal wave, T^*_{BST} is a burst period, T^*_{on} is a period of sinusoidal wave switch on in a burst wave period. Superscripts $*$ denote dimensional values.

We can represent the burst wave with other parameters depend on the objectives of studies. Especially, on the field of separated-flow control, burst ratio BR and burst frequency F^* are used instead of T^*_{BST} and T^*_{on}. Relations between these parameters are as follow:

$$BR = \frac{T^*_{on}}{T^*_{BST}}, \tag{2.2}$$

$$F^* = \frac{1}{T^*_{BST}}. \tag{2.3}$$

As other representing parameters, we can consider n which is a wave number in T^*_{on}. A relation between the parameters in Eq. 2.1 as flow:

$$n = f^*_{base} T^*_{on}. \tag{2.4}$$

When the BR, n, and f^*_{base} are used F^* is written as follow:

$$F^* = \frac{BR}{n} f^*_{base}. \tag{2.5}$$

As written above, we can decide the burst wave form with four parameters. Because A^* does not depend on other parameters, we only chose three parameters from BR, T^*_{BST}, T^*_{on}, F^*, f^*_{base}. Of course new parameters can be defined by combining these parameters. Table 2.1 shows combinations of the parameters.

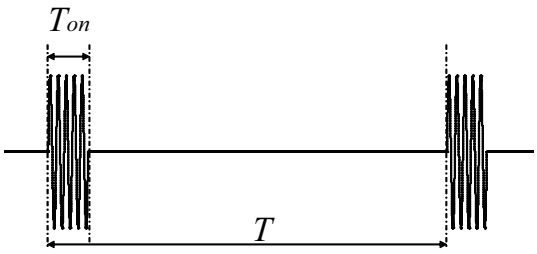

Figure 2.2: Schematic of burst wave.

Table 2.1: Combinations of the representing parameters for the burst wave.

	BR	T^*_{BST} or F^*	T^*_{on}	f^*_{base}	n
Set 1		✓		✓	✓
Set 2		✓	✓		✓
Set 3		✓	✓	✓	
Set 4	✓			✓	✓
Set 5	✓		✓		✓
Set 6	✓		✓	✓	
Set 7	✓	✓			✓
Set 8	✓	✓		✓	

2.3.2 Non-dimensionalization of Burst Frequency

In previous studies, the Non-dimensional burst frequency F^+_u is often discussed as an important parameter. F^+_u is obtained by non-dimensionalizing F^* with the chord length of airfoil c^* and the free stream velocity U^*_∞ as follow:

$$F^+{}_u = \frac{c^*}{u^*_\infty} F^* = \frac{c^*}{u^*_\infty} \frac{BR}{n} f_{base}{}^*. \tag{2.6}$$

We can also use the free stream sound velocity to non-dimensionalize F^*. When the non-dimensionalized burst frequency with the free stream sound velocity is denoted by F^+_a, a relation between F^+_a and F^+_u is as follow:

$$F^+_a = M_\infty F^+_u, \tag{2.7}$$

where subscript a and u show reference velocity (a: free stream sound velocity, u: free stream velocity).

Generally, non-dimensional frequencies based on free stream sound velocity and free stream velocity are transformed as follow:

$$f_u = \frac{f^*\ c^*}{U^*_\infty}, \tag{2.8}$$

$$f_a = M_\infty f_u. \tag{2.9}$$

Also non-dimensional times are transformed as follow:

$$t_a = \frac{1}{M_\infty} t_u. \tag{2.10}$$

F^+_a is represented by dimensional parameters as follow:

$$F^+_a = \frac{BR}{n} f_{base_a} = \frac{M_\infty\ BR}{n} f_{base_u} = \frac{M_\infty\ BR\ c^*}{n\ U^*_\infty} f_{base}{}^* \tag{2.11}$$

When we consider following condition,

$$f^*_{base} = 60\ [Hz],\ c^* = 1\ [m],\ U^*_\infty = 1\ [m/s],$$

$$BR = 0.1,\ n = 1,\ M_\infty = 0.2,$$

non-dimensional frequencies become by (2.8), (2.9), and (2.11), as follow:

$$f_{base_u} = 60,\ F^+_u = 6,$$

$$f_{base_a} = 12,\ F^+_a = 1.2.$$

2.3.3 Non-dimensional Parameters of DBD plasma Actuator and Fluid Analysis

In this study, compressible Navier-Stokes equations are adopted as fluid governing equations and the effect of DBD plasma actuator is introduced to the Navier-Stokes equations as source terms (body force terms). When the source terms are introduced to the Navier-Stokes equations, non-dimensional numbers D_c and Lr appear in the equations in addition to Reynolds number Re, Mach number M_∞. The D_c denotes a ratio between electrostatic energy added by plasma actuator and dynamical pressure. The Lr denotes a ratio between the reference length of fluid and the reference length of DBD plasma actuator. Each parameter is represented as follow:

$$Re_u = \frac{\rho_\infty^* U_\infty^* \, c^*}{\mu_\infty^*}, \; M_\infty = \frac{u_\infty^*}{a_\infty^*}, \; D_{c;u} = \frac{q_{ref}^* \phi_{ref}^*}{\rho_\infty^* {U_\infty^*}^2}, \; Lr = \frac{l^*}{c^*}. \tag{2.12}$$

If Mach numbers of the considering flows are low enough ($M_\infty \leq 0.3$) everywhere, it is known that the flow fields only whose Mach numbers are deferent can be regarded as almost same. When a compressible CFD code is used, from the computational efficiency perspective, high Mach number is chosen as the free stream condition as much as possible. In general, in compressible CFD code, velocity is non-dimensionalized by the free stream sound velocity. Re_u and $D_{c;u}$ based on free stream velocity are transformed to Re_a and $D_{c;a}$ as follows:

$$Re_a = \frac{Re_u}{M_\infty}, \; D_{c;a} = {M_\infty}^2 \; D_{c;u} \tag{2.13}$$

In this study, these non-dimensional parameters are set to follows:

$$Re_u = 63,000, \; M_\infty = 0.2, \; D_{c;u} = 1, \; 8, \; Lr = 0.01. \tag{2.14}$$

2.4 DBD Plasma Actuator Operating Conditions

The two operating conditions are adopted in the present study. One is the case called "normal mode" and the other is the case called "burst mode", where the normal mode denotes the operating condition in which normal alternative current is used as the input voltage to the DBD plasma actuator, and the burst mode denotes the operating condition in which the unsteady alternative current switched on and off periodically is used. The burst frequency F_u^+ is often discussed as an important parameter in the study of the DBD plasma actuator with burst wave. Many researchers investigate the optimum F_u^+

value for separation control over an airfoil, and there are two assertions that $F_u^+ \sim 1$ is the optimum frequency[44] and $F_u^+ \sim 6$ is the optimum frequency.[3] That is why, the values 1 and 6 are chosen as the non-dimensional burst frequency in this study. In addition, because the location of the DBD actuator is a little different in these studies, the 0 % and 5 % chord length from the leading edge are chosen as the locations of the DBD plasma actuator in this study, to investigate an effect of DBD plasma actuator location.

In the remainder of this thesis, non-dimensional parameters based on free stream velocity of the DBD plasma actuator are basically discussed. Therefore, non-dimensional parameters are abbreviated by omitting subscripts "u".

2.5 Case Names

The actual DBD plasma actuator parameters are shown in each Chapter 5, and 6. The flow-field without the DBD plasma actuator is calculated as the baseline case, and this case is named "DBD-off." In the normal mode case, D_c is varied to discuss about the effect of D_c. The cases of the normal mode are named "NM_DcXX" such as "NM_Dc8" which denotes normal mode and $D_c = 8$ case. The cases of the burst mode are named "BM_Xp_FX_DcXX" such as "BM_0p_F1_Dc8" which denotes that the actuator is operated in the burst mode and located at the leading edge, $F^+ = 1$ and $D_c = 8$ case.

Chapter 3

Numerical Methods

In this chapter, numerical methods used in the present study are presented. First, methods of fluid analysis are described. The in-house code LANS3D which is utilized for the analysis of the present study, is introduced. Then governing equations of fluid are noted. The numerical schemes to solve the equations, the boundary conditions, and the grid systems are explained. Finally, the numerical model of the DBD plasma Actuator is presented.

3.1 Methods of Fluid Analysis

3.1.1 LANS3D

In this research, in-house code LANS3D[68,69,70] (which stands for "LU-ADI[71,72,73,74] Navier-Stokes code for three-dimensional flows") developed at ISAS/JAXA, is used. This code was developed by Prof. Kozo Fujii and Prof. Shigeru Obayashi (Currently Tohoku University), and modified by their colleagues. This code is based on an efficient and accurate method for complicated flow field by solving compressible Navier-Stokes equations. In recent years, Dr. Nobuyuki Iizuka implemented "ADI-SGS" method, Dr. Soshi Kawai implemented "LES/RANS hybrid methodology" and "compact difference scheme" and Dr. Taku Nonomura implemented "weighted compact nonlinear scheme" for this code. The latest version is written in Fortran 90 and parallelized by message passing interface (MPI) and autoparallelization. In addition, the scalar tunning of the code has been extremely done.[75] The algorithm used in this code and how it has been improved so far explain two important aspects of the computational fluid dynamics (CFD) codes: efficiency and accuracy. Some of the application examples show the capability of the code for engineering problems[76] as well as physical problems.[77] The computa-

tional methods, which are implemented in LANS3D and also used in this research, are described in following sections.

3.1.2 Governing Equations

The conservation form of the compressible Navier-Stokes equations in the three-dimensional, which are the governing equations of the fluid dynamics, is introduced.[78,79,80]

Navier-Stokes Equations in Cartesian Coordinate System

Three-dimensional Navier-Stokes equations in the Cartesian coordinate system are written as follows.

$$\frac{\partial Q^*}{\partial t^*} + \frac{\partial E^*}{\partial x^*} + \frac{\partial F^*}{\partial y^*} + \frac{\partial G^*}{\partial z^*} = \frac{\partial E_v^*}{\partial x^*} + \frac{\partial F_v^*}{\partial y^*} + \frac{\partial G_v^*}{\partial z^*}, \tag{3.1}$$

$$Q^* = \begin{bmatrix} \rho^* \\ \rho^* u^* \\ \rho^* v^* \\ \rho^* w^* \\ e^* \end{bmatrix}, \quad E^* = \begin{bmatrix} \rho^* u^* \\ \rho^* u^{*2} + p^* \\ \rho^* u^* v^* \\ \rho^* u^* w^* \\ (e^* + p^*)\, u^* \end{bmatrix}, \quad F^* = \begin{bmatrix} \rho^* v^* \\ \rho^* v^* u^* \\ \rho^* v^{*2} + p^* \\ \rho^* v^* w^* \\ (e^* + p^*)\, v^* \end{bmatrix}, \quad G^* = \begin{bmatrix} \rho w^* \\ \rho^* w^* u^* \\ \rho^* w^* v^* \\ \rho^* w^{*2} + p^* \\ (e^* + p^*)\, w^* \end{bmatrix},$$

$$E_v{}^* = \begin{bmatrix} 0 \\ \tau_{xx}^* \\ \tau_{xy}^* \\ \tau_{xz}^* \\ \beta_x^* \end{bmatrix}, \quad F_v{}^* = \begin{bmatrix} 0 \\ \tau_{yx}^* \\ \tau_{yy}^* \\ \tau_{yz}^* \\ \beta_y^* \end{bmatrix}, \quad G_v{}^* = \begin{bmatrix} 0 \\ \tau_{zx}^* \\ \tau_{zy}^* \\ \tau_{zz}^* \\ \beta_z^* \end{bmatrix}, \tag{3.2}$$

$$\begin{aligned} \beta_x^* &= \tau_{xx}^* u^* + \tau_{xy}^* v^* + \tau_{xz}^* w^* - q_x^*, \\ \beta_y^* &= \tau_{yx}^* u^* + \tau_{yy}^* v^* + \tau_{yz}^* w^* - q_y^*, \\ \beta_z^* &= \tau_{zx}^* u^* + \tau_{zy}^* v^* + \tau_{zz}^* w^* - q_z^*, \end{aligned}$$

where ρ^* is the density, u^*, v^*, w^* are the x^*, y^*, z^* direction velocities, respectively. e^*

is the total energy per unit volume, p^* is the pressure, ${\tau_{ij}}^*$ is the viscous stress tensor. Moreover, ${q_i}^*$ is the heat flux vector. First row corresponds to the conservation law of mass, second, third and forth rows correspond to the conservation laws of x^*, y^* and z^* direction momentum, respectively, and fifth row corresponds to the conservation law of energy, where Q^* is the conservative variable vector, E^*, F^* and G^* are the x^*, y^* and z^* direction advection flux vectors, E_v^* F_v^* and G_v^* are the x^*, y^* and z^* direction viscous flux vectors. Asterisks denote the dimensional numbers.

The static pressure p^* is related with the density ρ^*, the velocities u^*, v^*, w^* and the total energy e^* by the equation of state for the ideal gas written as

$$p^* = \rho^* R^* T^* = (\gamma - 1)\left\{e^* - \frac{1}{2}\rho^*\left({u^*}^2 + {v^*}^2 + {w^*}^2\right)\right\}, \tag{3.3}$$

where R^*, T^*, γ represent the gas constant, static temperature and the ratio of specific heats, respectively. For air at standard conditions, R^*=287 [$\mathrm{m}^2/(\mathrm{s}^2 \cdot \mathrm{K})$] and $\gamma = 1.4$.

τ_{ij}^* represent the viscous stress tensor as shown Fig. 3.1. τ_{ij}^* is assumed to be a linear function of the rate of strain tensor. This assumption can be satisfied almost condition without flow past a strong shock wave.[81] τ_{ij}^* for Newtonian fluid becomes

$$\tau_{ij}^* = \mu^*\left(\frac{\partial u_i^*}{\partial x_j^*} + \frac{\partial u_j^*}{\partial x_i^*}\right) + \lambda^*\delta_{ij}\frac{\partial u_k^*}{\partial x_k^*}, \tag{3.4}$$

where μ^* is the dynamic viscosity coefficient, λ^* is the second viscosity coefficient. The tensor δ_{ij} is the Kronecker delta, defined as $\delta_{ij} = 1$ if $i = j$ and $\delta_{ij} = 0$ if $i \neq j$. Where the summation convention for repeated indices is used. Tortal surface stress tensor which consists of the static pressure p^* and the viscous stress tensor τ_{ij}^* is given by

$$\sigma_{ij}^* = -p^*\delta_{ij} + \tau_{ij}^*. \tag{3.5}$$

Consider the averaged normal viscous stress $\overline{P}^*$ (also called the mean pressure).

$$\overline{P}^* \equiv -\frac{\sigma_{ii}^*}{3} \tag{3.6}$$

$$= p^* - \left(\lambda^* + \frac{2}{3}\mu^*\right)\frac{\partial u_i^*}{\partial x_i^*} \tag{3.7}$$

$$= p^* - \mu_B^*\frac{\partial u_i^*}{\partial x_i^*}, \tag{3.8}$$

where the coefficient μ_B^* is called bulk viscosity coefficient, and assumed to be zero in the

Stokes's hypothesis: $\mu_B^* = 0$.[82] Thus, the second viscosity coefficient λ^* can be written as

$$\lambda^* = -\frac{2}{3}\mu^*, \tag{3.9}$$

and ${\tau_{ij}}^*$ becomes

$$\tau_{ij}^* = \mu^* \left(\frac{\partial u_i^*}{\partial x_j^*} + \frac{\partial u_j^*}{\partial x_i^*} - \frac{2}{3}\delta_{ij}\frac{\partial u_k^*}{\partial x_k^*} \right)$$

$$= \mu^* \begin{bmatrix} \frac{2}{3}\left(2\frac{\partial u^*}{\partial x^*} - \frac{\partial v^*}{\partial y^*} - \frac{\partial w^*}{\partial z^*}\right) & \frac{\partial u^*}{\partial y^*} + \frac{\partial v^*}{\partial x^*} & \frac{\partial w^*}{\partial x^*} + \frac{\partial u^*}{\partial z^*} \\ \frac{\partial u^*}{\partial y^*} + \frac{\partial v^*}{\partial x^*} & \frac{2}{3}\left(-\frac{\partial u^*}{\partial x^*} + 2\frac{\partial v^*}{\partial y^*} - \frac{\partial w^*}{\partial z^*}\right) & \frac{\partial u^*}{\partial y^*} + \frac{\partial v^*}{\partial x^*} \\ \frac{\partial w^*}{\partial x^*} + \frac{\partial u^*}{\partial z^*} & \frac{\partial v^*}{\partial z^*} + \frac{\partial w^*}{\partial y^*} & \frac{2}{3}\left(-\frac{\partial u^*}{\partial x^*} - \frac{\partial v^*}{\partial y^*} + 2\frac{\partial w^*}{\partial z^*}\right) \end{bmatrix}. \tag{3.10}$$

The dynamic viscosity coefficient is given by Surtherland's law,

$$\mu^* = \mu_0^* \left(\frac{T^*}{T_0^*}\right)^{\frac{3}{2}} \frac{T_0^* + T_1^*}{T^* + T_1^*}, \quad T_1^* = 111 \text{ [K]}, \quad T_0^* = 273 \text{ [K]}, \quad \mu_0^* = 1.716 \times 10^{-5} \text{ [Pa} \cdot \text{s]}, \tag{3.11}$$

for air.[83]

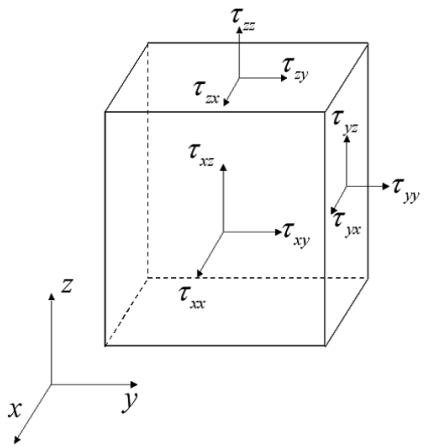

Figure 3.1: Components of viscous stress tensor.

Similar to the stress tensor, the heat flux vector ${q_i}^*$ is assumed to be a linear function

of the gradient of the temperature by Fourier's law:

$$q_i^* = -\kappa^* \frac{\partial T^*}{\partial x_i^*}, \tag{3.12}$$

where κ^* is the thermal conductivity. Moreover Eq. 3.12 is modified with the Prandtl number $Pr = \dfrac{\mu^* c_p^*}{\kappa^*}$ ($= 0.72$ for air) as follows.

$$q_i^* = -\kappa^* \frac{\partial T^*}{\partial x_i^*} = -\frac{\partial \left(\dfrac{\mu^* c_p^*}{Pr} T^* \right)}{\partial x_i^*} = -\frac{1}{\gamma - 1} \frac{\mu^*}{Pr} \frac{\partial a^{*2}}{\partial x_i^*}, \tag{3.13}$$

where c_p^* represents the specific heat at constant pressure, a^* is the speed of sound.

$$c_p{}^* = \frac{\gamma R^*}{\gamma - 1}, \qquad a^* = \sqrt{\gamma R^* T^*} = \sqrt{\gamma \frac{p^*}{\rho^*}}. \tag{3.14}$$

Non-dimensionalization of Navier-Stokes Equations

Equation 3.1 is written in a dimensional form. However it is not suitable to use various flow variables whose orders are different because of inconvenience of a display method and a round-off error. Therefore, in this section, Eq. 3.1 is put into a non-dimensional form.[80]

Flow variables are non-diemensionalized by introducing reference quantity, the density of ambient ρ_∞^*, the sound speed of the ambient condition a_∞^*, the viscosity coefficient of the ambient condition μ_∞^* and the reference length L^*

$$\begin{aligned} x_i &= \frac{x_i^*}{L^*}, \quad t = \frac{t^*}{L^*/a_\infty^*}, \quad \rho = \frac{\rho^*}{\rho_\infty^*}, \quad u_i = \frac{u_i^*}{a_\infty^*}, \quad e = \frac{e^*}{\rho_\infty^* {a_\infty^*}^2}, \\ p &= \frac{p^*}{\rho_\infty^* {a_\infty^*}^2} = \frac{p^*}{\gamma p_\infty^*}, \quad \tau_{ij} = \frac{\tau_{ij}^*}{\mu_\infty^* a_\infty^* / L^*}, \quad q_i{}^* = \frac{q^*}{\mu_\infty^* {a_\infty^*}^2 / L^*}, \end{aligned} \tag{3.15}$$

where no-asterisk variables denote non-dimensional numbers.

Substituting Eq. 3.15 to Eq. 3.1, the non-dimensional Navier-Stokes equations in the Cartesian coordinate system are obtained as follows.

$$\frac{\partial Q}{\partial t} + \frac{\partial E}{\partial x} + \frac{\partial F}{\partial y} + \frac{\partial G}{\partial z} = \frac{1}{Re} \left(\frac{\partial E_v}{\partial x} + \frac{\partial F_v}{\partial y} + \frac{\partial G_v}{\partial z} \right), \tag{3.16}$$

$$Q = \begin{bmatrix} \rho \\ \rho u \\ \rho v \\ \rho w \\ e \end{bmatrix}, \quad E = \begin{bmatrix} \rho u \\ \rho u^2 + p \\ \rho uv \\ \rho uw \\ (e+p)\,u \end{bmatrix}, \quad F = \begin{bmatrix} \rho v \\ \rho vu \\ \rho v^2 + p \\ \rho vw \\ (e+p)\,v \end{bmatrix}, \quad G = \begin{bmatrix} \rho w \\ \rho wu \\ \rho wv \\ \rho w^2 + p \\ (e+p)\,w \end{bmatrix},$$

$$E_v = \begin{bmatrix} 0 \\ \tau_{xx} \\ \tau_{xy} \\ \tau_{xz} \\ \beta_x \end{bmatrix}, \qquad F_v = \begin{bmatrix} 0 \\ \tau_{yx} \\ \tau_{yy} \\ \tau_{yz} \\ \beta_y \end{bmatrix}, \qquad G_v = \begin{bmatrix} 0 \\ \tau_{zx} \\ \tau_{zy} \\ \tau_{zz} \\ \beta_z \end{bmatrix}, \tag{3.17}$$

$$\begin{aligned} \beta_x &= \tau_{xx}u + \tau_{xy}v + \tau_{xz}w - q_x, \\ \beta_y &= \tau_{yx}u + \tau_{yy}v + \tau_{yz}w - q_y, \\ \beta_z &= \tau_{zx}u + \tau_{zy}v + \tau_{zz}w - q_z, \end{aligned}$$

$$p = (\gamma - 1)\left\{ e - \frac{1}{2}\rho\left(u^2 + v^2 + w^2\right)\right\}, \tag{3.18}$$

where Re is the Reynolds number and $M_\infty = u^*_\infty / a^*_\infty$ is the Mach number as defined below.

$$Re = \frac{\rho^*_\infty a^*_\infty L^*}{\mu^*_\infty} = \frac{1}{M_\infty}\frac{\rho^*_\infty u^*_\infty L^*}{\mu^*_\infty}. \tag{3.19}$$

Here, note that Eq. 3.1 and Eq. 3.16 are identical except for $1/Re$ in the right hand side.

The non-dimensional viscosity coefficient μ is given by

$$\mu = \frac{\mu^*}{\mu^*_\infty} = \mu^*_0 \left(\frac{T^*}{T^*_0}\right)^{\frac{3}{2}} \frac{T^*_0 + T^*_1}{T^* + T^*_1} \left[\mu^*_0 \left(\frac{T^*_\infty}{T^*_0}\right)^{\frac{3}{2}} \frac{T^*_0 + T^*_1}{T^*_\infty + T^*_1}\right]^{-1} = \frac{1 + T^*_1/T^*_\infty}{T + T^*_1/T^*_\infty} (T)^{\frac{3}{2}} \tag{3.20}$$

with $T^*_1 = 111$ [K] for air. Therefore in order to obtain a non-dimensional viscosity coefficient, we need to specify the ambient temperature T^*_∞. In the present study, T^*_∞ is set to 288.15 [K] for the international standard atmospher (ISA) at the sea-level condition.

Navier-Stokes Equations in Curvilinear Coordinate System

In order to compute fluid in the domain whose boundary is arbitrary, the Navier-Stokes equations in the Cartesian coordinate system are transformed to the Navier-Stokes equations in the curvilinear coordinate system. A transformation of coordinate system is written as follows.

$$\begin{cases} x = x\left(\xi, \eta, \zeta, \tau\right) \\ y = y\left(\xi, \eta, \zeta, \tau\right) \\ z = z\left(\xi, \eta, \zeta, \tau\right) \\ t = \tau \end{cases} \longleftrightarrow \begin{cases} \xi = \xi\left(x, y, z, t\right) \\ \eta = \eta\left(x, y, z, t\right) \\ \zeta = \zeta\left(x, y, z, t\right) \\ \tau = t \end{cases} \tag{3.21}$$

The differential form of transformation is

$$\begin{cases} dx &= x_\xi d\xi + x_\eta d\eta + x_\zeta d\zeta + x_\tau d\tau \\ dy &= y_\xi d\xi + y_\eta d\eta + y_\zeta d\zeta + y_\tau d\tau \\ dz &= z_\xi d\xi + z_\eta d\eta + z_\zeta d\zeta + z_\tau d\tau \\ dt &= t_\xi d\xi + t_\eta d\eta + t_\zeta d\zeta + t_\tau d\tau \end{cases} \rightarrow \begin{bmatrix} dx \\ dy \\ dz \\ dt \end{bmatrix} = \begin{bmatrix} x_\xi & x_\eta & x_\zeta & x_\tau \\ y_\xi & y_\eta & y_\zeta & y_\tau \\ z_\xi & z_\eta & z_\zeta & z_\tau \\ 0 & 0 & 0 & 1 \end{bmatrix} \begin{bmatrix} d\xi \\ d\eta \\ d\zeta \\ d\tau \end{bmatrix}, \tag{3.22}$$

where $t_\xi = t_\eta = t_\zeta = 0$ and $t_\tau = 1$. Similarly the differential form of the inverse transformation is

$$\begin{cases} d\xi &= \xi_x dx + \xi_y dy + \xi_z dz + \xi_t dt \\ d\eta &= \eta_x dx + \eta_y dy + \eta_z dz + \eta_t dt \\ d\zeta &= \zeta_x dx + \zeta_y dy + \zeta_z dz + \zeta_t dt \\ d\tau &= \tau_x dx + \tau_y dy + \tau_z dz + \tau_t dt \end{cases} \rightarrow \begin{bmatrix} d\xi \\ d\eta \\ d\zeta \\ d\tau \end{bmatrix} = \begin{bmatrix} \xi_x & \xi_y & \xi_z & \xi_t \\ \eta_x & \eta_y & \eta_z & \eta_t \\ \zeta_x & \zeta_y & \zeta_z & \zeta_t \\ 0 & 0 & 0 & 1 \end{bmatrix} \begin{bmatrix} dx \\ dy \\ dz \\ dt \end{bmatrix}, \tag{3.23}$$

where $\tau_x = \tau_y = \tau_z = 0$ and $\tau_t = 1$.

From the relations between Eq. 3.22 and Eq. 3.23, we obtain metrics ξ_x, ξ_y, ξ_z, ξ_t, $\cdots$ with the derivatives x_ξ, x_η, $\cdots$ as follows.

$$
\begin{bmatrix} \xi_x & \xi_y & \xi_z & \xi_t \\ \eta_x & \eta_y & \eta_z & \eta_t \\ \zeta_x & \zeta_y & \zeta_z & \zeta_t \\ 0 & 0 & 0 & 1 \end{bmatrix} = \begin{bmatrix} x_\xi & x_\eta & x_\zeta & x_\tau \\ y_\xi & y_\eta & y_\zeta & y_\tau \\ z_\xi & z_\eta & z_\zeta & y_\tau \\ 0 & 0 & 0 & 1 \end{bmatrix}^{-1}
$$

$$
= J \begin{bmatrix} y_\eta z_\zeta - y_\zeta z_\eta & z_\eta x_\zeta - z_\zeta x_\eta & x_\eta y_\zeta - x_\zeta y_\eta \\ y_\zeta z_\xi - y_\xi z_\zeta & z_\zeta x_\xi - z_\xi x_\zeta & x_\zeta y_\xi - x_\xi y_\zeta \\ y_\xi z_\eta - y_\eta z_\xi & z_\xi x_\eta - z_\eta x_\xi & x_\xi y_\eta - x_\eta y_\xi \\ 0 & 0 & 0 \end{bmatrix}
$$

$$
\begin{bmatrix} -x_\tau (y_\eta z_\zeta - y_\zeta z_\eta) - y_\tau (z_\eta x_\zeta - z_\zeta x_\eta) - z_\tau (x_\eta y_\zeta - x_\zeta y_\eta) \\ -x_\tau (y_\zeta z_\xi - y_\xi z_\zeta) - y_\tau (z_\zeta x_\xi - z_\xi x_\zeta) - z_\tau (x_\zeta y_\xi - x_\xi y_\zeta) \\ -x_\tau (y_\xi z_\eta - y_\eta z_\xi) - y_\tau (z_\xi x_\eta - z_\eta x_\xi) - z_\tau (x_\xi y_\eta - x_\eta y_\xi) \\ 1 \end{bmatrix}, \tag{3.24}
$$

where J is transformation Jacobian from (x, y, z, t) to (ξ, η, ζ, τ):

$$
\begin{aligned} J = \frac{\partial(\xi, \eta, \zeta)}{\partial(x, y, z)} = \left(\frac{\partial(x, y, z)}{\partial(\xi, \eta, \zeta)} \right)^{-1} = 1 / \begin{vmatrix} x_\xi & x_\eta & x_\zeta \\ y_\xi & y_\eta & y_\zeta \\ z_\xi & z_\eta & z_\zeta \end{vmatrix} \\ = \frac{1}{x_\xi y_\eta z_\zeta + x_\eta y_\zeta z_\xi + x_\zeta y_\xi z_\eta - x_\xi y_\zeta z_\eta - x_\eta y_\xi z_\zeta - x_\zeta y_\eta z_\xi}. \end{aligned} \tag{3.25}
$$

In addition, using the chain rule of the partial differentiation, Eq. 3.21 becomes

$$
\begin{aligned} \frac{\partial}{\partial x} &= \xi_x \frac{\partial}{\partial \xi} + \eta_x \frac{\partial}{\partial \eta} + \zeta_x \frac{\partial}{\partial \zeta} + 0 \\ \frac{\partial}{\partial y} &= \xi_y \frac{\partial}{\partial \xi} + \eta_y \frac{\partial}{\partial \eta} + \zeta_y \frac{\partial}{\partial \zeta} + 0 \\ \frac{\partial}{\partial z} &= \xi_z \frac{\partial}{\partial \xi} + \eta_z \frac{\partial}{\partial \eta} + \zeta_z \frac{\partial}{\partial \zeta} + 0 \\ \frac{\partial}{\partial t} &= \xi_t \frac{\partial}{\partial \xi} + \eta_t \frac{\partial}{\partial \eta} + \zeta_t \frac{\partial}{\partial \zeta} + \frac{\partial}{\partial \tau}. \end{aligned} \tag{3.26}
$$

In this study, we do not use any moving or deforming grids. Therefore a following relation is obtained.

$$
\xi_t = \eta_t = \zeta_t = 0 \tag{3.27}
$$

Considering Eq. 3.27, Navier-Stokes equations in the curvilinear coordinate system are

written as follows

$$\frac{\partial \hat{Q}}{\partial \tau}+\frac{\partial \hat{E}}{\partial \xi}+\frac{\partial \hat{F}}{\partial \eta}+\frac{\partial \hat{G}}{\partial \zeta}=\frac{1}{Re}\left(\frac{\partial \hat{E}_v}{\partial \xi}+\frac{\partial \hat{F}_v}{\partial \eta}+\frac{\partial \hat{G}_v}{\partial \zeta}\right), \tag{3.28}$$

where

$$\hat{Q}=J^{-1}\begin{bmatrix}\rho\\ \rho u\\ \rho v\\ \rho w\\ e\end{bmatrix},\quad \hat{E}=J^{-1}\begin{bmatrix}\rho U\\ \rho uU+\xi_x p\\ \rho vU+\xi_y p\\ \rho wU+\xi_z p\\ (e+p)\,U-\xi_t p\end{bmatrix},\quad \hat{F}=J^{-1}\begin{bmatrix}\rho V\\ \rho uV+\eta_x p\\ \rho vV+\eta_y p\\ \rho wV+\eta_z p\\ (e+p)\,V-\eta_t p\end{bmatrix}$$

$$\hat{G}=J^{-1}\begin{bmatrix}\rho w\\ \rho uW+\zeta_x p\\ \rho vW+\zeta_y p\\ \rho wW+\zeta_z p\\ (e+p)\,W-\zeta_t p\end{bmatrix},\quad \hat{E}_v=J^{-1}\begin{bmatrix}0\\ \xi_x\tau_{xx}+\xi_y\tau_{xy}+\xi_z\tau_{xz}\\ \xi_x\tau_{yx}+\xi_y\tau_{yy}+\xi_z\tau_{yz}\\ \xi_x\tau_{zx}+\xi_y\tau_{zy}+\xi_z\tau_{zz}\\ \xi_x\beta_x+\xi_y\beta_y+\xi_z\beta_z\end{bmatrix}$$

$$\hat{F}_v=J^{-1}\begin{bmatrix}0\\ \eta_x\tau_{xx}+\eta_y\tau_{xy}+\eta_z\tau_{xz}\\ \eta_x\tau_{yx}+\eta_y\tau_{yy}+\eta_z\tau_{yz}\\ \eta_x\tau_{zx}+\eta_y\tau_{zy}+\eta_z\tau_{zz}\\ \eta_x\beta_x+\eta_y\beta_y+\eta_z\beta_z\end{bmatrix},\quad \hat{G}_v=J^{-1}\begin{bmatrix}0\\ \zeta_x\tau_{xx}+\zeta_y\tau_{xy}+\zeta_z\tau_{xz}\\ \zeta_x\tau_{yx}+\zeta_y\tau_{yy}+\zeta_z\tau_{yz}\\ \zeta_x\tau_{zx}+\zeta_y\tau_{zy}+\zeta_z\tau_{zz}\\ \zeta_x\beta_x+\zeta_y\beta_y+\zeta_z\beta_z.\end{bmatrix} \tag{3.29}$$

U, V and W are so-called contra-variant velocities along the ξ, η and ζ direction as defined follow.

$$\begin{aligned}U&=\xi_x u+\xi_y v+\xi_z w\\ V&=\eta_x u+\eta_y v+\eta_z w\\ W&=\zeta_x u+\zeta_y v+\zeta_z w\end{aligned} \tag{3.30}$$

The metrics, which are given in Eq. 3.24, are rewritten as follow.

$$\begin{aligned}&\xi_x=J\left(y_\eta z_\zeta-y_\zeta z_\eta\right),\quad \xi_y=J\left(z_\eta x_\zeta-z_\zeta x_\eta\right),\quad \xi_z=J\left(x_\eta y_\zeta-x_\zeta y_\eta\right)\\ &\eta_x=J\left(y_\zeta z_\xi-y_\xi z_\zeta\right),\quad \eta_y=J\left(z_\zeta x_\xi-z_\xi x_\zeta\right),\quad \eta_z=J\left(x_\zeta y_\xi-x_\xi y_\zeta\right)\\ &\zeta_x=J\left(y_\xi z_\eta-y_\eta z_\xi\right),\quad \zeta_y=J\left(z_\xi x_\eta-z_\eta x_\xi\right),\quad \zeta_z=J\left(x_\xi y_\eta-x_\eta y_\xi\right)\end{aligned} \tag{3.31}$$

However it is known that we can not preserve freestream when the metrics are evaluated with Eq. 3.31.[79] In this study, the following conservative form of metrics is used to preserve a freestream for and the compact difference scheme discussed later.

$$\begin{aligned}
\xi_x &= J\left((y_\eta z)_\zeta - (y_\zeta z)_\eta\right), \quad \xi_y = J\left((z_\eta x)_\zeta - (z_\zeta x)_\eta\right), \quad \xi_z = J\left((x_\eta y)_\zeta - (x_\zeta y)_\eta\right) \\
\eta_x &= J\left((y_\zeta z)_\xi - (y_\xi z)_\zeta\right), \quad \eta_y = J\left((z_\zeta x)_\xi - (z_\xi x)_\zeta\right), \quad \eta_z = J\left((x_\zeta y)_\xi - (x_\xi y)_\zeta\right) \\
\zeta_x &= J\left((y_\xi z)_\eta - (y_\eta z)_\xi\right), \quad \zeta_y = J\left((z_\xi x)_\eta - (z_\eta x)_\xi\right), \quad \zeta_z = J\left((x_\xi y)_\eta - (x_\eta y)_\xi\right)
\end{aligned} \tag{3.32}$$

Equation 3.32 equals to Eq. 3.31 analytically. We can preserve a freestream with using metrics in Eq. 3.32 evaluated with the difference operator for advection terms.

3.1.3 Numerical Schemes

Discretization of Governing Equations

A temporal and spatial discretization of governing equations is required to numerically solve these equations whose form is partial differential. Using finite difference operators, Eq. 3.28 is becomes as follow.

$$\left(\delta_\tau \hat{Q}\right)\Big|_{j,k,l} + \left(\delta_\xi \hat{E} + \delta_\eta \hat{F} + \delta_\zeta \hat{G}\right)\Big|_{j,k,l} = \frac{1}{Re}\left(\delta_{v\xi}\hat{E}_v + \delta_{v\eta}\hat{F}_v + \delta_{v\zeta}\hat{G}_v\right)\Big|_{j,k,l}, \tag{3.33}$$

where δ_τ, δ_ξ, δ_η, δ_ζ, $\delta_{v\xi}$, $\delta_{v\eta}$ and $\delta_{v\zeta}$ are finite difference operators, and j, k and l subscripts are indices of discrete points. When the same discretization scheme is used for advection terms and viscous terms, Eq. 3.33 can be rewritten as flow.

$$\left(\delta_\tau \hat{Q}\right)\Big|_{j,k,l} = \left[\delta_\xi\left(-\hat{E} + \frac{1}{Re}\hat{E}_v\right) + \delta_\eta\left(-\hat{F} + \frac{1}{Re}\hat{F}_v\right) + \delta_\zeta\left(-\hat{G} + \frac{1}{Re}\hat{G}_v\right)\right]_{j,k,l} \tag{3.34}$$

The temporal and spatial accuracy depend on the evaluation of the finite difference operators. For example, when the Euler explicit scheme is used for the time integration

and numerical fluxes are introduced, Eq. 3.33 becomes

$$\hat{Q}^{n+1}_{j,k,l} = \hat{Q}^{n}_{j,k,l} - \Delta t \left[\frac{\tilde{E}_{j+\frac{1}{2},k,l} - \tilde{E}_{j-\frac{1}{2},k,l}}{\Delta\xi} + \frac{\tilde{F}_{j,k+\frac{1}{2},l} - \tilde{F}_{j,k-\frac{1}{2},l}}{\Delta\eta} + \frac{\tilde{G}_{j,k,l+\frac{1}{2}} - \tilde{G}_{j,k,l-\frac{1}{2}}}{\Delta\zeta} \right.$$
$$\left. - \frac{1}{Re} \left(\frac{\tilde{E}_{v;j+\frac{1}{2},k,l} - \tilde{E}_{v;j-\frac{1}{2},k,l}}{\Delta\xi} + \frac{\tilde{F}_{v;j,k+\frac{1}{2},l} - \tilde{F}_{v;j,k-\frac{1}{2},l}}{\Delta\eta} + \frac{\tilde{G}_{v;j,k,l+\frac{1}{2}} - \tilde{G}_{v;j,k,l-\frac{1}{2}}}{\Delta\zeta} \right) \right]^{n}. \tag{3.35}$$

In this equation, the temporal accuracy is first-order and the spacial accuracy depends on numerical fluxes. In this study, a second-order backward-difference implicit scheme is used for the temporal discretization. Partial differential equation Eq. 3.28 is discretized as follow:

$$\underbrace{\frac{3\hat{Q}^{n+1} - 4\hat{Q}^{n} + \hat{Q}^{n-1}}{2\Delta t}}_{\text{Second-order backward-difference}} + \mathcal{O}\left(\Delta t^2\right)$$
$$= \underbrace{- \left[\partial_\xi \hat{E} + \partial_\eta \hat{F} + \partial_\zeta \hat{G} - \frac{1}{Re} \left(\partial_\xi \hat{E}_v + \partial_\eta \hat{F}_v + \partial_\zeta \hat{G}_v \right) \right]^{n+1}}_{\text{Next time step (n+1) values for an implicit time integration}}, \tag{3.36}$$

where the symbols ∂_ξ, ∂_η and ∂_ζ denote the partial differential operators $\partial/\partial\xi$, $\partial/\partial\eta$ and $\partial/\partial\zeta$ respectively. To solve this implicit equation, the fluxes in the advection and viscous terms are linearized by Taylor expansion in the time direction as follow:

$$\hat{E}^{n+1} = \hat{E}^{n} + \left(\frac{\partial \hat{E}}{\partial \hat{Q}} \right)^{n} \left(\hat{Q}^{n+1} - \hat{Q}^{n} \right) + \mathcal{O}\left(\Delta t^2\right) = \hat{E}^{n} + \hat{A}^{n} \Delta \hat{Q}^{n} + \mathcal{O}\left(\Delta t^2\right), \tag{3.37}$$

where $\Delta\hat{Q}^n = \hat{Q}^{n+1} - \hat{Q}^n$ (delta-form approximate-factorization[84]), and $\hat{A}$, $\hat{B}$, $\hat{C}$, $\hat{A}_v$, $\hat{B}_v$ and $\hat{C}_v$ are flux Jacobian matrices which are defined as follows:

$$\hat{A} = \frac{\partial \hat{E}}{\partial \hat{Q}}, \ \hat{B} = \frac{\partial \hat{F}}{\partial \hat{Q}}, \ \hat{C} = \frac{\partial \hat{G}}{\partial \hat{Q}}, \ \hat{A}_v = \frac{\partial \hat{E}_v}{\partial \hat{Q}}, \ \hat{B}_v = \frac{\partial \hat{F}_v}{\partial \hat{Q}}, \ \hat{C}_v = \frac{\partial \hat{G}_v}{\partial \hat{Q}}, \tag{3.38}$$

By substituting Eq. 3.37 and $\Delta\hat{Q}^n$ into Eq. 3.36, the following equation is obtained:

$$\begin{aligned}\Bigg[I + \frac{2\Delta t}{3}\partial_\xi\left(\hat{A}\Delta\hat{Q}^n\right) + \partial_\eta\left(\hat{B}\Delta\hat{Q}^n\right) + \partial_\zeta\left(\hat{C}\Delta\hat{Q}^n\right) \\ -\frac{2\Delta t}{3Re}\partial_\xi\left(\hat{A}_v\Delta\hat{Q}^n\right) + \partial_\eta\left(\hat{B}_v\Delta\hat{Q}^n\right) + \partial_\zeta\left(\hat{C}_v\Delta\hat{Q}^n\right)\Bigg]^n + \mathcal{O}\left(\Delta t^2\right) \\ = \frac{\hat{Q}^n - \hat{Q}^{n-1}}{3} - \frac{2\Delta t}{3}\left[\partial_\xi\left(\hat{E} - \frac{1}{Re}\hat{E}_v\right) + \partial_\eta\left(\hat{F} - \frac{1}{Re}\hat{F}_v\right) + \partial_\zeta\left(\hat{G} - \frac{1}{Re}\hat{G}_v\right)\right]^n,\end{aligned} \tag{3.39}$$

We have to solve the Eq. 3.39 to obtain the solution of next time step. However obvious difficulty is expected to solve this equation, and solving it is not realistic because of enormous computational costs. Thus, generally, this equation is not solved directory but solved using approximate factorization. In this study, ADI-SGS factorization is used with Newton-Raphson iteration (which is often called as the sub-iteration[85,86]). These details are explained following sections.

Newton-Raphson iteration

Generally, approximate factorizations do not guarantee the time discretization accuracy. Thus, in order to guarantee the time discretization accuracy, Newton-Raphson iteration is used with approximate factorizations.[?] Multiplying by $2\Delta t/3$, we define the function $f(Q)$ to obtain the nolinear equation system for the unknown $Q = Q^{n+1}$ in Eq. 3.36

$$\begin{aligned}f(\hat{Q}) &= \frac{3\hat{Q}^{n+1} - 4\hat{Q}^n + \hat{Q}^{n-1}}{3} + \frac{2\Delta t}{3}\left[\partial_\xi\hat{E} + \partial_\eta\hat{F} + \partial_\zeta\hat{G} - \frac{1}{Re}\left(\partial_\xi\hat{E}_v + \partial_\eta\hat{F}_v + \partial_\zeta\hat{G}_v\right)\right]^{n+1} \\ &= \frac{3\hat{Q} - 4\hat{Q}^n + \hat{Q}^{n-1}}{3} + f_a(\hat{Q}) + f_v(\hat{Q}) \\ &= 0,\end{aligned} \tag{3.40}$$

where

$$\begin{aligned}f_a(\hat{Q}) &= \frac{2\Delta t}{3}\left[\partial_\xi\hat{E}(\hat{Q}) + \partial_\eta\hat{F}(\hat{Q}) + \partial_\zeta\hat{G}(\hat{Q})\right]^{n+1}, \\ f_v(\hat{Q}) &= -\frac{2\Delta t}{3Re}\left[\partial_\xi\hat{E}_v(\hat{Q}) + \partial_\eta\hat{F}_v(\hat{Q}) + \partial_\zeta\hat{G}_v(\hat{Q})\right]^{n+1},\end{aligned} \tag{3.41}$$

$f_a(\hat{Q})$ and $f_v(\hat{Q})$ are the advection term and the viscous term at the $n+1$ time step, which are functions of $\hat{Q}$. The numerical solution of the Eq 3.40 can be done using

Newton's method. One Newton step is given by:

$$\left.\frac{\partial f(\hat{Q})}{\partial \hat{Q}}\right|^{(m)} \Delta\hat{Q}^{(m)} = -f(\hat{Q}^{(m)}), \tag{3.42}$$

where the superscript (m) is a Newton iteration (which is often called as a sub-iteration) index, and $\Delta\hat{Q}^{(m)} = \hat{Q}^{(m+1)} - \hat{Q}^{(m)}$ is a delta form of the unknown $\hat{Q}$ in Newton iteration. We solve this linear equation system iteratively with system matrix $\left.\frac{\partial f(\hat{Q})}{\partial \hat{Q}}\right|^{(m)}$ using ADI-SGS factorization until the $\Delta\hat{Q}^{(m)}$ of the Eq. 3.42 converges. The system mtarix $\left.\frac{\partial f(\hat{Q})}{\partial \hat{Q}}\right|^{(m)}$ is written as follow:

$$\left.\frac{\partial f(\hat{Q})}{\partial \hat{Q}}\right|^{(m)} = I + \left.\frac{\partial f_a(\hat{Q})}{\partial \hat{Q}}\right|^{(m)} + \left.\frac{\partial f_v(\hat{Q})}{\partial \hat{Q}}\right|^{(m)}, \tag{3.43}$$

where

$$\begin{aligned}
\left.\frac{\partial f_a(\hat{Q})}{\partial \hat{Q}}\right|^{(m)} &= \left[\partial_\xi \frac{\partial \hat{E}(\hat{Q})}{\partial \hat{Q}} + \partial_\xi \frac{\partial \hat{F}(\hat{Q})}{\partial \hat{Q}} + \partial_\xi \frac{\partial \hat{G}(\hat{Q})}{\partial \hat{Q}}\right]^{(m)}, \\
\left.\frac{\partial f_v(\hat{Q})}{\partial \hat{Q}}\right|^{(m)} &= -\frac{1}{Re}\left[\partial_\xi \frac{\partial \hat{E}_v(\hat{Q})}{\partial \hat{Q}} + \partial_\xi \frac{\partial \hat{F}_v(\hat{Q})}{\partial \hat{Q}} + \partial_\xi \frac{\partial \hat{G}_v(\hat{Q})}{\partial \hat{Q}}\right]^{(m)}.
\end{aligned} \tag{3.44}$$

By substituting Eq. 3.38 and Eq. 3.44, Eq. 3.43 is rewritten as follow:

$$\left.\frac{\partial f(\hat{Q})}{\partial \hat{Q}}\right|^{(m)} = I + \frac{2\Delta t}{3}\left[\partial_\xi \hat{A} + \partial_\eta \hat{B} + \partial_\zeta \hat{C}\right]^{(m)} - \frac{2\Delta t}{3Re}\left[\partial_\xi \hat{A}_v + \partial_\eta \hat{B}_v + \partial_\zeta \hat{C}_v\right]^{(m)} \tag{3.45}$$

By substituting Eq. 3.45, Eq. 3.42 is rewritten as follow:

$$\begin{aligned}
&\left[I + \frac{2\Delta t}{3}\left(\partial_\xi \hat{A} + \partial_\eta \hat{B} + \partial_\zeta \hat{C}\right) - \frac{2\Delta t}{3Re}\left(\partial_\xi \hat{A}_v + \partial_\eta \hat{B}_v + \partial_\zeta \hat{C}_v\right)\right]^{(m)} \Delta\hat{Q}^{(m)} \\
&= -\frac{1}{3}\left(3\hat{Q}^{(m)} - 4\hat{Q}^n + \hat{Q}^{n-1}\right) - \frac{2\Delta t}{3}\left[\partial_\xi \hat{E} + \partial_\eta \hat{F} + \partial_\zeta \hat{G} - \frac{1}{Re}\left(\partial_\xi \hat{E}_v + \partial_\eta \hat{F}_v + \partial_\zeta \hat{G}_v\right)\right]^{(m)} \\
&\equiv (RHS)
\end{aligned} \tag{3.46}$$

The multiple sub-iterations of (m) are conducted in the Eq. 3.46. If $\Delta\hat{Q}^{(m)}$ converges to 0, by multiplying $3/2\Delta t$, the right hand side of Eq. 3.46 can be rewritten as follow:

$$\lim_{m\to\infty}\frac{3}{2\Delta t}(RHS) = \\ -\frac{3\hat{Q}^{n+1}-4\hat{Q}^{n}+\hat{Q}^{n-1}}{2\Delta t}-\left[\partial_\xi\hat{E}+\partial_\eta\hat{F}+\partial_\zeta\hat{G}-\frac{1}{Re}\left(\partial_\xi\hat{E}_v+\partial_\eta\hat{F}_v+\partial_\zeta\hat{G}_v\right)\right]^{n+1}=0, \tag{3.47}$$

where

$$\hat{Q}^{(m)_0}=\hat{Q}^{n},\ \hat{Q}^{(m)_\infty}=\hat{Q}^{n+1}, \tag{3.48}$$

$$\lim_{(m)\to\infty}\hat{Q}^{(m+1)}=\lim_{(m)\to\infty}\hat{Q}^{(m)}=\hat{Q}^{n+1},\ \lim_{(m)\to\infty}\Delta\hat{Q}^{(m)}=0. \tag{3.49}$$

The Eq. 3.47 corresponds to Eq. 3.36, and clearly satisfies unsteady Navier-Stokes equations which provide the flow variables fluctuating in time and space. That is, no matter what approximation is introduced into the left hand side of the equation 3.47 to inverse the implicit operator efficiently, exact temporal accuracy is realized if the sub-iterations converge. Thus, in the present study, second-order temporal accuracy is guaranteed by the three-level backward-differencing formula.

Spacial Difference Scheme

In this section, the compact difference scheme,[54] which is used in this study, is explained.

The compact difference scheme is proposed by Lele[54] and is extended to curvilinear coordinate system by Gaitonde and Visbal.[87,88] A high-order central difference discretization with spectral-like resolution that minimizes dispersive and dissipative numerical errors is preferable for LES. Due to their spectral-like resolution, high-order compact difference scheme[54] is an attractive choice for reducing dispersion, anisotropy and dissipation errors associated with the spatial discretization. Recently, the compact difference scheme is applied to several engineering problems such as vortical flow over delta and double-delta wings,[89,90,91,92,93] the unsteady flow over a wing section near stall condition.,[94,95,96,97] bypass transitional boundary Layer[98,99,100] and, analysis of noise sources inside the high speed flow over a bump.[101,102]

Note that spatial resolution of sixth-order compact difference scheme[54] is in general much finer than conventional second or third-order scheme (Total variation diminishing (TVD) scheme,[103,104,105] monotonic upstream scheme for conservation laws (MUSCL)[106,107] scheme) in each direction. Our experience[90,97] indicates that the results by the present method would correspond to that by the conventional method with 50

to 100 times more grids points in the vortical flows. The advantage of the compact difference scheme[54] was shown for the vortical flows compared with the conventional second or third-order scheme (TVD scheme,[103,104,105] MUSCL[106,107] scheme). In this study, the spatial derivatives of advection terms and viscous terms, metrics, and jacobian are evaluated by the sixth-order compact difference scheme in order to efficiently solve the boundary layer and shear layer.

First, the compact difference scheme for the approximation of a first differential is explained. Second, tri-diagonal filter which suppress the numerical oscillation is noted. Third, the compact difference scheme for the approximation of a second differential is explained. Finally the evaluation of metrics is explained.

Compact Difference Scheme for First Differential

In this study the sixth order compact scheme[54] is used. The sixth order compact scheme is written as follows.

$$\begin{aligned}\beta_{cmpt}\phi'_{i-2} + \alpha_{cmpt}\phi'_{i-1} + \phi'_i + \alpha_{cmpt}\phi'_{i+1} + \beta_{cmpt}\phi'_{i+2} = &\frac{a_{cmpt}}{2\Delta h}\left(\phi_{i+1} - \phi_{i-1}\right) \\ &\frac{b_{cmpt}}{4\Delta h}\left(\phi_{i+2} - \phi_{i-2}\right) \\ &\frac{c_{cmpt}}{6\Delta h}\left(\phi_{i+3} - \phi_{i-3}\right) \end{aligned} \tag{3.50}$$

Here, Δh shows discretization step size. The relations between the coefficients α, β, a, b and c are derived by matching the Taylor series coefficients of various orders.

$$\phi'_{i\pm1} = \sum_{n=0}^{\infty} \frac{(\pm h)^n}{n!}\phi_i^{n+1}, \phi'_{i\pm2} = \sum_{n=0}^{\infty} \frac{(\pm 2h)^n}{n!}\phi_i^{n+1} \tag{3.51}$$

$$\phi'_{i\pm1} = \sum_{n=0}^{\infty} \frac{(\pm h)^n}{n!}\phi_i^{n}, \phi'_{i\pm2} = \sum_{n=0}^{\infty} \frac{(\pm 2h)^n}{n!}\phi_i^{n} \tag{3.52}$$

The first unmatched coefficient determines the formal truncation error of the approxi-

mation (3.50). These constraints are:

$$1 + 2\alpha + 2\beta = a + b + c \quad (\text{second} - \text{order}) \tag{3.53}$$

$$2\frac{3!}{2!}(a + 2^2\beta) = a + 2^2 b + 3^2 c \quad (\text{fourth} - \text{order}) \tag{3.54}$$

$$2\frac{5!}{4!}(a + 2^4\beta) = a + 2^4 b + 3^4 c \quad (\text{sixth} - \text{order}) \tag{3.55}$$

$$2\frac{7!}{6!}(a + 2^6\beta) = a + 2^6 b + 3^6 c \quad (\text{eighth} - \text{order}) \tag{3.56}$$

$$2\frac{9!}{8!}(a + 2^8\beta) = a + 2^8 b + 3^8 c \quad (\text{tenth} - \text{order}) \tag{3.57}$$

The general relation (3.50) with ((3.51)), ((3.52)) can be regarded as a three-parameter family of fourth-order schemes. If the schemes are restricted to $\beta = 0$ a variety of tri-diagonal systems are obtained. For $\beta \neq 0$ penta-diagonal schemes are generated. If the additional constraint of sixth-order formal accuracy is imposed, a two-parameter family of sixth-order penta-diagonal schemes is obtained. These may be further specialized into a one-parameter family of eighth-order penta-diagonal schemes or a single tenth-order scheme. First the tri-diagonal schemes are described. These are generated by $\beta = 0$ to avoid inversion of penta-diagonal matrix. If a further choice of $c = 0$ is made to reduce a stencil of right hand side of (3.50), a one-parameter (a) family of fourth-order tri-diagonal schemes is obtained.

$$\beta = 0, a = \frac{2}{3}(\alpha + 2), b = \frac{1}{3}(4\alpha - 1), c = 0 \tag{3.58}$$

As $\alpha \to 0$ this family merges into the well-known fourth-order central difference scheme. Similarly for $\alpha = \frac{1}{4}$ the classical Padé scheme is recovered.
Furthermore, forth order error term diminish by the coefficient of $\alpha = \frac{1}{3}$, because in case of (3.58) truncation error of first term is $(\frac{4}{5!}(3\alpha - 1)h^4 f^{(5)})$. Finally, the compact difference scheme have only even-order error. the scheme is formally sixth-order accurate because next error term of forth-order is sixth-order. These coefficients are

$$\alpha = \frac{1}{3}, \beta = 0, a = \frac{14}{9}, b = \frac{1}{9}, c = 0 \tag{3.59}$$

These coefficients are used in this study. Typical coefficients are presented in Table3.1. Maximum order of (3.50) is tenth-order.
Eq. 3.50 is solved as follows. Replacing the right hand side of Eq. 3.50 with $RHS\,(i)$,

	α	β	a	b	c
4th order	1/4	0	3/2	0	0
6th order	1/3	0	14/9	1/9	0
8th order	4/9	1/36	40/27	25/24	0
10th order	1/2	1/20	17/12	101/150	1/100

Table 3.1: Coefficients of compact difference scheme

following expression is obtained.

$$\alpha_{cmpt}\phi'_{i-1} + \phi'_i + \alpha_{cmpt}\phi'_{i+1} = RHS\,(i) \tag{3.60}$$

A matrix form of Eq. 3.60 is

$$\begin{bmatrix}
1 & \alpha_{cmpt} & & & & & & & \\
\alpha_{cmpt} & 1 & \alpha_{cmpt} & & & & & & \\
 & \alpha_{cmpt} & 1 & \alpha_{cmpt} & & & & & \\
 & \ddots & \ddots & \ddots & \ddots & \ddots & & & \\
 & & \ddots & \ddots & \ddots & \ddots & \ddots & & \\
 & & & \ddots & \ddots & \ddots & \ddots & \ddots & \\
 & & & & \alpha_{cmpt} & 1 & \alpha_{cmpt} & & \\
 & & & & & \alpha_{cmpt} & 1 & \alpha_{cmpt} & \\
 & & & & & & \alpha_{cmpt} & 1 &
\end{bmatrix}
\begin{bmatrix}
\phi'_3 \\ \phi'_4 \\ \phi'_4 \\ \vdots \\ \vdots \\ \vdots \\ \phi'_{imax-4} \\ \phi'_{imax-3} \\ \phi'_{imax-2}
\end{bmatrix} =$$

$$\begin{bmatrix}
RHS(3) - \alpha_{cmpt}\phi_2 \\
RHS(4) \\
RHS(5) \\
\vdots \\
\vdots \\
\vdots \\
RHS(imax-4) \\
RHS(imax-3) \\
RHS(imax-2) - \alpha_{cmpt}\phi_{imax-1}
\end{bmatrix} \tag{3.61}$$

First, the right hand side of Eq. 3.61 is computed at every stencil. Then, this tri-diagonal or penta-diagonal matrix in the left hand side is inversed using LU decomposition which is a kind of direct methods. Finally, first derivative is evaluated. In the case that the advection terms are evaluated with this compact difference scheme,

numerical fluxes are constructed at every grid point, and then these numerical fluxes are substituted into Eq. 3.60 which is solved with the procedure discussed above. As the scheme above has five stencils in the right hand side and three stencils in the left hand side.

Treatment near the boundary

The sixth-order compact difference scheme can not be applied to near the boundary region, since the scheme above has five stencils in the right hand side and three stencils in the left hand side of 3.50. Though Visbal and Gaitonde[108] propose the evaluation method of first difference which maintain form of tri-diagonal or penta-diagonal matrix of the left hand side of 3.50 near the boundary region, the second order explicit difference schemes[109] are used near the boundary due to the emphasization of stable computation. (ϕ_{jmax-1}-ϕ_{jmax} are computed symmetrically.)

second order:

$$\begin{aligned} \phi'_1 &= \frac{1}{2}(-3\phi_1 + 4\phi_2 - \phi_3), \\ \phi'_2 &= \frac{1}{12}(\phi_1 - \phi_3) \end{aligned} \tag{3.62}$$

fourth order:

$$\begin{aligned} \phi'_1 &= \frac{1}{12}\left(-25\phi_1 + 48\phi_2 - 36\phi_3 + 16\phi_4 - 3\phi_5\right), \\ \phi'_2 &= \frac{1}{12}\left(-3\phi_1 - 10\phi_2 + 18\phi_3 - 6\phi_4 + \phi_5\right) \end{aligned} \tag{3.63}$$

Though the accuracy decrease near the boundary region by the second order explicit difference schemes,[109] this treatment does not matter because the grid points are clustered near the boundary.

Tri-diagonal Filter

The compact difference scheme is a central difference one which needs the filtering procedure for suppressing numerical oscillations except for in direct numerical simulations in which physical viscosities can suppress numerical oscillations. In this study, the following

implicit tenth order tri-diagonal filter[88,110] is used.

$$\alpha_f \acute{\phi}_{i-1} + \acute{\phi}_i + \alpha_f \acute{\phi}_{i+1} = \sum_{n=0}^{5} \frac{a_f^n}{2} \left(\phi_{i+n} + \phi_{i-n}\right) \tag{3.64}$$

where the superscript acute (ˊ) denotes a filtered quantity. The coefficients α_f are shown in table 3.2. If $\alpha_f = 0$ is used, this filter becomes explicit filter and does not to be solved tri-diagonal matrix.

Note that the near boundary formulation is

$$\alpha_f \acute{\phi}_{i-1} + \acute{\phi}_i + \alpha_f \acute{\phi}_{i+1} = \sum_{n=1}^{11} a_f^n \left(\phi_i\right) \tag{3.65}$$

(Near jmax, these values are evaluated symmetrically.) Coefficients are shown in Table 3.3. α_f varies from -0.5 to 0.5. The resolution of the filter becomes higher as α_f approaches to 0.5, while this filter is becoming not to be able to suppress numerical oscillations simultaneously. In this study $\alpha_f$is set to be 0.45. Equations 3.64-3.65 can be solved in a similar way as the previous section. Replacing the right hand side of Eq. 3.64 with $RHS\left(i\right)$, following expression is obtained.

$$\alpha_f \acute{\phi}_{i-1} + \acute{\phi}_i + \alpha_f \acute{\phi}_{i+1} = RHS\left(i\right) \tag{3.66}$$

A matrix form of Eq. 3.66 is

$$\begin{bmatrix} 1 & \alpha_f & & & & & & & \\ \alpha_f & 1 & \alpha_f & & & & & & \\ & \alpha_f & 1 & \alpha_f & & & & & \\ & & \ddots & \ddots & \ddots & & & & \\ & & & \ddots & \ddots & \ddots & & & \\ & & & & \ddots & \ddots & \ddots & & \\ & & & & & \alpha_f & 1 & \alpha_f & \\ & & & & & & \alpha_f & 1 & \alpha_f \\ & & & & & & & \alpha_f & 1 \end{bmatrix} \begin{bmatrix} \acute{\phi}_2 \\ \acute{\phi}_3 \\ \acute{\phi}_4 \\ \vdots \\ \vdots \\ \vdots \\ \acute{\phi}_{imax-3} \\ \acute{\phi}_{imax-2} \\ \acute{\phi}_{imax-1} \end{bmatrix} = \begin{bmatrix} RHS(2) - \alpha\phi_1 \\ RHS(3) \\ RHS(4) \\ \vdots \\ \vdots \\ \vdots \\ RHS(imax-3) \\ RHS(imax-2) \\ RHS(imax-1) - \alpha\phi_{imax} \end{bmatrix}. \quad (3.67)$$

First, the right hand side of Eq. 3.67 are computed at every stencil. Then, the tri-diagonal matrix in left hand side is inversed using LU decomposition which is a kind of direct methods. This filtering procedures in ξ, η and ζ directions are used for each conservative value for suppressing numerical oscillations once per a time step (not per a sub-iteration of inner iteration) after time integration.

Table 3.2: Coefficients $a_{f,n}$ in tenth order tri-diagonal filtering.

a_f^0	a_f^1	a_f^2	a_f^3	a_f^4	a_f^5
$\frac{193+126\alpha_f}{256}$	$\frac{105+302\alpha_f}{256}$	$\frac{-15+30\alpha_f}{64}$	$\frac{45-90\alpha_f}{512}$	$\frac{-5+10\alpha_f}{256}$	$\frac{1-2\alpha_f}{512}$

Table 3.3: Coefficients $a_{f,k}^n$ in tenth order tri-diagonal filtering.

k	$a_{f,k}^1$	$a_{f,k}^2$	$a_{f,k}^3$	$a_{f,k}^4$	$a_{f,k}^5$	$a_{f,k}^6$	$a_{f,k}^7$	$a_{f,k}^8$	$a_{f,k}^9$	$a_{f,k}^{10}$	$a_{f,k}^{11}$
2	$\frac{1+1022\alpha_f}{1024}$	$\frac{507+10\alpha_f}{512}$	$\frac{45+934\alpha_f}{1024}$	$\frac{-15+30\alpha_f}{128}$	$\frac{105-210\alpha_f}{512}$	$\frac{-63+126\alpha_f}{256}$	$\frac{105-210\alpha_f}{512}$	$\frac{-15+30\alpha_f}{128}$	$\frac{45-90\alpha_f}{1024}$	$\frac{-5+10\alpha_f}{512}$	$\frac{1-2\alpha_f}{1024}$
3	$\frac{-1+2\alpha_f}{1024}$	$\frac{5+502\alpha_f}{512}$	$\frac{979+90\alpha_f}{1024}$	$\frac{15+98\alpha_f}{128}$	$\frac{-105+210\alpha_f}{512}$	$\frac{63-126\alpha_f}{256}$	$\frac{-105+210\alpha_f}{512}$	$\frac{15-30\alpha_f}{128}$	$\frac{-45+90\alpha_f}{1024}$	$\frac{5-10\alpha_f}{512}$	$\frac{-1+2\alpha_f}{1024}$
4	$\frac{1-2\alpha_f}{1024}$	$\frac{-5+10\alpha_f}{512}$	$\frac{45+930\alpha_f}{1024}$	$\frac{113-30\alpha_f}{128}$	$\frac{105+302\alpha_f}{512}$	$\frac{-63+126\alpha_f}{256}$	$\frac{105-210\alpha_f}{512}$	$\frac{-15+30\alpha_f}{128}$	$\frac{45-90\alpha_f}{1024}$	$\frac{-5+10\alpha_f}{512}$	$\frac{1-2\alpha_f}{1024}$
5	$\frac{-1+2\alpha_f}{1024}$	$\frac{5-10\alpha_f}{512}$	$\frac{-45+90\alpha_f}{1024}$	$\frac{15+98\alpha_f}{128}$	$\frac{407+210\alpha_f}{512}$	$\frac{63+130\alpha_f}{256}$	$\frac{-105+210\alpha_f}{512}$	$\frac{15-30\alpha_f}{128}$	$\frac{-45+90\alpha_f}{1024}$	$\frac{5-10\alpha_f}{512}$	$\frac{-1+2\alpha_f}{1024}$

Evaluation of Metrics

In this study, metrics and jacobian (Eq. 3.32) are evaluated with the difference formula Eq. 3.50, Eq. 3.62 and Eq. 3.62. In this way, the freestream can be preserved.

Viscous Terms

In the following, the evaluation of viscous terms is explained. Viscous fluxs are evaluated with the second difference operator. Though Lele evaluated viscous fluxs with the second difference operator,[54] in this way the viscous terms are evaluated with twice operations of the difference operator.

Nagarajan *et al.*.[111] reported that a more robust scheme can be constructed using the second difference operator, or the evaluation of viscous terms on cell-centers because the viscous terms can be evaluated up to a very high wave number. However, in this study, viscous terms are not evaluated in these ways because the compact difference scheme with the filtering is adopted which is stable enough.

The following sixth order compact difference scheme is used.

$$\begin{aligned} \beta\phi"_{i-2} + \alpha\phi"_{i-1} + \phi"_{i} + \alpha\phi"_{i+1} + \beta\phi"_{i+2} = & \frac{a}{2h}\left(\phi'_{i+1} - \phi'_{i-1}\right) \\ + & \frac{b}{4h}\left(\phi'_{i+2} - \phi'_{i-2}\right) \\ + & \frac{c}{6h}\left(\phi'_{i+3} - \phi'_{i-3}\right) \end{aligned} \tag{3.68}$$

Note that Eq. 3.62 are used near boundary region. On the other hand, the compact difference scheme is used for the evaluation of advection terms, the sixth order compact difference scheme (Eq. 3.50 and Eq. 3.62)is also used for the evaluation of viscous terms.

First, approximate ξ, η, ζ direction first differential values of u, v, w and q are evaluated the difference operator. Then, these differential values are transformed into x, y, z direction differential ones of u, v, w and q. This transform is based on the chain rule of the partial differential which is written with general function ϕ as follows,

$$\begin{aligned} \phi_x &= \xi_x\phi_\xi + \eta_x\phi_\eta + \zeta_x\phi_\zeta \\ \phi_y &= \xi_y\phi_\xi + \eta_y\phi_\eta + \zeta_y\phi_\zeta \\ \phi_z &= \xi_z\phi_\xi + \eta_z\phi_\eta + \zeta_z\phi_\zeta \end{aligned} \tag{3.69}$$

The viscous tensor is constructed with x, y, z direction differential values, and then the viscous flux in Eq. 3.28 is calculated at each grid points. Finally, the viscous flux is

differenced with the difference operator Eq. 3.69. The same coefficients of first difference operator are used in second difference operator.

Though above procedure does not have the effect of suppression of high frequency oscillation in viscous term, the above procedure does not matter due to using the filtering at the same time in this study.

Time integration

The numerical scheme which has higher temporal accuracy is preferable for the analysis of the temporal behavior of the flow field using LES. In addition to the temporal accuracy, total simulation time (time step size Δt $\times$ total iteration number) is also important since the time-averaged and phase-averaged flow quantities, which is one of the most important issues from an engineering viewpoint, need to be created by averaging the flow field for sufficiently long time of the unsteady flow simulations. Thus, the numerical scheme have to be efficient to reduce the total simulation time. The choice of the time integration scheme is the trade-off between the temporal accuracy and total simulation time. There are mainly two choices of the time integration scheme; one is the explicit time integration method, and the other is the implicit time integration method. The explicit time marching method is one choice. Even the simplest Euler explicit scheme has at least first-order temporal accuracy, and it is easy to extend temporal accuracy of the explicit schemes using Runge-Kutta method.[112] However, the time step size Δt for the explicit schemes is strongly restricted by the local Courant-Friedrichs-Lewy (CFL) number,[113] and the restriction becomes very strict when the grid clustered near the wall to resolve the boundary layer. The restriction derives the long total simulation time, and it is almost impossible to simulate the phenomena considered in the present study. The flow field considered here is essentially unsteady, and it is necessary to resolve unsteady flows both in time and space for the LES. Therefore the local CFL number must be kept at a magnitude of order unity,[114] or the appropriate number of inner iterations must be used for the implicit time integration method.

ADI-SGS factorization algorithm

Alternative direction implicit-symmetric gauss seidel (ADI-SGS) implicit scheme is used for the time integration in this study to overcome the restriction of the time step size Δt. Although ADI-SGS implicit time integration scheme is numerically efficient, the

temporal accuracy of the scheme is less than first-order due to the errors of linearization, alternative direction implicit and etc. Therefore, multiple sub-iterations (Newton-Raphson iteration)[85,86] are adopted and the errors due to the linearization, alternative direction implicit and etc. are eliminated. With regard to time integration, considering the properties of the super computer used in the present study (NEC, SX-6 and SX-9), an alternative direction implicit-symmetric gauss seidel (ADI-SGS) implicit scheme[115,116,117] is employed.

This algorithm uses the same type of idea as a four-factor symmetric Gauss-Seidel (FF-SGS) method,[118] which uses both lower-upper symmetric alternating direction implicit (LU-ADI) methods[71,72,73,74] and lower-upper symmetric Gauss-Seidel (LU-SGS) methods.[119,120] Concretely, the spectral radius is used to obtain the upwind difference in each direction of the LU-ADI scheme.

When we consider the first-order Euler implicit scheme, the Navier-Stokes equations can be written as

$$\hat{Q}^{n+1} - \hat{Q}^{n} = -\Delta t \left[\frac{\partial \hat{E}}{\partial \xi} + \frac{\partial \hat{F}}{\partial \eta} + \frac{\partial \hat{G}}{\partial \zeta} - \frac{1}{Re} \left(\frac{\partial \hat{E}_v}{\partial \xi} + \frac{\partial \hat{F}_v}{\partial \eta} + \frac{\partial \hat{G}_v}{\partial \zeta} \right) \right]^{n+1} \tag{3.70}$$

Then the flux vectors in the time direction are linearized by Taylor series expansion[84] , and $\hat{E}$, $\hat{F}$ and $\hat{G}$ is descried as:

$$\begin{aligned}
\hat{E}^{n+1} &= \hat{E}^{n} + \left(\frac{\partial \hat{E}}{\partial \hat{Q}} \right)^{n} \left(\hat{Q}^{n+1} - \hat{Q}^{n} \right) + O\left(\Delta t^2 \right) \\
\hat{F}^{n+1} &= \hat{F}^{n} + \left(\frac{\partial \hat{F}}{\partial \hat{Q}} \right)^{n} \left(\hat{Q}^{n+1} - \hat{Q}^{n} \right) + O\left(\Delta t^2 \right) \\
\hat{G}^{n+1} &= \hat{G}^{n} + \left(\frac{\partial \hat{G}}{\partial \hat{Q}} \right)^{n} \left(\hat{Q}^{n+1} - \hat{Q}^{n} \right) + O\left(\Delta t^2 \right)
\end{aligned} \tag{3.71}$$

By substituting Eq. 3.1.3 for Eq. 3.70 and importing $\Delta\hat{Q} = \hat{Q}^{n+1} - \hat{Q}^{n}$(delta-form approximate-factorization[84]), The followings are obtained:

$$\Delta \hat{Q}^{n} = -\Delta t \left[\frac{\partial}{\partial \xi} \left(\hat{E} + \hat{A}\Delta\hat{Q} \right) + \frac{\partial}{\partial \eta} \left(\hat{F} + \hat{B}\Delta\hat{Q} \right) + \frac{\partial}{\partial \varsigma} \left(\hat{G} + \hat{C}\Delta\hat{Q} \right) - Q \left(\frac{1}{J} \right)_{\tau} \right]^{n} \tag{3.72}$$

where $\hat{A}, \hat{B}, \hat{C}$ are called flux jacobian matrices and are described as:

$$\hat{A} = \frac{\partial \hat{E}}{\partial \hat{Q}}, \hat{B} = \frac{\partial \hat{F}}{\partial \hat{Q}}, \hat{C} = \frac{\partial \hat{G}}{\partial \hat{Q}}, \hat{A}_v = \frac{\partial \hat{E}_v}{\partial \hat{Q}}, \hat{B}_v = \frac{\partial \hat{F}_v}{\partial \hat{Q}}, \hat{C}_v = \frac{\partial \hat{G}_v}{\partial \hat{Q}} \tag{3.73}$$

and given by

$$\hat{A} \ or \ \hat{B} \ or \ \hat{C} = \begin{bmatrix} \kappa_t & \kappa_x & \kappa_y & \kappa_z & 0 \\ \kappa_x\phi^2 - v\theta & \kappa_t + \theta - (\gamma-2)\kappa_x u & \kappa_x u - (\gamma-1)\kappa_y v & \kappa_z u - (\gamma-1)\kappa_x w & (\gamma-1)\kappa_x \\ \kappa_y\phi^2 - v\theta & \kappa_x v - (\gamma-1)\kappa_y u & \kappa_t + \theta - (\gamma-2)\kappa_y v & \kappa_z v - (\gamma-1)\kappa_y w & (\gamma-1)\kappa_y \\ \kappa_z\phi^2 - w\theta & \kappa_x w - (\gamma-1)\kappa_z u & \kappa_y w - (\gamma-1)\kappa_z v & \kappa_t + \theta - (\gamma-2)\kappa_z w & (\gamma-1)\kappa_z \\ -\theta(\frac{\gamma e}{\rho} - 2\phi^2) & \kappa_x(\frac{\gamma e}{\rho} - \phi^2) - (\gamma-1)\theta u & \kappa_y(\frac{\gamma e}{\rho} - \phi^2) - (\gamma-1)\theta v & \kappa_z(\frac{\gamma e}{\rho} - \phi^2) - (\gamma-1)\theta w & \kappa_t + \gamma\theta \end{bmatrix} \tag{3.74}$$

where

$$\begin{aligned} \theta &= \kappa_u + \kappa_y v + \kappa_z w \\ \phi^2 &= \frac{1}{2}(\gamma-1)(u^2 + v^2 + w^2) \end{aligned} \tag{3.75}$$

with $\kappa = \xi$, η or ζ for $\hat{A}$, $\hat{B}$, $\hat{C}$, respectively. The term of $\hat{Q}^n$ is moved to the left hand side,

$$\left[I + \Delta t \left(\frac{\partial \hat{A}}{\partial \xi} + \frac{\partial \hat{B}}{\partial \eta} + \frac{\partial \hat{C}}{\partial \zeta} \right) - \frac{\Delta t}{Re} \left(\frac{\partial \hat{A}_v}{\partial \xi} + \frac{\partial \hat{B}_v}{\partial \eta} + \frac{\partial \hat{C}_v}{\partial \zeta} \right) \right]^n \Delta \hat{Q}^n$$

$$= -\Delta t \left[\frac{\partial \hat{E}}{\partial \xi} + \frac{\partial \hat{F}}{\partial \eta} + \frac{\partial \hat{G}}{\partial \zeta} - \frac{1}{Re} \left(\frac{\partial \hat{E}_v}{\partial \xi} + \frac{\partial \hat{F}_v}{\partial \eta} + \frac{\partial \hat{G}_v}{\partial \zeta} \right) \right]^n \tag{3.76}$$

By neglecting the viscous terms in the left-hand side of Eq. 3.76, assuming that they

can be dealt with explicitly.[121,122]

$$\left[I+\Delta t\left(\frac{\partial \hat{A}}{\partial \xi}+\frac{\partial \hat{B}}{\partial \eta}+\frac{\partial \hat{C}}{\partial \zeta}\right)\right]^{n}\Delta \hat{Q}^{n}$$

$$=-\Delta t\left[\frac{\partial \hat{E}}{\partial \xi}+\frac{\partial \hat{F}}{\partial \eta}+\frac{\partial \hat{G}}{\partial \zeta}-\frac{1}{Re}\left(\frac{\partial \hat{E}_{v}}{\partial \xi}+\frac{\partial \hat{F}_{v}}{\partial \eta}+\frac{\partial \hat{G}_{v}}{\partial \zeta}\right)\right]^{n} \tag{3.77}$$

The implicit operator (ADI operator) inside [ ] of the left hand side of 3.77 is sparse but block non-band matrix, and it is a tough work to inverse it. Here, ADI factorization is a good choice;

$$\begin{aligned}&\left[I+\Delta t\left(\frac{\partial \hat{A}}{\partial \xi}+\frac{\partial \hat{B}}{\partial \eta}+\frac{\partial \hat{C}}{\partial \zeta}\right)\right]^{n}\Delta \hat{Q}^{n}\\ \rightarrow&\left(I+\Delta t\frac{\partial \hat{A}}{\partial \xi}\right)^{n}\left(I+\Delta t\frac{\partial \hat{B}}{\partial \eta}\right)^{n}\left(I+\Delta\frac{\partial \hat{C}}{\partial \zeta}\right)^{n}\Delta \hat{Q}^{n}+O\left(\Delta t^{2}\right)\end{aligned} \tag{3.78}$$

The implicit operator of 3.77 can be factored by the approximate factorization[84] as

$$\begin{aligned}&\left(I+\Delta t\frac{\partial \hat{A}}{\partial \xi}\right)^{n}\left(I+\Delta t\frac{\partial \hat{B}}{\partial \eta}\right)^{n}\left(I+\Delta t\frac{\partial \hat{C}}{\partial \zeta}\right)^{n}\Delta \hat{Q}^{n}\\ =&-\Delta t\left[\frac{\partial \hat{E}}{\partial \xi}+\frac{\partial \hat{F}}{\partial \eta}+\frac{\partial \hat{G}}{\partial \zeta}-\frac{1}{Re}\left(\frac{\partial \hat{E}_{v}}{\partial \xi}+\frac{\partial \hat{F}_{v}}{\partial \eta}+\frac{\partial \hat{G}_{v}}{\partial \zeta}\right)\right]^{n}=-\Delta t\cdot R_{j}^{n}\end{aligned} \tag{3.79}$$

This reduces the complex inversion of Matrix to three stages of one dimensional Matrix inversion. If we apply second order central differences for spatial derivatives, each of three matrices will be a tri-diagonal matrix with its components as flux jacobians. where, $\delta\xi$, $\delta\eta$ and $\delta\zeta$ which are the finite difference operator for each direction are applied to the left hand side of Eq. 3.79,

$$\begin{aligned}&\left(I+\Delta t\frac{\partial \hat{A}}{\partial \xi}\right)^{n}\left(I+\Delta t\frac{\partial \hat{B}}{\partial \eta}\right)^{n}\left(I+\Delta t\frac{\partial \hat{C}}{\partial \zeta}\right)^{n}\\ =&\left(I+\Delta t\delta_{\xi}\hat{A}\right)^{n}\left(I+\Delta t\delta_{\eta}\hat{B}\right)^{n}\left(I+\Delta t\delta_{\zeta}\hat{C}\right)^{n}\end{aligned} \tag{3.80}$$

The followings are obtained:

$$\left(I+\Delta t\delta_\xi \hat{A}\right)^n \left(I+\Delta t\delta_\eta \hat{B}\right)^n \left(I+\Delta t\delta_\zeta \hat{C}\right)^n \Delta\hat{Q}^n = -\Delta t\left[\frac{\partial \hat{E}}{\partial \xi}+\frac{\partial \hat{F}}{\partial \eta}+\frac{\partial \hat{G}}{\partial \zeta}-\frac{1}{Re}\left(\frac{\partial \hat{E}_v}{\partial \xi}+\frac{\partial \hat{F}_v}{\partial \eta}+\frac{\partial \hat{G}_v}{\partial \zeta}\right)\right]^n$$

Approximate Lower-Diagonal-Upper (LDU) factorization,[84] which is more stable than simple Lower-Upper (LU) factorization[123] due to diagonally dominant, is applied to the operator in the left hand side of (3.81). This basic idea of LDU factorization is proposed as DDADI factorization by Lombard et al.[124]

$$\begin{aligned}&\left(I+\Delta t\delta_\xi \hat{A}\right)\left(I+\Delta t\delta_\eta \hat{B}\right)\left(I+\Delta t\delta_\zeta \hat{C}\right)\\ &=[L_\xi+D_\xi+U_\xi][L_\eta+D_\eta+U_\eta][L_\zeta+D_\zeta+U_\zeta] \qquad (3.81)\\ &\approx \left\lfloor (L_\xi+D_\xi)\,D_\xi^{-1}\,(D_\xi+U_\xi)\right\rfloor \left\lfloor (L_\eta+D_\eta)\,D_\eta^{-1}\,(D_\eta+U_\eta)\right\rfloor \left\lfloor (L_\zeta+D_\zeta)\,D_\zeta^{-1}\,(D_\zeta+U_\zeta)\right\rfloor\end{aligned}$$

Then, equation 3.81 can be rewritten as

$$\begin{aligned}&\left\lfloor (L_\xi+D_\xi)\,D_\xi^{-1}\,(D_\xi+U_\xi)\right\rfloor \left\lfloor (L_\eta+D_\eta)\,D_\eta^{-1}\,(D_\eta+U_\eta)\right\rfloor \left\lfloor (L_\zeta+D_\zeta)\,D_\zeta^{-1}\,(D_\zeta+U_\zeta)\right\rfloor \Delta\hat{Q}^n\\ &=(RHS) \qquad (3.82)\end{aligned}$$

where I, L, D and U are the identity matrix, the left-lower triangle, the diagonal and the right-upper triangle of the matrix, respectively as

$$\begin{aligned}L_\xi &= -\Delta t\hat{A}_{j-1}, D_\xi = I+\Delta t\left\lfloor\left(\hat{A}^+-\hat{A}^-\right)\Big/\Delta\xi\right\rfloor, U_\xi = \Delta t\hat{A}^+_{j+1}\\ L_\eta &= -\Delta t\hat{B}_{j-1}, D_\eta = I+\Delta t\left\lfloor\left(\hat{B}^+-\hat{B}^-\right)\Big/\Delta\eta\right\rfloor, U_\eta = \Delta t\hat{B}^+_{j+1} \qquad (3.83)\\ L_\zeta &= -\Delta t\hat{A}_{j-1}, D_\zeta = I+\Delta t\left\lfloor\left(\hat{A}^+-\hat{A}^-\right)\Big/\Delta\zeta\right\rfloor, U_\zeta = \Delta t\hat{C}^+_{j+1}\end{aligned}$$

$$\begin{aligned}L_\xi+D_\xi &= I+\Delta t\left(\delta_\xi^-\hat{A}^+-\hat{A}^-\Big/\Delta\xi\right)\\ D_\xi &= I+\Delta t\left[\left(\hat{A}^+-\hat{A}^-\right)\Big/\Delta\xi\right] \qquad (3.84)\\ D_\xi+U_\xi &= I+\Delta t\left(\delta_\xi^+\hat{A}^--\hat{A}^+\Big/\Delta\xi\right)\end{aligned}$$

$$\begin{aligned} L_\eta + D_\eta &= I + \Delta t \left(\delta_\eta^- \hat{B}^+ - \hat{B}^- \Big/ \Delta\eta \right) \\ D_\eta &= I + \Delta t \left[\left(\hat{B}^+ - \hat{B}^- \right) \Big/ \Delta\eta \right] \\ D_\eta + U_\eta &= I + \Delta t \left(\delta_\eta^+ \hat{B}^- - \hat{B}^+ \Big/ \Delta\eta \right) \end{aligned} \tag{3.85}$$

$$\begin{aligned} L_\zeta + D_\zeta &= I + \Delta t \left(\delta_\zeta^- \hat{C}^+ - \hat{C}^- \Big/ \Delta\zeta \right) \\ D_\zeta &= I + \Delta t \left[\left(\hat{C}^+ - \hat{C}^- \right) \Big/ \Delta\zeta \right] \\ D_\zeta + U_\zeta &= I + \Delta t \left(\delta_\zeta^+ \hat{C}^- - \hat{C}^+ \Big/ \Delta\zeta \right) \end{aligned} \tag{3.86}$$

As for the jacobian matrix of the convective numerical fluxes, $\hat{A^{\pm}}$, $\hat{B^{\pm}}$ and $\hat{C^{\pm}}$, the eigenvalues of "+" matrices are nonnegative and those of "-" matrices are nonpositive.[125] Finite difference operators of δ_ξ^+, δ_η^+ and δ_ζ^+ are first-order forward difference operators and δ_ξ^-, δ_η^- and δ_ζ^- are first-order backward difference operators using the idea of 1st upwind difference, as follows:

$$\delta_\xi^+ \hat{A}^- = \frac{\hat{A}^-_{j+1,k,l} - \hat{A}^-_{j,k,l}}{\Delta\xi}, \delta_\xi^- \hat{A}^+ = \frac{\hat{A}^+_{j,k,l} - \hat{A}^+_{j-1,k,l}}{\Delta\xi} \tag{3.87}$$

$$\delta_\eta^+ \hat{B}^- = \frac{\hat{B}^-_{j,k+1,l} - \hat{B}^-_{j,k,l}}{\Delta\eta}, \delta_\eta^- \hat{B}^- = \frac{\hat{B}^+_{j,k,l} - \hat{B}^+_{j,k-1,l}}{\Delta\eta} \tag{3.88}$$

$$\delta_\zeta^+ \hat{C}^- = \frac{\hat{C}^-_{j,k+1,l} - \hat{C}^-_{j,k,l}}{\Delta\zeta}, \delta_\zeta^- \hat{C}^+ = \frac{\hat{C}^+_{j,k,l} - \hat{C}^+_{j,k-1,l}}{\Delta\zeta} \tag{3.89}$$

In the solution process, operation of the equation (3.82) using the finite difference operators of the equations (3.89) consists of three steps for each direction (a number of total steps are nine times).

ξ direction

First step

$$\left[I + \Delta t \left(\hat{A}^+_{j,k,l} - \hat{A}^-_{j,k,l} \right) \right] \Delta\hat{Q}^*_{j,k,l} = (RHS) + \Delta t \left(\hat{A}^+ \Delta\hat{Q}^* \right)_{j-1,k,l}$$

where

$$\Delta\hat{Q}^{*}_{j,k,l} = D_{\xi}^{-1}\left[D_{\xi} + U_{\xi}\right]\Delta\hat{Q}^{**}_{j,k,l}$$

Second step

$$\left[I + \Delta t\left(\hat{A}^{+}_{j,k,l} - \hat{A}^{-}_{j,k,l}\right)\right]^{-1}\Delta\hat{Q}^{**}_{j,k,l} = \Delta\hat{Q}^{*}_{j,k,l}$$

where

$$\Delta\hat{Q}^{**}_{j,k,l} = D_{\xi}^{-1}\left[D_{\xi} + U_{\xi}\right]\Delta\hat{Q}^{***}_{j,k,l}$$

Third step

$$\left[I + \Delta t\left(\hat{A}^{+}_{j,k,l} - \hat{A}^{-}_{j,k,l}\right)\right]\Delta\hat{Q}^{***}_{j,k,l} = \Delta\hat{Q}^{**}_{j,k,l} - \Delta t\left(\hat{A}^{-}\Delta\hat{Q}^{***}\right)_{j+1,k,l}$$

η direction

First step

$$\left[I + \Delta t\left(\hat{A}^{+}_{j,k,l} - \hat{A}^{-}_{j,k,l}\right)\right]\Delta\hat{Q}^{*}_{j,k,l} = (RHS) + \Delta t\left(\hat{A}^{+}\Delta\hat{Q}^{*}\right)_{j-1,k,l}$$

where $\Delta\hat{Q}^{*}_{j,k,l} = D_{\xi}^{-1}\left[D_{\xi} + U_{\xi}\right]\Delta\hat{Q}^{**}_{j,k,l}$

Second step

$$\left[I + \Delta t\left(\hat{A}^{+}_{j,k,l} - \hat{A}^{-}_{j,k,l}\right)\right]^{-1}\Delta\hat{Q}^{**}_{j,k,l} = \Delta\hat{Q}^{*}_{j,k,l}$$

where $\Delta\hat{Q}^{**}_{j,k,l} = D_{\xi}^{-1}\left[D_{\xi} + U_{\xi}\right]\Delta\hat{Q}^{***}_{j,k,l}$

Third step

$$\left[I + \Delta t\left(\hat{A}^{+}_{j,k,l} - \hat{A}^{-}_{j,k,l}\right)\right]\Delta\hat{Q}^{***}_{j,k,l} = \Delta\hat{Q}^{**}_{j,k,l} - \Delta t\left(\hat{A}^{-}\Delta\hat{Q}^{***}\right)_{j+1,k,l}$$

ζ direction

First step

$$\left[I + \Delta t\left(\hat{A}^{+}_{j,k,l} - \hat{A}^{-}_{j,k,l}\right)\right]\Delta\hat{Q}^{*}_{j,k,l} = (RHS) + \Delta t\left(\hat{A}^{+}\Delta\hat{Q}^{*}\right)_{j-1,k,l}$$

where $\Delta\hat{Q}^{*}_{j,k,l} = D_{\xi}^{-1}\left[D_{\xi} + U_{\xi}\right]\Delta\hat{Q}^{**}_{j,k,l}$

Second step

$$\left[I + \Delta t\left(\hat{A}^{+}_{j,k,l} - \hat{A}^{-}_{j,k,l}\right)\right]^{-1}\Delta\hat{Q}^{**}_{j,k,l} = \Delta\hat{Q}^{*}_{j,k,l}$$

where $\Delta\hat{Q}^{**}_{j,k,l} = D_{\xi}^{-1}\left[D_{\xi} + U_{\xi}\right]\Delta\hat{Q}^{***}_{j,k,l}$

Third step

$$\left[I + \Delta t\left(\hat{A}^{+}_{j,k,l} - \hat{A}^{-}_{j,k,l}\right)\right]\Delta\hat{Q}^{***}_{j,k,l} = \Delta\hat{Q}^{**}_{j,k,l} - \Delta t\left(\hat{A}^{-}\Delta\hat{Q}^{***}\right)_{j+1,k,l}$$

ξ direction

First step

$$\left[I + \Delta t\left(\hat{A}^{+}_{j,k,l} - \hat{A}^{-}_{j,k,l}\right)\right]\Delta\hat{Q}^{*}_{j,k,l} = (RHS) + \Delta t\left(\hat{A}^{+}\Delta\hat{Q}^{*}\right)_{j-1,k,l} \tag{3.90}$$

where

$$\Delta\hat{Q}^{*}_{j,k,l} = D_{\xi}^{-1}\left[D_{\xi} + U_{\xi}\right]\Delta\hat{Q}^{**}_{j,k,l}$$

Second step

$$\left[I + \Delta t\left(\hat{A}^{+}_{j,k,l} - \hat{A}^{-}_{j,k,l}\right)\right]^{-1}\Delta\hat{Q}^{**}_{j,k,l} = \Delta\hat{Q}^{*}_{j,k,l} \tag{3.91}$$

where

$$\Delta\hat{Q}^{**}_{j,k,l} = D_{\xi}^{-1}\left[D_{\xi} + U_{\xi}\right]\Delta\hat{Q}^{***}_{j,k,l}$$

Third step

$$\left[I + \Delta t\left(\hat{A}^{+}_{j,k,l} - \hat{A}^{-}_{j,k,l}\right)\right]\Delta\hat{Q}^{***}_{j,k,l} = \Delta\hat{Q}^{**}_{j,k,l} - \Delta t\left(\hat{A}^{-}\Delta\hat{Q}^{***}\right)_{j+1,k,l} \tag{3.92}$$

η direction

Fourth step

$$\left[I + \Delta t\left(\hat{B}^{+}_{j,k,l} - \hat{B}^{-}_{j,k,l}\right)\right]\Delta\hat{Q}^{***}_{j,k,l} = (RHS) + \Delta t\left(\hat{B}^{+}\Delta\hat{Q}^{***}\right)_{j,k-1,l} \tag{3.93}$$

where

$$\Delta\hat{Q}^{***}_{j,k,l} = D_\eta^{-1}\left[D_\eta + U_\eta\right]\Delta\hat{Q}^{****}_{j,k,l}$$

Fifth step

$$\left[I + \Delta t\left(\hat{B}^{+}_{j,k,l} - \hat{B}^{-}_{j,k,l}\right)\right]^{-1}\Delta\hat{Q}^{****}_{j,k,l} = \Delta\hat{Q}^{***}_{j,k,l} \tag{3.94}$$

where

$$\Delta\hat{Q}^{****}_{j,k,l} = D_\eta^{-1}\left[D_\eta + U_\eta\right]\Delta\hat{Q}^{*****}_{j,k,l}$$

Sixth step

$$\left[I + \Delta t\left(\hat{B}^{+}_{j,k,l} - \hat{B}^{-}_{j,k,l}\right)\right]\Delta\hat{Q}^{*****}_{j,k,l} = \Delta\hat{Q}^{****}_{j,k,l} - \Delta t\left(\hat{B}^{-}\Delta\hat{Q}^{*****}\right)_{j,k+1,l} \tag{3.95}$$

ζ direction

Seventh step

$$\left[I + \Delta t\left(\hat{C}^{+}_{j,k,l} - \hat{C}^{-}_{j,k,l}\right)\right]\Delta\hat{Q}^{*****}_{j,k,l} = (RHS) + \Delta t\left(\hat{C}^{+}\Delta\hat{Q}^{*****}\right)_{j,k,l-1} \tag{3.96}$$

where

$$\Delta\hat{Q}^{*****}_{j,k,l} = D_\zeta^{-1}\left[D_\zeta + U_\zeta\right]\Delta\hat{Q}^{n}_{j,k,l}$$

Eighth step

$$\left[I + \Delta t\left(\hat{C}^{+}_{j,k,l} - \hat{C}^{-}_{j,k,l}\right)\right]^{-1}\Delta\hat{Q}^{******}_{j,k,l} = \Delta\hat{Q}^{****}_{j,k,l} \tag{3.97}$$

where

$$\Delta\hat{Q}^{*****}_{j,k,l} = D_\zeta^{-1}\left[D_\zeta + U_\zeta\right]\Delta\hat{Q}^{n}_{j,k,l}$$

Ninth step

$$\left[I + \Delta t\left(\hat{C}^{+}_{j,k,l} - \hat{C}^{-}_{j,k,l}\right)\right]\Delta\hat{Q}^{n}_{j,k,l} = \Delta\hat{Q}^{******}_{j,k,l} - \Delta t\left(\hat{C}^{-}\Delta\hat{Q}^{n}\right)_{j,k,l+1} \tag{3.98}$$

where $\Delta\xi = \Delta\eta = \Delta\zeta = 1$ for simplicity. There are several ways to evaluate such as Steger-Warming FVS[125] etc., though, following definition is much easier and cost effective. To reduce the computational cost, The idea of LU-SGS[119,120] or Lax-Friedrich scheme[126] is employed instead of the diagonal form[127] of LU-ADI. Therefore, in the ADI-SGS implicit time integration scheme, the following approximation is then applied to the Jacobian matrices, $\hat{A}^{\pm}$, $\hat{B}^{\pm}$ and $\hat{C}^{\pm}$,

$$\begin{aligned} \hat{A}^{\pm} &= \frac{\hat{A} + \sigma(\hat{A})I}{2} \\ \sigma(\hat{A}) &= \max_i \left(|\lambda_i|\right) \\ &= |\xi_t + U| + a\sqrt{\xi_x^2 + \xi_y^2 + \xi_z^2} \end{aligned} \tag{3.99}$$

λ_i : ith eigen value of $\hat{A}$

$$\begin{aligned} \hat{B}^{\pm} &= \frac{\hat{B} + \sigma(\hat{B})I}{2} \\ \sigma(\hat{B}) &= \max_i \left(|\lambda_i|\right) \\ &= |\eta_t + V| + a\sqrt{\eta_x^2 + \eta_y^2 + \eta_z^2} \end{aligned} \tag{3.100}$$

λ_i : ith eigen value of $\hat{B}$

$$\begin{aligned} \hat{C}^{\pm} &= \frac{\hat{C} + \sigma(\hat{C})I}{2} \\ \sigma(\hat{C}) &= \max_i \left(|\lambda_i|\right) \\ &= |\zeta_t + W| + a\sqrt{\zeta_x^2 + \zeta_y^2 + \zeta_z^2} \end{aligned} \tag{3.101}$$

λ_i : ith eigen value of $\hat{C}$

where $\sigma(\hat{A})$, $\sigma(\hat{B})$ and $\sigma(\hat{C})$ represent the maximum eigen values of the Jacobian matrices, so-called spectral radius. Then, the left hand side of equations (3.90)-(3.98) becomes

$$\left[I + \Delta t\left(\hat{A}^{+}_{j,k,l} - \hat{A}^{-}_{j,k,l}\right)\right] = \left[1{+}\Delta t\sigma(\hat{A})\right] I \tag{3.102}$$

$$\left[I + \Delta t\left(\hat{B}^{+}_{j,k,l} - \hat{B}^{-}_{j,k,l}\right)\right] = \left[1{+}\Delta t\sigma(\hat{B})\right] I \tag{3.103}$$

$$\left[I + \Delta t\left(\hat{C}^{+}_{j,k,l} - \hat{C}^{-}_{j,k,l}\right)\right] = \left[1{+}\Delta t\sigma(\hat{C})\right] I \tag{3.104}$$

These procedures turns matrix inversion to scalar division.

The inversion of the implicit operator of Eq. 3.82 requires only one forward sweep for the inversion of $L_\xi + D_\xi$ and one backward sweep for that of $D_\xi^{-1}(L_\xi + D_\xi)$.

Finally, the ADI-SGS scheme can be described by using the similar decomposition for the other implicit operators of the other directions η and ζ in 3.82,

The equations 3.98-3.98 can be rewritten from three steps and two steps and the sweeps are conducted below to each factor (i.e., 6 times in total per iteration) as follow

$$\begin{aligned} L_\xi + D_\xi &: \left(I + \Delta t\sigma(\hat{A})\right)\Delta\hat{Q}^*_{j,k,l} - \Delta t\hat{A}_j, k, l^+\Delta\hat{Q}^*_{j-1,k,l} = R \quad \text{:forward sweep} \\ I + D_\xi^{-1}U_\xi &: \Delta\hat{Q}^{**}_{j,k,l} + \frac{1}{1+\Delta t\sigma(\hat{A})}\Delta t\hat{A}^-_{j,k,l}\Delta\hat{Q}^{**}_{j-1,k,l} = \Delta\hat{Q}^*_{j,k,l} \quad \text{:backward sweep} \end{aligned} \tag{3.105}$$

$$\begin{aligned} L_\eta + D_\eta &: \left(I + \Delta t\sigma(\hat{B})\right)\Delta\hat{Q}^{**}_{j,k,l} - \Delta t\hat{B}^+_k\Delta\hat{Q}^{**}_{j,k-1,l} = R \quad \text{:forward sweep} \\ I + D_\eta^{-1}U_\eta &: \Delta\hat{Q}^{***}_{j,k,l} + \frac{1}{1+\Delta t\sigma(\hat{B})}\Delta t\hat{B}^-_{j,k,l}\Delta\hat{Q}^{***}_{j,k-1,l} = \Delta\hat{Q}^{**}_{j,k,l} \quad \text{:backward sweep} \end{aligned} \tag{3.106}$$

$$\begin{aligned} L_\zeta + D_\zeta &: \left(I + \Delta t\sigma(\hat{C})\right)\Delta\hat{Q}^{***}_{j,k,l} - \Delta t\hat{C}^+_{j,k,l}\Delta\hat{Q}^{***}_{j,k,l-1} = R \quad \text{:forward sweep} \\ I + D_\zeta^{-1}U_\zeta &: \Delta\hat{Q}_{j,k,l} + \frac{1}{1+\Delta t\sigma(\hat{C})}\Delta t\hat{C}^-_{j,k,l}\Delta\hat{Q}_{j,k,l-1} = \Delta\hat{Q}^{***}_{j,k,l} \quad \text{:backward sweep} \end{aligned} \tag{3.107}$$

This implicit method is highly suitable for Vector/Parallel hybrid architecture because along a direction in being swept, there still remain two directions free that can be vectorized/parallelized, for three-dimensional case, while in general a Gauss-Seidel relaxation is not suitable for Vector/Parallel hybrid system. The ADI-SGS scheme eliminates the need for the inversions of block diagonal matrices, as seen in the LU-ADI scheme, without using a diagonalization procedure, and can achieve further reduction of calculation processes compared to the LU-ADI scheme. In addition, the ADI-SGS scheme is more diagonally dominant, i.e., more stable than the LU-ADI scheme due to the approximation of the split Jacobian matrices with those spectral radius. The ADI-SGS scheme introduces several approximation (e.g. linear approximation and approximate factorization) to inverse the implicit operator efficiently. Especially for the approximation of the Eqs. 3.99-3.101, the numerical dissipation corresponding to the eigen values of each wave is added, and the excessive numerical dissipation may introduce to a specific wave. Therefore its temporal accuracy is less than the first-order. As a result, ADI-SGS implicit scheme cannot be applied to an unsteady flow simulation unless the local CFL

number is kept at a magnitude of order unity. Therefore, in the present study, multiple sub-iterations are adopted and the errors are eliminated.

Treatment of Viscous Term in the Time Integration

Though it is assumed above that the viscous terms in the left-hand side of Eq. 3.72 can be dealt with explicitly, it is possible to add the viscous terms to the left-hand side as implicit operators.[128,129] However, the operators on the left-hand side are variously approximated, and the strictness of these approximations is not specially needed. Therefore, for practical use, it is known that the viscous terms can be put only in the right-hand side and dealt with explicitly.[121,122] However, in the calculation of low Reynolds number (i.e., less than 10^4), it is known that the calculation diverges because of the disagreement of left- and right- hand sides, then some kinds of approximation operators are indispensable. In the present research, a comparatively high Reynolds number are dealt, in the turbulent boundary layer, the viscosity becomes very high, and the Reynolds number virtually seems to decrease.

For simplicity and efficiency, in the present study, the following approximate operator of the viscous terms introduced by Obayashi *et al.*[130] which is similar to the implicit MacCormack scheme[131] is added in the diagonal matrix in the left hand side of the Eqs. 3.99, 3.100 and 3.101. Thus, to add the effect of the viscosity, the equations are modified by:

$$
\begin{aligned}
\sigma_\xi &= |\xi_t + U| + c\sqrt{\zeta_x^2 + \zeta_y^2 + \zeta_z^2} + 2\hat{\nu} \\
\hat{\nu} &= \frac{\mu\left(\xi_x^2 + \xi_y^2 + \xi_z^2\right)}{Re \cdot \rho \cdot \Delta\xi} \\
\sigma_\eta &= |\eta_t + V| + c\sqrt{\eta_x^2 + \eta_y^2 + \eta_z^2} + 2\hat{\nu} \\
\hat{\nu} &= \frac{\mu\left(\eta_x^2 + \eta_y^2 + \zeta_z^2\right)}{Re \cdot \rho \cdot \Delta\eta} \\
\sigma_\zeta &= |\zeta_t + W| + c\sqrt{\zeta_x^2 + \zeta_y^2 + \zeta_z^2} + 2\hat{\nu} \\
\hat{\nu} &= \frac{\mu\left(\zeta_x^2 + \zeta_y^2 + \zeta_z^2\right)}{Re \cdot \rho \cdot \Delta\zeta}
\end{aligned}
\tag{3.108}
$$

Turbulence Modeling

Large-eddy simulation (LES) is adopted in the study to resolve the three-dimensional fine vortex structures of the flow inside and outside the cavity, turbulent boundary layer

and separated shear layer. Direct numerical simulation (DNS) is not used because the present computational resources are not sufficient for DNS, and the analysis of vortex structure that can be resolved using LES is sufficient for understanding the flow control mechanism. LES does not solve the full range of scales (unlike DNS), but it solves a much larger range of scales than RANS. Hence, LES is potentially more accurate than RANS, since less modeling errors are introduced. In LES approaches, required resolution is coarser than in DNS, while much finer resolution is needed than in RANS.

Large eddy simulation (LES) is a popular technique for simulating turbulent flows. An implication of Kolmogorov's theory of self similarity is that the large eddies of the flow are dependant on the geometry while the smaller scales more universal.[52] This feature allows one to explicitly solve for the large eddies in a calculation and implicitly account for the small eddies by using a subgrid-scale model (SGS model) such as Smagorinsky model[132]as shown in Fig 3.2.

With a traditional LES approach, physical dissipation at the Kolmogorov scale is not represented. For spatially non-dissipative numerical schemes, without use of SGS models, this leads to an accumulation of energy at high mesh wave numbers, and ultimately to numerical instability. Explicitly added SGS models are then employed as a means to dissipate this energy.

In this study, the implicit LES (ILES) is used instead of SGS model. The ILES approach which any explicit sub-grid scale terms are not used while numerical viscosity (dissipation and dispersion) or high-order filtering procedure[65,66,67] are used to dissipate the small waves compared with grid size. As a result, reasonable energy spectra are obtained with the ILES approaches. In the present methodology, the effect of the smallest fluid structures is accounted for by an ILES technique, which has been successfully utilized for a number of turbulent and transitional computations, some of which will subsequently be described. The ILES approach was first introduced by Visbal et al.[?] as a formal alternative to conventional methodologies, and is predicated upon the high-order compact differencing and low-pass spatial filtering schemes, without the inclusion of additional SGS modeling. This technique is similar to monotonically integrated large-eddy simulation (MILES)[133] in that it relies upon the numerical solving procedure to provide the dissipation of upwinding scheme[62,63,133,64] that is typically supplied by traditional SGS models. Unlike MILES however, dissipation is contributed only at high spatial wave numbers where the solution is poorly resolved, by the aforementioned high-order Padé -type low-pass filter. This allows a mechanism for the turbulence energy to be dissipated at scales that cannot be accurately resolved on a given mesh system, in a fashion similar to sub-grid modeling. For purely laminar flows, filtering may be required

to maintain numerical stability and preclude a transfer of energy to high-frequency spatial modes due to spurious numerical events. The ILES methodology thereby permits a seamless transition from large-eddy simulation to direct numerical simulation as the resolution is increased. In the ILES approach, the unfiltered governing equations may be employed, and the computational expense of evaluating sub-grid models, which can be substantial, is avoided. Therefore, ILES is sufficient stable and the computational cost is small compared with an explicit LES. The procedure, which uses unfiltered governing equations, also enables the unified simulation of flow-fields where laminar, transitional, and turbulent regions simultaneously coexist.

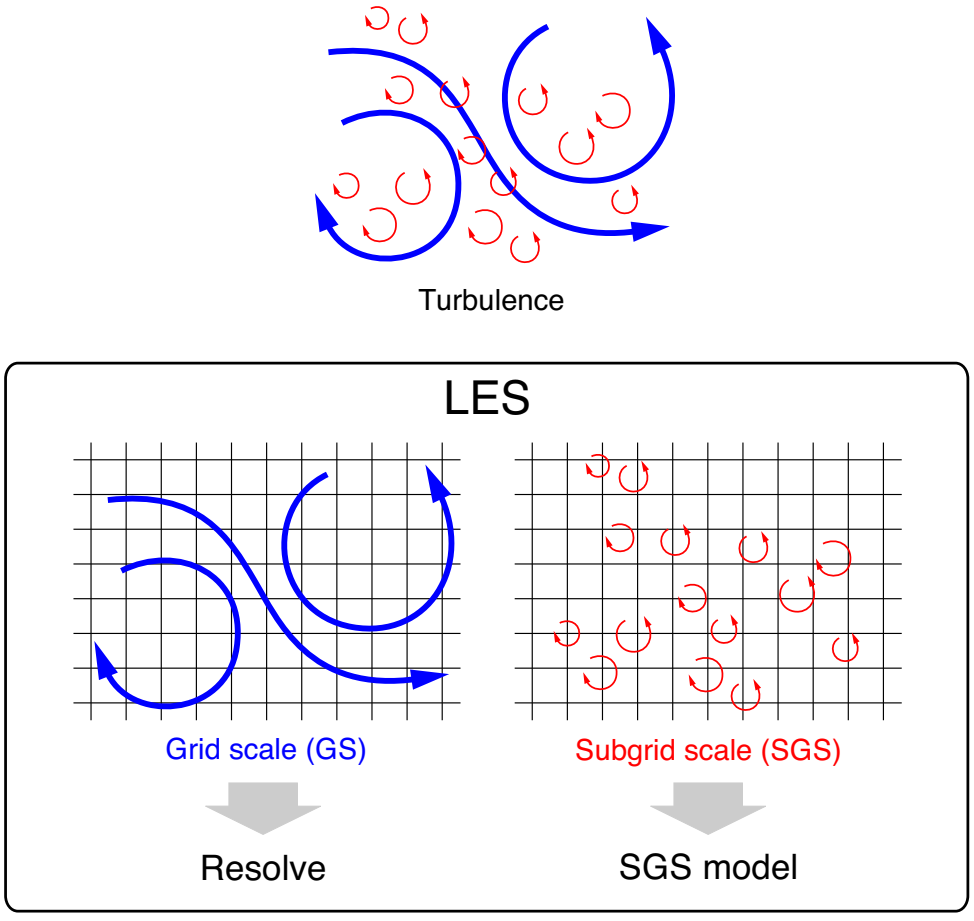

Figure 3.2: Concept of LES.

3.1.4 Computational Domain, Grid System, and Time Step Size

The zonal method[134] is employed to treat the small DBD plasma actuator region. Figure 3.3 shows the computational grids and coordinates, where the DBD plasma actuator model is applied at 5 % chord length from the leading edge. Every four grid points in each direction are presented in this figure. The grids for ILES consist of two parts. The blue grid (Zone 1) is the grid for the flow around the airfoil and the red grid (Zone 2) is the fine grid for the flow around the DBD plasma actuator. Computation procedure consists of the following three steps. At first, the body force is calculated with Suzen model on the green grid (actuator grid) corresponding to the DBD plasma actuator model region. Then, the body force is mapped to the Zone 2 grid from the actuator grid. The Zone 1 is the C type grid and the length from the wing surface to the exterior boundary is 20 times chord length. The length of the computational region in span direction (y-direction) is 0.2. The numbers of grip points in the each case of different actuator location are shown in Table 3.4. In the chapter 5 and the chapter 6, different grid resolutions are adopted. This reason is explained in the chapter 4. Note that the spatial resolution of a sixth-order compact difference scheme is, in general, much finer than a conventional second-order scheme.[54] Our experience indicates that the results with the present method would correspond to those from a conventional method with 50 to 100 times more grid points. The Zone 2 is overlapped with the Zone 1, and the flow variables are interpolated at the seven grid points on the edge of the Zone 2 from the Zone 1. In the same way, the flow variables are interpolated at the Zone 1 from the Zone 2 except the seven grid points of the edge. The minimum grid size in the direction normal to the airfoil surface is 0.00012 in Zone 1 and Zone 2. The computational time step is 0.0002 in non-dimensional time so that the maximum Courant-Friedrichs-Lewy (CFL) number becomes approximately 1.6. This time step size is enough small to resolve the base sinusoidal wave of DBD plasma actuator because the period of base sinusoidal wave is 0.017 in non-dimensional time. At the outflow boundary, all variables are extrapolated from one point front of the outflow boundary. On the airfoil surface, no-slip conditions are adopted. Periodic boundary condition is applied to the spanwise boundaries and the flow variables of five grid points are directly exchanged without any interpolation.

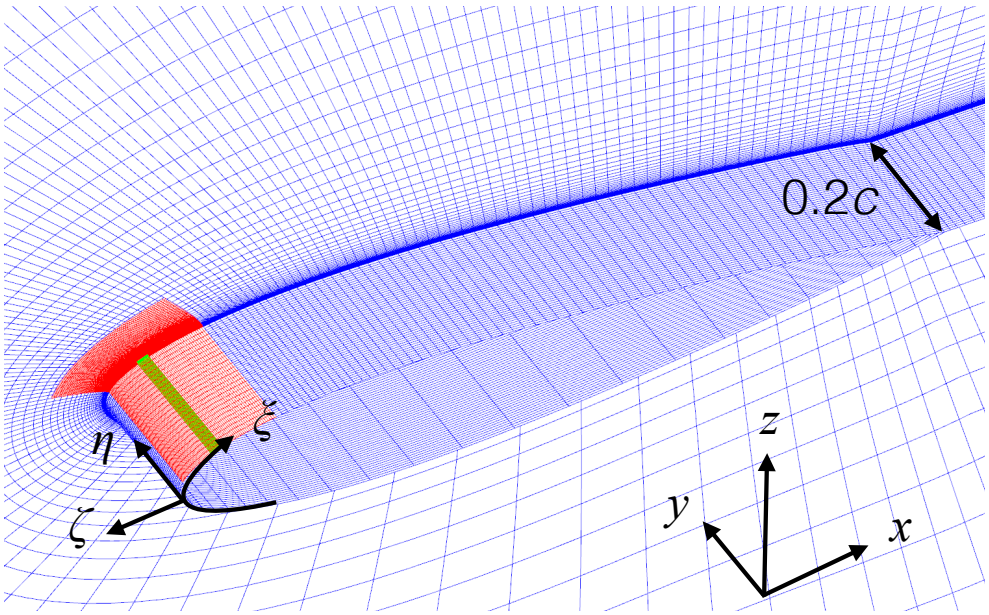

Figure 3.3: computational grid.

Table 3.4: Grid points.

Grid set	DBD location	Zone 1	Zone 2	Total grid points
Set #1 (chapter 5)	0 %	351 × 101 × 121	115 × 101 × 201	6,624,186
	5 %		301 × 101 × 201	10,400,172
Set #2 (chapter 6)	5 %	795 × 134 × 179	129 × 131 × 61	20,099,709

3.1.5 Boundary Conditions

In this subsection, the boundary conditions used in fluid analyses are explained.

Far-Fields Condition

Here the far-fields condition is explained. With regard to the condition at the second point of the boundary, two cases are switched. In this procedure, contra-variant velocity is used for the switching.

If the flow is going out from the computational domain, flow variables at far fields boundaries are fixed to the ambient condition as follows.

$$Q_{far-field} = Q_{\infty}. \tag{3.109}$$

If the flow is coming into computational domain, flow variables at the far field boundary are extrapolated from the inner computational domain except for the static pressure.

$$\begin{bmatrix} \rho \\ \rho u \\ \rho v \\ \rho w \\ e \end{bmatrix}_{far-field} = \begin{bmatrix} \rho\,|_{inner} \\ \rho u\,|_{inner} \\ \rho v\,|_{inner} \\ \rho w\,|_{inner} \\ \frac{p_{subsonic/supersonic}}{\gamma-1} + \frac{1}{2}\rho\left(u^2+v^2+w^2\right), \end{bmatrix}, \tag{3.110}$$

where $p_{subsonic/supersonic}$ is switched on a local Mach number at second point of the boundary as follows,

$$p_{subsonic/supersonic} = \begin{cases} p_{\infty} & \text{flow is subsonic} \\ p_{inner} & \text{flow is supersonic.} \end{cases} \tag{3.111}$$

Basically, a local Mach number of the second point of the boundary is less than unity due to the buffer region as discussed below. In addition, the simple one-point first order extrapolation is used in Eq. 3.110.

With this boundary condition, non-physical waves, such as reflected waves, occurs. However, in this study grid-stretching is used in buffer region and unsteady motion of fluids and acoustics are dumped until these motion reaches to the boundary. The grid stretching ratio is decided with several a prior tests because very large grid stretching ratio may cause unphysical acoustic waves. (If we use even the more advanced methods, such as perfect matched layer[135,136] or absorbing layers[137] to dump the waves or vortices,

we must conduct a priori tests to avoid non-physical waves.[138])

Wall Condition

The wall condition is used at the synthetic jet and backward-facing step wall. There are many evaluation methods for a wall condition.[139] In this study, we adopt the wall condition proposed by Rizzi.[140]

Solid wall boundary at the surface of the body is treated as "non-slip" wall, and the velocity components at the wall are given as

$$u = x_\tau, v = y_\tau, w = z_\tau \tag{3.112}$$

where x_τ, y_τ and z_τ represent the velocities of the grid point at the wall. The density is extrapolated from an adjacent node,

$$\rho_{l=1} = \rho_{l=2} \tag{3.113}$$

Static pressure is defined from the equilibrium condition of the momentum normal to the wall ("normal momentum equation"),

$$\frac{\partial p}{\partial n} = -\rho \frac{u_\parallel^2}{R} \tag{3.114}$$

where n is the unit vector normal to the wall, $u_\parallel$ is the velocity component parallel to the wall, and R is the radius of the curvature of the wall. Equation 3.114 is expressed in the generalized coordinate system as follows

$$A\frac{\partial p}{\partial \xi} + B\frac{\partial p}{\partial \eta} + \frac{\partial p}{\partial \zeta} = C \tag{3.115}$$

where

$$\begin{cases} A = \frac{1}{D}\xi_x\zeta_x + \xi_y\zeta_y + \xi_z\zeta_z \\ B = \frac{1}{D}\eta_x\zeta_x + \eta_y\zeta_y + \eta_z\zeta_z \\ C = \frac{1}{D}\left[\rho\left(\frac{\partial\zeta_t}{\partial\tau} + u\frac{\partial\zeta_x}{\partial\tau} + v\frac{\partial\zeta_y}{\partial\tau} + w\frac{\partial\zeta_z}{\partial\tau}\right) - \rho U\left(\zeta_x\frac{\partial u}{\partial\xi} + \zeta_y\frac{\partial v}{\partial\xi} + \zeta_z\frac{\partial w}{\partial\xi}\right)\right. \\ \left.-\rho V\left(\zeta_x\frac{\partial u}{\partial\eta} + \zeta_y\frac{\partial v}{\partial\eta} + \zeta_z\frac{\partial w}{\partial\eta}\right)\right] \\ D = \zeta_x^2 + \zeta_y^2 + \zeta_z^2 \end{cases} \tag{3.116}$$

Here, the wall is ζ = const plane. The first term of C in the right hand side of the equation 3.116 is the term due to accelerated motion and deformation of grid. In the present study, x_τ, y_τ and z_τ are calculated from Eq. . Unknown variables in the equation 3.114 are only differential terms of pressure, and pressure distribution over the flow field ($l \geq 2$) is known. Second-order one sided differencing is applied to the difference operator in ζ direction,

$$Ap_\xi + Bp_\eta + \frac{-p_{j,k,3} + 4p_{j,k,2} - 3p_{j,k,1}}{2\Delta\zeta} = C. \tag{3.117}$$

$\Longleftrightarrow$

$$-\frac{2\Delta\zeta}{3}\left(Ap_\xi + Bp_\eta\right) + p_{j,k,1} = -\frac{2}{3}\Delta\zeta\left(C - \frac{-p_{j,k,3} + 4p_{j,k,2}}{2\Delta\zeta}\right) \tag{3.118}$$

The following approximate factorization is applied to the operator in the left hand side of equation 3.118,

$$\left[I - \frac{2}{3}\Delta\zeta A\delta_\xi\right]\left[I - \frac{2}{3}\Delta\zeta B\delta_\eta\right]p_{j,k,1} = -\frac{2}{3}\Delta\zeta\left(C - \frac{-p_{j,k,3} + 4p_{j,k,2}}{2\Delta\zeta}\right) \tag{3.119}$$

where the difference operators in ξ and η directions are second-order central difference operators as

$$p_\xi = \frac{p_{j+1,k,1} - p_{j-1,k,1}}{2\Delta\xi}, p_\eta = \frac{p_{j,k,1+1} - p_{j,k,1-1}}{2\Delta\eta} \tag{3.120}$$

The tri-diagonal equation 3.119 can be solved by LU decomposition which is a kind

of direct methods through a sequence of operations, and pressure $p_{j,k,1}$ on the wall is given then.

Periodic Condition

The periodic conditions are used in the $\eta(k)$ direction boundary. The six points are overlapped in the case of all zones in which the compact scheme is used. These overlapped points are determined for maintaining seventh order and tenth order at interior points (not overlapped points) for the the compact scheme, respectively.

The periodic condition in all zones (six points overlap) is explained. Overlapped indexes are written as follows.

$$\begin{aligned} k = 1 &\leftrightarrow k = k_{max} - 5 \\ k = 2 &\leftrightarrow k = k_{max} - 4 \\ &\vdots \\ k = 5 &\leftrightarrow k = k_{max} - 1 \\ k = 6 &\leftrightarrow k = k_{max} \end{aligned} \tag{3.121}$$

Flow variables are exchanged as follows.

$$\begin{aligned} Q_{k=1} &\leftarrow Q_{k=k_{max}-5} \\ Q_{k=2} &\leftarrow Q_{k=k_{max}-4} \\ Q_{k=3} &\leftarrow Q_{k=k_{max}-3} \\ Q_{k=k_{max}-2} &\leftarrow Q_{k=4} \\ Q_{k=k_{max}-1} &\leftarrow Q_{k=5} \\ Q_{k=k_{max}} &\leftarrow Q_{k=6} \end{aligned} \tag{3.122}$$

Zonal Interface

On the boundaries of zonal grids connected to other ones, twelve grid points are overlapped exactly and the flow variables are directly exchanged without any interpolation[134] in every zonal interfaces at the same time due to avoid numerical oscillations. Therefore, there are no errors for the interpolation of conservative value. Figure 3.4 shows zonal interface between zone A and zone B. Red grid points mean solved grid and green grid points mean exchanged grid points from overlapped grid points (red grid points). This

method maintains the order of accuracy (sixth-order) at such connecting points. This procedure is used for each conservative value for suppressing numerical oscillations per each time steps (including per each sub-iterations of inner iteration).

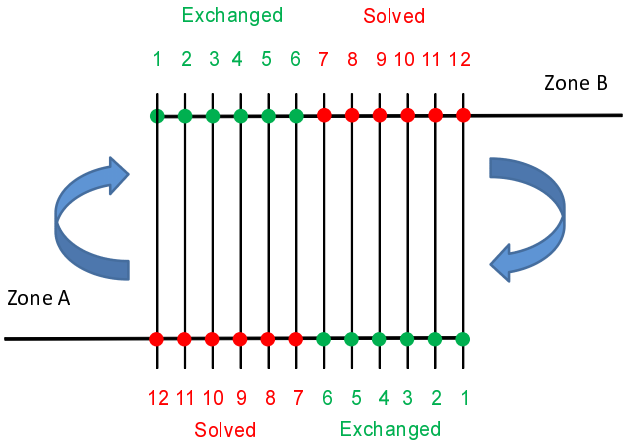

Figure 3.4: Zonal interface.

3.2 DBD Plasma Actuator Modeling

The momentum addition by the plasma discharge to fluid can be introduce to the fluid governing equations as a body force. Some DBD plasma actuator models are proposed to couple the plasma effect with fluid governing equations. Shyy et al.[141] propose a most simple model. They assume the body force distribution as a triangle shape. Corke et al.[142,143] They model discharge of the DBD plasma actuator as capacitors of electric circuit.

In this study, DBD plasma actuator is introduced as a body force to Navier-Stokes equations. The body force is obtained by a model designed by Suzen and Huang (S-H model),[144,145,146,147] which is relatively simple but physically-based model.

3.2.1 Suzne and Huang Model

The working principle of the S-H model stem from the splitting of the electric potential into two governing modes; one describing the effects of electric field and the other characterizing the effects of furface charge density.

The S-H model studied the implication of splitting the total electric potential term (Φ) into two parts: one being influenced by external electric field (φ), and the other potential affected by the net charge density (ϕ).

$$\nabla \cdot (\epsilon_r \nabla \phi) = 0, \tag{3.123}$$

$$\nabla \cdot (\epsilon_r \nabla \varphi) = \rho_c/\epsilon_0, \tag{3.124}$$

where ϵ_0 is the vacuum permittivity, ϵ_r is the relative permittivity, and ρ_c is the surface charge potential.

The net charge density potential (φ) can be eliminated by utilizing the Debye length (λ_D) which relates φ to ρ_c through

$$\rho_c/\epsilon_0 = \left(-1/\lambda_D^2\right)\varphi, \tag{3.125}$$

which combined with Eq. 3.124 yields

$$\nabla \cdot (\epsilon_r \nabla \rho_c) = (\rho_c/\lambda_D^2). \tag{3.126}$$

Thus, the model consists of solving Eqs. 3.123 and 3.126 with suitable boundary conditions. Finally, the Lorentz body force which is used in the Navier-Stokes equations is obtained through

$$F_b = \rho_c(-\nabla\phi). \tag{3.127}$$

The two equations (Eqs. (3.123) and (3.126) above) defining the electric field potential (φ) and the surface charge potential (ρ_c) can be solved initially before the Navier-Stokes equation as these equations do not contain a time derivative term.

3.2.2 Coupling with Fluid Governing Equations

In the nondimensional form, governing equations with the source terms of DBD plasma actuator are represented as follows:

$$\frac{\partial \rho}{\partial t} + \frac{\partial \rho u_k}{\partial x_k} = 0 \tag{3.128}$$

$$\frac{\partial \rho u_i}{\partial t} + \frac{\partial (\rho u_i u_k + p\delta_{ik})}{\partial x_k} = \frac{1}{Re}\frac{\partial \tau_{ik}}{\partial x_k} + D_c F_{bi} \tag{3.129}$$

$$\frac{\partial e}{\partial t} + \frac{\partial \left((e+p)u_k\right)}{\partial x_k} = \frac{1}{Re}\frac{\partial u_l \tau_{kl}}{\partial x_k} + \frac{1}{(\gamma-1)PrReM_\infty^2}\frac{\partial q_k}{\partial x_k} + D_c u_k F_{bk} \tag{3.130}$$

In Eq. (3.129), (3.130), $D_c F_{bi}$ term and $D_c u_k F_{bk}$ term represent the momentum and energy provided by plasma actuator.

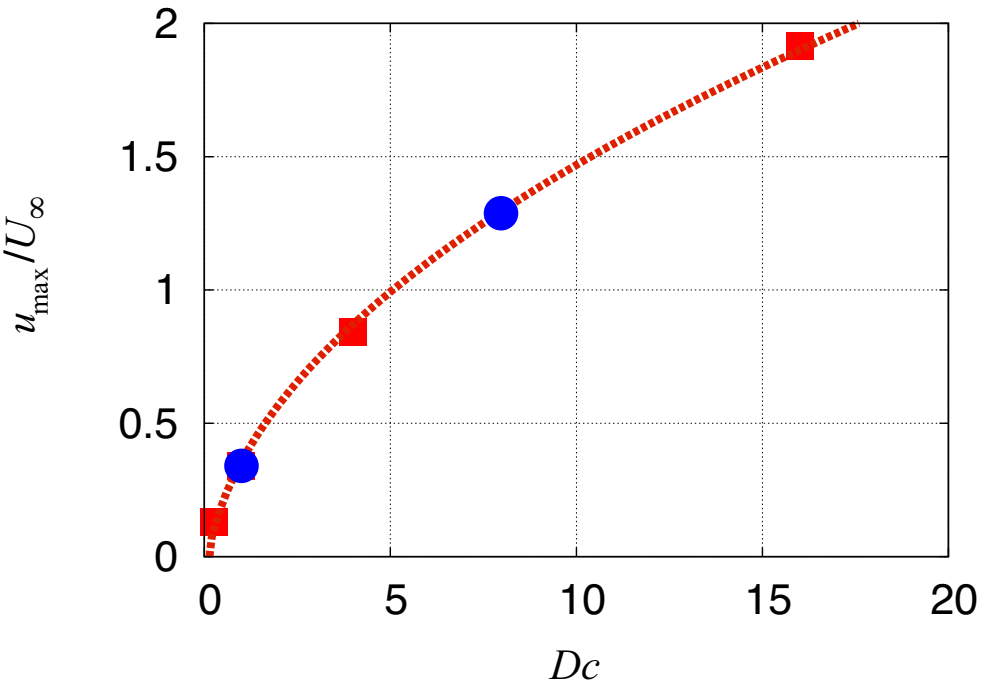

Figure 3.5: Maximum induced velocity u_{max} vs D_c. The data is provided by Dr. Aono[6]. Circles denote D_c values used in the current study. Squares are sample values which are previously computed.

The body force F_{bi} induced by the DBD plasma actuator is obtained by Eq. (3.127) D_c is the non-dimensional number relating to the electromagnetic force, and determines the magnitude of the body force. In this study, F_{bi} is determined by S-H model on the steady boundary condition, and unsteadiness is added simply as follow;

$$F_{bi} = F_{bmax,i} \sin^2(2\pi f_{base} t) \tag{3.131}$$

where $F_{bmax,i}$ is calculated by the S-H model when the exposed electrode potential is positive constant value and insulated electrode potential is zero. Concerning D_c, Actual DBD plasma actuator can induce several meters per second. Thus D_c is set to a value with which the actuator can induce the comparable level velocity to free stream when the free stream is set to 1 [m/s]. Figure 3.5 shows maximum induced velocity u_{max} vs D_c. In the chapter 5, $D_c = 8$ is chosen as a realistic D_c value. With progress the present study, we find that the flow can be controlled by smaller D_c than $D_c = 8$. Therefore in the chapter 6, $D_c = 1$ is chosen.

The instantaneous force vector distribution of S-H model is shown in Fig. 3.6. Contour surface is body force magnitude and yellow vectors show body force direction. The two white lines are the electrodes. This model has two characteristic body forces. One is

the force vertical to the airfoil surface and the other is the force along the airfoil surface. Fig. 3.7 shows the body force magnitude distribution for the present computation. The model region is 0.0015×0.001, and the center of the model region is body surface. The body force distribution in the span direction is uniform. This body force model is rotated around the definition point indicated the red arrow and installed on the airfoil surface at the leading edge and 5 % chord length from the leading edge. The DBD plasma actuator is set in the direction that the actuator induces the flow in the free stream direction.

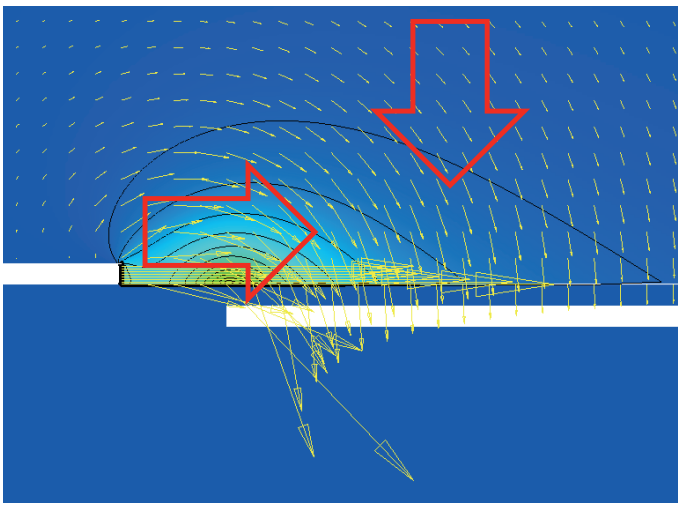

Figure 3.6: Force vectors obtaind by the Suzen-Huang model.

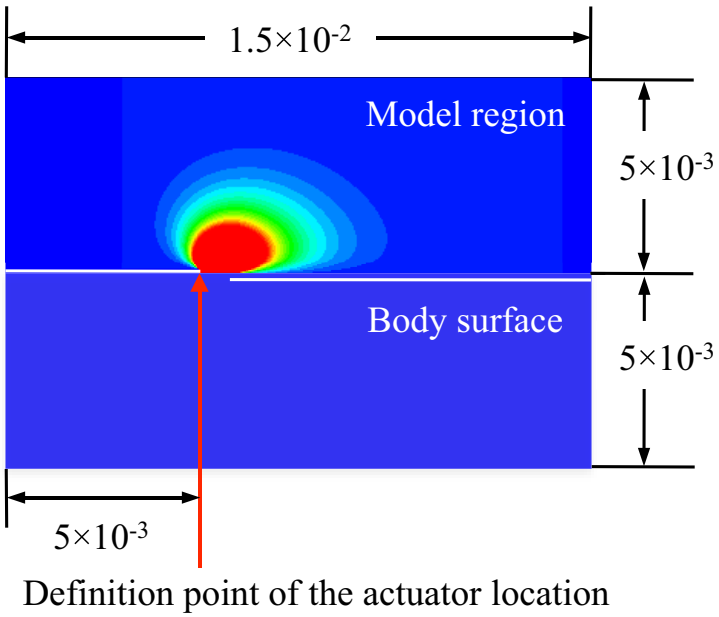

Figure 3.7: Force distribution of Suzen-Huang model.

3.3 Data Processing

In this section, basic data processing is noted. First, computations of averaged values and fluctuation in chapter 5 are explained. Then, processing of ensemble average in chapter 6 are described.

3.3.1 Averaged Value and Fluctuation

In chapter 5, flow data is averaged after the flow is converged to the quasi-steady flow, and totally 50,000 to 500,000 time steps are computed.

$$\langle \phi \rangle = \frac{1}{N} \sum_{n=1}^{N} \phi\left(n\right), \tag{3.132}$$

where $\phi(n)$ is instantaneous flow data (e.g. u, v, and w) at the n-th time step. Fluctuations $\phi'(n)$ are written as follow:

$$\phi'(n) = \phi\left(n\right) - \langle \phi \rangle. \tag{3.133}$$

The averaged product $\langle \phi_1' \phi_2' \rangle$ of $\phi_1'(n)$ and $\phi_2'(n)$ is obtained as follow:

$$\begin{aligned}
\langle \phi_1' \phi_2' \rangle &= \langle \left(\phi_1\left(n\right) - \langle \phi_1 \rangle\right) \left(\phi_2\left(n\right) - \langle \phi_2 \rangle\right) \rangle \\
&= \langle \phi_1\left(n\right) \phi_2\left(n\right) + \phi_1\left(n\right) \langle \phi_2 \rangle + \langle \phi_1 \rangle \phi_2\left(n\right) + \langle \phi_1 \rangle \langle \phi_2 \rangle \rangle \\
&= \langle \phi_1 \phi_2 \rangle - \langle \phi_1 \rangle \langle \phi_2 \rangle \\
&= \frac{1}{N} \sum_{n=1}^{N} \phi_1\left(n\right) \phi_2\left(n\right) - \left[\frac{1}{N} \sum_{n=1}^{N} \phi_1\left(n\right)\right] \left[\frac{1}{N} \sum_{n=1}^{N} \phi_2\left(n\right)\right].
\end{aligned} \tag{3.134}$$

Therefore, the square values of fluctuations are computed as follow:

$$\langle \left(\phi'\right)^2 \rangle = \frac{1}{N} \sum_{n=1}^{N} \phi\left(n\right)^2 - \left[\frac{1}{N} \sum_{n=1}^{N} \phi\left(n\right)\right]^2. \tag{3.135}$$

The root-mean-square values $\langle \phi' \rangle_{\mathbf{rms}}$ of fluctuations are obtained as follow:

$$\langle \phi' \rangle_{\mathbf{rms}} = \sqrt{\langle \left(\phi'\right)^2 \rangle} = \sqrt{\frac{1}{N} \sum_{n=1}^{N} \phi\left(n\right)^2 - \left[\frac{1}{N} \sum_{n=1}^{N} \phi\left(n\right)\right]^2}. \tag{3.136}$$

Turbulence kinetic energy is obtained as flow:

$$TKE = \frac{1}{2}\left(\langle (u')^2 \rangle + \langle (v')^2 \rangle + \langle (w')^2 \rangle\right). \tag{3.137}$$

3.3.2 Ensemble Average of Transient States

In chapter 6, the transient processes in which the separated flow is controlled and the separated region is suppressed gradually, are discussed. In this study, in order to extract coherent flow features and take statistics, ensemble averages of 20 computations are conducted for each computational case. Every computations are started from different time step of massively-separated-flow fields (Fig. 3.8), and the controlled transients of flow reattachments are gathered and averaged. The start times are named as "station XX". Thus, there are 20 start times from "station 01" to "station 20". Every stations are delayed for 25,000 steps ($tU_\infty/c = 1$). In chapter 6, unsteady flow data is stored at each 10 time steps and every second grid points in the each direction. Besides, totally 200,000 time steps ($tU_\infty/c = 8$) are computed.

The computational results in chapter 6 are averaged by three ways (Fig. 3.9). First, the results of every stations are averaged. Second, the spanwise averages are conducted. Finally, partial-time averages are conducted. The ensemble averaged value is written as follow:

$$\langle \phi(j,l,m) \rangle = \frac{1}{N} \sum_{n=N(m-1)+1}^{N} \frac{1}{I} \sum_{i=1}^{I} \frac{1}{K} \sum_{k=1}^{K} \phi(i,j,k,l,n), \tag{3.138}$$

where $\phi(i,j,k,l,n)$ is a instantaneous flow data at the n-th times step, i denotes each time station, j,k,l are grid indices, m is the index of the ensemble averaged value, and I,K,N are the number of samples of each averaging respectively. The I,K,N is

$$I = 20, \quad K = \left\lfloor \frac{k_{max}-1}{2} \right\rfloor + 1, \quad N = \left\lfloor \frac{T_{\mathrm{BST}}}{10\Delta t} \right\rfloor, \tag{3.139}$$

respectively. $\lfloor\ \rfloor$ is the floor function. We obtain the 2D cross-section data by taking the process explained above.

3.3.3 Viscous Wall Unit

In the present study, in order to treat turbulent boundary layer, wall-resolved LES is conducted. The wall-resolved LES directly resolves inner-layer-scale vortices. Thus a fine grid resolution is required enough to resolve the inner-layer-scale vortices. When we consider the inner-layer physics, we can normalize physical quantities by the appropriate

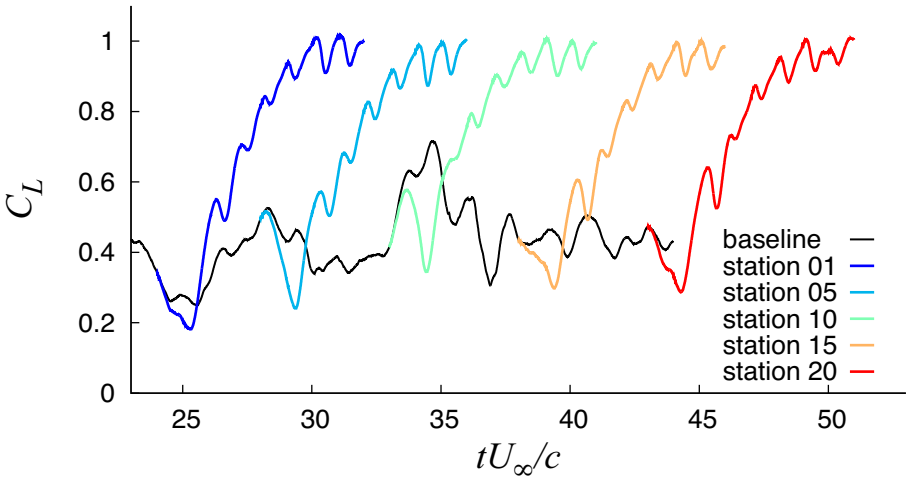

Figure 3.8: Histories of the lift coefficients C_L in chapter 6.

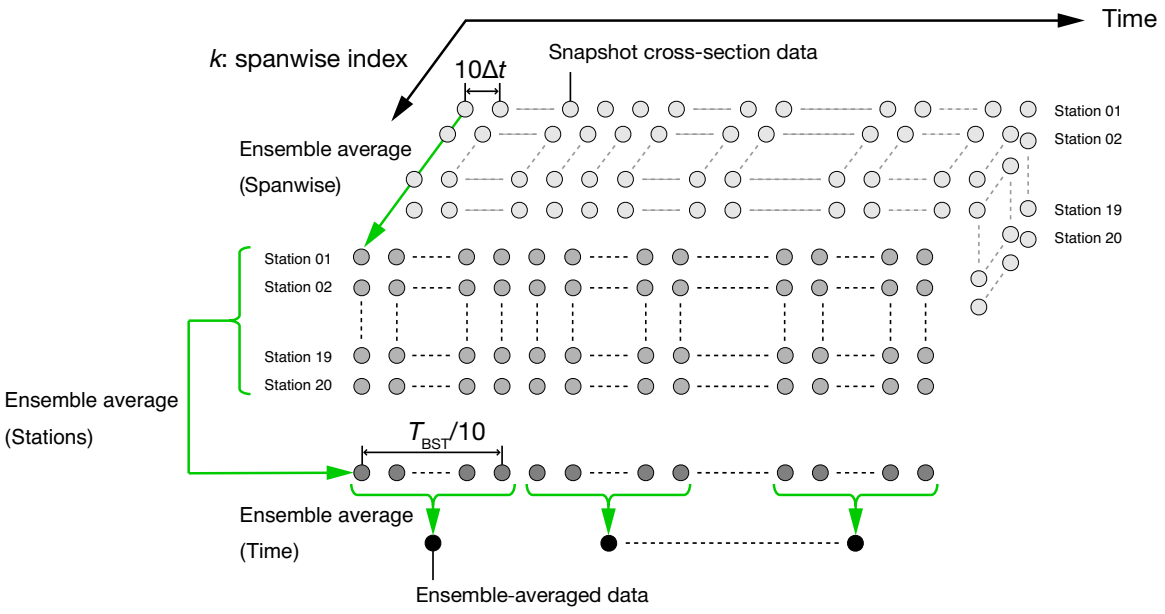

Figure 3.9: Schematic of ensemble average in chapter 6.

velocity scales and length scales in the near-wall region. These are the friction velocity

$$u_\tau^* \equiv \sqrt{\frac{\tau_{\mathrm{w}}^*}{\rho^*}}, \tag{3.140}$$

and the viscous length scale

$$\delta_\nu^* \equiv \nu^* \sqrt{\frac{\rho^*}{\tau_{\mathrm{w}}^*}} = \frac{\nu^*}{u_{\tau^*}}, \tag{3.141}$$

where τ_{w}^* is the wall shear stress and is obtained by[148]

$$\tau_{\mathrm{w}}^* = \mu^* |\boldsymbol{\omega}^*|_{\mathrm{w}}, \tag{3.142}$$

and $|\boldsymbol{\omega}^*|_{\mathrm{w}}$ is the vorticity at the wall. A near-wall length in viscous wall unit y^+ is denoted by

$$y^+ \equiv \frac{y^*}{\delta_\nu^*}, \tag{3.143}$$

Chapter 4

Validation and Verification of the Computational Methods

4.1 Validation and Verification of the Computational Methods

In this study, we focus on control of massive separation from the leading edge. Thus, a post-stall angle of attack is chosen. Figure 4.1 shows the mean pressure coefficients along the airfoil compared to the experiment results,[3] and the computational results at three different angles of attack $\alpha = 4°$, $12°$, $14°$. Solid lines show the present computational results with the grid set #1 in Table 3.4 and symbols show the experimental results.[3] At Reynolds number 63,000, the flows are regarded as stalled at α=12 degs in the Fig. 2.1. The experimental result have flat distribution on a suction side at α=12 in the Fig. 4.1. This pressure distribution indicate a leading edge separation. However the corresponding computational result show a quite different pressure distribution. This is because the angle of attack α=12 degs is a boundary angle between pre-stall and post-stall, and is very sensitive. This sensitivity can be seen in the Fig. 2.1. At Reynolds number 100,000, the flow is regarded as pre-stall at α=12 degs. In this study, massively separated-flow from the leading edge is targeted for separated-flow control. Thus, α=14 degs is chosen as an angle of attack in chapter 5. Figs. 4.2, 4.3, 4.4 show grid resolutions in viscous wall units along the airfoil. Figures 4.2 and 4.3 are the computational results without DBD plasma actuator at the different angles. Figure 4.4 show the result of controlled case. In the each computational case, grid resolutions are $\Delta\xi^+ \lesssim 35$, $\Delta\eta^+ \lesssim 15$, and $\Delta\zeta^+ \lesssim 1$. except for regions near the leading edge where the flows are attached laminar flow. These resolutions are enough to resolve the vortices of inner-layer at turbulent

boundary layer.[98]

With progress of the present study and computational resources, we know that the discrepancy of pressure distribution at $\alpha = 12$ is caused by grid resolution. Therefore in chapter 6, the finer grid resolution (grid set #2 in Table 3.4) is utilized in order to discuss computational results more quantitatively, and angle of attack is set to $\alpha = 12$ because the wealth of experiments have done at this angle of attack in the previous studies.[3,149] The knowledges obtained by the computational results with the grid set #1 in Table 3.4 are verified by Nonomura *et al.*[150] with the grid set #2 in Table 3.4. They show their results agree with the present results which is shown in chapter 5 qualitatively. Figures 4.5 and 4.6 show mean pressure coefficients along the airfoil compared to the corresponding experiment,[3] and the computational results on four different grid resolutions at $\alpha = 10°$ and $\alpha = 12°$. Medium grid is the grid set #2 in Table 3.4. Each grid resolution is shown in Table 4.1. Figures 4.7 and 4.8 show mean streamwise (tangential) velocity profiles, and Figures 4.9 and 4.10 show root-mean-square profiles of streamwise (tangential) velocity fluctuation. These figures show that the computational results converge except for the results with the ultra coarse grid. Figures 4.11 and 4.12 are the computational results without DBD plasma actuator at the different angles. In the each computational case, grid resolutions are $\Delta\xi^+ \lesssim 10$, $\Delta\eta^+ \lesssim 10$, and $\Delta\zeta^+ \lesssim 1$ except for regions near the leading edge where the flows are attached laminar flow. These resolutions are much finer than the resolutions which is adopted in general wall-resolved LES of turbulent boundary layer.[98]

Table 4.1: Grid resolutions for a grid convergence study.

Case name	Resolution ($\xi \times \eta \times \zeta$)	Total grid points
Ultra coarse	$397 \times 58 \times 113$	2,601,938
Coarse	$562 \times 100 \times 153$	8,598,600
Medium (zone 1 of grid set #2)	$795 \times 134 \times 179$	19,068,870
Fine	$1124 \times 180 \times 215$	43,498,800

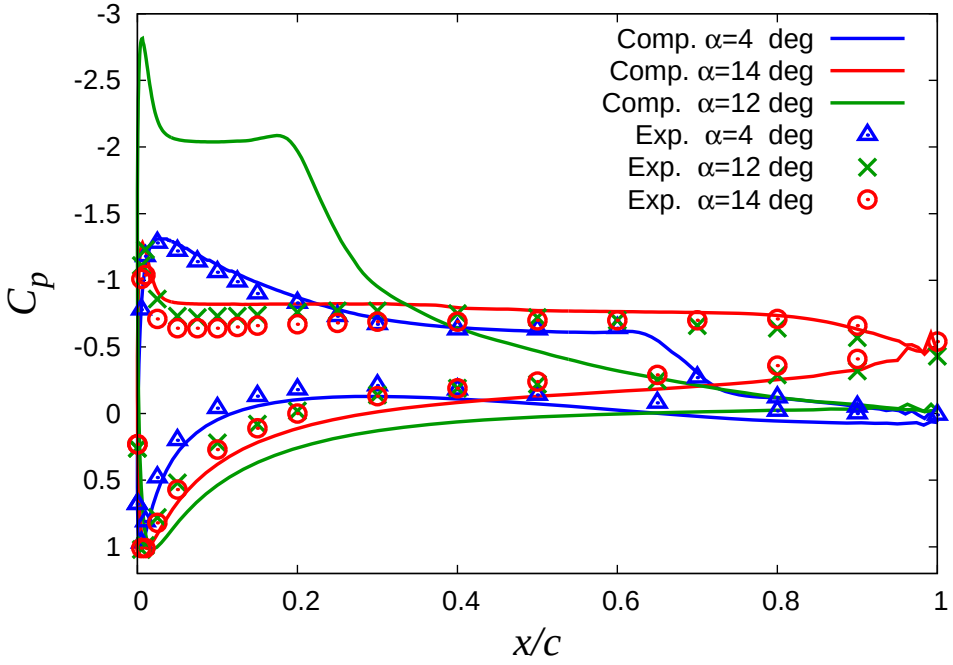

Figure 4.1: Mean pressure coefficients along the airfoil compared to the corresponding experiment, and the computational results with the grid set #1 at three different angles of attack $\alpha = 4°, 12°, 14°$.

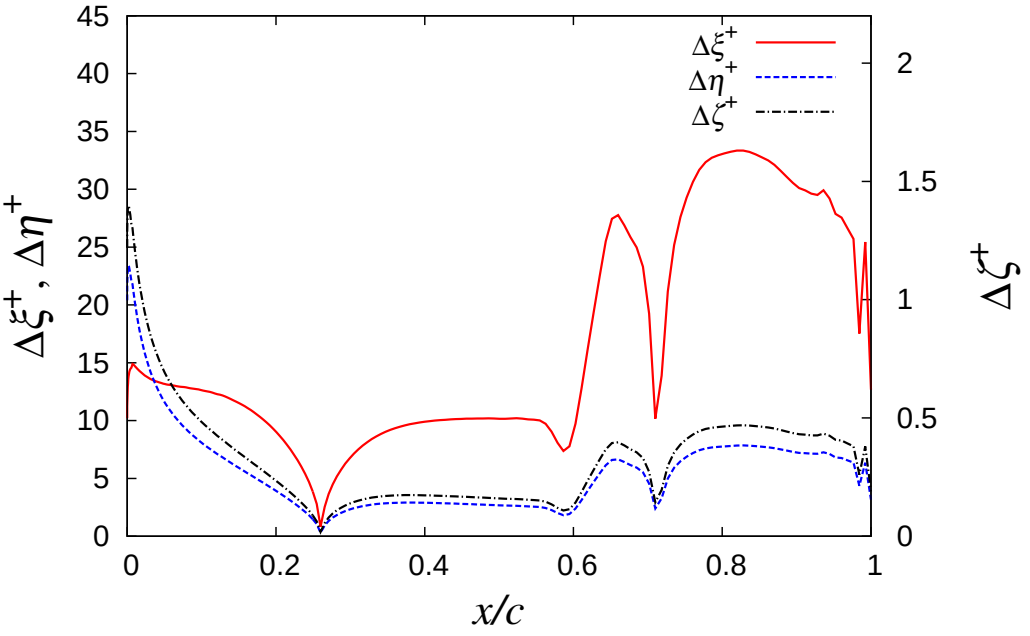

Figure 4.2: Grid resolutions of the grid set #1 in viscous wall units along the airfoil at $\alpha = 4°$.

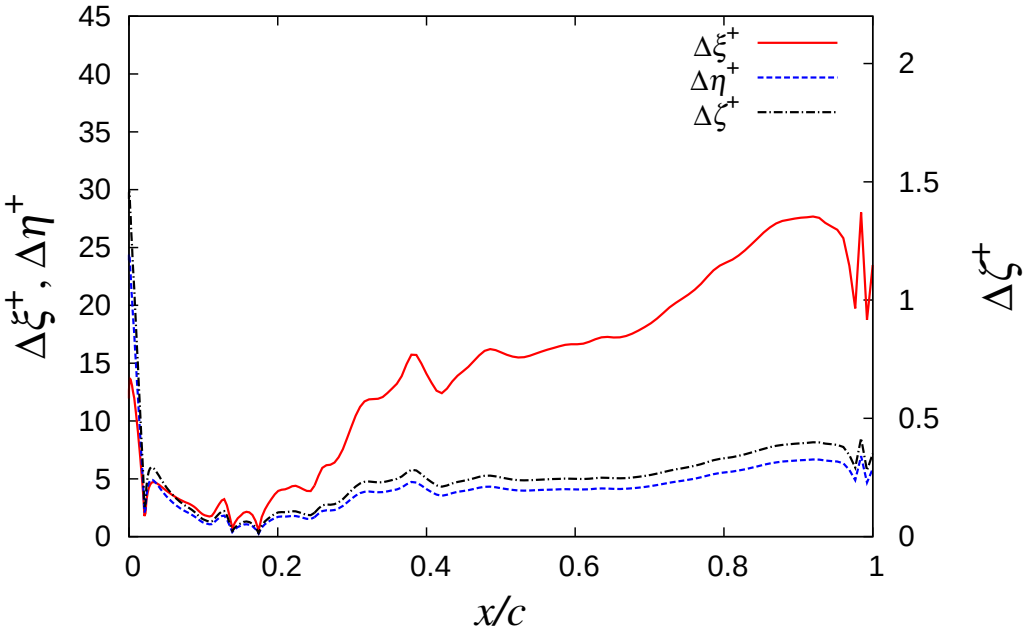

Figure 4.3: Grid resolutions of the grid set #1 in viscous wall units along the airfoil at $\alpha = 14°$.

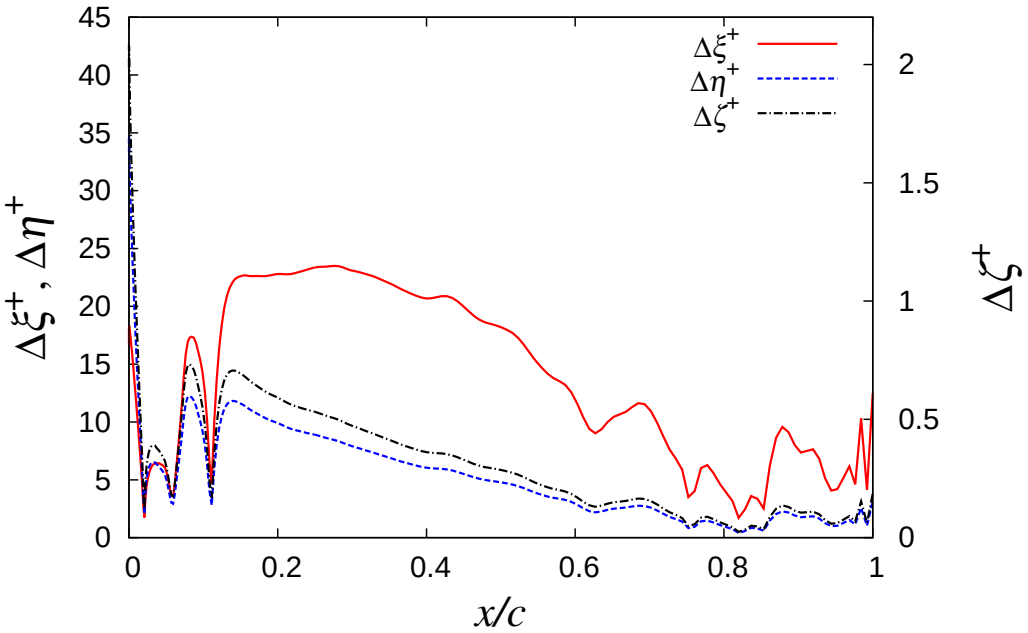

Figure 4.4: Grid resolutions of the grid set #1 in viscous wall units obtained with the burst actuation $F^+ = 1$ along the airfoil at $\alpha = 14°$.

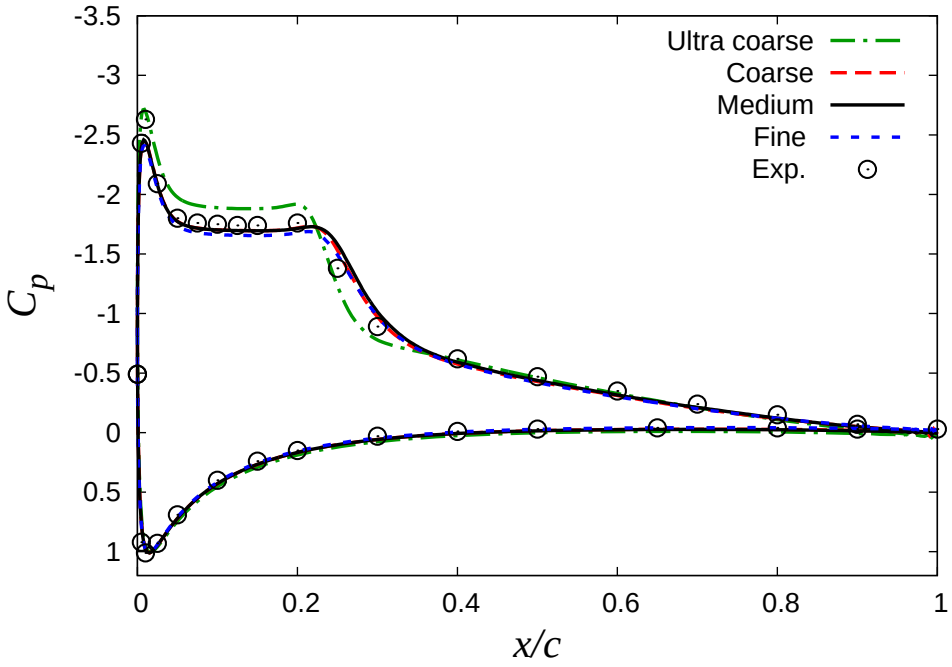

Figure 4.5: Mean pressure coefficients along the airfoil compared to the corresponding experiment, and the computational results on four different grid resolutions at $\alpha = 10°$. Medium grid is the grid set #2.

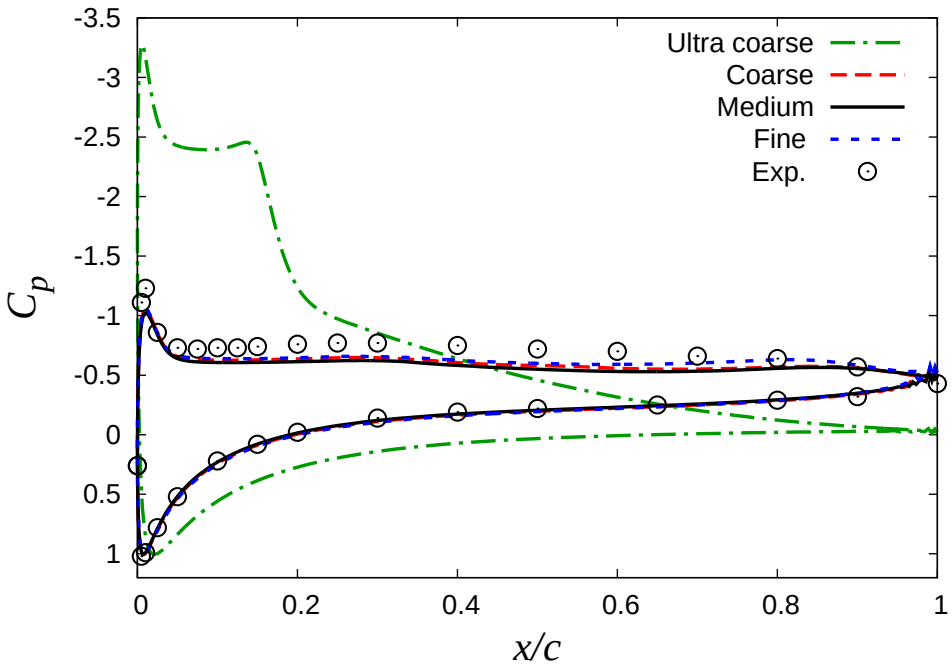

Figure 4.6: Mean pressure coefficients along the airfoil compared to the corresponding experiment, and the computational results on four different grid resolutions at $\alpha = 12°$. Medium grid is the grid set #2.

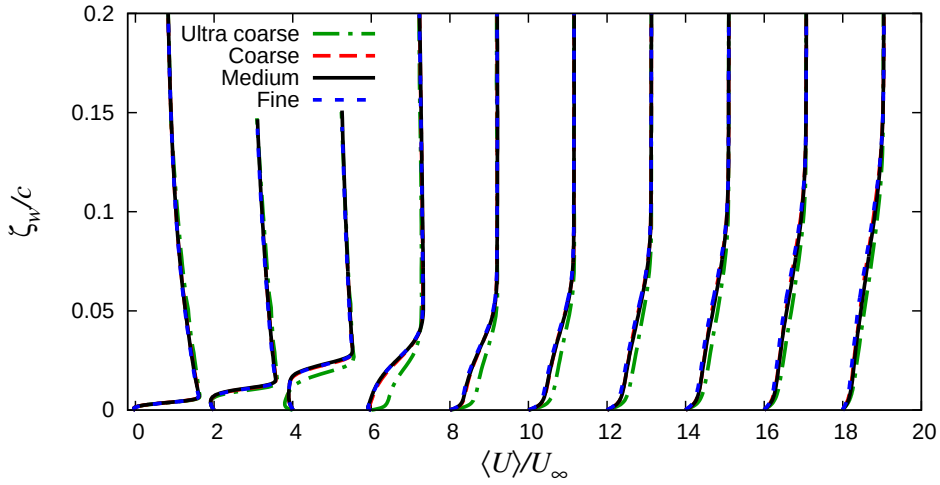

Figure 4.7: Mean streamwise (tangential) velocity profiles as a function of wall-normal distance at $x/c = 0.05, 0.1, 0.2, 0.3, 0.4, 0.5, 0.6, 0.7, 0.8, 0.9$, and $\alpha = 10°$ on four different grid resolutions. Each plot is separated by horizontal offset of 2.0. Medium grid is the grid set #2.

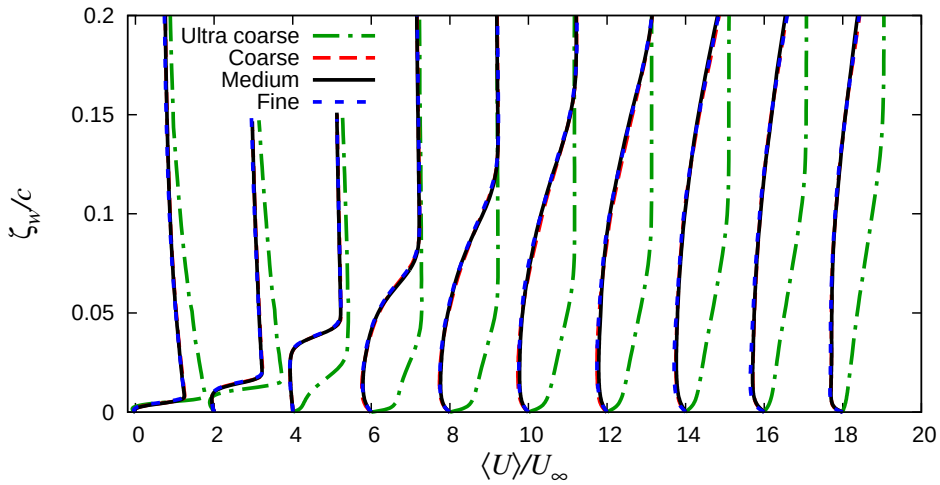

Figure 4.8: Mean streamwise (tangential) velocity profiles as a function of wall-normal distance at $x/c = 0.05, 0.1, 0.2, 0.3, 0.4, 0.5, 0.6, 0.7, 0.8, 0.9$, and $\alpha = 12°$ on four different grid resolutions. Each plot is separated by horizontal offset of 2.0. Medium grid is the grid set #2.

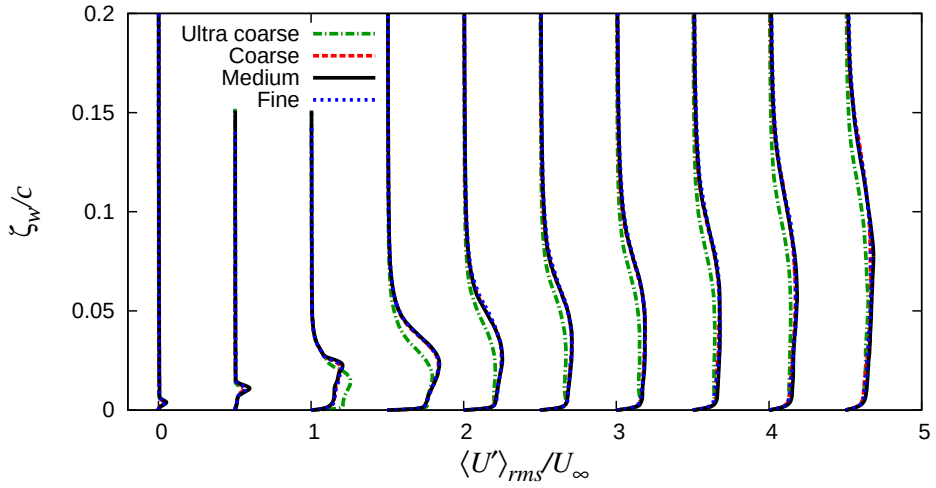

Figure 4.9: Root-mean-square profiles of streamwise (tangential) velocity fluctuation as a function of wall-normal distance at $x/c = 0.05, 0.1, 0.2, 0.3, 0.4, 0.5, 0.6, 0.7, 0.8, 0.9$, and $\alpha = 10°$ on four different grid resolutions. Each plot is separated by horizontal offset of 0.5. Medium grid is the grid set #2.

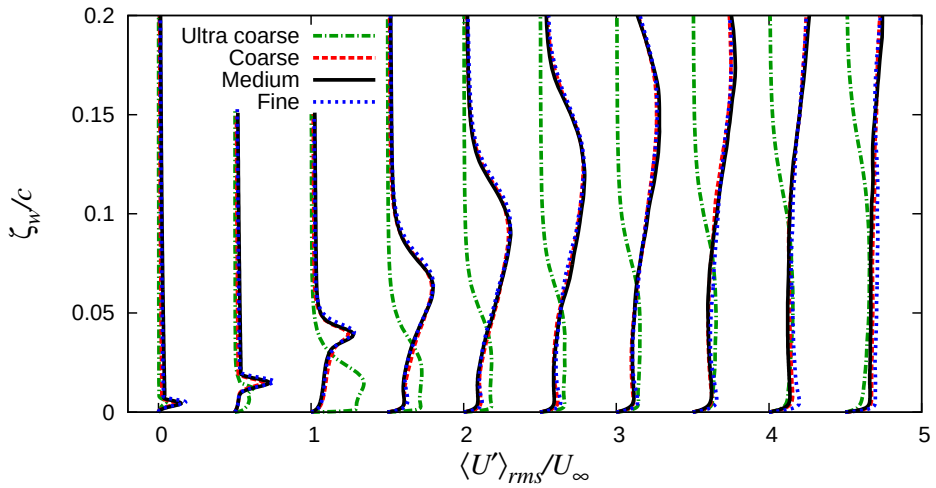

Figure 4.10: Root-mean-square profiles of streamwise (tangential) velocity fluctuation as a function of wall-normal distance at $x/c = 0.05, 0.1, 0.2, 0.3, 0.4, 0.5, 0.6, 0.7, 0.8, 0.9$, and $\alpha = 12°$ on four different grid resolutions. Each plot is separated by horizontal offset of 0.5. Medium grid is the grid set #2.

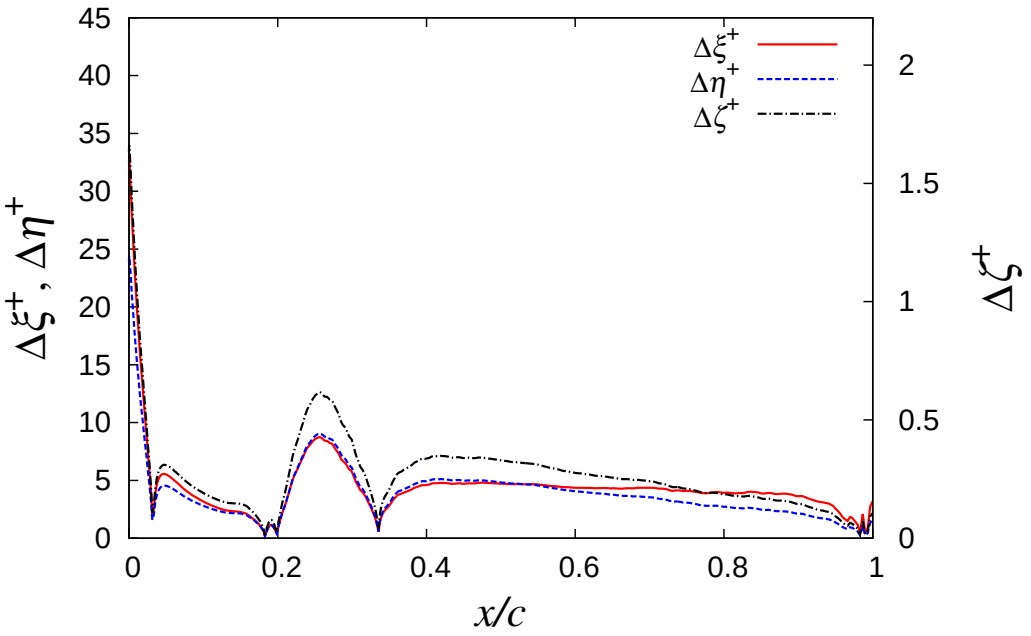

Figure 4.11: Grid resolutions with the grid set #2 in viscous wall units along the airfoil at $\alpha = 10°$.

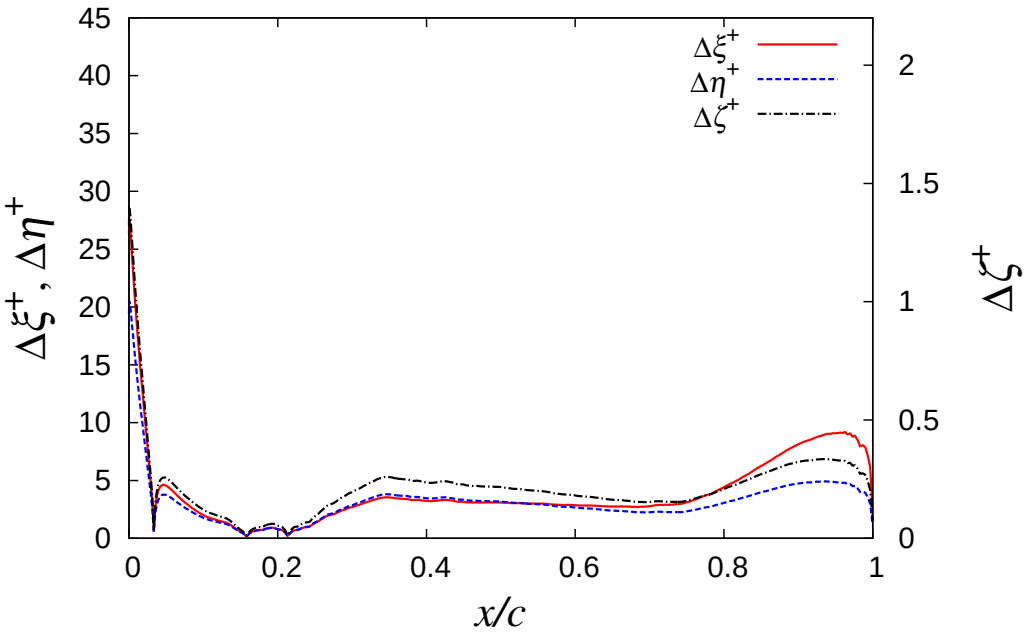

Figure 4.12: Grid resolutions with the grid set #2 in viscous wall units along the airfoil at $\alpha = 12°$.

4.2 Investigation of Effects of Mach Number

In general, the free stream Mach number is set to higher value than the actual value because of computational efficiency. In this section, we investigate effects of free-stream Mach number on the computational results. To clarify the effects of free-stream Mach number, we conduct computations at different free-stream Mach numbers $M_\infty = 0.1$ and $M_\infty = 0.2$ with a grid set #2 at $\alpha = 12°$. Figures 4.13 and 4.14 show mean pressure coefficients C_p along the airfoil at $M_\infty = 0.1$ and $M_\infty = 0.2$. Significant differences of C_p distribution between $M_\infty = 0.1$ and $M_\infty = 0.2$ are not found in Figures 4.13 and 4.14 although C_p distributions are slightly different at plateau region ($x/c \sim 0.05$-0.15) in the Fig. 4.13. Especially, differences of C_p distribution between $F^+ = 1$ and $F^+ = 6$ are not affected by free-stream Mach number. For example, higher values of negative-pressure peak and larger plateau region on the $F^+ = 6$ case than that on the $F^+ = 1$ case. Figures 4.15 and 4.16, and Figures 4.17 and 4.18 show mean streamwise (tangential) velocity profiles and root-mean-square profiles of streamwise (tangential) velocity fluctuation respectively. These figures also show that there are no significant differences between $M_\infty = 0.1$ and $M_\infty = 0.2$.

Figures 4.19 and 4.20 show time histories of the lift coefficient C_L and drag coefficient C_D obtained with the burst actuation $F^+ = 1$ at $M_\infty = 0.1$ and $M_\infty = 0.2$ on transient states in which initial flows separated from the leading edge and gradually controlled by the DBD plasma actuator. Figures 4.21 and 4.22 also show same values as Fig. 4.19 and 4.20 on the $F^+ = 6$ case. Shapes of variation of C_L and C_D are different when the free-stream Mach number is different. However variation magnitudes and periods are comparable level between $M_\infty = 0.1$ and $M_\infty = 0.2$. Moreover characteristics of burst frequency effect which are discussed in chapter 5 and in chapter 6, is not changed by different Mach number.

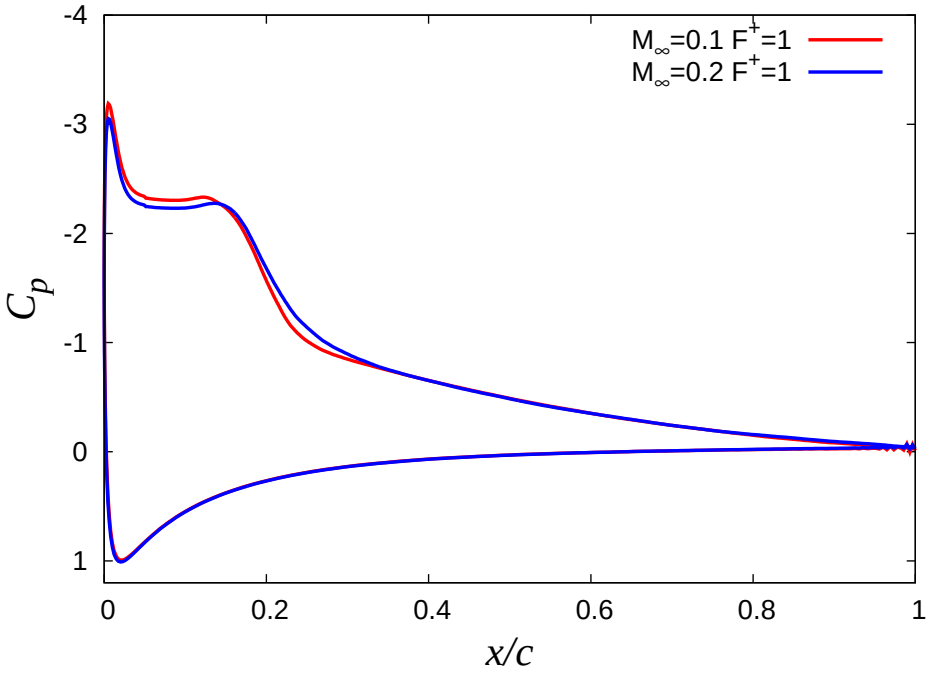

Figure 4.13: Mean pressure coefficients C_p obtained with the burst actuation $F^+ = 1$ along the airfoil at $M_\infty = 0.1$ and $M_\infty = 0.2$.

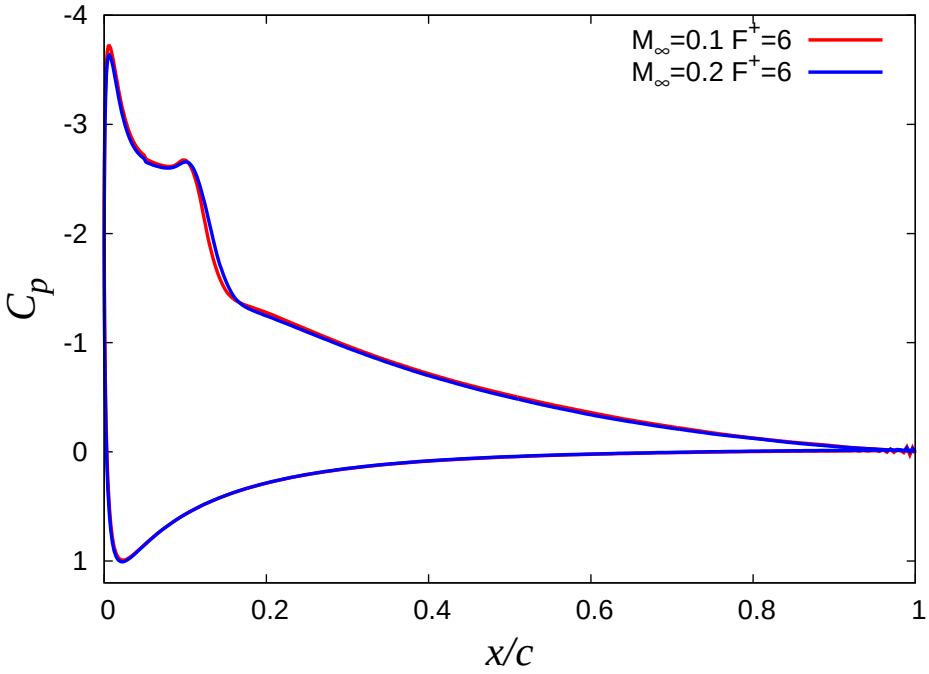

Figure 4.14: Mean pressure coefficients C_p obtained with the burst actuation $F^+ = 6$ along the airfoil at $M_\infty = 0.1$ and $M_\infty = 0.2$.

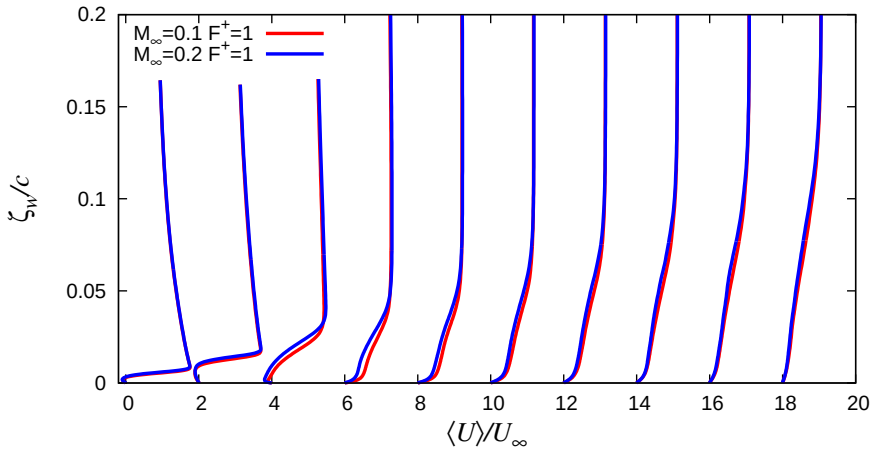

Figure 4.15: Mean streamwise (tangential) velocity profiles as a function of wall-normal distance obtained with the burst actuation $F^+ = 1$ at $M_\infty = 0.1$ and $M_\infty = 0.2$, and $x/c = 0.05, 0.1, 0.2, 0.3, 0.4, 0.5, 0.6, 0.7, 0.8, 0.9$. Each plot is separated by horizontal offset of 2.0.

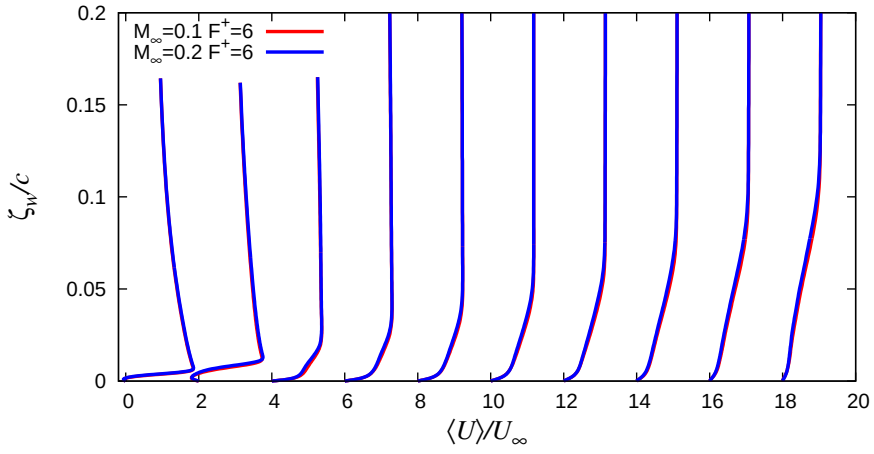

Figure 4.16: Mean streamwise (tangential) velocity profiles as a function of wall-normal distance obtained with the burst actuation $F^+ = 6$ at $M_\infty = 0.1$ and $M_\infty = 0.2$, and $x/c = 0.05, 0.1, 0.2, 0.3, 0.4, 0.5, 0.6, 0.7, 0.8, 0.9$. Each plot is separated by horizontal offset of 2.0.

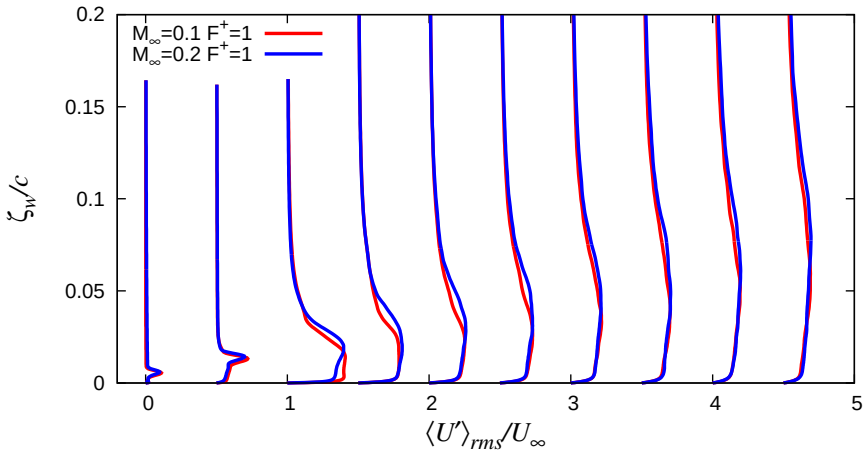

Figure 4.17: Root-mean-square profiles of streamwise (tangential) velocity fluctuation as a function of wall-normal distance obtained with the burst actuation $F^+ = 1$ at $x/c = 0.05, 0.1, 0.2, 0.3, 0.4, 0.5, 0.6, 0.7, 0.8, 0.9$. Each plot is separated by horizontal offset of 0.5.

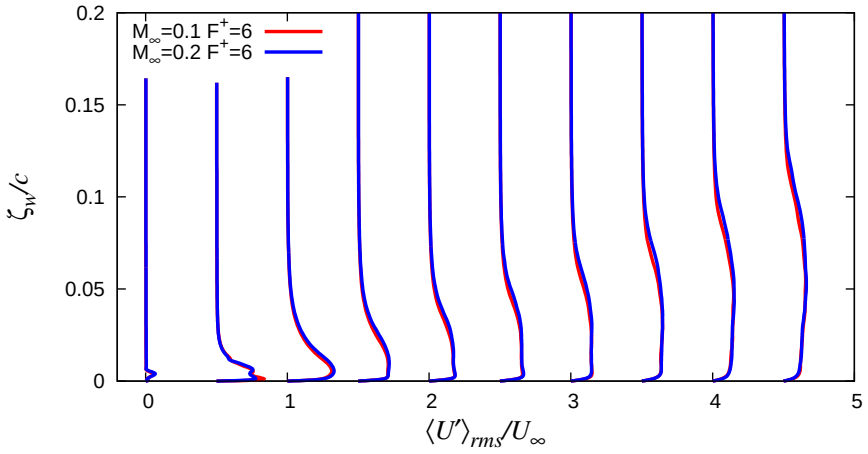

Figure 4.18: Root-mean-square profiles of streamwise (tangential) velocity fluctuation as a function of wall-normal distance obtained with the burst actuation $F^+ = 6$ at $x/c = 0.05, 0.1, 0.2, 0.3, 0.4, 0.5, 0.6, 0.7, 0.8, 0.9$. Each plot is separated by horizontal offset of 0.5.

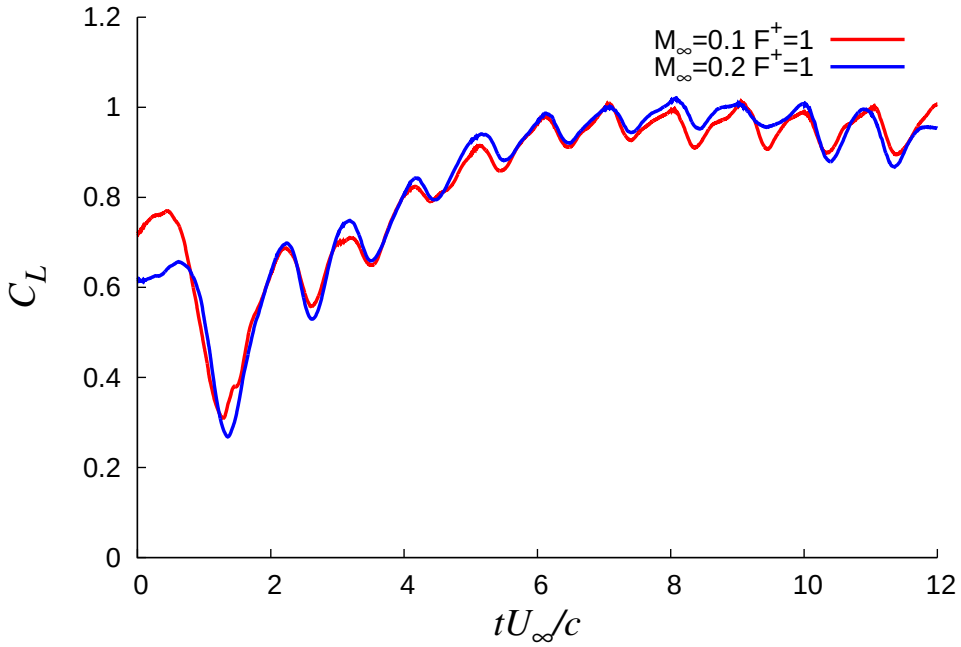

Figure 4.19: Time histories of the lift coefficient C_L obtained with the burst actuation $F^+ = 1$ at $M_\infty = 0.1$ and $M_\infty = 0.2$. The time is normalized by c/U_∞.

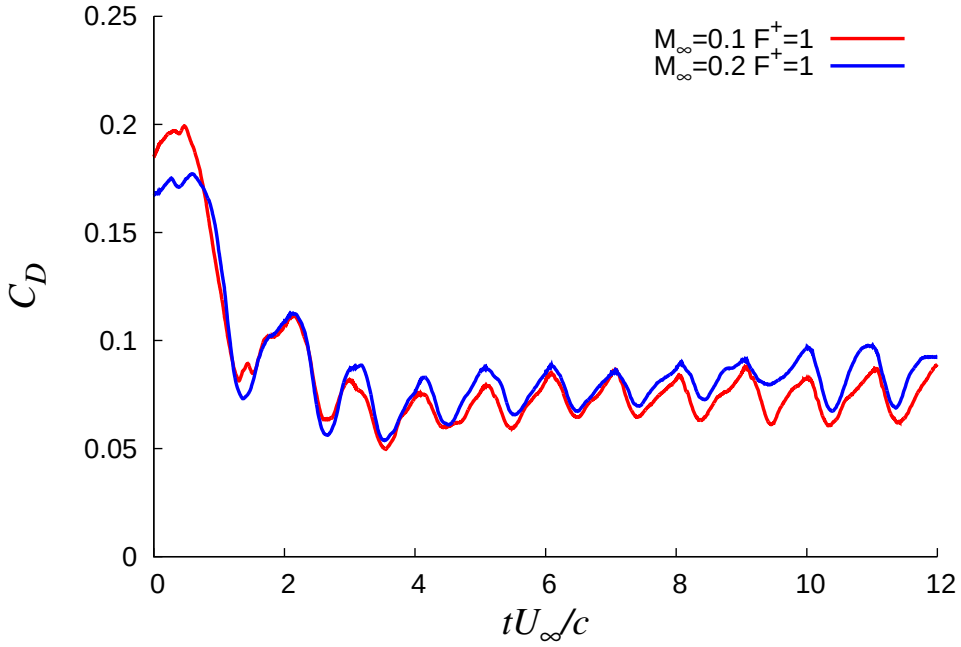

Figure 4.20: Time histories of the drag coefficient C_D obtained with the burst actuation $F^+ = 1$ at $M_\infty = 0.1$ and $M_\infty = 0.2$. The time is normalized by c/U_∞.

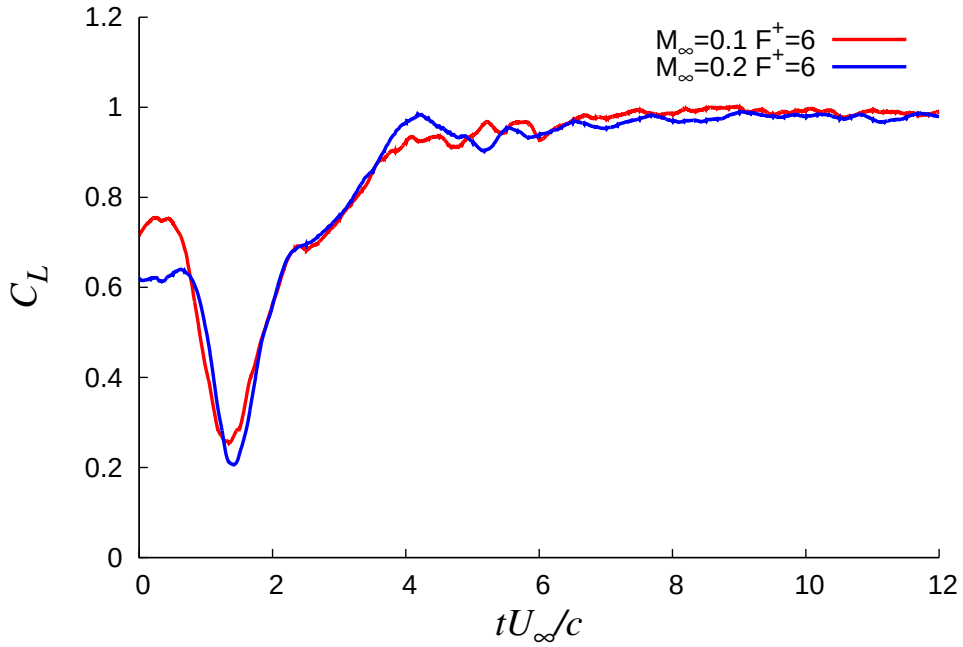

Figure 4.21: Time histories of the lift coefficient C_L obtained with the burst actuation $F^+ = 6$ at $M_\infty = 0.1$ and $M_\infty = 0.2$. The time is normalized by c/U_∞.

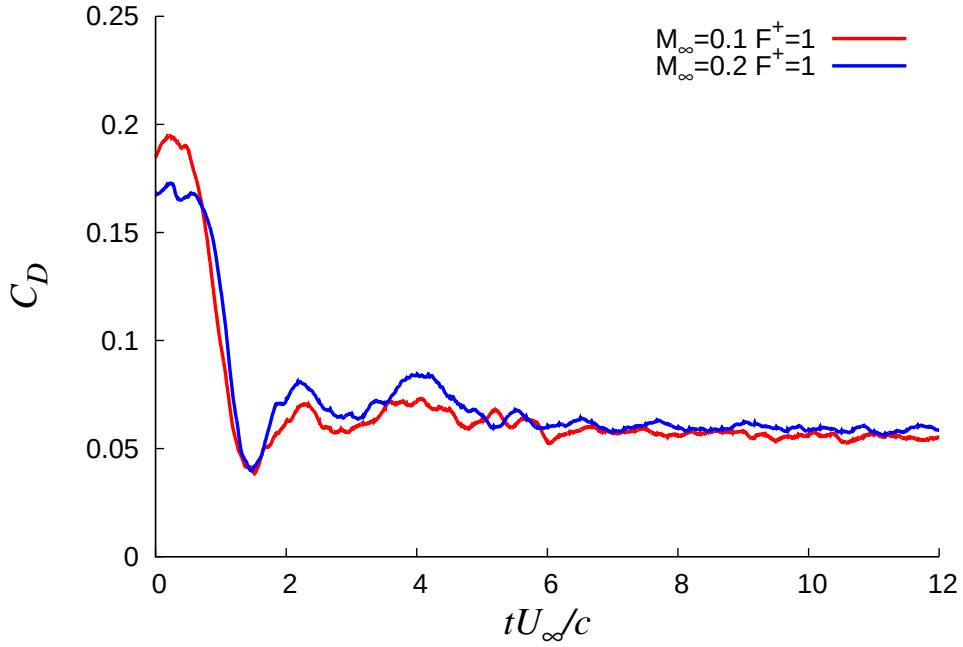

Figure 4.22: Time histories of the drag coefficient C_D obtained with the burst actuation $F^+ = 6$ at $M_\infty = 0.1$ and $M_\infty = 0.2$. The time is normalized by c/U_∞.

4.3 Verification of DBD Plasma Actuator Model

Aono *et al.* verified the DBD plasma actuator model[6] which is utilized in the present study with same numerical settings as in the present study. Induced flow fields by a dielectric barrier discharge (DBD) plasma actuator installed on a flat plate in quiescent flow are analyzed numerically. The produced airflow resulting from a simple sine waveform and burst modulations is discussed. The correlation between the operating mode of DBD plasma actuator and the resulting flow fields generated in temporal and average domains is presented. The generated flow resulting from a simple sine waveform is quasi-steady and fluctuates with base frequency of actuation. On the other hand, the induced flow structure by the burst modulations is unsteady and shows the dependency of actuation modes in terms of instantaneous sense. These characteristics and trends are agree with the experimental results.[151] Figure 4.23 shows Schlieren photographs of a experimental result (upper) and a computational result (lower) obtained by Suzen and Huzng model. The near-wall-jet distribution of computational result agrees with that of experimental result qualitatively.

4.4 Summary

In this chapter, we discuss the validation of the numerical analysis.

First, we discuss the target angle of attack and grid resolutions comparing the computational results with the experimental results. The comparison shows that the flow obtained by the computational result with grid set #1 in Table 3.4, does not massively separate from the leading edge at $\alpha = 12^\circ$ at which the flow obtained by the experiment massively separates from the leading edge because the angle of attack $\alpha = 12^\circ$ is a boundary angle between pre-stall and post-stall. On the other hand, at the $\alpha = 14^\circ$, the flow obtained by the computation is separated from the leading edge, and pressure distribution is well predicted comparing the experimental result. In addition, grid resolutions in viscous wall-unit are enough to resolve turbulent boundary layer at the angle. Thus we chose $\alpha = 14^\circ$ as an angle of attack for analysis of quasi-steady flows in chapter 5 because the objective of the present study is to discuss separation control mechanism qualitatively.

With progress of the present study and computational resources, we know that the discrepancy of pressure distribution at $\alpha = 12^\circ$ is caused by grid resolution. Therefore in chapter 6, the finer grid resolution (grid set #2 in Table 3.4) is utilized in order to discuss computational results more quantitatively. We also show the grid convergence

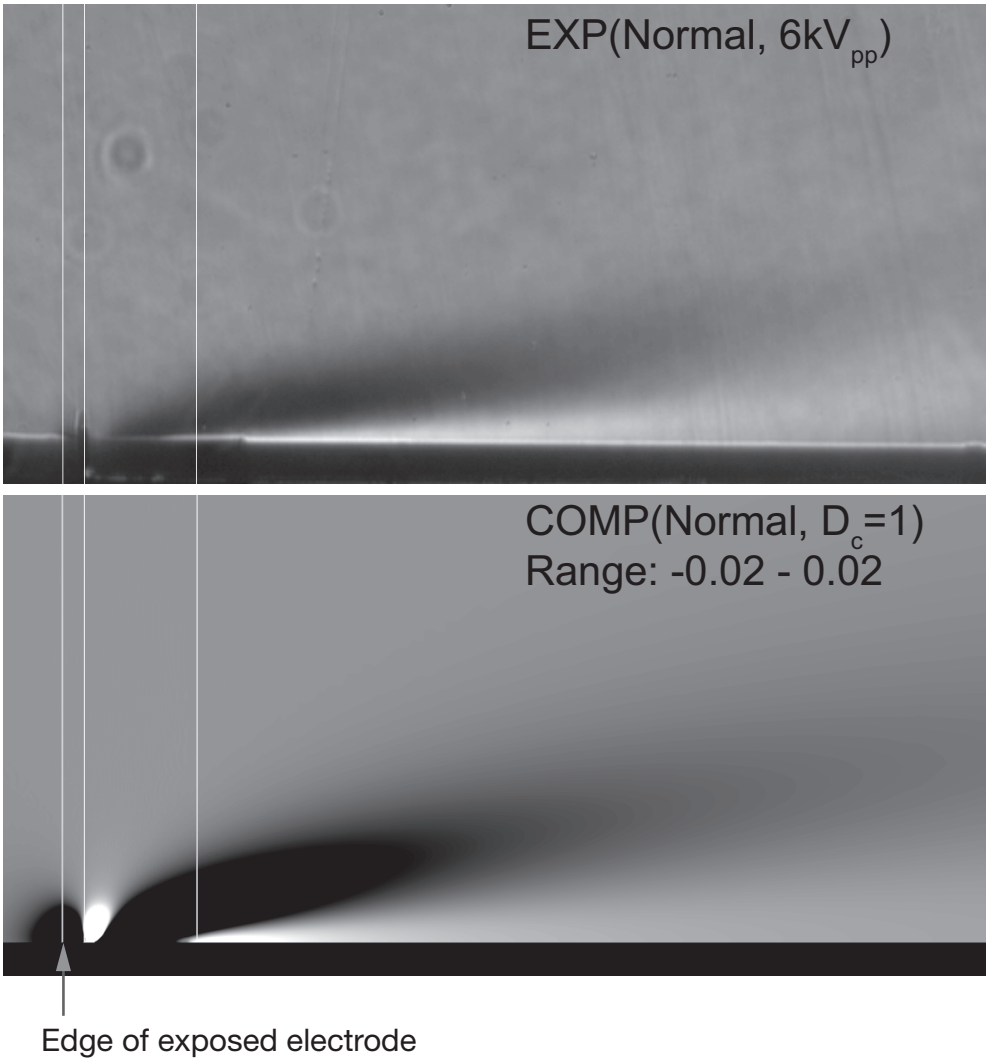

Figure 4.23: Schlieren photographs of a experimental result (upper) and a computational result (lower) obtained by Suzen and Huzng model. The data is provided by Dr. Aono[6].

study on grid set #2, and the results show that results obtained with the grid set #2 well converge.

Second, we investigate effects of free-stream Mach number by conducting computation at the different free-stream Mach number $M_\infty = 0.1$ and $M_\infty = 0.2$. The results show that there are no significant difference between the results at the both Mach numbers.

Finally, we introduce of the verification study on the DBD plasma actuator model (Suzen-Huzng model) which is utilized in the present study. The results show the present model is enough accurate for qualitative discussion.

Chapter 5

Quasi-steady flows

In this chapter, quasi-steady flows which are controlled by the DBD plasma actuator are discussed. First, the relationship between aerodynamics characteristics and the effect of separation control is discussed. Second, the burst frequency effect is discussed.

5.1 Computational Cases

The "normal mode" and "burst mode" are adopted as the operating conditions of the DBD plasma actuator in the present study. The normal mode denotes the operating condition in which normal alternative current is used as the input voltage to the DBD plasma actuator, and the burst mode denotes the operating condition in which the unsteady alternative current switched on and off periodically is used. The burst frequency F^+ is often discussed as an important parameter in the study of the DBD plasma actuator with burst wave. Many researchers investigate the optimum F^+ value for separation control over an airfoil, and there are two assertions that $F^+ = 1$ is the optimum frequency[44] and $F^+ = 6$ is the optimum frequency.[3] That is why, the values 1 and 6 are chosen as the non-dimensional burst frequency in this study. In addition, because the location of the DBD actuator is a little different in these studies, the 0 % and 5 % chord length from the leading edge are chosen as the locations of the DBD plasma actuator in this study, to investigate an effect of DBD plasma actuator location.

The non-dimensional parameters (based on the chord length and the free stream velocity) of DBD plasma actuator are shown in Tabel 5.1. The flow field without the DBD plasma actuator is calculated as the baseline case, and this case is named "DBD-off." On the normal mode case, D_c is varied to discuss about the effect of D_c. The cases of normal mode are named "NM_DcXX" such as "NM_Dc8" which denotes normal mode and $D_c = 8$ case. The cases of burst mode are named "BM_Xp_FX_DcXX" such as

"BM_0p_F1_Dc8" which denotes that the actuator is operated in burst mode and located at the leading edge, $F^+ = 1$ and $D_c = 8$ case. On the burst mode case, D_c is set to be eight.

On the normal mode case and the burst mode case, the computation is conducted from the initial conditions that previously controlled. All the seven cases except for the baseline case (DBD-off) are computed at $\alpha = 14$ deg.

Table 5.1: Operating conditions denoted by non-dimensional parameters of the DBD plasma actuator for the investigation of quasi-steady flows.

	DBD location [%]	D_c	f_{base}	BR [%]	F^+
DBD-off	N/A	N/A	N/A	N/A	N/A
NM_Dc8	5	8	60	100	N/A
NM_Dc32	5	32	60	100	N/A
NM_Dc64	5	64	60	100	N/A
BM_0p_F1_Dc8	0	8	60	10	1
BM_0p_F6_Dc8	0	8	60	10	6
BM_5p_F1_Dc8	5	8	60	10	1
BM_5p_F6_Dc8	5	8	60	10	6

5.2 Aerodynamic Performance and Flow Fields

5.2.1 Aerodynamic Coefficients

In this section, aerodynamic characteristics are discussed. The lift and drag coefficients, and lift-drag ratio are shown in Fig. 5.1. These actual values are presented in Table 5.2. In the cases in which leading edge separation is suppressed (NM_Dc32, NM_Dc64, BM_0p_F1_Dc8, BM_5p_F1_Dc8, BM_5p_F6_Dc8), the lift-drag ratios (L/D) are over 10 and clearly larger than those in the other cases. The L/D of the NM_Dc64 case is the largest of all cases and the L/D of the BM_0p_F6_Dc8 case is the second-largest. However, the number of the impulse added to the flow in the NM_Dc64 case is 640 times more than the BM_0p_F6_Dc8 case during the same duration, and even in the NM_Dc32 case in which L/D is the third-largest, the inpulse is 320 times higher than the BM_0p_F6_Dc8. These facts indicate that in the case that the DBD plasma actuator is operated in normal mode, D_c (corresponding to the input voltage) have to be over 320 times burst mode to achieve the equivalent effect of operating DBD plasma actuator in burst mode. On the other hand, although the C_L of the NM_Dc32 case is higher than

the BM_0p_F6_Dc8 case, L/D of the BM_0p_F6_Dc8 case is higher than NM_Dc32 case. This is because the flow fields of normal mode cases have the large separation bubble, and the bubble contributes to the increase in C_L and C_D. That is why the relationship between L/D and C_L is affected by the state of separation bubble and the flow field must be paid attention to when the effect of separation control is discussed.

Figure 5.2 shows attached and separated region on each case. Blue color denotes attached region and red color denotes separated region. As mentioned above, normal mode cases have the large separation bubble. On the other hand, burst mode case have smaller separated bubble although separated near the trailing edge. the relation between these attached region and, C_L and L/D are shown in Figs. 5.3 and 5.4. If the suppressing separated region corresponds with enhancement of C_L and L/D, the C_L and L/D should increase with the total attached region. Thus we have to define the criteria clearly when discuss "effect of separation".

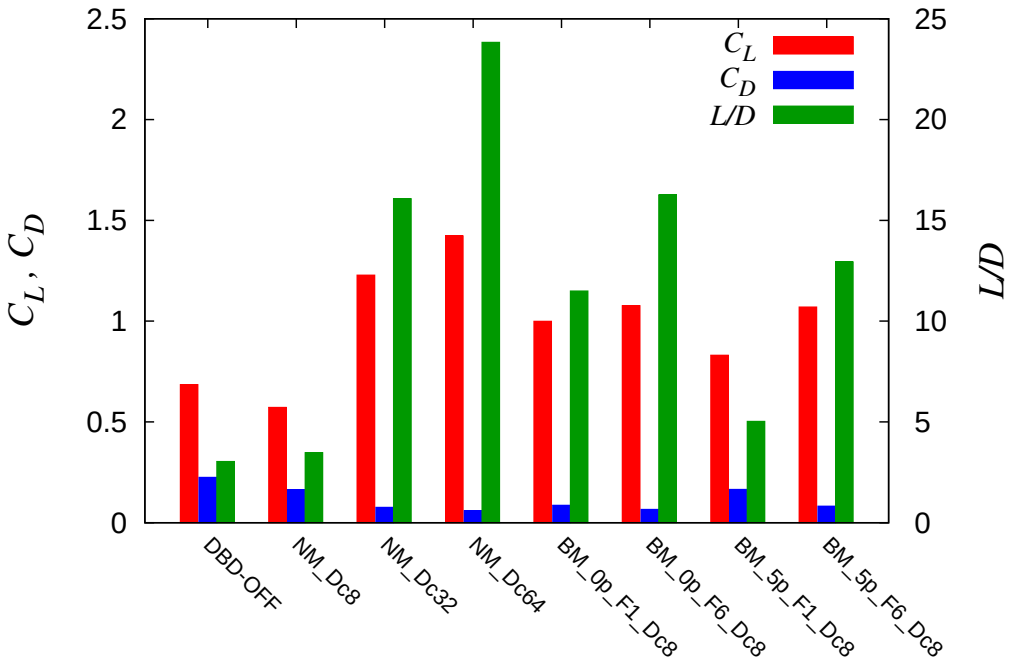

Figure 5.1: Aerodynamic coefficients (lift and drag coefficients, and lift-to-drag ratio)

Table 5.2: Aerodynamic coefficients (lift, drag and pitching moment coefficients and lift-to-drag ratio)

	C_L	C_D	L/D
DBD-off	0.69	0.225	3.04
NM_Dc8	0.57	0.164	3.48
NM_Dc32	1.23	0.076	16.07
NM_Dc64	1.42	0.059	23.83
BM_0p_F1_Dc8	1.00	0.869	11.50
BM_0p_F6_Dc8	1.08	0.066	16.27
BM_5p_F1_Dc8	0.83	0.165	5.03
BM_5p_F6_Dc8	1.07	0.082	12.94

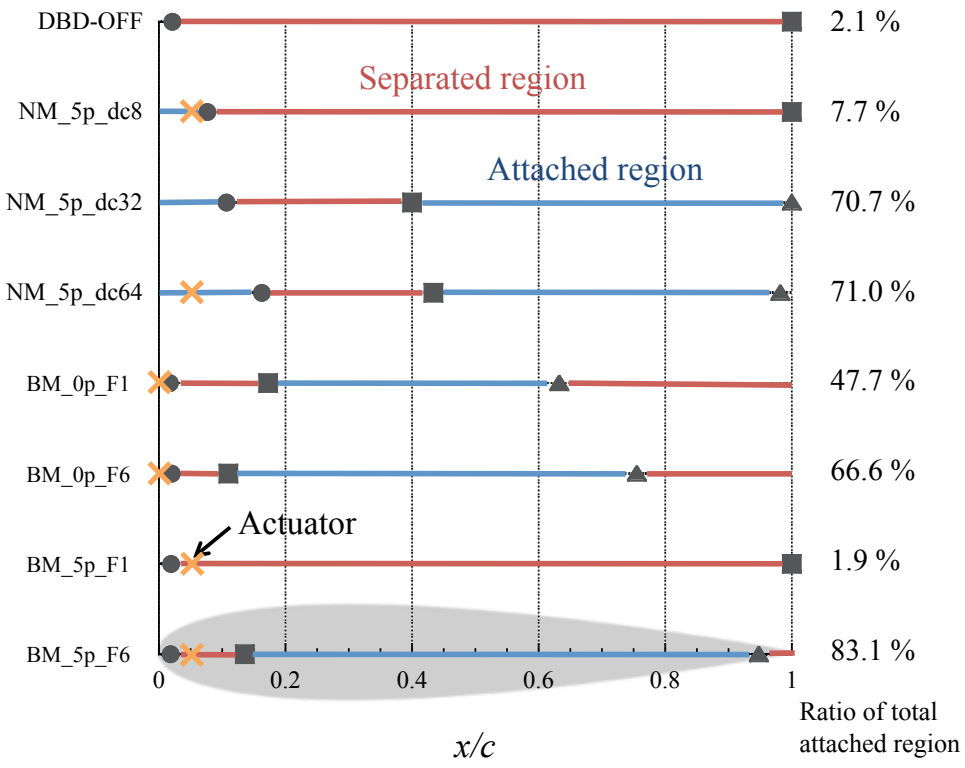

Figure 5.2: Schematics of separated and attached regions

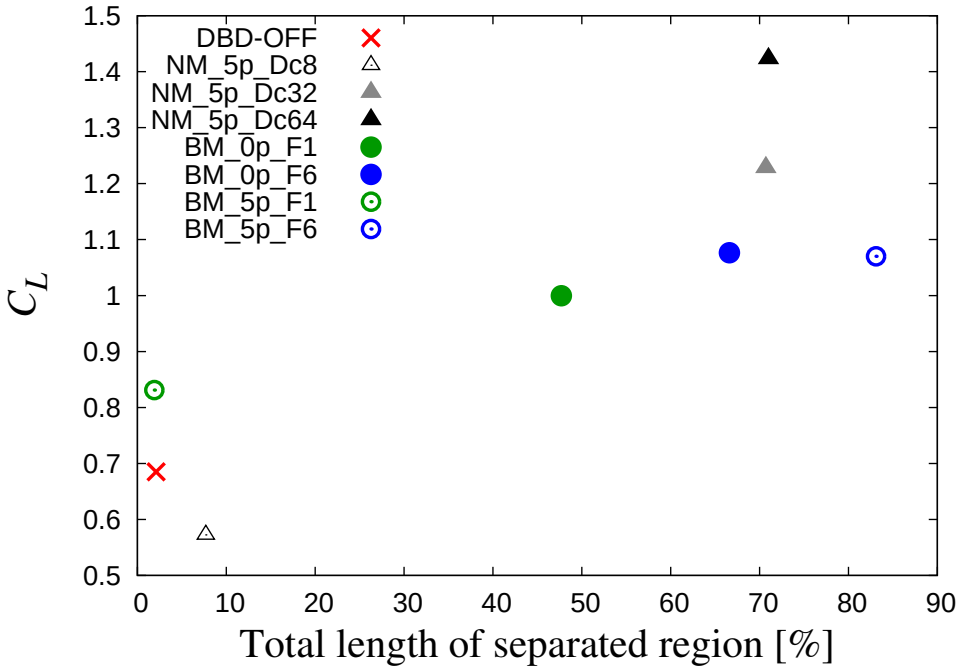

Figure 5.3: Lift coefficient C_L vs total attached region.

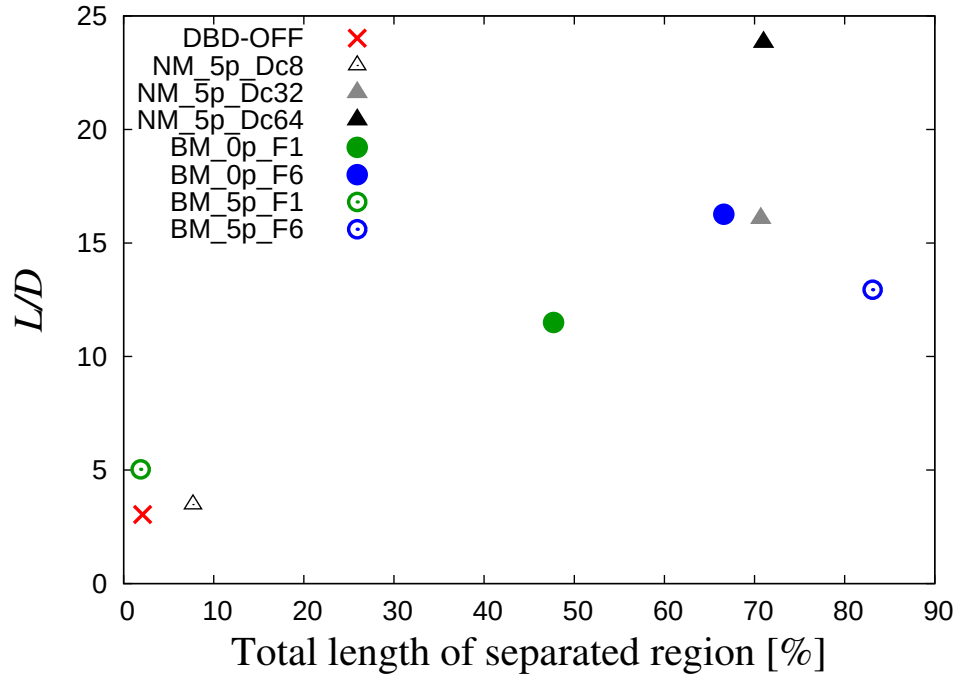

Figure 5.4: Lift drag ratio L/D vs total attached region.

5.2.2 Mean Flow Fields

In this section, time averaged flow fields are discussed. The flow fields are averaged in the span-direction too. The distributions of chord-directional velocity and stream lines at $\alpha = 14$ deg are shown in Fig. 5.5. In the DBD-off case, the flow field makes a separation from the leading edge and has large recirculation region (denoted as blue area in the Fig. 5.5) and pressure restoration is not enough at the trailing edge ($x = 1$). Although the similar flow field is seen in the NM_Dc8 case, the degree of separated shear layer is slightly shallower than it in the DBD-off case because of actuation by the DBD plasma actuator. The NM_Dc8 case is already reported in the previous study,[59] and leading edge separation seemed to be suppressed. However the flow field included the effect of initial condition and computational time was not enough in that previous study. In the present study, computation and time-average are conducted for a longer time period (50 nondimensional time is averaged) and the flow field of the NM_Dc8 case has the leading edge separation clearly. In the NB_Dc32 and NB_Dc64 case, the leading edge separation is suppressed by the DBD plasma actuator but there are the large separation bubble from $x \sim 0.1$ to $x \sim 0.4$. These results indicate that inputting the lager momentum is more effective on the separation control. On the other hand, in burst mode cases (BM_0p_F1_Dc8, BM_0p_F6_Dc8, BM_5p_F1_Dc8, BM_5p_F6_Dc8), the separation bubble is much smaller than that in the normal mode cases (NM_Dc32, NM_Dc64) and the flow fields have trailing edge separation. In addition, in the burst mode cases, flow fields have subtle differences between cases. In the cases of $F^+ = 6$, the separation region is smaller than those in the case of $F^+ = 1$. In particular, in the BM_5p_F1_Dc8 case, the flow field has relatively large separation region. This is because in the BM_5p_F1_Dc8 case, the leading edge separation alternate with attached flow.

The distributions of pressure coefficient (C_p) are showed in Fig. 5.6. In Fig. 5.6(a), the distributions of pressure coefficient (C_p) in normal mode cases and the DBD-off case are plotted. In the DBD-off case, pressure coefficient is distributed flatly on the upper surface, which means the flow field separated from the leading edge. In the NM_Dc8 case, C_p is distributed flatly at the almost whole upper surface same as the DBD-off case. But the negative pressure value is larger than that in the DBD-off case near the leading edge because of actuation by the DBD plasma actuator. On the other hand, pressure distributions have the clear peek in the NM_Dc32 case and the NM_Dc64 case. The peak value of negative C_p in the NM_Dc64 case is the largest of all cases including the burst mode cases. At $x = 0.05$, there are sharp rising of pressure caused by impinging flow induced by the DBD plasma actuator in the normal mode cases. From $x \sim 0.1$ to

$x \sim 0.4$, C_p is distributed flatly and this region correspond to the separation bubble region.

In Fig. 5.6(b) the C_p distributions in burst mode cases and the DBD-off case are plotted. The flow fields are similar to each other in burst mode cases except for the BM_5p_F1_Dc8 case. In the BM_5p_F1_Dc8 case, the C_p distribution has the characteristics of other burst mode cases and the DBD-off case. For example, the negative C_p distribution has the clear peak near the leading edge while the pressure restoration is not enough at the trailing edge. As previously mentioned, this is because the leading edge separation alternate with attached flow. In the other burst mode cases, the C_p is distributed flatly (this indicate the separation bubble) at the small region near the leading edge and its distribution has the clear peak at the leading edge.

The difference between normal mode cases and burst mode cases when the leading edge separation is suppressed are described briefly as follows. In the normal mode cases, the flow fields have the clear peak of C_p distribution and large separation bubble. On the other hand, in the burst mode cases, the flow fields have the clear peak of C_p distribution too, but separation bubble is smaller than that in the normal mode cases.

5.2.3 Summary

In this section, the relation between aerodynamic characteristics and the effectiveness of separation control with the DBD plasma actuator over the airfoil are discussed.

DBD plasma actuator in normal mode generates moderately separated region (separation bubble) over the airfoil and the airfoil gains lift by negative pressure at the vortex center. On the other hand, burst mode does not make the large separation bubble, and the different aerodynamic characteristics are appeared with burst frequency. The burst mode with nondimensional burst frequency of one enhances the vortex shedding from the separated shear layer and avoid the massive separation from the leading edge. The burst mode with nondimensional burst frequency of six improves the airfoil performance by suppressing the separation region and this condition is preferable for aircraft because the flow fields and lift coefficients are stable and the energy consumption of DBD plasma actuator is the lowest in all cases. Thus considering unsteady-aerodynamic-characteristics are important for actual design.

In addition, the maximum C_L case does not correspond with the maximum L/D case in the present study. This is because C_L and L/D is affected by the state of separation bubble which contribute to increasing the C_L and C_D. This fact indicates that it is not enough to evaluating the effectiveness of separation control only by C_L, and other

evaluation-indexes such as L/D should be considered for any purpose.

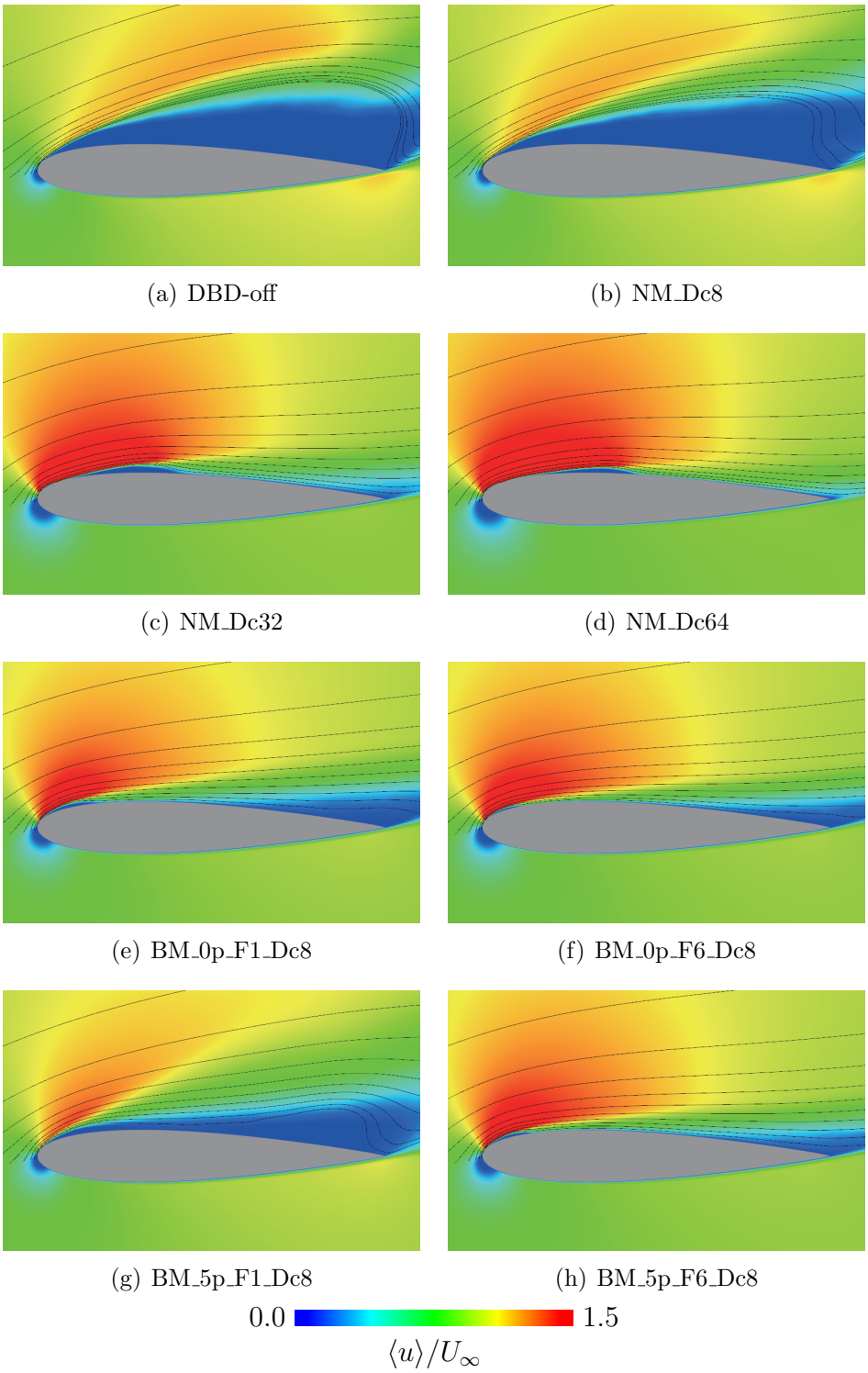

(a) DBD-off (b) NM_Dc8

(c) NM_Dc32 (d) NM_Dc64

(e) BM_0p_F1_Dc8 (f) BM_0p_F6_Dc8

(g) BM_5p_F1_Dc8 (h) BM_5p_F6_Dc8

Figure 5.5: Time averaged flow fields (distributions of chord-directional velocity and stream lines at $\alpha = 14$ deg).

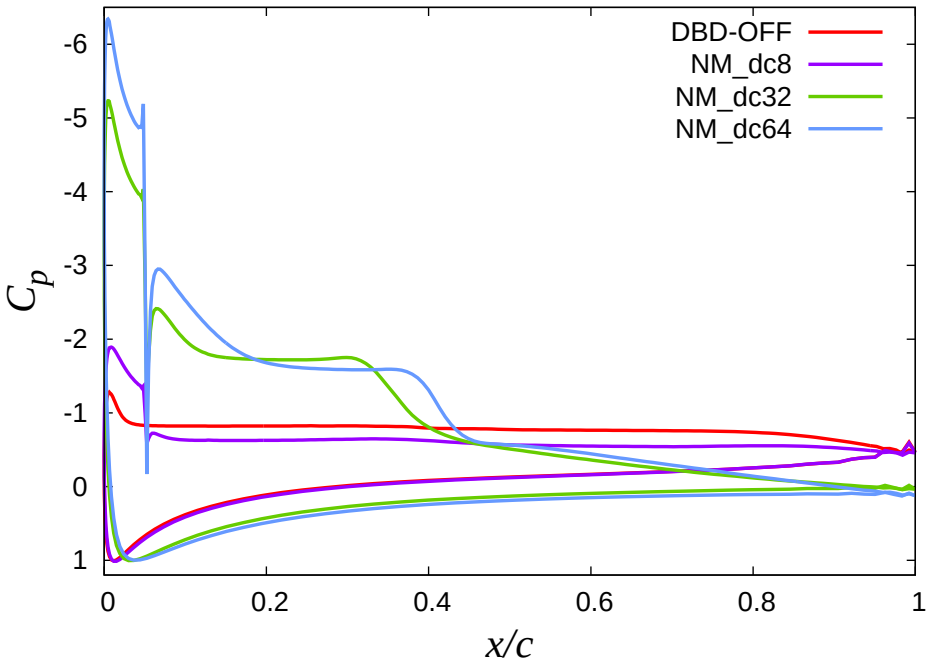

(a) Normal mode cases and the DBD-off case

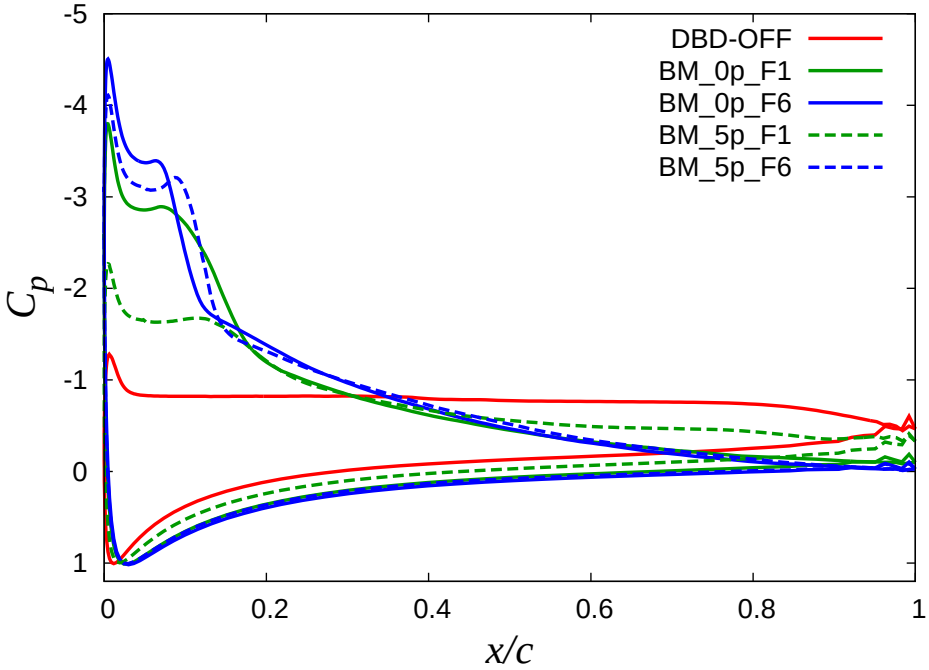

(b) Burst mode cases and the DBD-off case

Figure 5.6: Distributions of pressure coefficient.

5.3 Investigation of Effects of Burst mode

In this section, first, differences between the burst mode and the normal mode cases are discussed. Second, the burst frequency effect of the DBD plasma actuator on the control of separated flow over the airfoil is discussed.

5.3.1 Baseline Flow Fields

Before we discuss the controlled-flow fields, We explain the DBD-off case as the Baseline case briefly. Figure 5.7 shows the time averaged flow field. The flow field makes a separation from the leading edge and has large recirculation region which denoted as blue area. Figure 5.8 shows the instantaneous flow field. In this figure, the shear layer separated of the leading edge makes the spanwise vortices because of the Kelvin-Helmholtz instability, and these vortices break down into the three-dimensional vortices with the negative pressure gradient. In this case lift coefficient oscillate with the approximately non-dimensional frequency of 0.7.

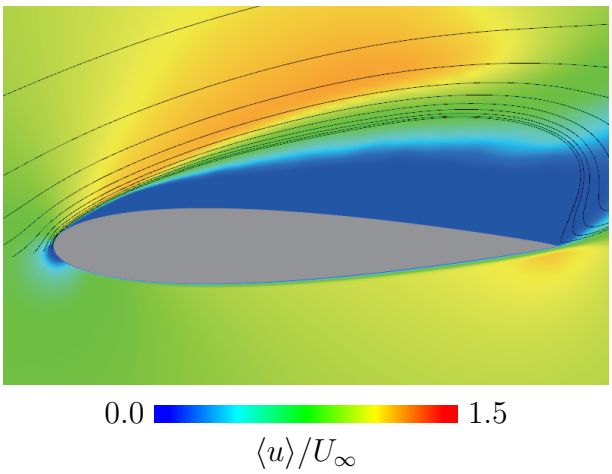

Figure 5.7: Mean chordwise velocity distributions and stream lines in the DBD-off case.

5.3.2 Effect of Burst Mode

In Fig. 5.9, the representative instantaneous flow fields of the normal mode (NM_Dc32) and burst mode (NM_5p_F6_Dc8) are shown. The massive separation from the leading edge is suppressed in the both cases. In the normal mode case, the separated shear layer is clearly observed, and the flow field is similar to the flow field of the DBD-off case in Fig. 5.8. However the separated shear layer is pulled toward the airfoil surface by momentum

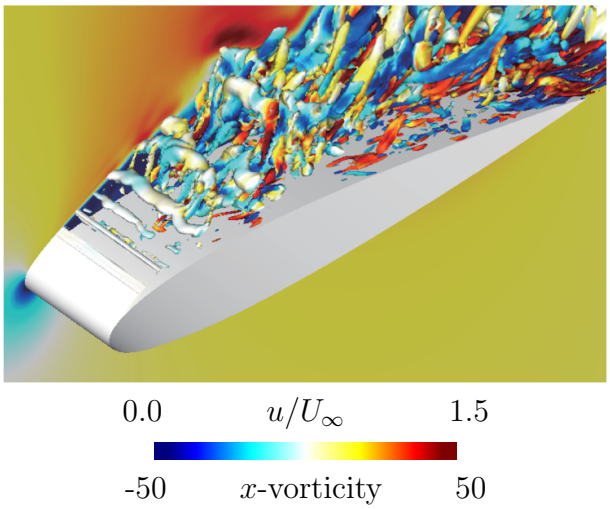

Figure 5.8: Instantaneous flow fields in the DBD-off case (iso-surfaces of second invariant of the velocity gradient tensors and chord-directional velocity distributions (back ground). The iso-surfaces is colored by chord-direction vorticity and green lines near the leading edge denote the DBD plasma actuator location).

addition of the DBD plasma actuator. On the other hand, the flow field of the burst mode quite is different. A lot of fine vortices are observed immediately downstream from the DBD plasma actuator. We can find the effect of these vortices in the distributions of turbulence kinetic energy (TKE) in Fig. 5.10. In this figure, the large magnitude region represent that flow is mixed actively and the free-stream momentum is transfered into the boundary layer. This result indicates that for the burst mode, vortices generated by the DBD plasma actuator enhance fluid mixing, and free stream momentum is induced into the separated region indirectly.

5.3.3 Mean Flow Statistics

In this section, mean flow fields and statistics are discussed. The distributions of chord-directional velocity and stream lines are shown in Fig. 5.5. Leading edge separation is suppressed for all the burst mode cases (BM_0p_F1_Dc8, BM_0p_F6_Dc8, BM_5p_F1_Dc8, BM_5p_F6_Dc8) compared to DBD-off case, though flow fields have subtle differences in between the burst mode cases. In BM_0p_F1_Dc8, BM_0p_F6_Dc8 and BM_5p_F6_Dc8 cases, flows are attached on the almost upper surface except for on the vicinity of the leading edge and trailing edge. In BM_5p_F1_Dc8 case, there are large recirculation region on the upper surface although the massive separation from the leading edge is suppressed.

Distributions of pressure coefficient (C_p) are shown in Fig. 5.6. In the DBD-off case,

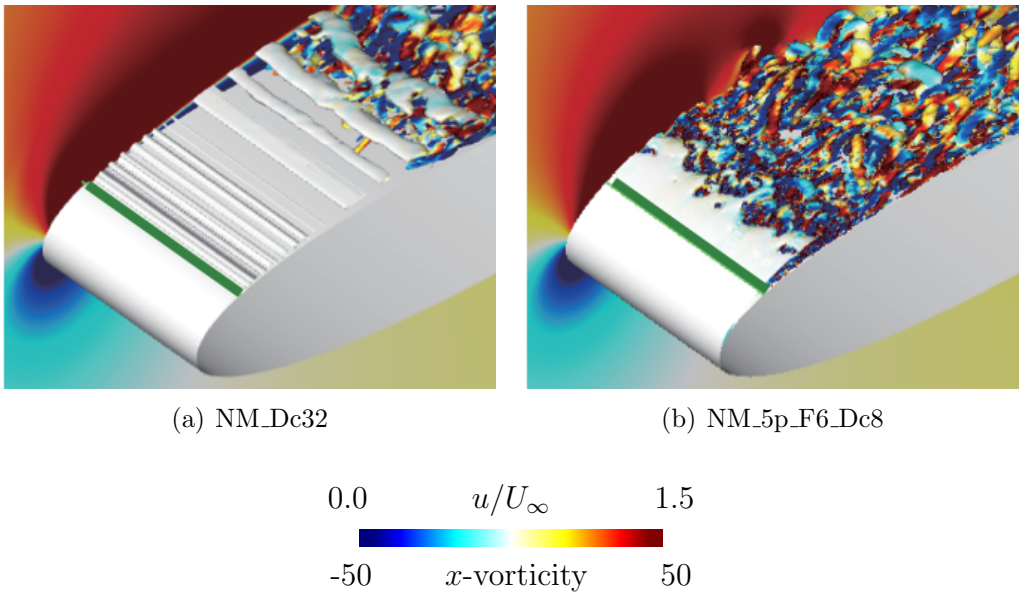

(a) NM_Dc32 (b) NM_5p_F6_Dc8

Figure 5.9: Closeups of instantaneous flow fields of the NM_Dc32 and NM_5p_F6_Dc8 (iso-surfaces of second invariant of the velocity gradient tensors and chord-directional velocity distributions (back ground)). The iso-surfaces is colored by chord-direction vorticity and green lines near the leading edge denote the DBD plasma actuator location.

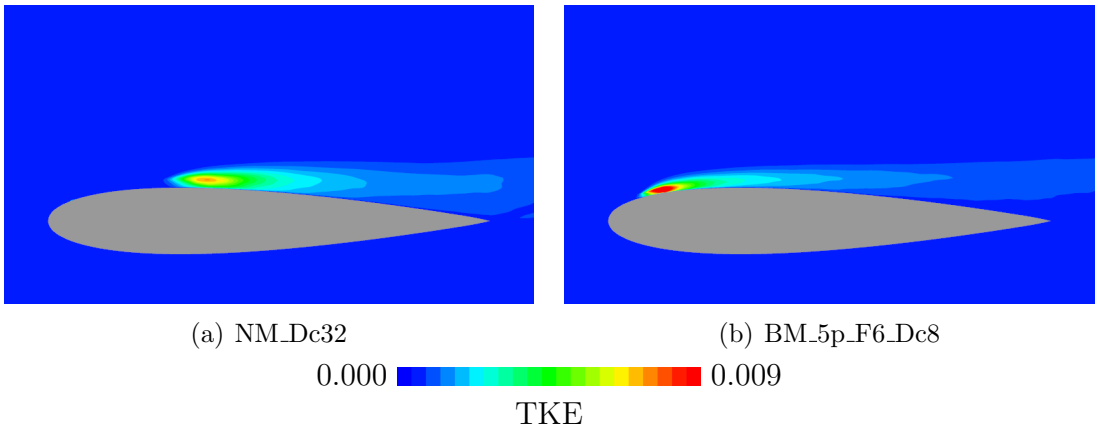

(a) NM_Dc32 (b) BM_5p_F6_Dc8

Figure 5.10: Turbulence kinetic energy (TKE) distributions of the flow fields of the NM_Dc32 and NM_5p_F6_Dc8.

pressure recovery is not enough at the trailing edge ($x = 1$) and the C_p is distributed flatly on wide region of the upper surface. because the flow field makes a separation from the leading edge and has large recirculation region. On the other hand, in burst mode cases except for the BM_5p_F1_Dc8 case, the C_p is distributed flatly (this indicate the separation bubble) only at the small region near the leading edge and its distribution has the clear peak at the leading edge. Especially in the $F^+ = 6$ case, the negative peek value of C_p is very high and sharp. In the BM_5p_F1_Dc8 case, the C_p distribution has the characteristics of other burst mode cases and the DBD-off case. For example,

the negative C_p distribution has the clear peak near the leading edge while the pressure recovery is not enough at the trailing edge. This reason will be explained in the following section.

Figures 5.11 and 5.11 show the chordwise velocity profiles. The chordwise velocity is positive and flow is attached at $x = 0$ in each case, and the maximum value of velocity magnitude is large in the BM_5p_F6_Dc8, BM_0p_F6_Dc8 and BM_0p_F1_Dc8 case. This high speed flow makes the large negative peak value of C_p in these cases in Fig. 5.6. The flows reattach at $x = 0.1 - 0.2$ in the order of BM_0p_F6_Dc8, BM_5p_F6_Dc8, BM_0p_F1_Dc8 and BM_5p_F1_Dc8, although velocities are negative and flows are separated at $x = 0.5$ in all the controlled cases. Especially in the $F^+ = 6$ case, the reattachment is earlier than in the $F^+ = 1$. These results indicate the $F^+ = 6$ is more effective for suppressing separation and $F^+ = 1$ is sensitive to the actuator location.

Figure 5.13 shows the Turbulence kinetic energy (TKE) distributions and Figs. 5.14 and 5.15 show TKE profiles. In these figure, the large magnitude region represent that flow is mixed actively and the free-stream momentum is transfered into the boundary layer. In the $F^+ = 6$ case, the large Reynolds stress region concentrates locally and the magnitude of the Reynolds stress is higher than in the $F^+ = 1$. This is because the actuator enhance the turbulence transition in the $F^+ = 6$ case.[59] On the other hand, the Reynolds stress distributed widely in in the $F^+ = 1$ case.

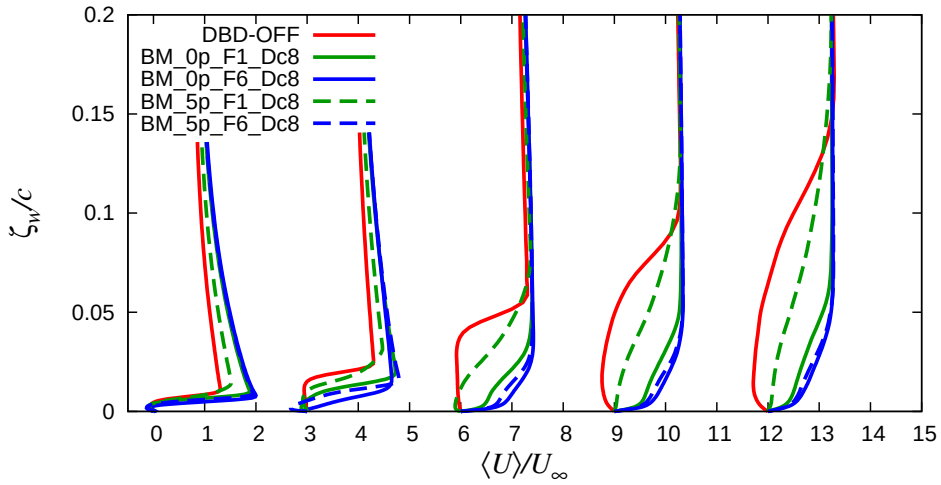

Figure 5.11: Mean streamwise (tangential) velocity $\langle U \rangle$ profiles as a function of wall-normal distance ζ_w at $x/c = 0.05, 0.1, 0.2, 0.3, 0.4$. Each plot is separated by horizontal offset of 2.0.

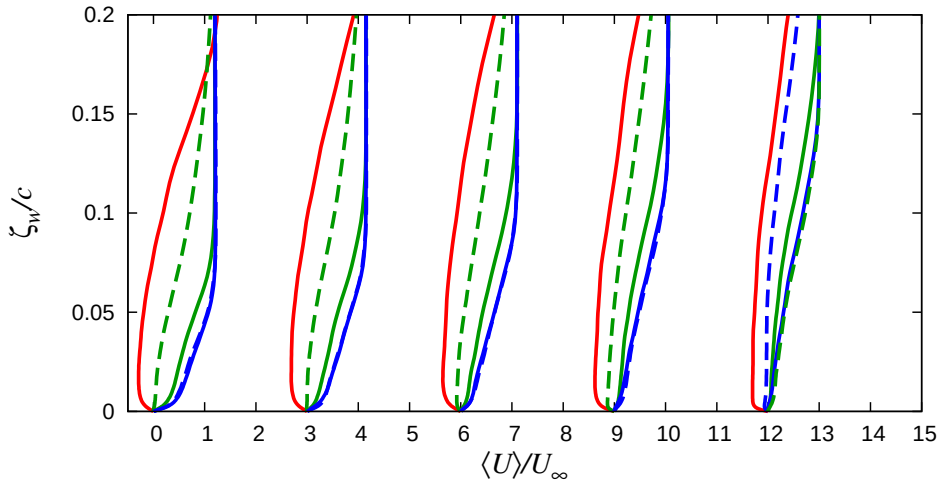

Figure 5.12: Mean streamwise (tangential) velocity $\langle U \rangle$ profiles as a function of wall-normal distance ζ_w at $x/c = 0.5, 0.6, 0.7, 0.8, 0.9$. Each plot is separated by horizontal offset of 2.0. Lines as in Fig. 5.11.

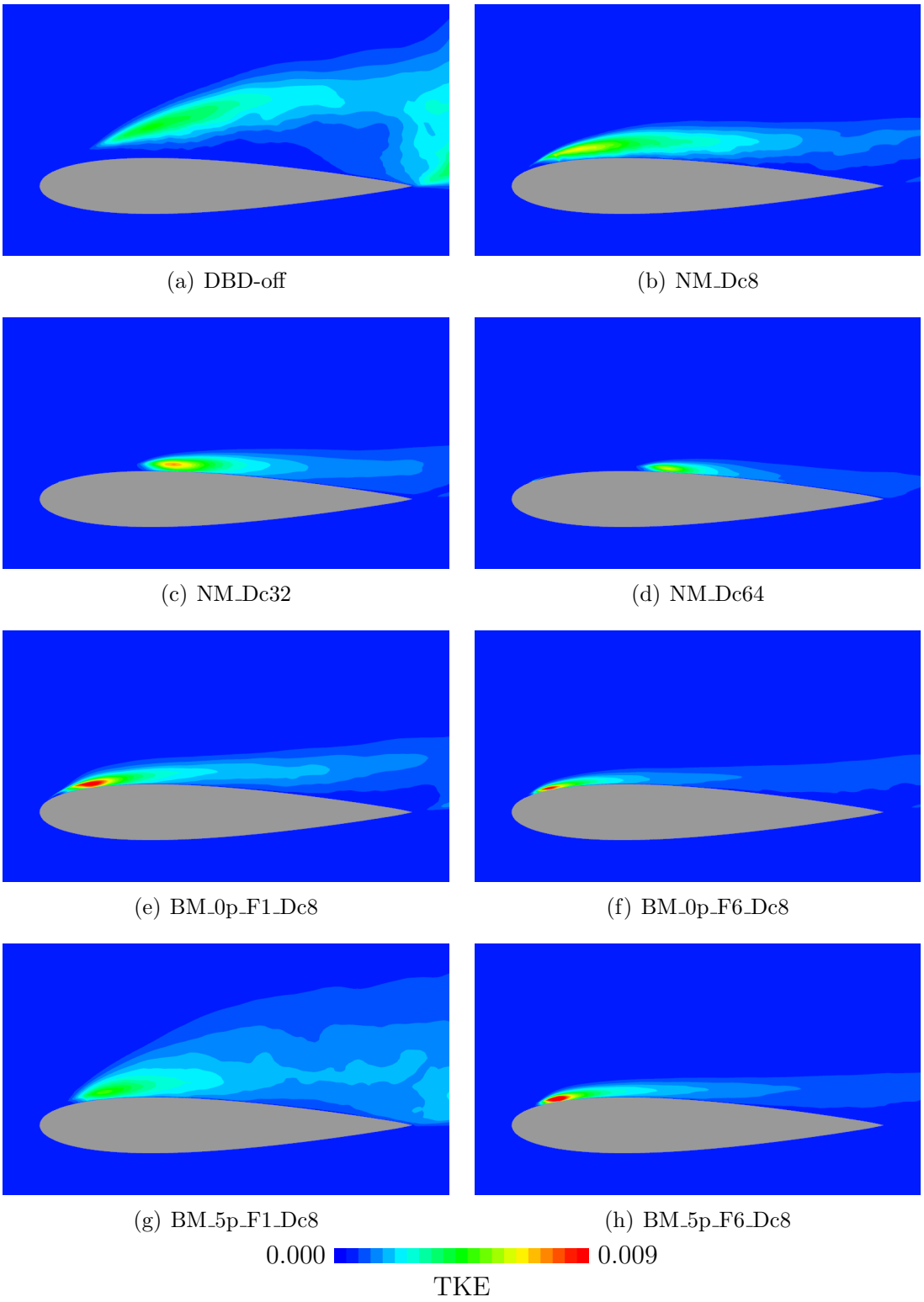

(a) DBD-off (b) NM_Dc8

(c) NM_Dc32 (d) NM_Dc64

(e) BM_0p_F1_Dc8 (f) BM_0p_F6_Dc8

(g) BM_5p_F1_Dc8 (h) BM_5p_F6_Dc8

Figure 5.13: Turbulence kinetic energy (TKE) distributions of the flow fields obtained with the burst actuations.

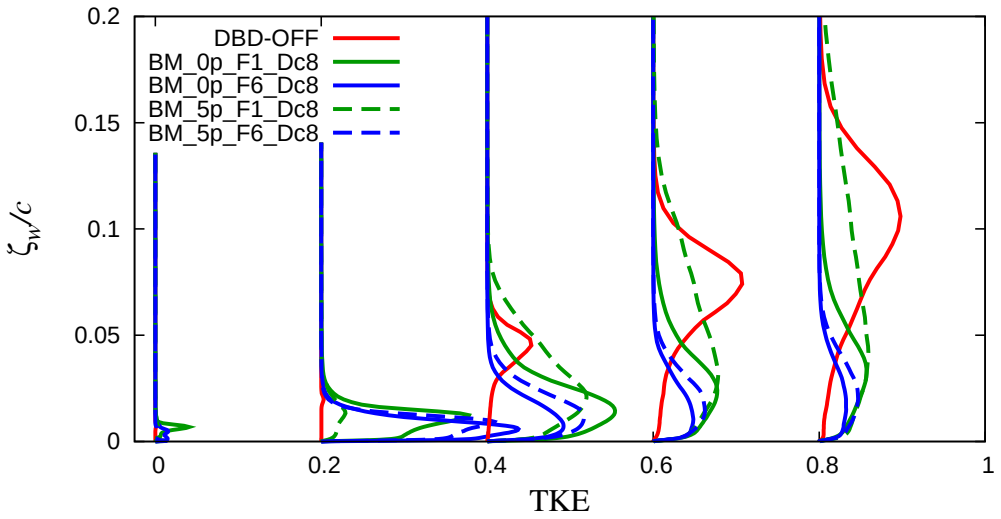

Figure 5.14: Turbulence kinetic energy (TKE) profiles of the flow fields obtained with the burst actuations as a function of wall-normal distance ζ_w at $x/c = 0.05, 0.1, 0.2, 0.3, 0.4$. Each plot is separated by horizontal offset of 0.2.

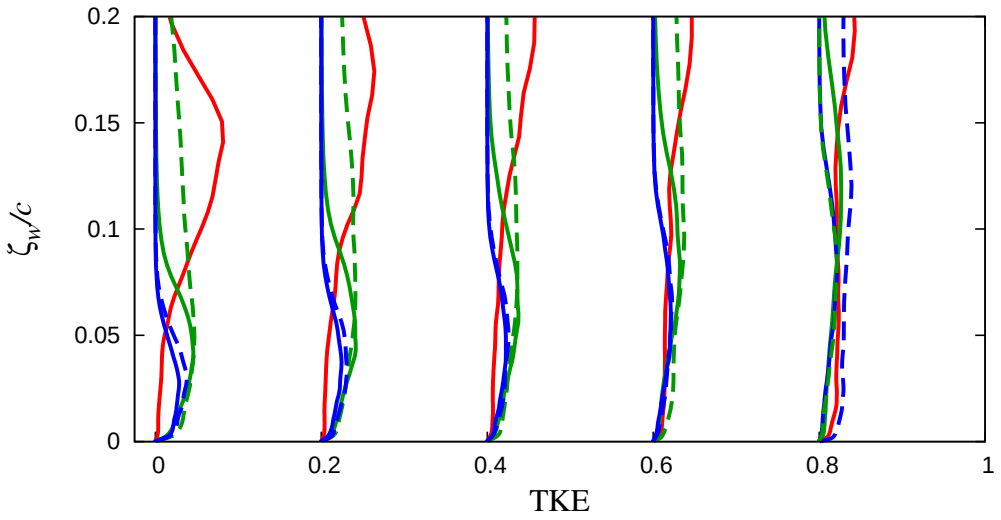

Figure 5.15: Turbulence kinetic energy (TKE) profiles of the flow fields obtained with the burst actuations as a function of wall-normal distance ζ_w at $x/c = 0.5, 0.6, 0.7, 0.8, 0.9$. Each plot is separated by horizontal offset of 0.2. Lines as in Fig. 5.14.

5.3.4 Instantaneous Flow Fields

In this section, instantaneous flow fields are discussed. Figure 5.16 shows iso-surfaces of second invariant of the velocity gradient tensors and chord-directional velocity distributions (back ground). On the DBD-off case, the shear layer separated of the leading edge makes the spanwise vortices because of the Kelvin-Helmholtz instability, and these vortices break down into the three-dimensional vortices with the negative pressure gradient. On the NM_Dc8 case, the flow field differs from that on the DBD-off case, and the small chord-directional vortices are observed in the downstream from the actuator. The other normal mode cases ("NM_Dc32", "NM_Dc64") are clearly different from the other cases including the burst mode cases. The flow fields of these cases have large separation bubble and the breaking down into the three-dimensional vortices are delayed in comparison with the other cases. As previously mentioned in section 5.2.2, on the BM_5p_F1_Dc8 case, the C_p distribution has the characteristics of other burst mode cases and the DBD-off case. This is because the flow field which has leading edge separation alternates with the attached flow. Figure 5.18 shows the history of lift coefficient (C_L) in the BM_5p_F1_Dc8 case. In this figure, lift decrease sharply at $tU_\infty/c \sim 6$ because the flow field has the massive separation from the leading edge. The snapshot at this phase is shown in the Fig. 5.16(g). Thus the flow field of the BM_5p_F1_Dc8 case is similar to the flow field of the DBD-off case. In the other burst mode cases ("BM_0p_F1_Dc8", "BM_0p_F6_Dc8", "BM_5p_F6_Dc8"), separation is well suppressed and very fine vortices are observed. In addition, many fine vortices can be observed at the region where the TKE is high in Fig. 5.13. Especially $F+ = 6$ case has finer vortices than $F+ = 1$ case as shown in Fig. 5.17. Figure 5.17 shows closeups of instantaneous flow fields of BM_0p_F1_Dc8 and BM_0p_F6_Dc8 case. On BM_0p_F1_Dc8 case, a large spanwise vortex structure can be found.

5.3.5 Burst Frequency and the Effect of Separation Control

In this section, the burst frequency effect on separation control is discussed. Figure 5.19 shows recirculation (separated) region of separation bubbles near the leading edge. The separation bubbles of $F^+ = 6$ cases are smaller than the separation bubbles of $F^+ = 1$ cases. In addition, the separated region of BM_5p_F1_Dc8 is very large. As mentioned above, the flow of BM_5p_F1_Dc8 is not suppressed the massive separation completely. This result indicate that the $F^+ = 6$ is more robust against the installed locations than $F^+ = 1$.

In Fig. 5.20, time histories of C_L and force fluctuation $\sin^2(2\pi f_{base}t)$ are shown. Fig.

5.21 shows the BM_0p_F1_Dc8 case. In this case, C_L oscillates very much in synchronization with the body force fluctuation. On the other hand, in the BM_0p_F6_Dc8 case shown in Fig. 5.21, the C_L value is relatively stable and fluctuation weak.

In order to discuss the reason for this, local C_L values are shown with the contour lines of cord-directional velocity in Fig. 5.24 and 5.25. Figure 5.3.6 shows the right before phase of actuator blowing. In this phase, the flow field has the large separation region near the leading edge. This separation region contributes to lift augmentation, and C_L values is highest in the period of C_L fluctuation. Figure 5.3.6 shows the phase after the actuator blowing. Two spanwise vortices are generated by the actuator at the location of 10 % and 20 % chord length. These vortices draw the separated shear layer toward the airfoil surface. This vortex generation makes the separation region near the leading edge small, and lift start to decrease. The vortex generated first does not disappear and convect toward the down stream. In the Fig. 5.3.6, the first vortex convect to the 70 % chord length. In this phase, the separated shear layer gets away from the airfoil surface again and lift is restored because the separation region near the leading edge becomes large as in Fig. 5.3.6. The BM_0p_F1_Dc8 case repeat above sequence. The frequency of $F^+ = 1$ is a little higher than the frequency of the C_L fluctuation in the DBD-off case. In the BM_0p_F1_Dc8 case, the actuator is blown before the separated shear layer gets away from the leading edge completely and avoid the massive separation from the leading edge.

On the other hand, in the BM_0p_F6_Dc8 case shown in 5.25, the shear layer stays near the airfoil surface in the each phase. In addition, although one of the spanwise vortices generated by the actuator does not disappear and convects to the downstream in the BM_0p_F1_Dc8 case, the spanwise vortices generated by the actuator in the Fig. 5.3.6 disappear immediately in the Fig. 5.3.6. This is because the spanwise vortices generated by the actuator interact with each other and promote the breakdown into three dimensional vortices.

In view of these facts, the causes of inadequacy of the separation-control-effect in the BM_5p_F1_Dc8 case is considered as follows. The distance between the actuator and separated shear layer can be larger in the $F^+ = 1$ case than in the $F^+ = 6$ case. Additionally when the actuator installed at the 5 % chord length from the leading edge, that distance can be much longer than when the actuator installed at the 0 % chord length from the leading edge. That is why the actuator can not excite the separated shear layer and the separation-control-effect is not enough in the BM_5p_F1_Dc8 case.

5.3.6 Unsteady Aerodynamic Characteristics

About the unsteady aerodynamic characteristics are not discussed in previous studies. In this section, the characteristic cases (BM_0p_F1_Dc8, BM_0p_F6_Dc8) are discussed. In Fig. 5.20, 5.21, time histories of C_L and force fluctuation $\sin^2(2\pi f_{base}t)$ are shown. Fig. 5.20 shows the BM_0p_F1_Dc8 case. In this case, the C_L oscillates very much in synchronization with the body force fluctuation. This is because the actuator enhances the vortex shedding from the separated shear layer and avoid the massive separation from the leading edge. On the other hand, in the BM_0p_F6_Dc8 case, the C_L value is relatively stable and fluctuate slightly.

5.3.7 Summary

In this section, the burst frequency effect of the DBD plasma actuator on the control of separated flow over the airfoil is discussed. The DBD plasma actuator is installed at the 0 % and 5 % chord length from the leading edge, and actuated in burst mode. For the burst mode, nondimensional burst frequency is set to 1 and 6.

In the case that actuator installed at the leading edge, each burst frequency is effective in suppressing massive separation from the leading. On the other hand in the case that actuator installed at the 5 % chord length from the leading edge, the nondimensional burst frequency of 6 can suppress the massive separation from the leading but the nondimensional burst frequency of 1 is not effective enough to suppress the massive separation and the flow field having leading edge separation alternates with the attached flow field.

This is because the separation mechanism is different between the nondimensional burst frequency of 1 and 6. The nondimensional burst frequency of 1 enhance the vortex shedding from the separation shear layer and the flow field has the unsteady large separated region near the leading edge although the massive separation from the leading edge is avoided. That is why this mechanism associated with the large fluctuation of lift. The nondimensional burst frequency of 6 improves the airfoil performance by suppressing the separation region and the flow field is relatively stable.

In addition, it is clarified that the first mechanism is more sensitive to the location of the DBD plasma actuator than the second mechanism because the separated shear layer oscillate very much and distance between the actuator and separated shear layer can be large in the first mechanism.

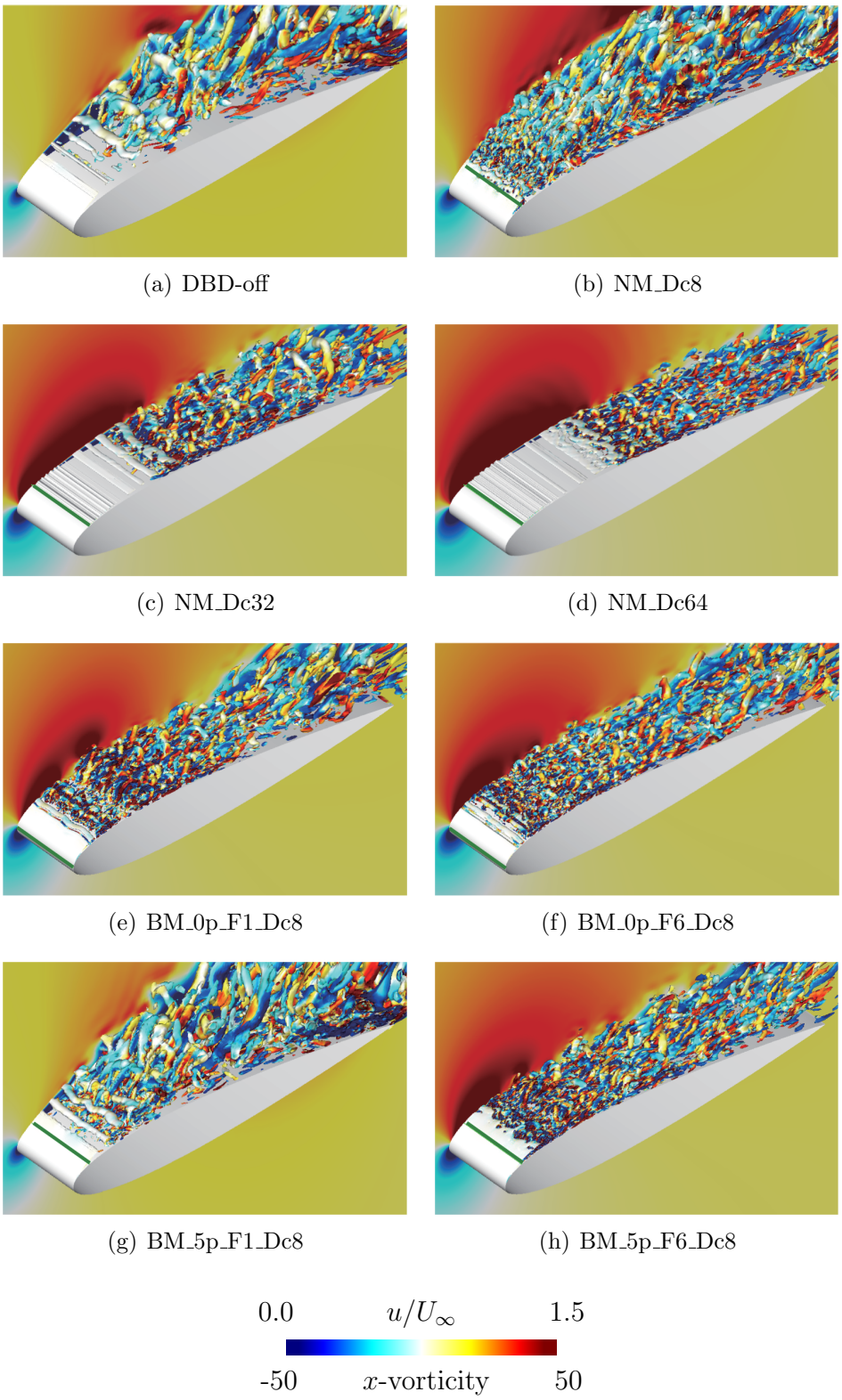

(a) DBD-off (b) NM_Dc8

(c) NM_Dc32 (d) NM_Dc64

(e) BM_0p_F1_Dc8 (f) BM_0p_F6_Dc8

(g) BM_5p_F1_Dc8 (h) BM_5p_F6_Dc8

Figure 5.16: Instantaneous flow fields (iso-surfaces of second invariant of the velocity gradient tensors and chord-directional velocity distributions (back ground)). The iso-surfaces is colored by chord-direction vorticity and green lines near the leading edge denote the DBD plasma actuator location.

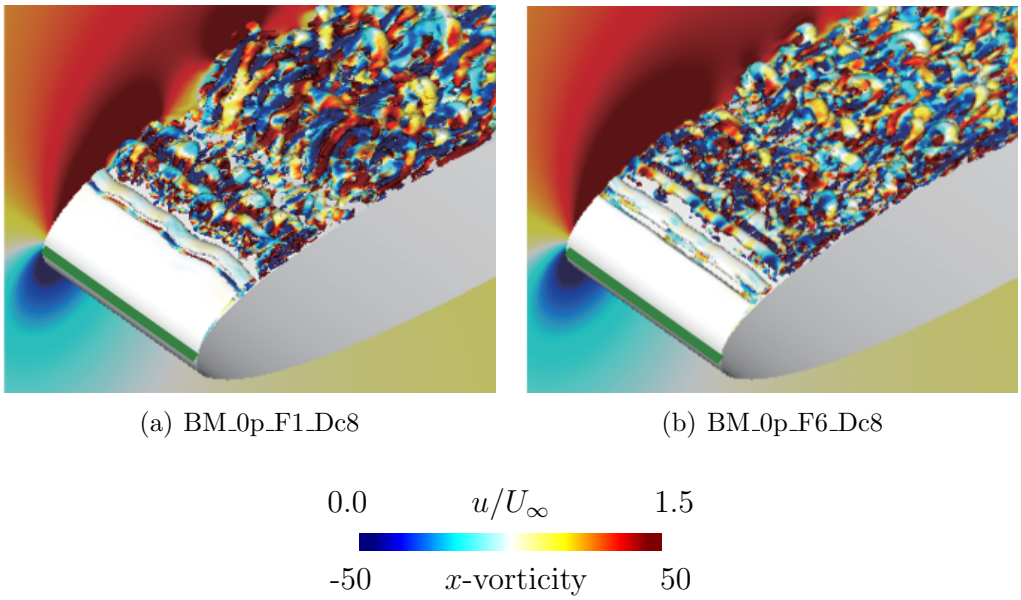

(a) BM_0p_F1_Dc8 (b) BM_0p_F6_Dc8

Figure 5.17: Closeups of instantaneous flow fields (iso-surfaces of second invariant of the velocity gradient tensors and chord-directional velocity distributions (back ground)). The iso-surfaces is colored by chord-direction vorticity and green lines near the leading edge denote the DBD plasma actuator location.

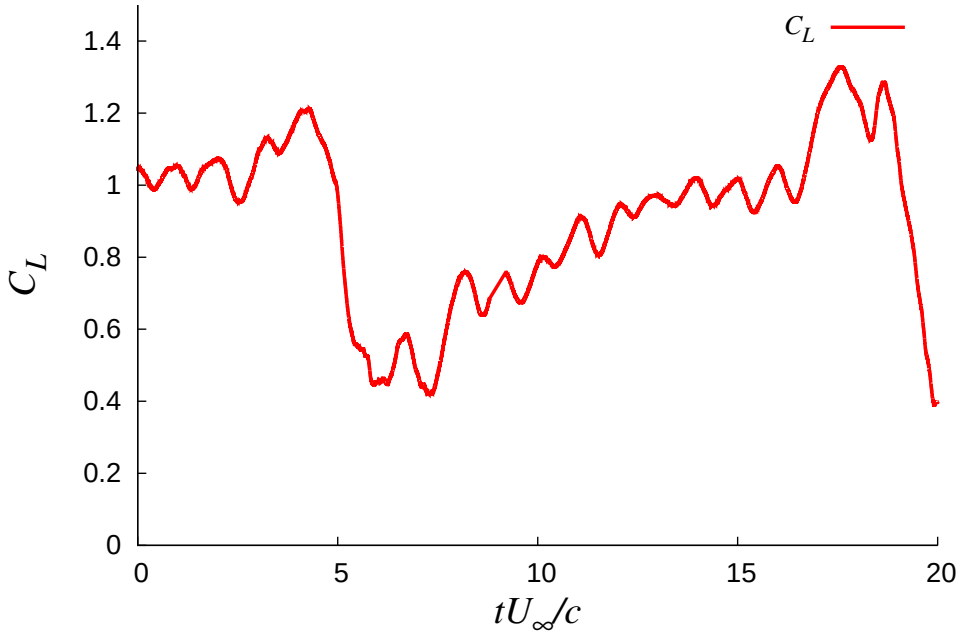

Figure 5.18: Lift coefficient (C_L) history in the BM_0p_F1_Dc8 case.

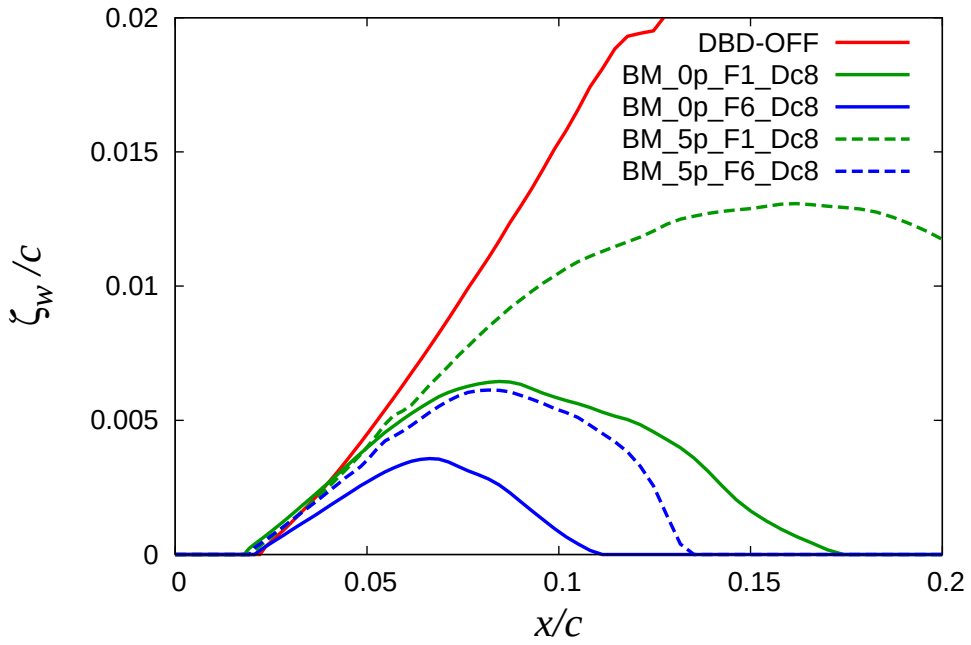

Figure 5.19: Recirculation region of separation bubbles near the leading edge.

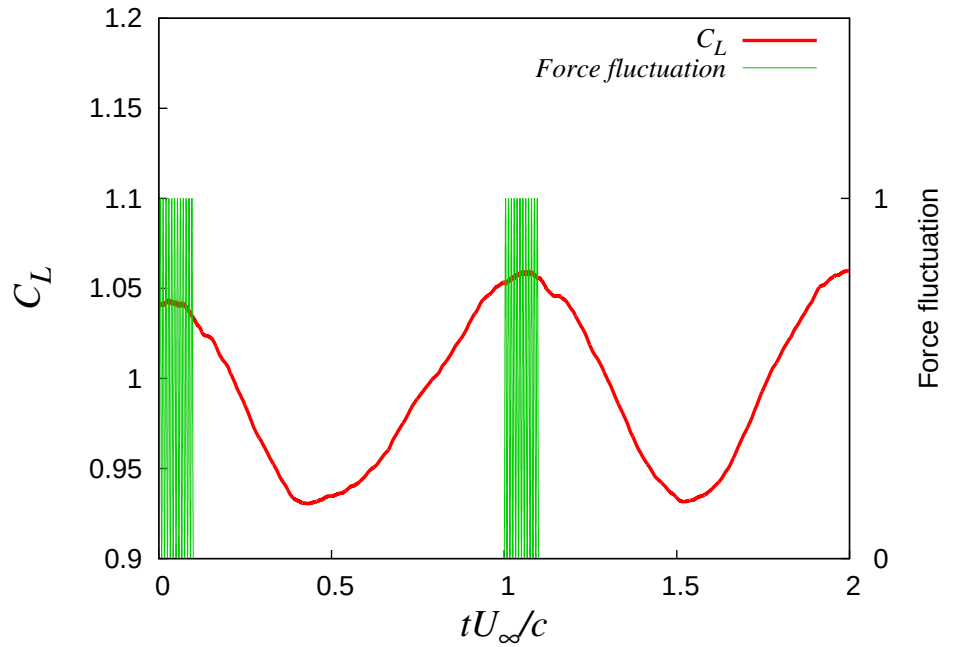

Figure 5.20: Time histories of the lift coefficient C_L obtained with the burst actuation $F^+ = 1$ and body force fluctuation. The time is normalized by c/U_∞.

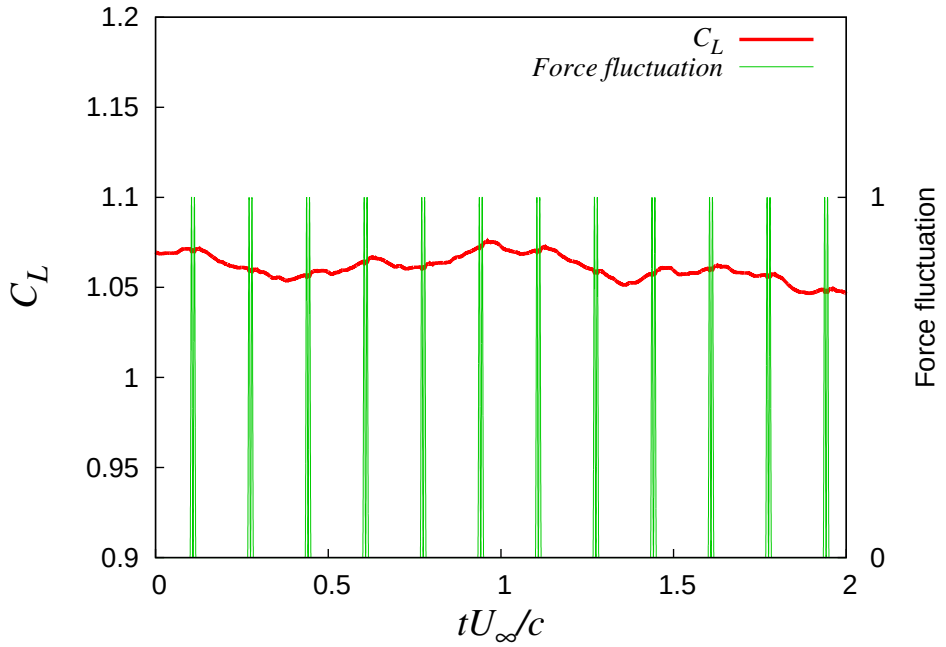

Figure 5.21: Time histories of the lift coefficient C_L obtained with the burst actuation $F^+ = 6$ and body force fluctuation. The time is normalized by c/U_∞.

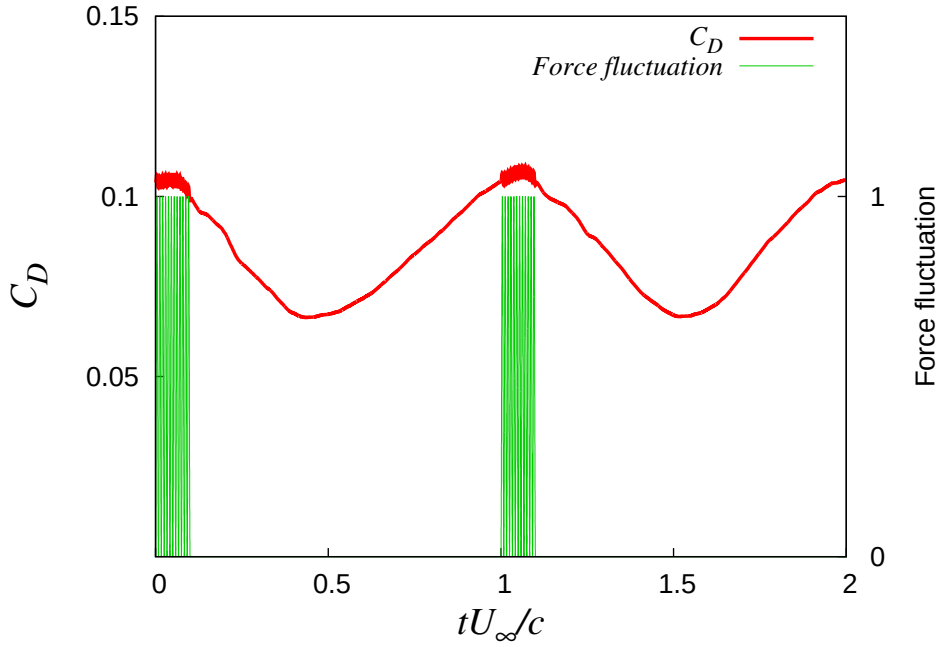

Figure 5.22: Time histories of the drag coefficient C_D, and body force fluctuation obtained with the burst actuation $F^+ = 1$. The time is normalized by c/U_∞.

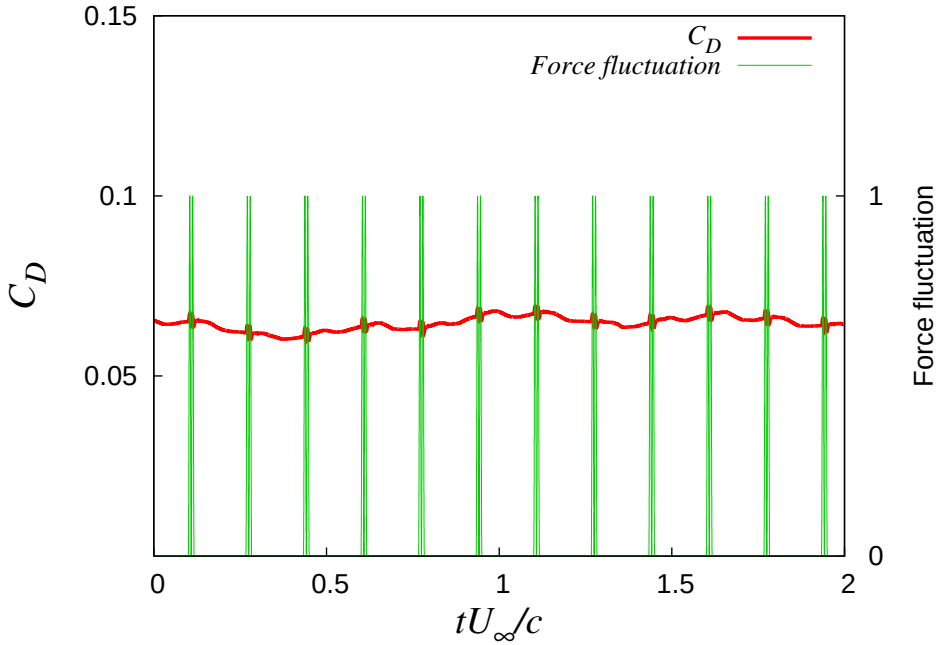

Figure 5.23: Time histories of the drag coefficient C_D, and body force fluctuation obtained with the burst actuation $F^+ = 6$. The time is normalized by c/U_∞.

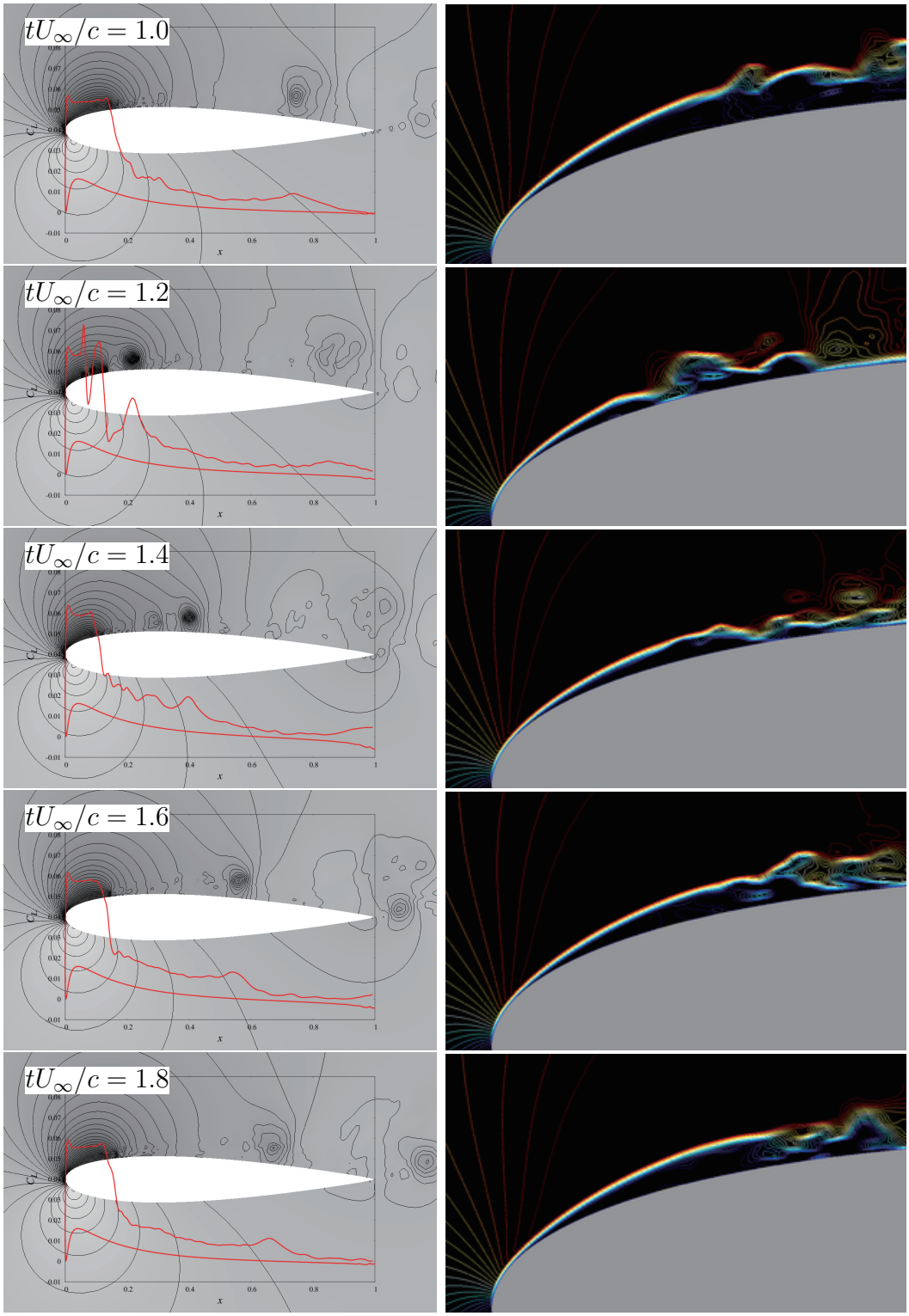

Figure 5.24: Local C_L distributions and C_p distributions of BM_0p_F1_Dc8.

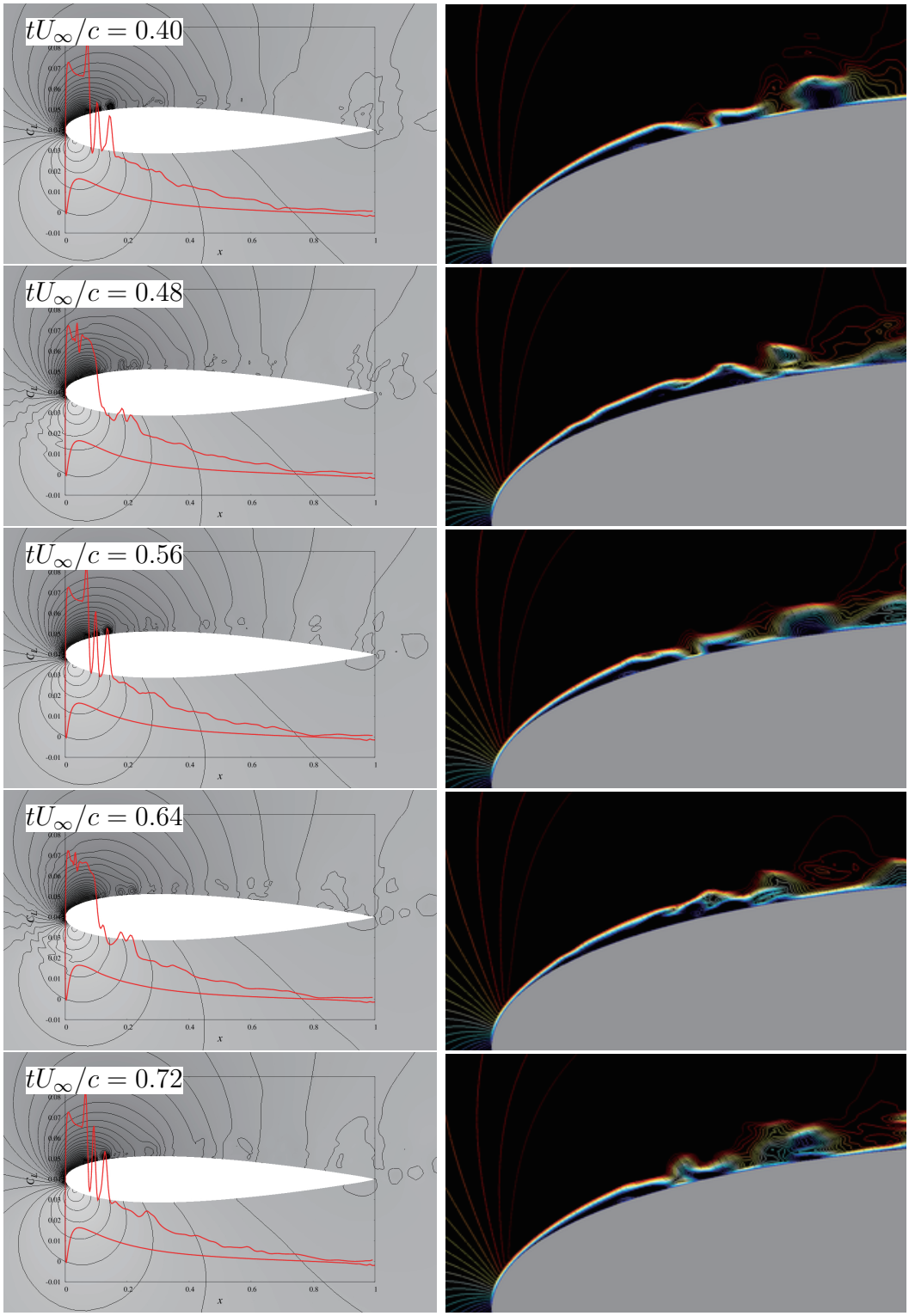

Figure 5.25: Local C_L distributions and C_p distributions of BM_0p_F6_Dc8.

Chapter 6

Controlled Transients Associated with Flow Reattachment and Separation

6.1 Computational Cases

In this chapter, the transient processes in which the separated flow is controlled and the separated region is suppressed gradually, are discussed. As mentioned in chapter 3 and chapter 4, the angle of attack is set to 12° and the D_c is set to $D_c = 1$. Two characteristic cases in the previous study[150] is chosen. The non-dimensional parameters (based on the chord length and the free stream velocity) of DBD plasma actuator are shown in Tabel 6.1. In this study, in order to take ensemble averages, 20 computations are conducted for each case.

Table 6.1: Operating conditions denoted by non-dimensional parameters of the DBD plasma actuator for the investigation of transient flows.

	DBD location [%]	D_c	f_{base}	BR [%]	F^+
BM_5p_F1	5	1	60	10	1
BM_5p_F6	5	1	60	10	6

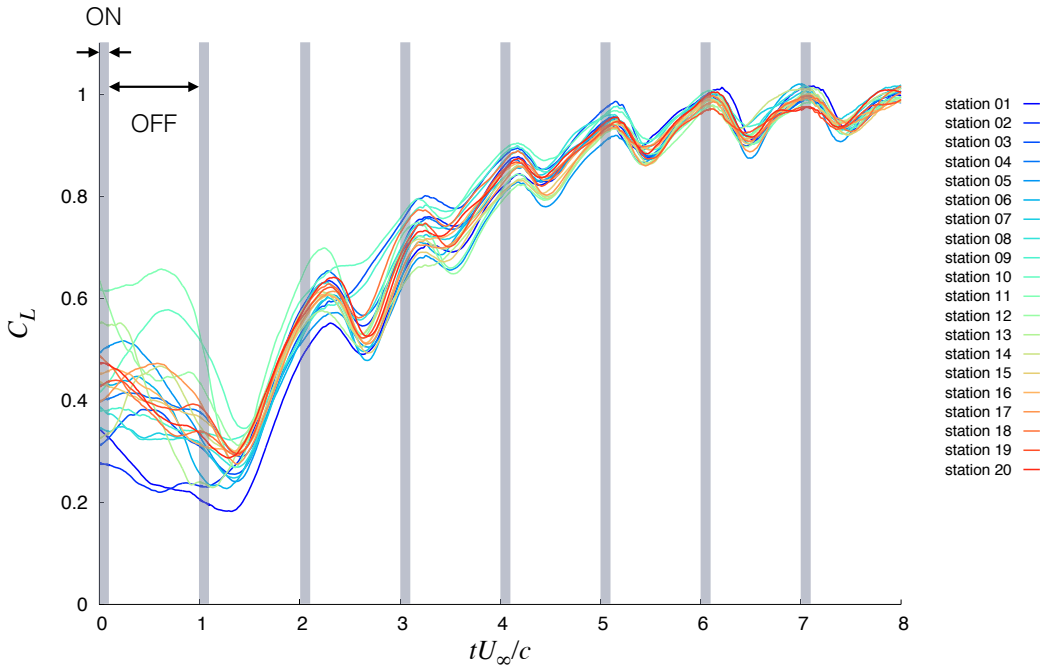

Figure 6.1: Time histories of the lift coefficient C_L obtained with the burst actuation $F^+ = 1$. The time is normalized by c/U_∞. "ON" denotes the duration in which the DBD plasma actuator is actuated, and "OFF" denotes the duration in which the DBD plasma actuator is not actuated.

6.2 Unsteady Characteristics of Aerodynamic Coefficients

Figure 6.1 shows time histories of the lift coefficient C_L obtained with the burst actuation $F^+ = 1$. The time is normalized by c/U_∞. In this figure, the start times of the computations are moved to zero. Therefore, the burst periods are synchronized.

Figure 6.2 and 6.3 show time histories of the lift coefficient C_L obtained with the burst actuation $F^+ = 1, 6$. The time is normalized by c/U_∞. The ensemble average of C_L is taken. The solid lines denote the ensemble average values of C_L and the color filled areas denote the possible value areas, i.e. the upper lines denote maximum C_L values of all stations, and the lower lines denote minimum C_L values of all stations.

First, these figures describe the each C_L value converges on a quasi-steady value which is almost same with ensemble averaged value, although initial C_L values are quite-variable among stations. Second, the transient times in two cases are same order and in the range approximately 5 - 8. The C_L of $F^+ = 6$ case converges relatively quickly. Third, large lift decreasing which are temporarily observed in the initial stage of transient state ($tU_\infty/c \sim 1.5$) in the both cases. This large lift decreasing is caused by advection of

a spanwise vortex and the vortex involves the free stream to the airfoil surface. Further discussion is done in section 6.4.

Figure 6.4 and 6.5 show time histories of the drag coefficient C_D obtained with the burst actuation $F^+ = 1, 6$. The time is normalized by c/U_∞. The ensemble average of C_D is taken same as figure 6.2 and 6.3. The solid lines denote the ensemble average values of C_D and the color filled areas denote the possible value areas, i.e. the upper lines denote maximum C_D values of all stations, and the lower lines denote minimum C_D values of all stations.

We find the same trends with the C_L values. First, in these figures, the each C_D value converges on the ensemble averaged value as C_L values in Fig. 6.2 and 6.3 from various initial C_D values. Second, the transient times in two cases are almost same and approximately 5, although the C_L convergence of $F^+ = 6$ is faster than the C_L convergence of $F^+ = 1$ in the 6.2 and 6.3. Third, rapid drag decreasing which are temporarily observed in the initial stage of transient state ($tU_\infty/c \sim 1.5$) in the both cases. This drag decreasing is caused by same reason as lift decreasing in Fig. 6.2 and 6.3. The advection of the spanwise vortex involves the free-stream to the airfoil surface. Then impinging of the involved flow makes suction side pressure increase, and a pressure drag is reduced.

In addition, from the present results, we find that the transient states consist of following three stages (Fig. 6.6): 1) the large lift and drag decreasing temporally occur. 2) the peak of negative pressure near the leading edge gradually recovers. 3) the fluid mixing region moves upstream gradually, and the flow goes to the quasi-steady state. The stage 1) is partially discussed in this section, and the details of the stages 1), 2), and 3) are discussed in the following sections.

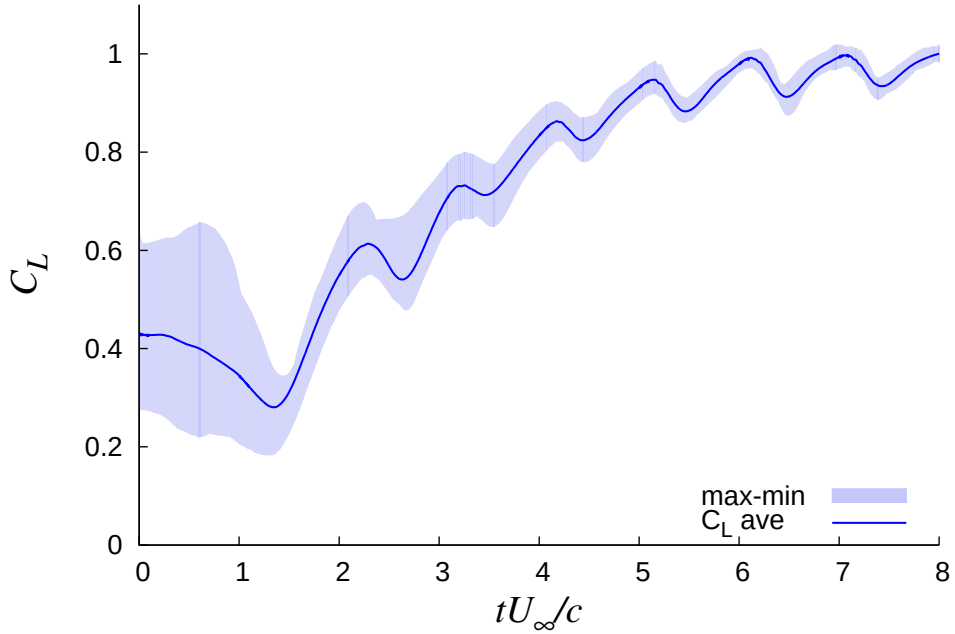

Figure 6.2: Time histories of the lift coefficient C_L obtained with the burst actuation $F^+ = 1$. The time is normalized by c/U_∞. The solid line denotes the ensemble-average values of C_L and the color filled areas denote the possible value areas.

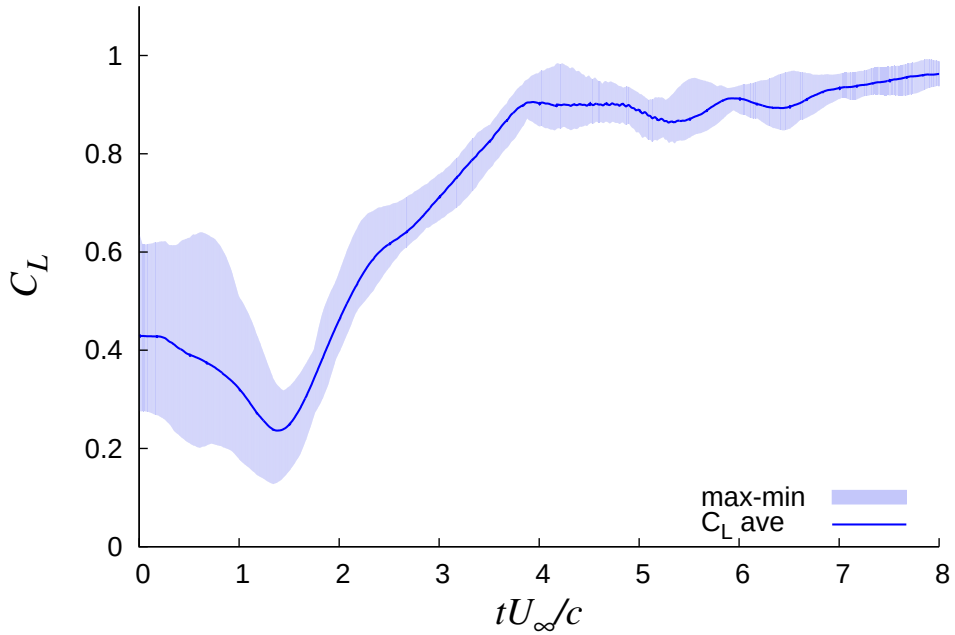

Figure 6.3: Time histories of the lift coefficient C_L obtained with the burst actuation $F^+ = 6$. The time is normalized by c/U_∞. The solid line denotes the ensemble-average values of C_L and the color filled areas denote the possible value areas.

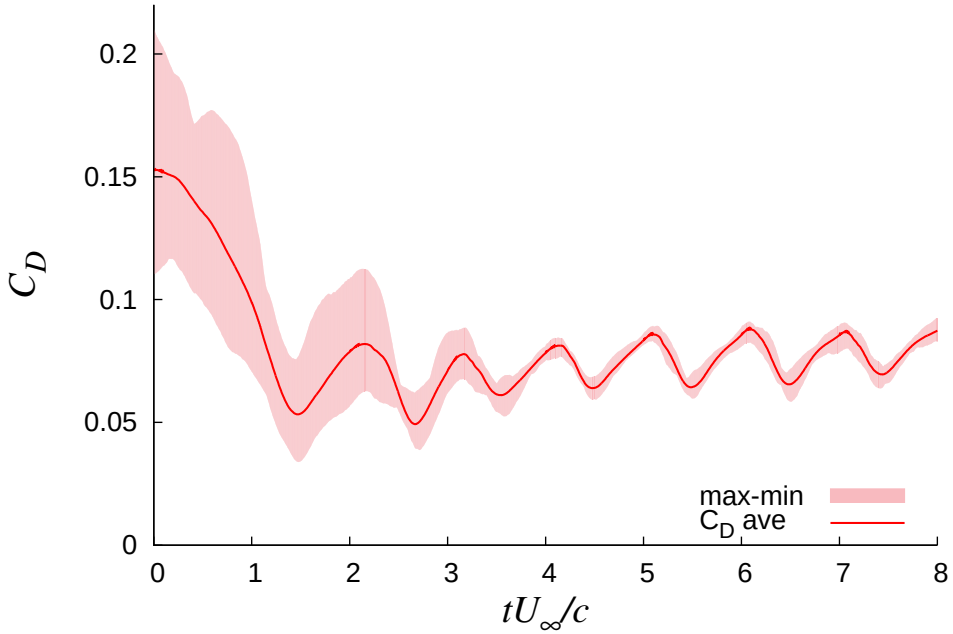

Figure 6.4: Time histories of the drag coefficient C_D obtained with the burst actuation $F^+ = 1$. The time is normalized by c/U_∞. The solid line denotes the ensemble-average values of C_D and the color filled areas denote the possible value areas.

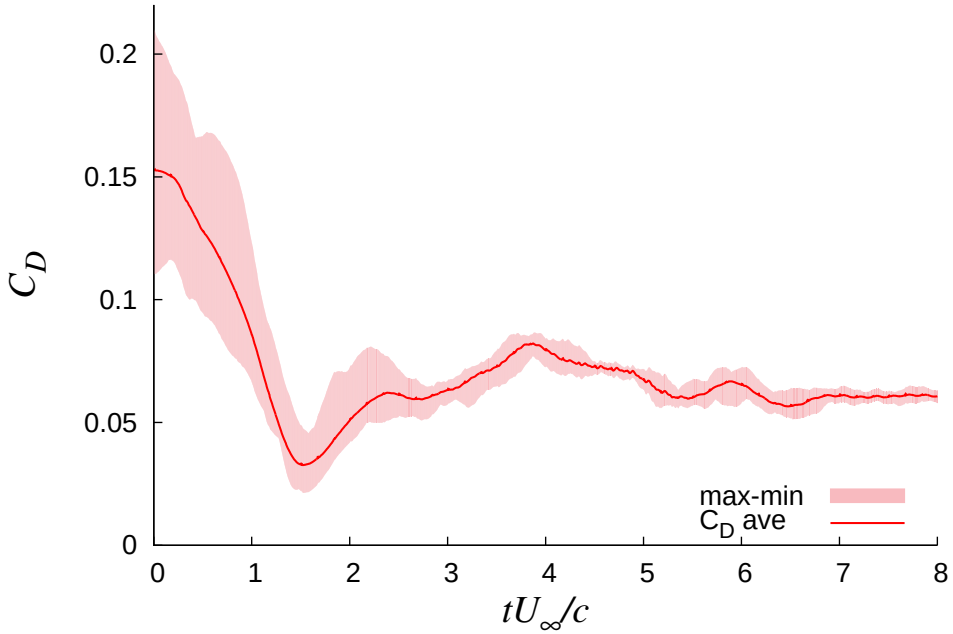

Figure 6.5: Time histories of the drag coefficient C_D obtained with the burst actuation $F^+ = 6$. The time is normalized by c/U_∞. The solid line denotes the ensemble-average values of C_D and the color filled areas denote the possible value areas.

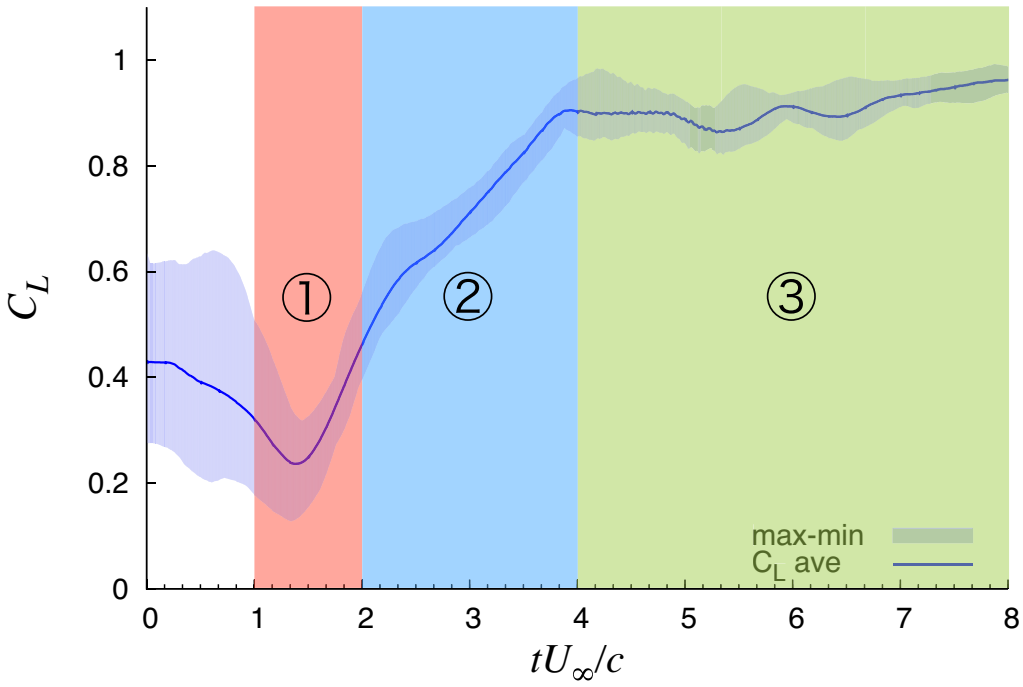

Figure 6.6: Schematic of the characteristic transient stages.

6.3 Instantaneous Flow Fields

First of all, to understand basic flow features instantaneous flow fields are discussed. Figures 6.7 and 6.9 show instantaneous flow fields obtained with the burst actuation $F^+ = 1, 6$. Color contour is a chord-directional velocity and iso-surfaces are second invariant of the velocity gradient tensors Q. Figures 6.8 and 6.10 show the closeups of the same flow fields as Figs. 6.7 and 6.9.

On the $F^+ = 1$ case, the region in which the free-stream is involved to the airfoil surface is found at the middle of chord length near the airfoil surface in Fig. 6.7(a). This involving is caused by the advection of the spanwise vortex which is generated by the first actuation of the DBD plasma actuator. Similar flow is found in the Fig. 6.9(a). This spanwise vortex can be found clearly in Fig. 6.11 and is discussed later. After the first actuation, one or two spanwise vortices are generated upstream ($x/c \sim 0.3$) and merge into one large vortex downstream ($x/c \sim 0.6$) every burst period. With the passage of the burst period, the separated shear layer near the leading edge comes toward airfoil surface, and the accelerated flow region near the leading edge (pink contour region) becomes large gradually. On the other hand, on the $F^+ = 6$ case, separated region (blue contour region) near the trailing edge become smaller quickly than the $F^+ = 1$ case (Fig. 6.9(b)). Several spanwise strong vortices are generated and the three dimensional fine vortices are temporally disappear on the middle of airfoil surface (tU_∞/c = 3-4). Then the three dimensional vortices are induced again by vortex merging of the spanwise strong vortices. The region where these three dimensional vortices are found, grows upstream gradually. At $tU_\infty/c = 8$, the flow becomes quasi-steady, and three dimensional vortices are found over a wide range.

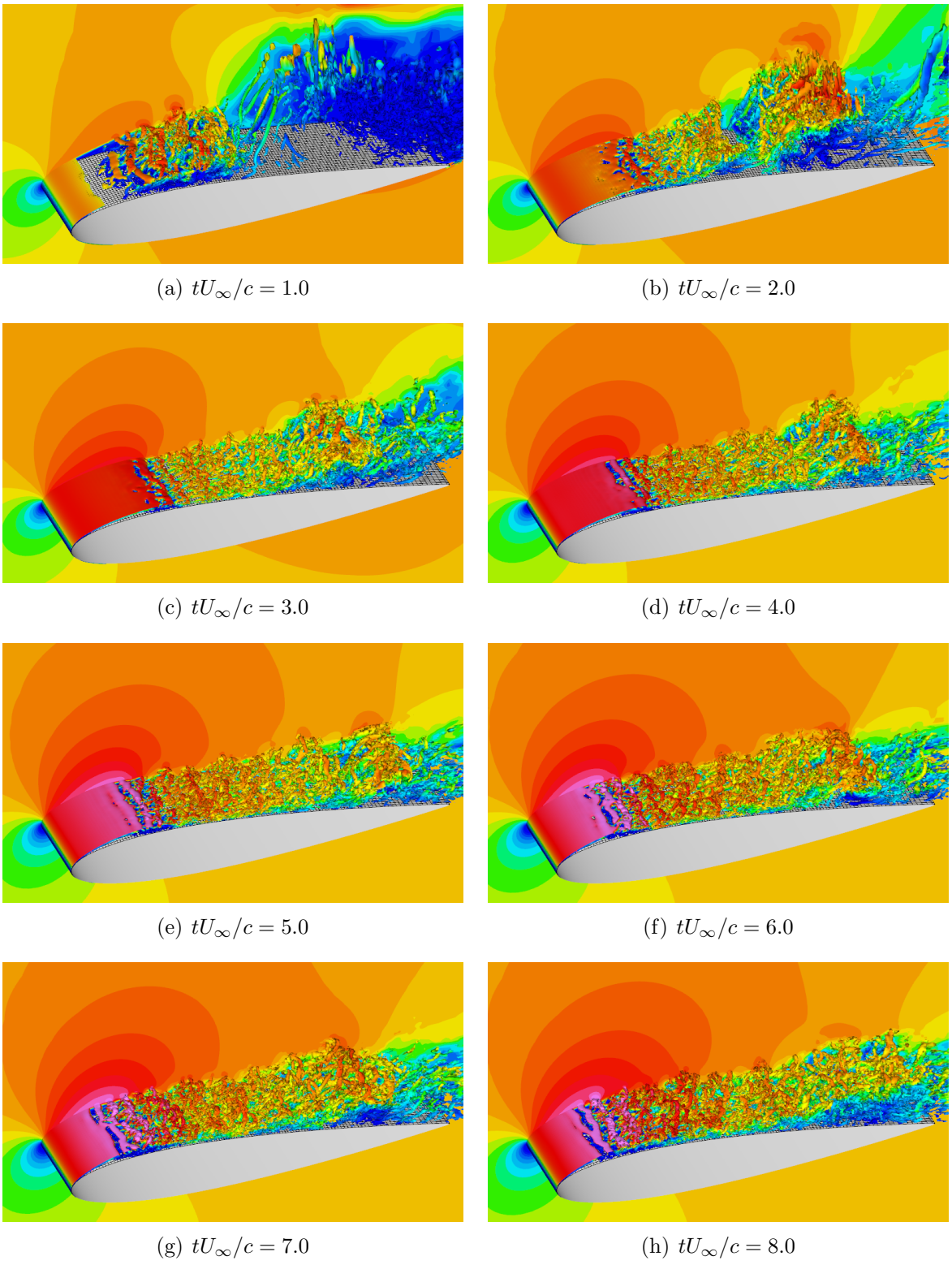

(a) $tU_\infty/c = 1.0$ (b) $tU_\infty/c = 2.0$

(c) $tU_\infty/c = 3.0$ (d) $tU_\infty/c = 4.0$

(e) $tU_\infty/c = 5.0$ (f) $tU_\infty/c = 6.0$

(g) $tU_\infty/c = 7.0$ (h) $tU_\infty/c = 8.0$

Figure 6.7: Instantaneous flow fields obtained with the burst actuation $F^+ = 1$. Color contour is a chord-directional velocity and iso-surfaces are second invariant of the velocity gradient tensors Q.

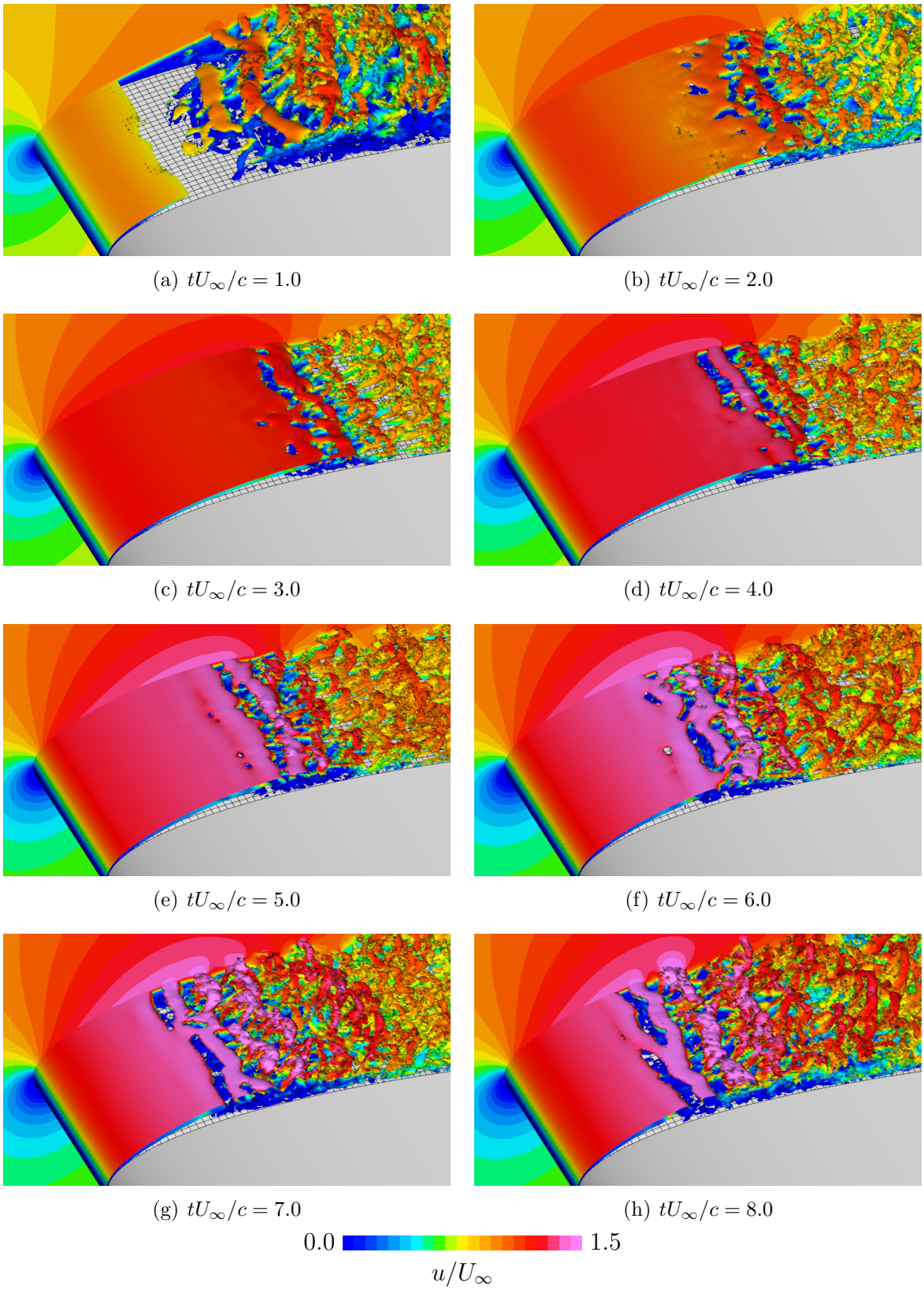

(a) $tU_\infty/c = 1.0$ (b) $tU_\infty/c = 2.0$

(c) $tU_\infty/c = 3.0$ (d) $tU_\infty/c = 4.0$

(e) $tU_\infty/c = 5.0$ (f) $tU_\infty/c = 6.0$

(g) $tU_\infty/c = 7.0$ (h) $tU_\infty/c = 8.0$

Figure 6.8: Closeups of instantaneous flow fields obtained with the burst actuation $F^+ = 1$ near the leading edge. Color contour is a chord-directional velocity and iso-surfaces are second invariant of the velocity gradient tensors Q.

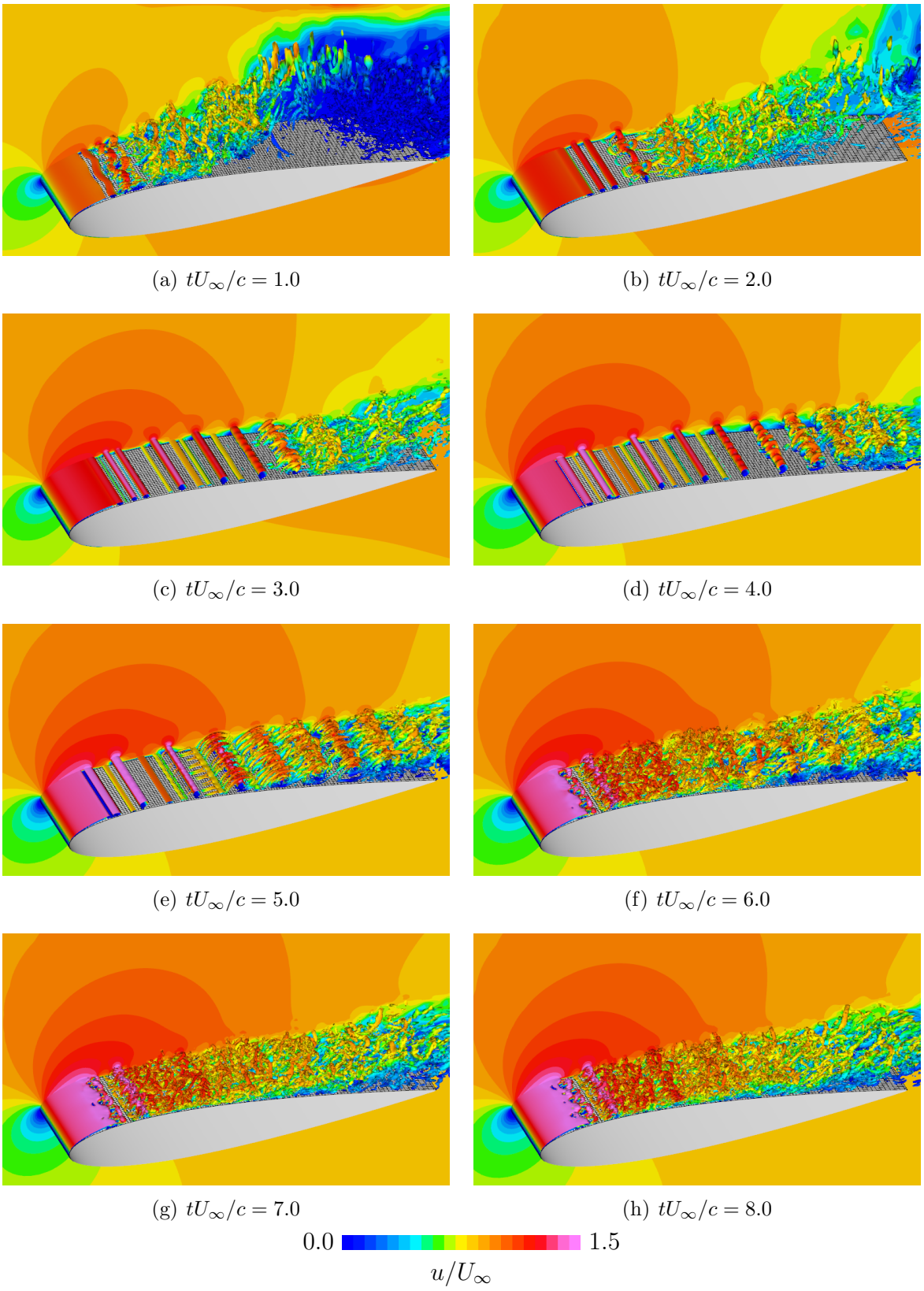

Figure 6.9: Instantaneous flow fields obtained with the burst actuation $F^+ = 6$. Color contour is a chord-directional velocity and iso-surfaces are second invariant of the velocity gradient tensors Q.

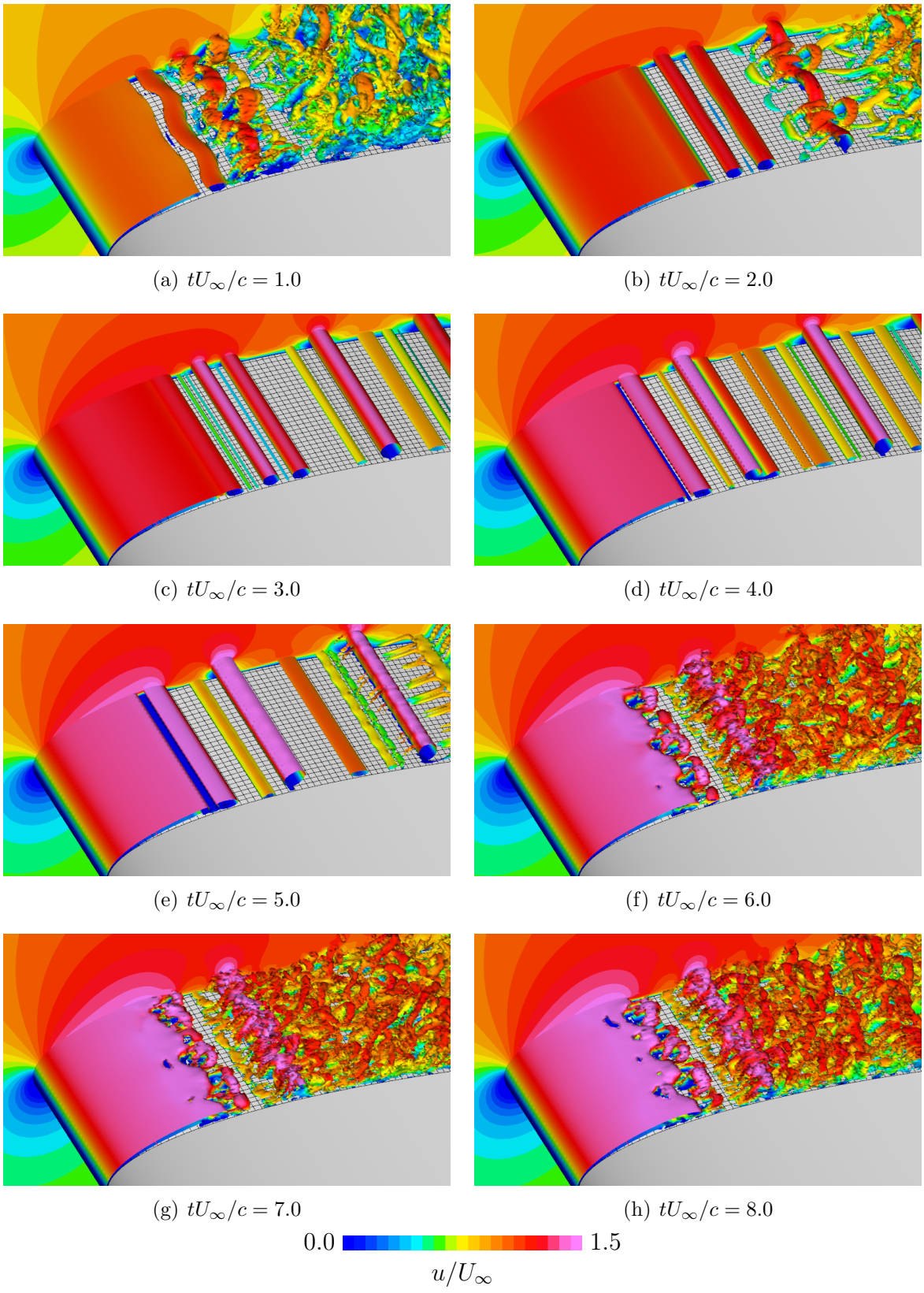

(a) $tU_\infty/c = 1.0$ (b) $tU_\infty/c = 2.0$

(c) $tU_\infty/c = 3.0$ (d) $tU_\infty/c = 4.0$

(e) $tU_\infty/c = 5.0$ (f) $tU_\infty/c = 6.0$

(g) $tU_\infty/c = 7.0$ (h) $tU_\infty/c = 8.0$

Figure 6.10: Closeups of instantaneous flow fields obtained with the burst actuation $F^+ = 6$ near the leading edge. Color contour is a chord-directional velocity and iso-surfaces are second invariant of the velocity gradient tensors Q.

6.4 Ensemble Averaged Flow Fields

Figure 6.11 shows ensemble and moving averaged flow fields obtained with the burst actuation $F^+ = 1$ at $tU_\infty/c = 1, 2, 3, 4, 5, 6, 7, 8$. Color contour is a chord-directional velocity and black contour lines are second invariant of the velocity gradient tensors Q. In every figures of Fig. 6.11, a large spanwise vortex is observed at $x/c \sim 0.8$. Especially, there is a large spanwise vortex at $tU_\infty/c = 1$. This vortex is generated by actuations of first burst period. High speed region is observed at the middle of chord length near the airfoil surface. This region is caused by the advection of the spanwise vortex which involves the free-stream to the airfoil surface. Then impinging of the involved flow makes suction side pressure increase and makes C_L decrease. This C_L decreasing is temporarily observed in the initial stage of transient state ($tU_\infty/c \sim 1.5$) in Fig. 6.2. After the first actuation, one or two spanwise vortices are generated upstream ($x/c \sim 0.3$) and merge into one large vortex downstream ($x/c \sim 0.6$) every burst period. With the passage of the burst period, the separated shear layer near the leading edge comes toward airfoil surface, and the accelerated flow region near the leading edge (red contour region) becomes large gradually.

Figure 6.12 shows ensemble and moving averaged flow fields obtained with the burst actuation $F^+ = 6$ at $tU_\infty/c = 1, 2, 3, 4, 5, 6, 7, 8$. Color contour is a chord-directional velocity and black contour lines are second invariant of the velocity gradient tensors Q. As with the flow of $F^+ = 6$ at the first burst period, there is a large spanwise vortex at $tU_\infty/c = 1$. This vortex is generated by the same way as $F^+ = 6$ case. Also high speed region is observed at the middle of chord length near the airfoil surface and impinging of the involved flow which makes C_L decrease in the initial stage of transient state ($tU_\infty/c \sim 1.5$) in Fig. 6.3. The separation region near the leading edge is relatively smaller than the flow of $F^+ = 1$. In the $F^+ = 6$ case, separated region (blue contour region) near the trailing edge become smaller quickly than the $F^+ = 1$ case (Fig. 6.12(b)). However at $tU_\infty/c \sim 5.0$, the separated region temporarily becomes large again, and gradually become small. This sequence of trailing separation relates to advections of vortices generated by the DBD plasma actuator. The vortices are advect as follow. Several spanwise strong vortices are generated *e.g.* at least eight vortices are observed at $tU_\infty/c \sim 4.0$. These vortices merge into six vortices at $tU_\infty/c \sim 8.0$. This number of vortices correspond with the non-dimensional burst frequency. This vortex merging induces fine three-dimensional vortices and weaken the spanwise vortices. The accelerated flow region near the leading edge (red contour region) becomes large gradually as with the flow of $F^+ = 6$.

Figure 6.13 shows ensemble and moving averaged pressure coefficients C_p obtained with the burst actuation $F^+ = 1$ along the airfoil. At $tU_\infty/c \sim 1.0$, there is high pressure region at the middle of chord length on the suction side. As mentioned above, this region is caused by the advection of the spanwise vortex which involves the free-stream to the airfoil surface. Then impinging of the involved flow makes suction side pressure increase and makes C_L decrease. This C_L decreasing is temporarily observed in the initial stage of transient state ($tU_\infty/c \sim 1.5$) in Fig. 6.2. Near the leading edge, plateau distribution of C_p which is caused by the separation babble is found at every time stages. With the passage of the burst period, peak of negative pressure becomes strong gradually because the accelerated flow region near the leading edge becomes large gradually.

Figure 6.14 shows ensemble and moving averaged pressure coefficients C_p obtained with the burst actuation $F^+ = 6$ along the airfoil. High pressure region is also found at the middle of chord length on the suction side, at $tU_\infty/c \sim 1.0$. From $tU_\infty/c \sim 2.0$ to $tU_\infty/c \sim 5.0$, local C_p oscillations are found. These oscillations are made by strong spanwise vortices, and gradually disappear by vortex merging. The vortex merging of the strong spanwise vortices is accompanied by induction of fine three-dimensional vortices which diffuses the energy of spanwise vortices and makes a velocity profile like turbulent boundary layer. That is why, the local C_p oscillations weaken.

Figure 6.15 shows ensemble and moving averaged skin friction coefficients C_f obtained with the burst actuation $F^+ = 1$ along the airfoil on the suction side of the airfoil. Attached regions are shown with a red color and separated regions are shown with a blue color. At $tU_\infty/c \sim 1.0$, there is an attached region at the middle of chord length. This area corresponds to the high pressure region in the Fig. 6.13. Involving the free stream into the airfoil surface makes the flow reattach and the high pressure region. This attached region becomes large gradually.

Figure 6.16 shows ensemble and moving averaged skin friction coefficients C_f obtained with the burst actuation $F^+ = 6$ along the airfoil on the suction side of the airfoil. At $tU_\infty/c \sim 1.0$, there is an attached region at the middle of chord length like $F^+ = 1$ case. In addition, the area in which attached and separated areas frequently change each other is found at $x/c = 0.15$. This area is made by strong spanwise vortices and temprorally becomes large, and gradually disappear by vortex merging. Then the downstream from $x/c = 0.2$ becomes almost attached flow. Same trends are shown in Fig. 6.17 and 6.18. These figures show recirculation region obtained with the burst actuation $F^+ = 1$ and $F^+ = 1$ along the airfoil.

Finaly, Reynolds shear stresses ($-u'v'/U_\infty^2$) of ensemble and moving averaged flow fields obtained with the burst actuation $F^+ = 1, 6$ are shown in Fig. 6.19 and 6.20. Black

contour lines are second invariant of the velocity gradient tensors Q. Basic charastaristics of the flow fields are already discussed in Fig. 6.11 and 6.12. After the first actuation, the large spanwise vortex is generated by the actuation and is found at $x/c \sim 0.8$ in Fig. 6.19(a). This vortex brings Reynolds shear stress and the strong Reynolds-shear-stress area is observed around the vortex. At $tU_\infty/c = 2$, large spanwise vortex brigs the strong Reynolds-shear-stress. After $tU_\infty/c = 3$, the large spanwise vortices also brig the Reynolds-shear-stress. However a magnitude of the stress is smaller than the magnitude of the stress at $tU_\infty/c = 1, 2$. On the other hand, a magnitude of the stress near the reatatchment point $x/c \sim 0.25$ becomes stronger gradually. On the $F^+ = 6$ case, the strong Reynolds-shear-stress area is also observed around the large spanwise vortex. From these results, It is thought that the large spanwise vortex play an important role to suppress the separation at the initial stage (tU_∞/c = 1-2). This strong Reynolds-shear-stress area disappears relatively soon as compared to $F^+ = 1$ case. Other strong Reynolds-shear-stress areas appear at $tU_\infty/c = 4$. This area is caused by vortex merging of strong spanwise vortices. The strong Reynolds-shear-stress area goes upstream gradually, and the area concentrates reatatchment point $x/c \sim 0.2$ at the quasi-steady state. This strong Reynolds-shear-stress area is caused by fine three dimensional vortices, and keep the flow attach.

6.5 Summary

In this chapter, the transient processes in which the separated flow is controlled and the separated region is suppressed gradually are discussed. As the computational cases, characteristic operating conditions of DBD plasma actuator are chosen: $F^+ = 1$ and $F^+ = 6$, and the actuator installed at the 5 % chord length from the leading edge. To discuss the statistics of these transient states, 20 computations are conducted and ensemble averages are taken for each case.

First, aerodynamic characteristics (C_L, C_D) are discussed. On the each, C_L and C_D values converge on a quasi-steady values although initial C_L and C_D values are quite-variable among stations. This results show the initial flow conditions does not affect the quasi-steady state if the separation is suppressed on the quasi-steady flows. The transient times on the two cases are same order and in the range approximately 5 - 8. The C_L of $F^+ = 6$ case converges relatively quickly. large lift decreasing which are temporarily found in the initial stage of transient state ($tU_\infty/c \sim 1.5$) on the both cases. This large lift decreasing is caused by advection of a spanwise vortex and the vortex involves the free-stream to the airfoil surface. The same trends are found on the C_D values.

Second, to understand basic flow features, instantaneous flow fields are discussed. On the both $F^+ = 1$ and $F^+ = 6$ case, the region in which the free-stream is involved to the airfoil surface is found at the middle of chord length near the airfoil surface. This involving is caused by the advection of the spanwise vortex which is generated by the first actuation of the DBD plasma actuator. This spanwise vortex causes temporally lift decreasing in the initial stage of transient state. On the $F^+ = 1$ case, After the first actuation, one or two spanwise vortices are generated upstream ($x/c \sim 0.3$) and merge into one large vortex downstream ($x/c \sim 0.6$) every burst period. With the passage of the burst period, the separated shear layer near the leading edge comes toward airfoil surface, and the accelerated flow region near the leading edge (pink contour region) becomes large gradually. On the other hand, on the $F^+ = 6$ case, separated region near the trailing edge become smaller quickly than the $F^+ = 1$ case. Several spanwise strong vortices are generated and the three dimensional fine vortices are temporally disappear on the middle of airfoil surface (tU_∞/c = 3-4). Then the three dimensional vortices are induced again by vortex merging of the spanwise strong vortices. The region where these three dimensional vortices are found grows upstream gradually. At $tU_\infty/c = 8$, the flow becomes quasi-steady, and three dimensional vortices are found over a wide range.

Finally, ensemble-averaged flow fields and some statistics are discussed. The large spanwise vortex which is generated by the first actuation of the DBD plasma actuator and is already discussed on the instantaneous flow, can be found clearly by taking ensemble averages. This vortex involves the free-stream to the airfoil surface. Then impinging of the involved flow makes suction side pressure decrease and makes C_L decrease. This C_L decreasing is temporarily observed in the initial stage of transient state ($tU_\infty/c \sim 1.5$). The strong Reynolds-shear-stress area is observed around this vortex. At the initial stage on the both $F^+ = 1$ and $F^+ = 6$ case, large spanwise vortex brigs the strong Reynolds-shear-stress. It is thought that the large spanwise vortex plays an important role to suppress the separation at the initial stage (tU_∞/c = 1-2). On the $F^+ = 1$ case, after $tU_\infty/c \sim 3$, the large spanwise vortices also brig the Reynolds-shear-stress. However a magnitude of the stress is smaller than the magnitude of the stress before. On the other hand, a magnitude of the stress near the reattachment point $x/c \sim 0.25$ becomes stronger gradually. After the first actuation, one or two spanwise vortices are generated upstream ($x/c \sim 0.3$) and merge into one large vortex downstream ($x/c \sim 0.6$) every burst period. With the passage of the burst period, the separated shear layer near the leading edge comes toward airfoil surface, and the accelerated flow region near the leading edge (red contour region) becomes large gradually.

On the $F^+ = 6$ case, separated region near the trailing edge and the strong Reynolds-

shear-stress region which is found in the initial stage, become smaller quickly than the $F^+ = 1$ case. However at $tU_\infty/c \sim 5.0$, the separated region temporarily becomes large again, and gradually becomes small. This is caused by advections of several spanwise strong vortices which are generated by DBD plasma actuator. The strong spanwise vortices make the C_p oscillations and make separated region near the trailing edge. These vortices merge into six vortices at the quasi-steady state. This number of vortices correspond with the non-dimensional burst frequency. This vortex merging induces fine three-dimensional vortices and make flow attach again. The accelerated flow region near the leading edge becomes large gradually.

From these results, it is clarified that the transient times which is normalized by the chard length and the free-stream velocity are same order ($t \sim$ 5-6) between each case. However the aerodynamic coefficients (C_L and C_D) of $F^+ = 6$ converges relatively quick ($t \sim 5$). The large lift decreasing which are temporarily observed in the initial stage of transient state caused by advections of the spanwise vortices which involve the free-stream to the airfoil surface. It is thought that this large spanwise vortices play an important role to suppress the separation at the initial stage ($tU_\infty/c =$ 1-2). In each case, quasi-steady state is independent of initial flow state.

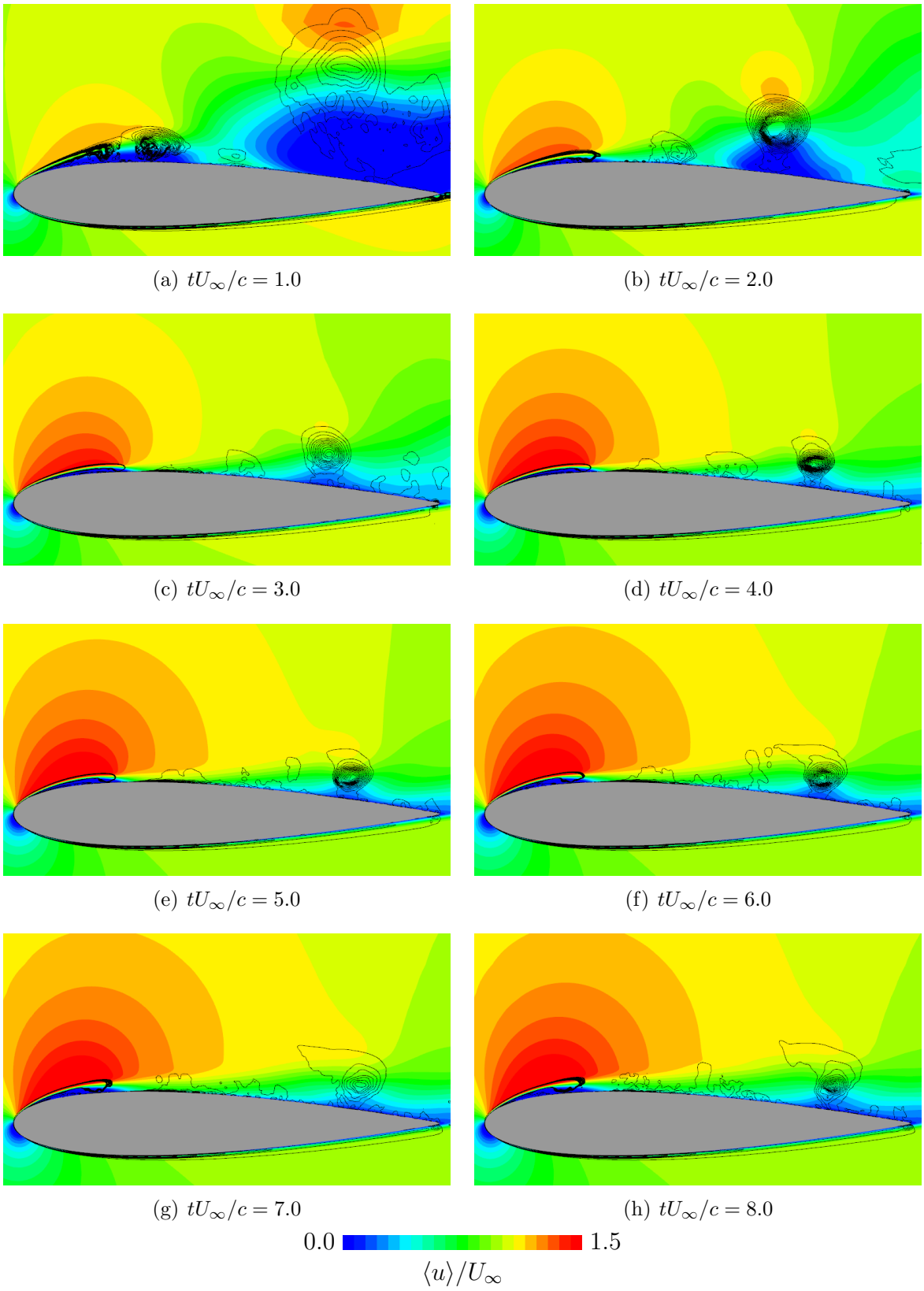

Figure 6.11: Ensemble and moving averaged flow fields obtained with the burst actuation $F^+ = 1$. Color contour is a chord-directional velocity and black contour lines are second invariant of the velocity gradient tensors Q.

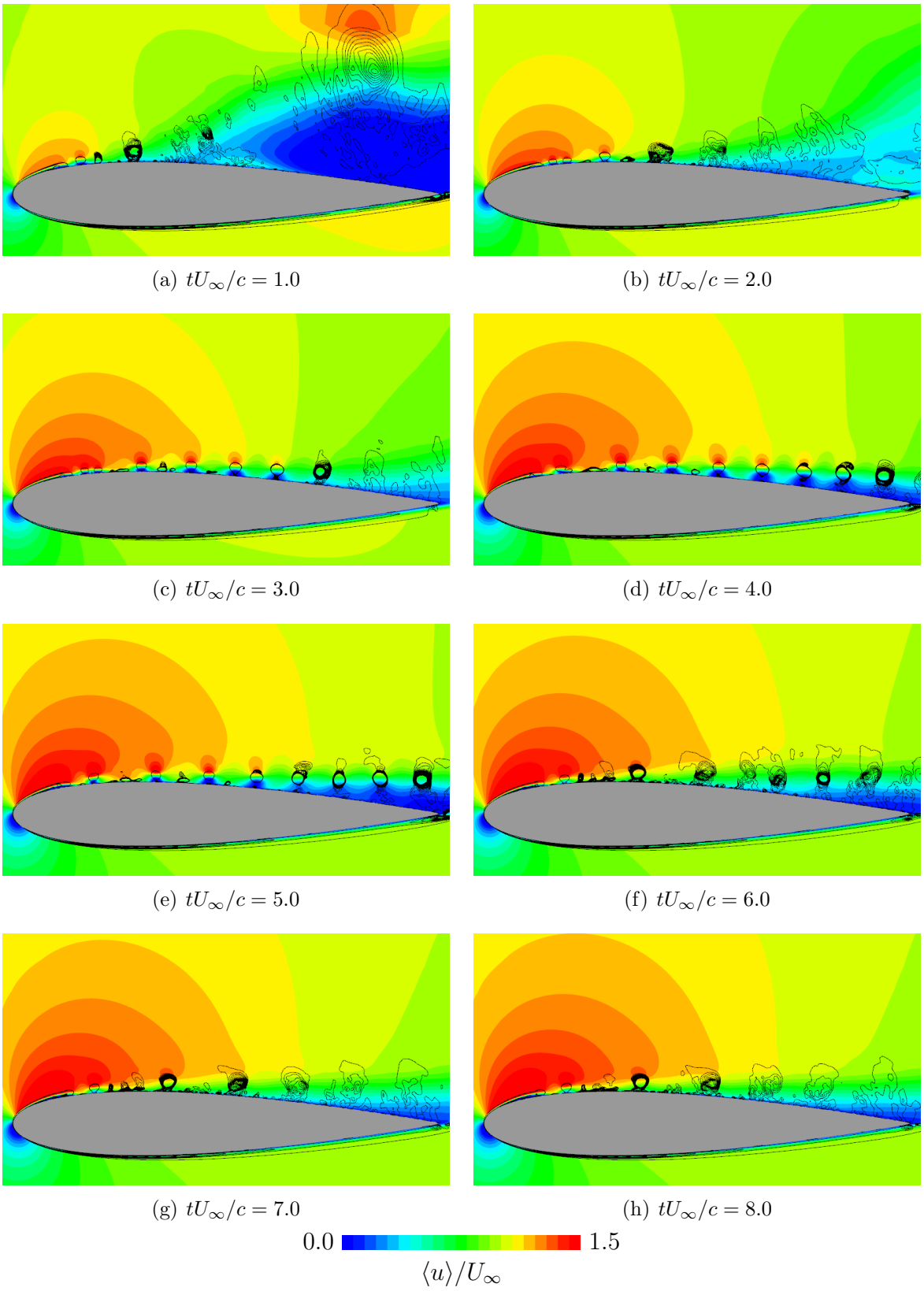

Figure 6.12: Ensemble and moving averaged flow fields obtained with the burst actuation $F^+ = 6$. Color contour is a chord-directional velocity and black contour lines are second invariant of the velocity gradient tensors Q.

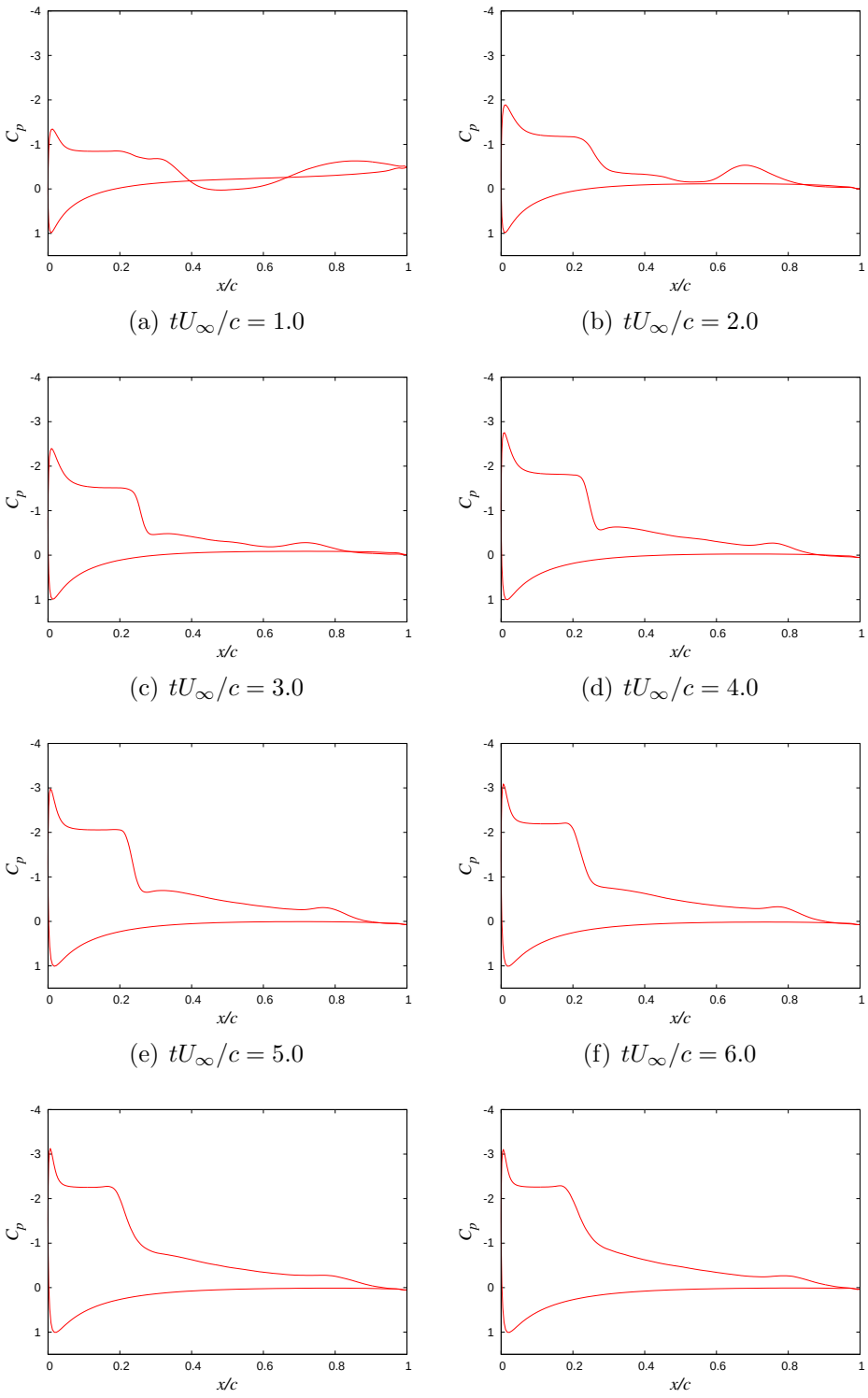

(a) $tU_\infty/c = 1.0$ (b) $tU_\infty/c = 2.0$

(c) $tU_\infty/c = 3.0$ (d) $tU_\infty/c = 4.0$

(e) $tU_\infty/c = 5.0$ (f) $tU_\infty/c = 6.0$

(g) $tU_\infty/c = 7.0$ (h) $tU_\infty/c = 8.0$

Figure 6.13: Ensemble and moving averaged pressure coefficients C_p obtained with the burst actuation $F^+ = 1$ along the airfoil.

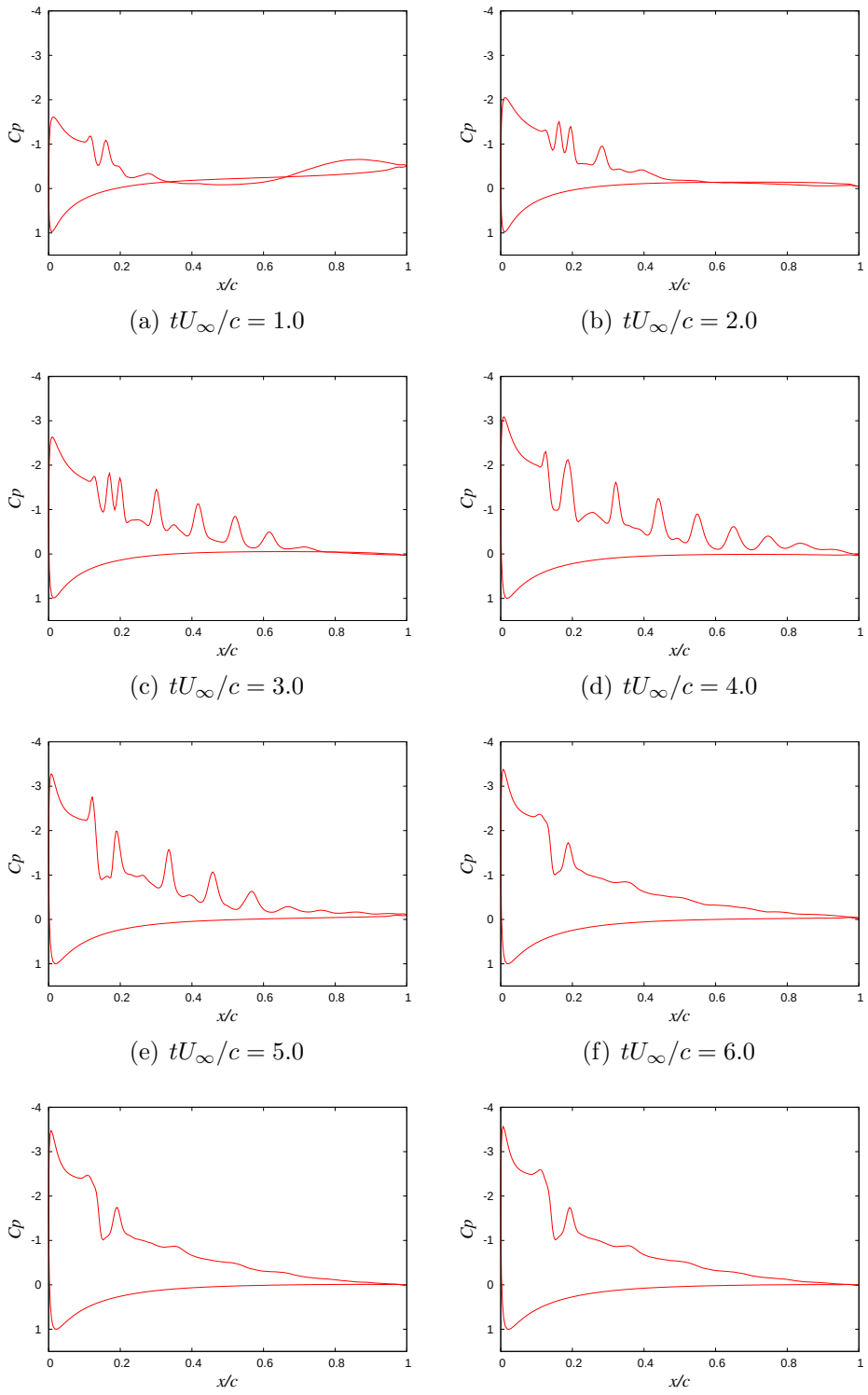

(a) $tU_\infty/c = 1.0$ (b) $tU_\infty/c = 2.0$

(c) $tU_\infty/c = 3.0$ (d) $tU_\infty/c = 4.0$

(e) $tU_\infty/c = 5.0$ (f) $tU_\infty/c = 6.0$

(g) $tU_\infty/c = 7.0$ (h) $tU_\infty/c = 8.0$

Figure 6.14: Ensemble and moving averaged pressure coefficients C_p obtained with the burst actuation $F^+ = 6$ along the airfoil.

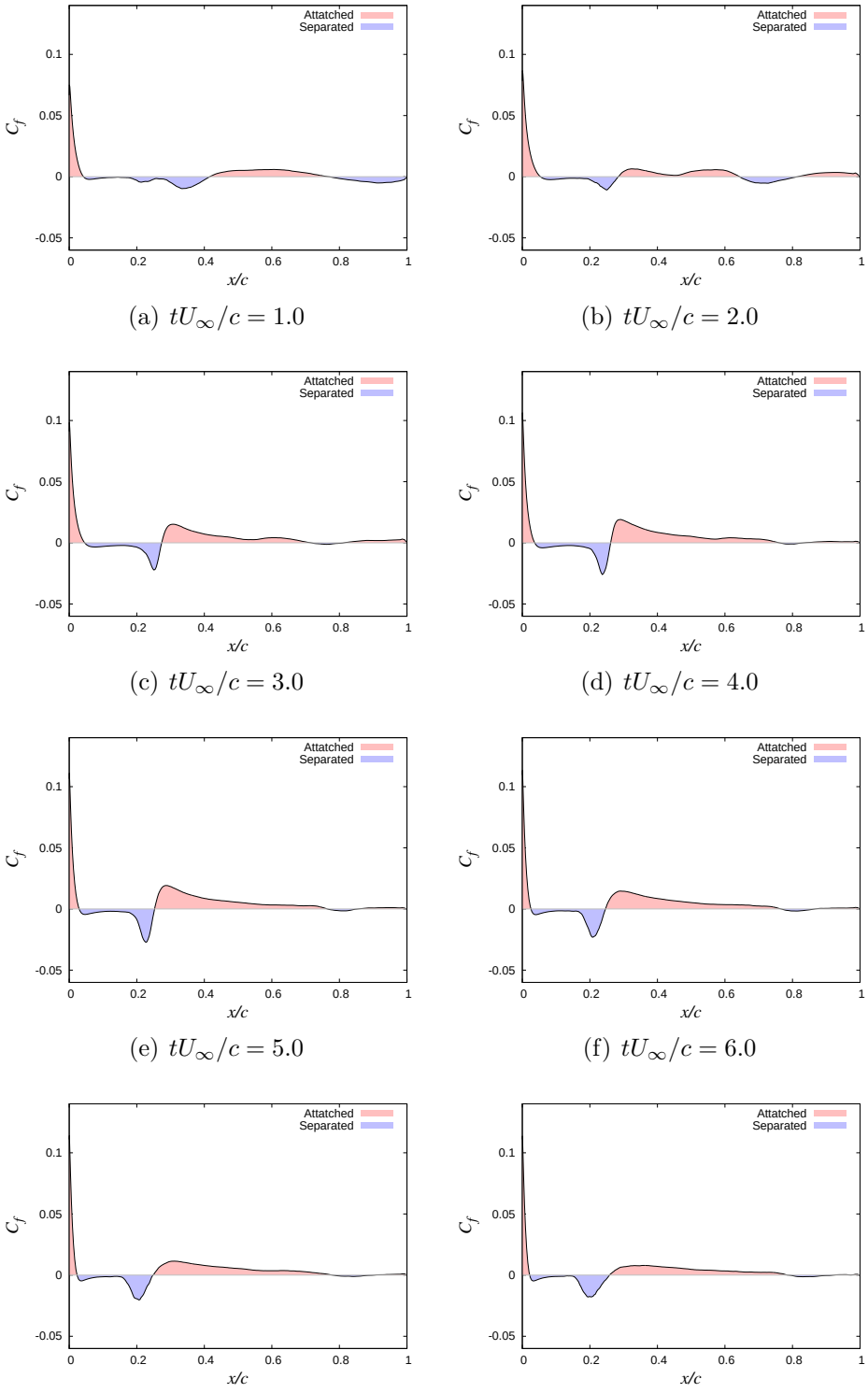

(a) $tU_\infty/c = 1.0$ (b) $tU_\infty/c = 2.0$

(c) $tU_\infty/c = 3.0$ (d) $tU_\infty/c = 4.0$

(e) $tU_\infty/c = 5.0$ (f) $tU_\infty/c = 6.0$

(g) $tU_\infty/c = 7.0$ (h) $tU_\infty/c = 8.0$

Figure 6.15: Ensemble and moving averaged skin friction coefficients C_f obtained with the burst actuation $F^+ = 1$ on the suction side of the airfoil.

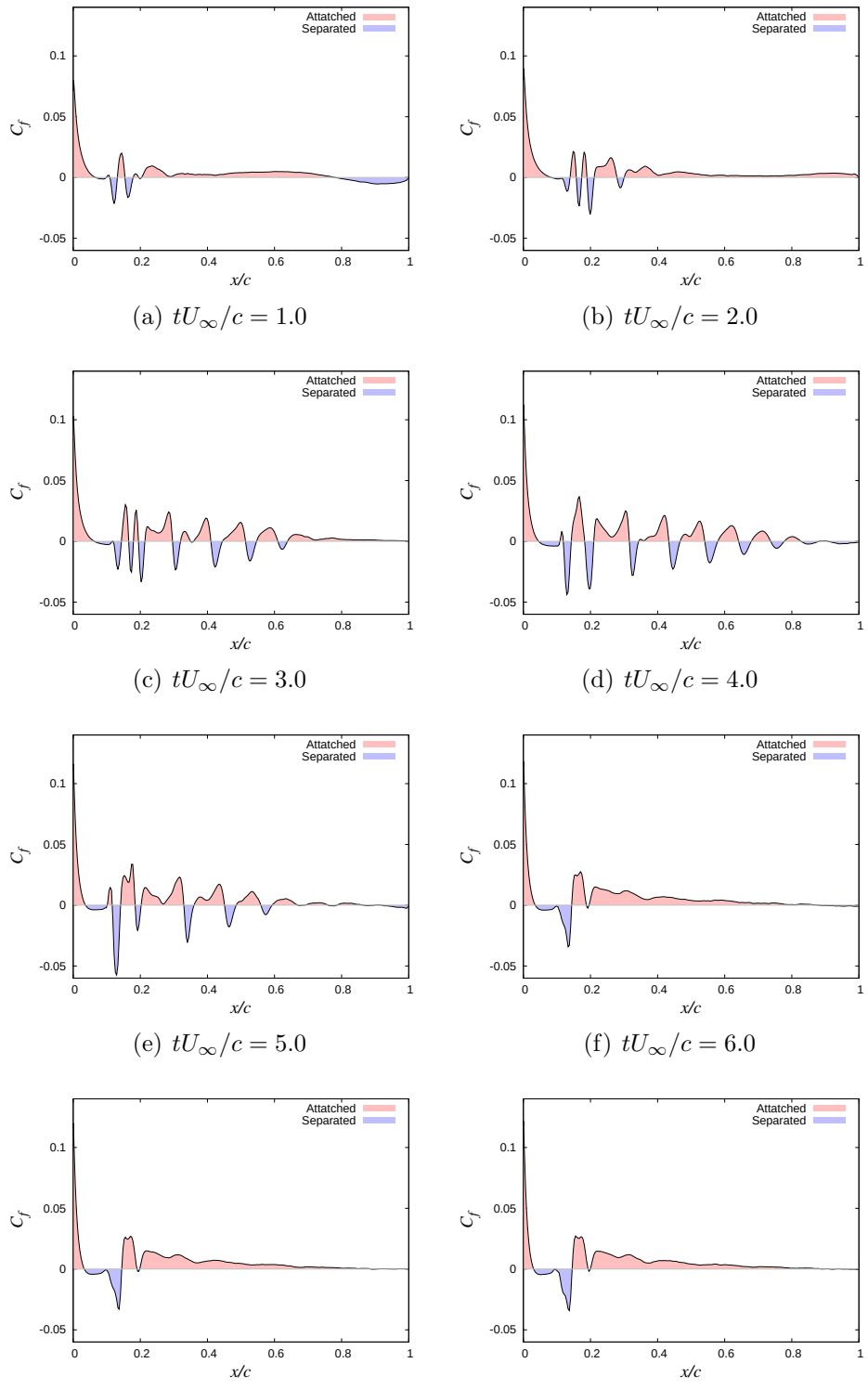

(a) $tU_\infty/c = 1.0$ (b) $tU_\infty/c = 2.0$

(c) $tU_\infty/c = 3.0$ (d) $tU_\infty/c = 4.0$

(e) $tU_\infty/c = 5.0$ (f) $tU_\infty/c = 6.0$

(g) $tU_\infty/c = 7.0$ (h) $tU_\infty/c = 8.0$

Figure 6.16: Ensemble and moving averaged skin friction coefficients C_f obtained with the burst actuation $F^+ = 6$ on the suction side of the airfoil.

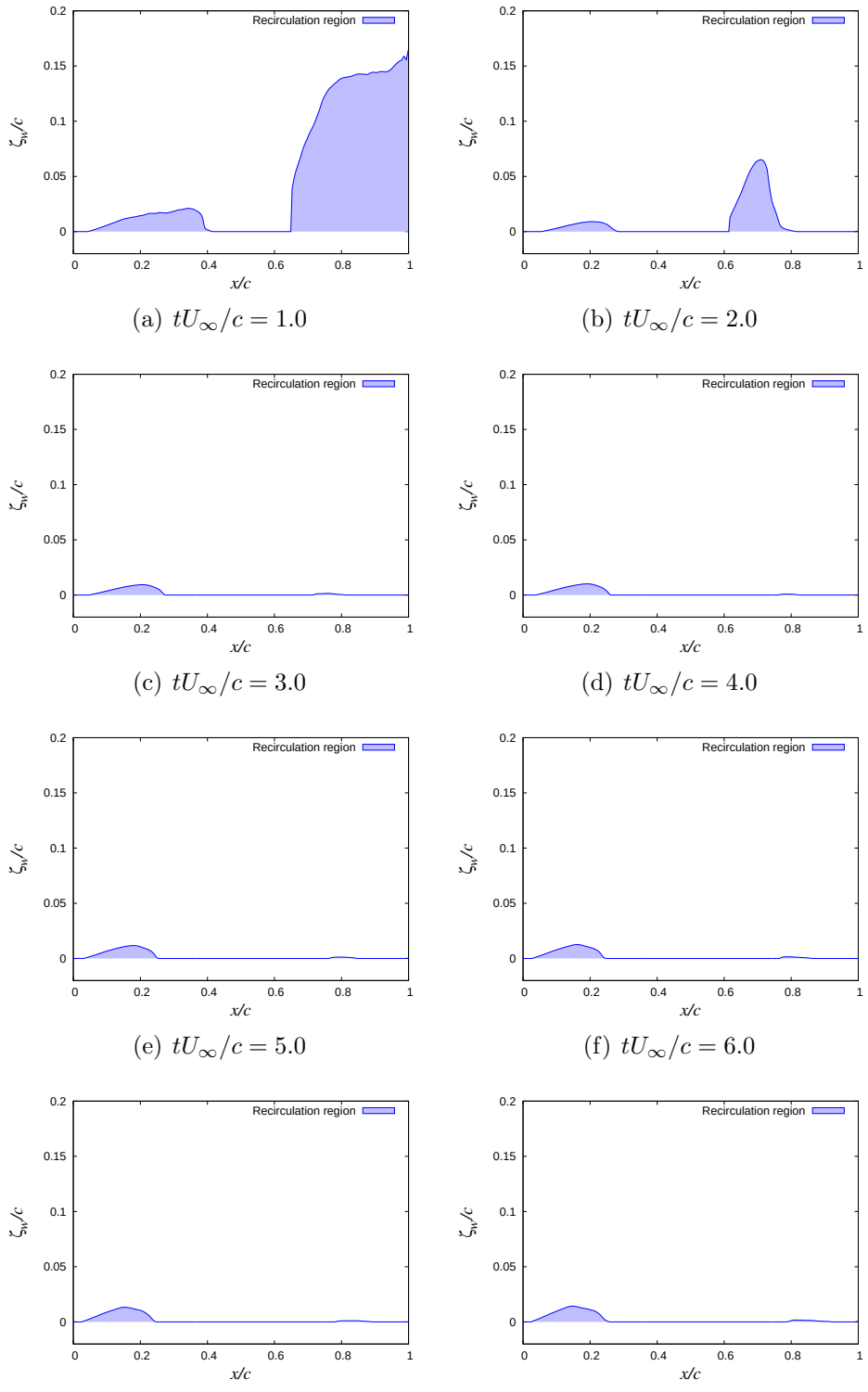

(a) $tU_\infty/c = 1.0$ (b) $tU_\infty/c = 2.0$

(c) $tU_\infty/c = 3.0$ (d) $tU_\infty/c = 4.0$

(e) $tU_\infty/c = 5.0$ (f) $tU_\infty/c = 6.0$

(g) $tU_\infty/c = 7.0$ (h) $tU_\infty/c = 8.0$

Figure 6.17: Recirculation region obtained with the burst actuation $F^+ = 1$ along the airfoil.

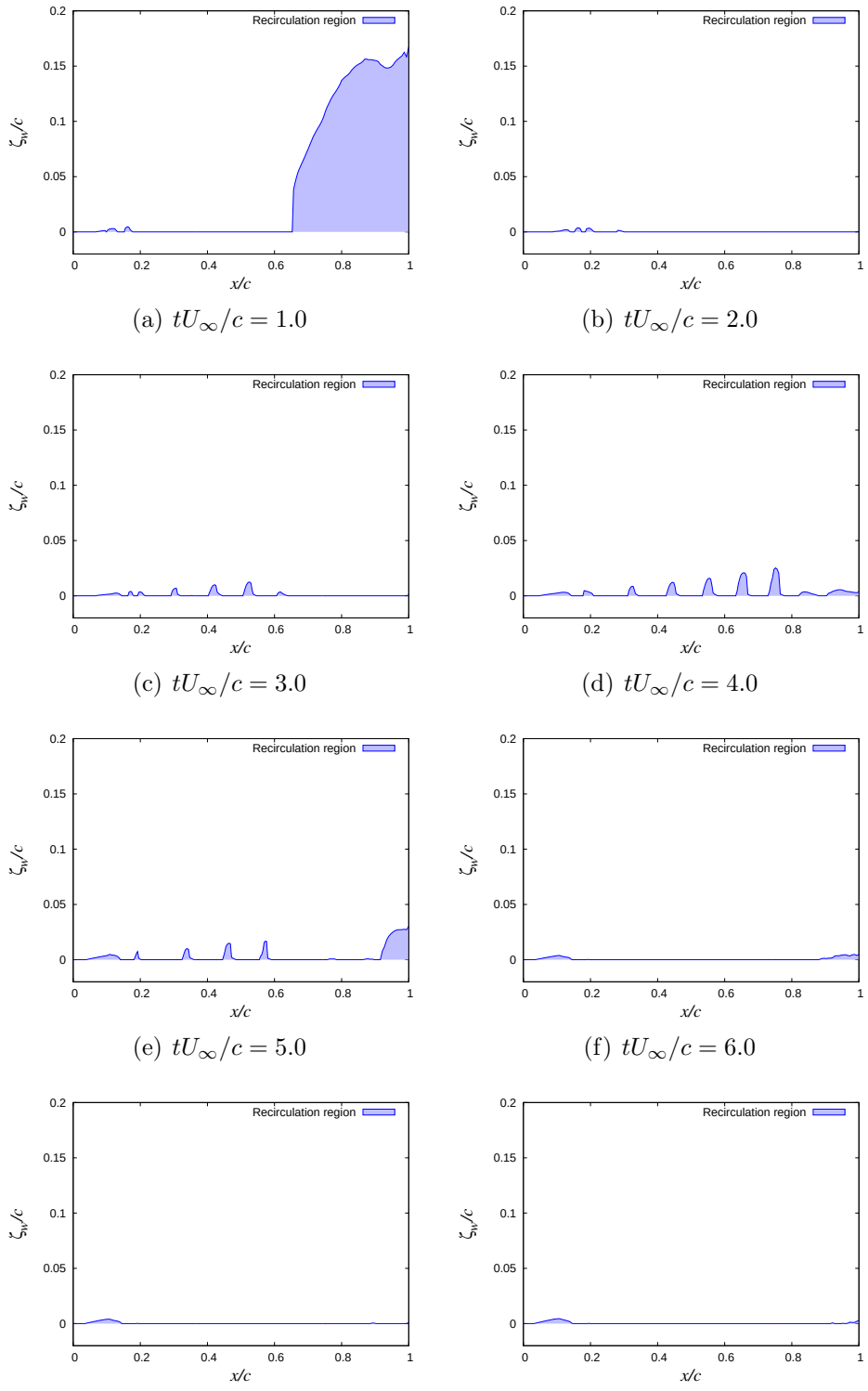

(a) $tU_\infty/c = 1.0$ (b) $tU_\infty/c = 2.0$

(c) $tU_\infty/c = 3.0$ (d) $tU_\infty/c = 4.0$

(e) $tU_\infty/c = 5.0$ (f) $tU_\infty/c = 6.0$

(g) $tU_\infty/c = 7.0$ (h) $tU_\infty/c = 8.0$

Figure 6.18: Recirculation region obtained with the burst actuation $F^+ = 6$ along the airfoil.

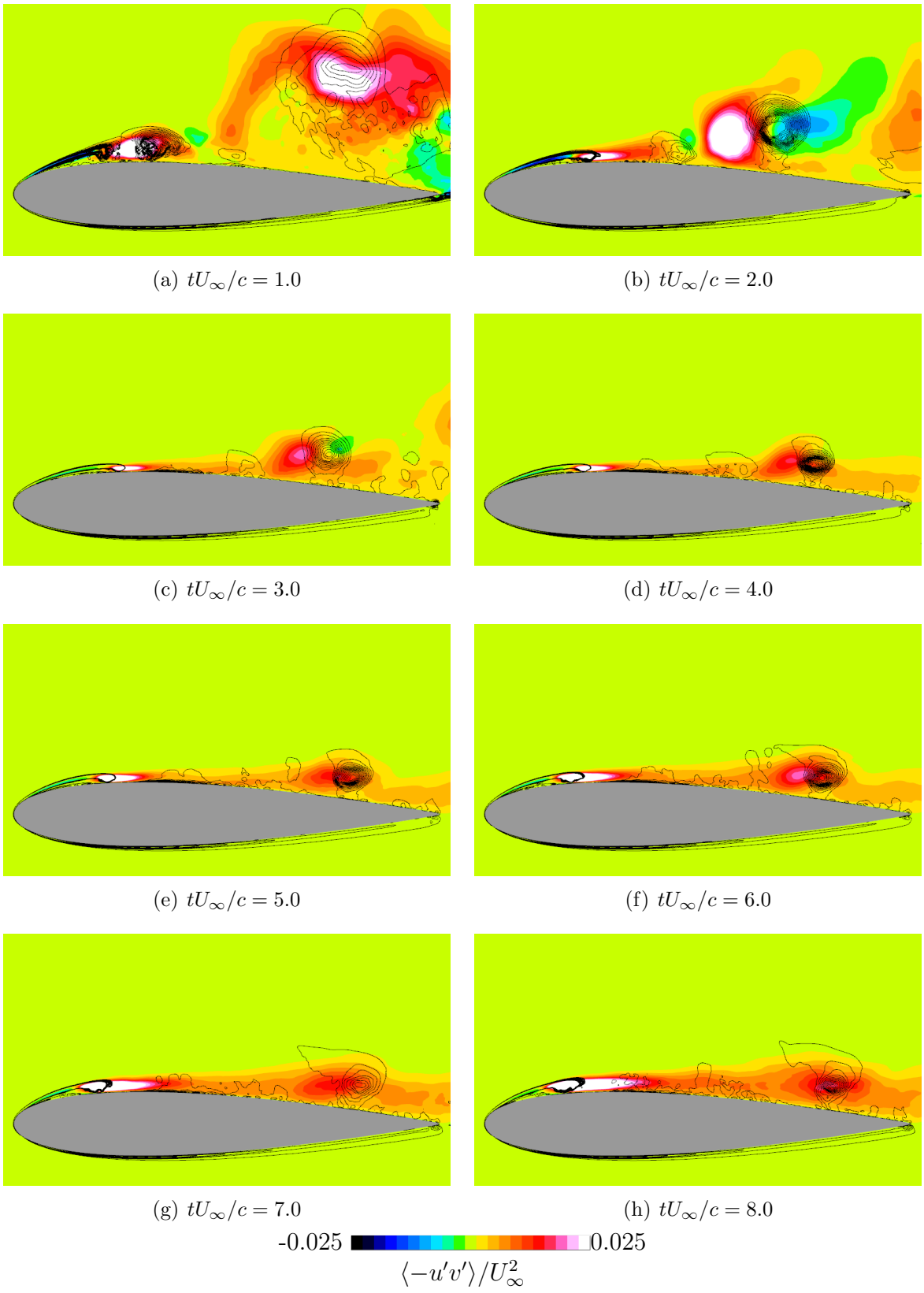

Figure 6.19: Ensemble and moving averaged flow fields obtained with the burst actuation $F^+ = 1$. Color contour is a Reynolds shear stress ($\langle -u'v' \rangle / U_\infty^2$) and black contour lines are second invariant of the velocity gradient tensors Q.

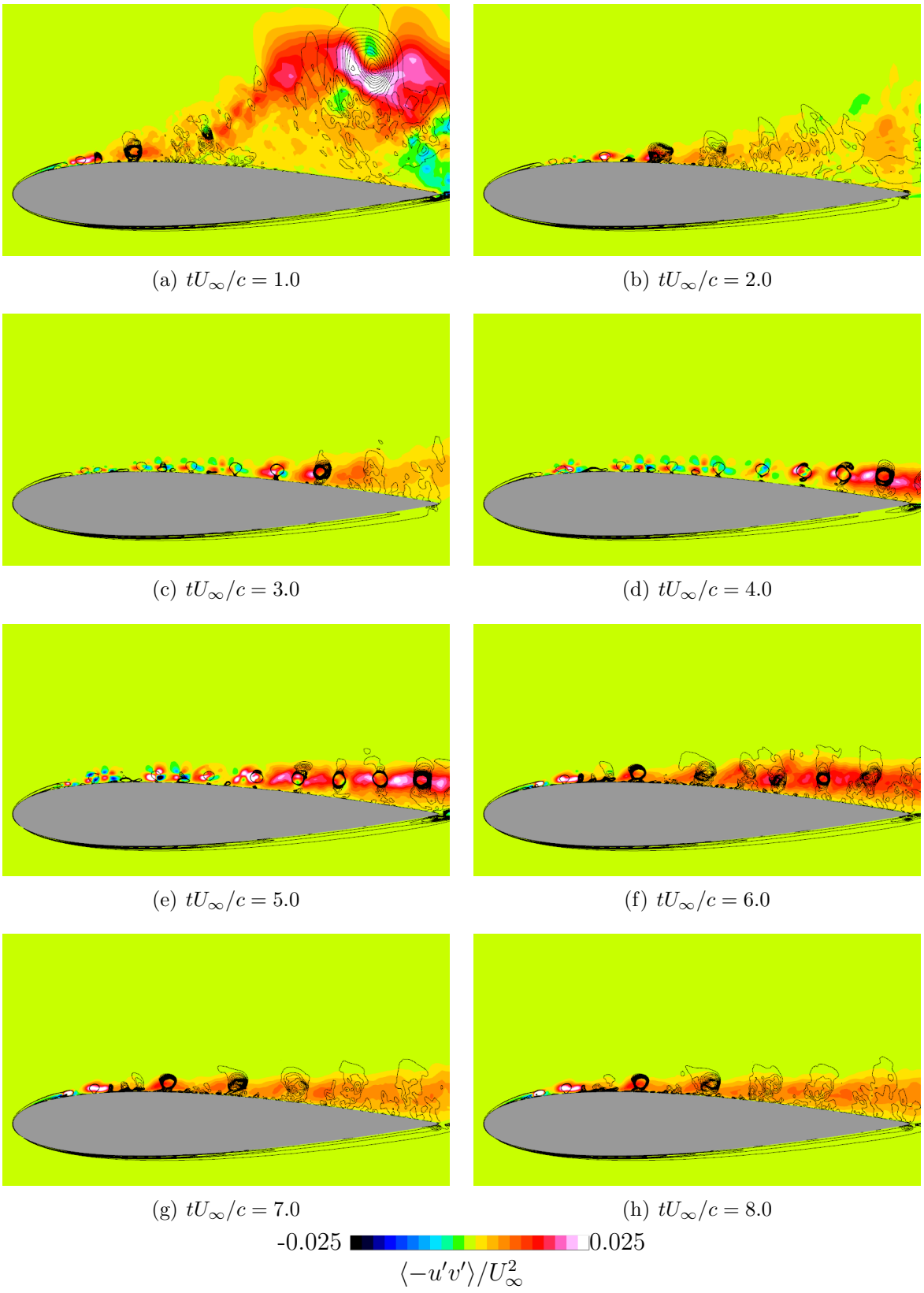

Figure 6.20: Ensemble and moving averaged flow fields obtained with the burst actuation $F^+ = 6$. Color contour is a Reynolds shear stress ($\langle -u'v' \rangle / U_\infty^2$) and black contour lines are second invariant of the velocity gradient tensors Q.

Chapter 7

Concluding Remarks

In this thesis, in order to clarify the mechanism of separated-flow control of DBD plasma actuator on quasi-steady states and transient states, and to provide guidelines for practical use of DBD plasma actuator, The flow-fields controlled by DBD plasma actuator on burst mode around the NACA0015 airfoil are simulated with implicit large eddy simulation (ILES) using compact difference scheme.

In chapter 4 validation results of this study are described. First, for the section 5.2 mean pressure values and grid resolutions are discussed. Second, for the section 5.3 mean statistics and a grid convergence and grid resolutions are discussed.

In chapter 5 quasi-steady flows which are controlled by the DBD plasma actuator are discussed. The Reynolds number based on chord length is set to 6,3000 and the angle of attack is set to 14 [deg]. The DBD plasma actuator is installed at the 0 % and 5 % chord length from the leading edge, and actuated in normal mode and burst mode. For the normal mode, D_c is set to 8, 32 and 64. For the burst mode, D_c is set to 8 and the non-dimensional burst frequency is set to one and six.

First, the relationship between aerodynamics characteristics and the effect of separation control is discussed. DBD plasma actuator in normal mode generates moderately separated region (separation bubble) over the airfoil and the airfoil gains lift by negative pressure at the vortex center. On the other hand, burst mode does not make the large separation bubble, and the different aerodynamic characteristics are appeared with burst frequency. The burst mode with non-dimensional burst frequency of one enhances the vortex shedding from the separated shear layer and avoid the massive separation from the leading edge. The burst mode with non-dimensional burst frequency of six improves the airfoil performance by suppressing the separation region and this condition is preferable for aircraft because the flow-fields and lift coefficients are stable and the energy consumption of DBD plasma actuator is the lowest in all cases. Thus considering

unsteady-aerodynamic-characteristics are important for actual design. In addition, the maximum C_L case does not correspond with the maximum L/D case in the present study. This is because C_L and L/D is affected by the state of separation bubble which contribute to increasing the C_L and C_D. This fact indicate that it is not enough to evaluating the effectiveness of separation control only by C_L, and other evaluation-indexes such as L/D should be considered for any purpose when averaged flows of quasi-steady state are evaluated.

Second, the burst frequency effect is discussed. On the case that actuator installed at the leading edge, each burst frequency is effective in suppressing massive separation from the leading. On the other hand in the case that actuator installed at the 5 % chord length from the leading edge, the non-dimensional burst frequency of six can suppress the massive separation from the leading but the non-dimensional burst frequency of one is not effective enough to suppress the massive separation and the flow field having leading edge separation alternates with the attached flow.

This is because the separation mechanism is different between the non-dimensional burst frequency of one and six. The non-dimensional burst frequency of one enhance the vortex shedding from the separation shear layer and the flow-field has the unsteady large separated region near the leading edge although the massive separation from the leading edge is avoided. That is why this mechanism associated with the large fluctuation of lift. The non-dimensional burst frequency of six improves the airfoil performance by suppressing the separation region and the flow-field is relatively stable. In addition, it is clarified that the first mechanism is more sensitive to the location of the DBD plasma actuator than the second mechanism because the separated shear layer oscillate very much and distance between the actuator and separated shear layer can be large in the first mechanism. This location sensitivity is one of the reason for inconsistency of optimum burst frequency in the previous studies.

Finally, in chapter 6, transient states in which separated flows are controlled and separated regions are gradually suppressed, are discussed. As the computational cases, characteristic operating conditions of DBD plasma actuator are chosen: non-dimensional burst frequency of one and six, and the actuator installed at the 5 % chord length from the leading edge. To discuss the statistics of these transient states, 20 computations are conducted and ensemble averages are taken for each case. From the results, it is clarified that the transient times which is normalized by the chord length and the free-stream velocity are same order (from five to six) between in each case. However the aerodynamic coefficients (C_L and C_D) of $F^+ = 6$ converges relatively quick. The large lift decreasing which are temporarily observed in the initial stage of transient state caused by advections

of the spanwise vortices which involve the free-stream to the airfoil surface. We also found that this large spanwise vortices play an important role to suppress the separation at the initial stage (tU_∞/c = 1-2). On each case, quasi-steady state is independent of initial flow state.

The conclusions gathered from this study are as follows: There are three mechanisms of separated flow control. The first one is a direct momentum addition into the separated boundary layer (Normal mode), the second one is a vortex advection to downstream ($F^+ = 1$) and the third one is a mixing enhancement ($F^+ = 6$). At low Reynolds number like this study, the third mechanism is most preferable for separation control because the robustness to the location of DBD plasma actuator and stable aerodynamic characteristics.

Toward practical use of DBD plasma actuator for a control of massively separated-flow from near the leading edge. In the flow regime of present study (at moderate Reynolds number 63,000 and over NACA0015), using burst wave is more useful than using continuous sinusoidal wave when a basic DBD plasma actuator is used, in the terms of energy consumption and avoiding declaration of the DBD plasma actuator. Especially, non-dimensional burst frequency six is more preferable for separated-flow control than non-dimensional burst frequency one because the robustness to the location of the DBD plasma actuator and stable aerodynamic characteristics. In addition, on the transient process, we can obtain stable aerodynamic coefficients quickly by using non-dimensional burst frequency six. Concerning a location of DBD plasma actuator, the leading edge which is the vicinity of separation point is appropriate. Moreover at the transient state, homogeneous shape in a spanwise is desirable because inducing two dimensional vortices play an important role. However, the mechanisms of separated-flow control at the transient state and keeping the quasi-steady state are different. Thus we can design optimum shape of DBD plasma actuator for each state respectively, switch the operating device from the transient shape to the quasi-steady shape.

References

[1] Forte, M., Jolibois, J., Moreau, E., Touchard, G., and Cazalens, M., "Optimization of a Dielectric Barrier Discharge Actuator by Stattionary and Non-stationary Measurements of the Induced Flow Velocity - Application to Airflow Control," *AIAA 2006-2863*, 2006.

[2] Abe, T., Takizawa, Y., Sato, S., and Kimura, N., "Experimental Study for Momentum Transfer in a Dielectric Barrier Discharge Plasma Actuator," *AIAA Journal*, Vol. 46, No. 9, September 2008, pp. 2248–2256.

[3] Asada, K., Ninomiya, Y., Oyama, A., and Fujii, K., "Airfoil Flow Experiment on the Duty Cycle of DBD Plasma Actuator," *AIAA-2009-531*, 2009.

[4] Tsubakino, D., Tanaka, Y., and Fujii, K., "Effective Layout of Plasma Actuators for a Flow Separation Control on a Wing," *AIAA-2007-474*, 2007.

[5] Ferziger, J. H. and Peric, M., *Computational Methods for Fluid Dynamics*, Spinger Verlag, 2002.

[6] Aono, H., Nonomnura, T., and Fujii, K., "Numerical Analysis of Fluid Dynamics Associated with a Dielectric Barrier Discharge Plasma Actuator Model in Quiescent Flow," *Proceedings of JSME Fluids Engineering Division Conference*, 2012, in Japanese.

[7] Jabbal, M., Liddle, S. C., and Crowther, W. J., "Active Flow Control Systems Architectures for Civil Transport Aircraft," *Journal of Aircraft*, Vol. 47, No. 6, November-December 2010, pp. 1966–1981.

[8] Shmilovich, A. and Yadlin, Y., "Flow Control Techniques for Transport Aircraft," *AIAA Journal*, Vol. 49, No. 3, March 2011, pp. 489–502.

[9] Shmilovich, A. and Yadlin, Y., "Flow Control for the Systematic Buildup of High Lift Systems," *AIAA 2006-2855*, 2006.

[10] Shmilovich, A. and Yadlin, Y., "FLOW CONTROL TECHNIQUES FOR TRANSPORT AIRCRAFT," *26TH INTERNATIONAL CONGRESS OF THE AERONAUTICAL SCIENCES*, 2008.

[11] Shmilovich, A. and Yadlin, Y., "Active Flow Control for Practical High-Lift Systems," *AIAA-2007-3971*, 2007.

[12] Reneaux, J., "OVERVIEW ON DRAG REDUCTION TECHNOLOGIES FOR CIVIL TRANSPORT AIRCRAFT," *European Congress on Computational Methods in Applied Sciences and Engineering*, 2004.

[13] Gobert, J.-L., D.Barberis, T.Mitchell, P.Molton, Archambaud, J.-P., G.Pailhas, and M.Corrége, "Active Flow Control Activities at Onera," *Active Control Technology for Enhanced Performance Operation Capabilities of Military Aircraft, Land Vehicles and Sea Vehicles*, 2001.

[14] Schmitt, V. and Destarac, D., "Recent Progress in Drag Prediction and Reduction for Civil Transport Aircraft at ONERA," *AIAA-1998-137*, 1998.

[15] Tilmann, C. P., Kimmel, R. L., Addington, G. A., and Myatt, J. H., "Flow Control Research and Applications at the AFRL's Air Vehicles Directorate," *AIAA-2004-2622*, 2004.

[16] Jirasek, A., "A Vortex Generator Model and its Application to Flow Control," *AIAA-2004-4965*, 2004.

[17] Prandtl, L., "Turbulent flow," Technical Memorandum 435, NACA, 1927.

[18] Miyaji, K., Fujii, K., and Karashima, K., "Enhancement of the leading-edge separation vortices by the trailing-edge lateral blowing," *AIAA-1994-181*, 1994.

[19] Miyaji, K. and Arasawa, T., "Studies on High-Lift Devices for a Delta Wing Installed around a Trailing-Edge," *AIAA-2001-2465*, June 2001.

[20] Miyaji, K. and Arasawa, T., "High-Lift Devices for a Delta Wing Installed Around a Trailing-Edge," *Journal of Aircraft*, Vol. 40, No. 5, September-October 2003, pp. 932–937.

[21] Okada, S. and Hiraoka, K., "Experimental Studies of Reduction of the Wing Tip Vortex by Suction," *AIAA-2003-3533*, 2003.

[22] Zha, G.-C., Gaoy, W., Paxton, C. D., and Palewicz, A., "Numerical Investigations of Co-Flow Jet Airfoil with and without Injection," *AIAA-2006-1061*, 2006.

[23] Post, M. L. and Corke, T. C., "Separation Control on High Angle of Attack Airfoil Using Plasma Actuators," *AIAA Journal*, Vol. 42, No. 11, November 2004, pp. 2177–2184.

[24] Corke, T. C., Post, M. L., and Orlov, D. M., "Single-Dielectric Barrier Discharge Plasma Enhanced Aerodynamics: Concepts, Optimization, and Applications," *Journal of Propulsion and Power*, Vol. 24, No. 5, September 2008, pp. 935–945.

[25] Corke, T. C., Enloe, C. L., and P.Wilkinson, S., "Dielectric Barrier Discharge Plasma Actuators for Flow Control," *Annual Review of Fluid Mechanics*, 2010.

[26] Moreau, E., "Airflow control by non-thermal plasma actuators," *Journal of PhysicsD: Applied Physics*, Vol. 40, 2007, pp. 605–636.

[27] Seifert, A., Theofilis, V., and Joslin, R. D., "ISSUES IN ACTIVE FLOW CONTROL: THEORY, SIMULATION AND EXPERIMENT," *AIAA-2002-3277*, 2002.

[28] Okada, K., Oyama, A., Fujii, K., and Miyaji, K., "Computational Study on Effect of Synthetic Jet Design Parameters," *International Journal of Aerospace Engineering*, Vol. 2010, 2010.

[29] Greenblatt, D., Kastantin, Y., Nayeri, C. N., and Paschereit, C. O., "Delta-Wing Flow Control Using Dielectric Barrier Discharge Actuators," *AIAA Journal*, Vol. 46, No. 6, June 2008, pp. 1554–1560.

[30] Fujii, K. and Matsuno, T., "DBD Plasma Actuator -New Flow Control Technology using Barrier Discharge-," *News letter of JSME Fluids Engineering Division*, December 2007, in Japanese.

[31] Roth, J. R., Sherman, D. M., and Wilkinson, S. P., "Electrohydrodynamic Flow Control with a Glow-Discharge Surface Plasma," *AIAA Journal*, Vol. 38, No. 7, 2000, pp. 1166–1172.

[32] Corke, T. C., Jumper, E. J., Post, M. L., Orlov, D., and McLaughlin, T. E., "APPLICATION OF WEAKLY-IONIZED PLASMAS AS WING FLOW-CONTROL DEVICES," *AIAA 2002-0350*, 2002.

[33] Corke, T. C. and Post, M. L., "Separation Control Using Plasma Actuators - Stationary and Oscillating Airfoils," *AIAA 2004-0841*, 2004.

[34] Post, M. L. and Corke, T. C., "Separation Contral on High Angle of Attack Airfoil Using Plasma Actuators," *AIAA-2003-1024*, 2003.

[35] Benard, N., Balcon, N., and Moreau, E., "Electric Wind Produced by a Single Dielectric Barrier Discharge Actuator Operating in Atmospheric Flight Conditins - Pressure Outcome," *AIAA 2008-3792*, 2008.

[36] Gregory, J. W., Enloe, C. L., Font, G. I., and McLaughlin, T. E., "Force Production Mechanism of a Dielectric-Barrier Discharge Plasma Actuator," *AIAA 2007-185*, 2007.

[37] Abe, T., Hattori, Y., Sato, S., and Kimura, N., "A Parametric Experimental Study for Momentum Transfer by Plasma Actuator," *AIAA 2007-187*, 2007.

[38] Enloe, C. L., McLaughlin, T., Font, G. I., and Baughn, J. W., "Parameterization of Temporal Structure in the Single-Dielectric-Barrier Aerodynamic Plasma Actuator," *AIAA Journal*, Vol. 44, No. 6, 2006, pp. 1127–1136.

[39] Baird, C., Enloe, C. L., McLaughlin, T. E., and Baughn, J. W., "Acoustic testing of the dielectric barrier discharge (DBD) plasma actuator," *AIAA-2005-565*, January 2005.

[40] Porter, C. O., Baughn, J. W., McLaughlin, T. E., Enloe, C. L., and Font, G. I., "Plasma Actuator Force Measurements," *AIAA Journal*, Vol. Vol.45, No. No.7, July 2007, pp. 1562–1570.

[41] Font, G. I., Enloe, C. L., and McLaughlin, T. E., "Plasma Volumetric Effects on the Force Production of a Plasma Actuator," *AIAA Journal*, Vol. 48, 2010, pp. 1869–1874.

[42] Font, G., Enloe, C., Newcomb, J., Teague, A., Vasso, A., and McLaughlin, T., "Effects of Oxygen content on dielectric barrier discharge plasma actuator behavior," *AIAA Journal*, Vol. 49, 2011, pp. 1366–1373.

[43] Nishida, H. and Abe, T., "Validation Study of Numerical Simulation of Discharge Plasma on DBD Plasma Actuator," *AIAa 2011-3913*, 2011.

[44] Corke, T. C., He, C., and Patelz, M. P., "PLASMA FLAPS AND SLATS: AN APPLICATION OF WEAKLY-IONIZED PLASMA ACTUATORS," *AIAA-2004-2127*, 2004.

[45] Patel, M. P., Ng, T. T., Vasudevan, S., Corke, T. C., Post, M. L., McLaughlin, T. E., and Suchomel, C. F., "Scaling Effects of an Aerodynamic Plasma Actuator," *AIAA-2007-635*, 2007.

[46] Sidorenko, A. A., Zanin, B. Y., Postnikov, B. V., Budovsky, A. D., Starikovskii, A. Y., Roupassov, D. V., Zavialov, I. N., Malmuth, N. D., Smereczniak, P., and Silkey, J. S., "Pulsed Discharge Actuators for Rectangular Wings Separation Control," *AIAA-2007-941*, 2007.

[47] Visbal, M. R., Gaitonde, D. V., and Roy, S., "Control of Transitional and Turbulent Flows Using Plasma-Based Actuators," *AIAA-2006-3230*, 2006.

[48] Greenblatt, D. and Wygnanski, I. J., "The control of flow separation by periodic excitation," *Progress in Aerospace Sciences*, Vol. 36, 2000, pp. 487–545.

[49] Glezer, A., Amitay, M., and Honohan, A. M., "Aspects of Low- and High-Frequency Actuation for Aerodynamic Flow Control," *AIAA Journal*, Vol. 43, No. 7, July 2005, pp. 1501–1511.

[50] Amitay, M. and Glezer, A., "Controlled transients of flow reattachment over stalled airfoils," *International Journal of Heat and Fluid Flow*, Vol. 23, 2002, pp. 690–699.

[51] Visbal, M. R. and Gaitonde, D. V., "Control of Vortical Flows Using Simulated Plasma Actuators," *AIAA-2006-505*, 2006.

[52] Pope, S. B., *Turbulent Flows*, Cambridge University Press, 2000.

[53] Kawai, S., *Computational Analysis of the Caracteristcs of High Speed Base Flows*, Ph.D. thesis, University of Tokyo, 2005.

[54] Lele, S. K., "Compact Finite Difference Schemes with Spectral-like Resolution." *Journal of Computational Physics*, Vol. 103, No. 1, 1992, pp. 16–42.

[55] Nonomura, T. and Fujii, K., "Development of Optimized WCNS and Evaluation of Resolution of the Optimized WCNS and High order WCNS," *Proceedings of International Conference on Computational Methods 2007*, 2007.

[56] Nonomura, T., Iizuka, N., and Fujii, K., "Freestream and vortex preservation properties of high-order WENO and WCNS on curvilinear grids," *Computers & Fluids*, Vol. 39, No. 2, 2010, pp. 197–214.

[57] Rizzetta, D. P. and Visbal, M. R., "Numerical Investigation of Plasma-Based Control for Low-Reynolds Number Airfoil Flows," *AIAA 2010-4255*, June 2010.

[58] Rizzetta, D. P. and Visbal, M. R., "Numerical Investigation of Plasma-Based Control for Low-Reynolds-Number Airfoil Flows," *AIAA Journal*, Vol. 49, No. 2, February 2011, pp. 411–425.

[59] Asada, K. and Fujii, K., "Computational Analysis of Unsteady Flow-field Induced by Plasma Actuator in Burst Mode," *AIAA-2010-5090*, June 2010.

[60] Kaneda, I., Asada, K., and Fujii, K., "Effective Three-dimensional Layout of Imaginary Body Force for Separation Control," *AIAA-2011-738*, 2011.

[61] Riherd, M., Roy, S., Rizzetta, D., and Visbal, M., "Study of Transient and Unsteady Effects of Plasma Actuation in Transitional Flow over an SD7003 Airfoil," *AIAA 2011-1075*, 2011.

[62] Kuwahara, K., "Unsteady Flow Simulation and Its Visualization," *AIAA-1999-3405*, 1999.

[63] Kuwahara, K. and Komurasaki, S., "Direct Simulation of a Flow around an Airfoil," *Proceedings of 14th Computational Fluid Dynamics symposium*, 2000.

[64] Ooida, J. and Kuwahara, K., "Implicit LES of Turbulence Generated by a Lattice," *AIAA-2003-4097*, 2003.

[65] Visbal, M. R. and Rizzetta, D. P., "Large-eddy Simulationn on General Geometries Using Compact Differencing and Filtering Schemes," *AIAA-2002-288*, 2002.

[66] Sherer, S. E. and Visbal, M. R., "Implicit Large Eddy Simulations Using a High-Order Overset Grid Solver," *AIAA-2004-2530*, 2004.

[67] Matsuura, K. and Kato, C., "Large-Eddy Simulation of Compressible Transitional Flows in a Low-Pressure Turbine Cascade," *AIAA Journal*, Vol. 45, No. 2, February 2007, pp. 442–457.

[68] Fujii, K. and Tamura, Y., "Capability of current supercomputers for the computational fluid dynamics," *Supercomputing '89: Proceedings of the 1989 ACM/IEEE conference on Supercomputing*, ACM, New York, NY, USA, 1989, pp. 71–80.

[69] Fujii, K., "Developing an Accurate and Efficient Method for Compressible Flow Simulations -Example of CFD in Aeronautics-," *The Proceedings: Fifth International Conference on Numerical Ship Hydrodynamics*, 1990.

[70] Fujii, K. and Satofuka, N., "Flashback: 30 Years Numerical Fluid Mechanics and Aerodynamics in Japan, other Asian Countries and the Western Pacific Rim," *100 Volumes of 'Notes on Numerical Fluid Mechanics'*, edited by E. Hirschel and E. Krause, Vol. 100 of *Notes on Numerical Fluid Mechanics and Multidisciplinary Design*, Springer Berlin / Heidelberg, 2009, pp. 109–115.

[71] Fujii, K. and Obayashi, S., "Practical Applications of New LU-ADI Scheme for the Three-Dimensional Navier-Stokes Computation of Transonic Viscous Flows," *AIAA-1986-513*, January 1986.

[72] Obayashi, S., Matsushima, K., Fujii, K., and Kuwahara, K., "Improvements in Efficiency and Reliability for Navier-Stokes Computations Using the LU-ADI Factorization Algorithm," *AIAA-1986-513*, 1986.

[73] Fujii, K. and Obayashi, S., "Navier-Stokes Simulations of Transonic Flows over a Wing-Fuselage Combination," *AIAA Journal*, Vol. 25, December 1987, pp. 1587–1596.

[74] Obayashi, S., Fujii, K., and Gavali, S., "Navier-Stokes Simulation of Wind-Tunnel Flow Using LU-ADI Factorization Algorithm," TM 100042, NASA, 1988.

[75] Aono, H., Nonomura, T., Iizuka, N., Ohsako, T., Inari, T., Hashimoto, Y., Takaki, R., and Fujii, K., "Scalar Tuning of a Fluid Solver using Compact Scheme for a Supercomputer with a Distributed Memory Architecture," *CFD letters*, Vol. 5, No. 4, 2013, pp. 143–152.

[76] Fujii, K., "Progress and Future Prospects of CFD in Aerospace-Wind Tunnel and Beyond," *Progress in Aerospace Sciences*, Vol. 41, 2005, pp. 455–470.

[77] Fujii, K., "CFD contributions to high-speed shock-related problems," *Shock Waves*, Vol. 18, 2008, pp. 145–154.

[78] Hirsh, R. S., "Higher Order Accurate Difference Solutions of Fluid Mechanics Problems by a Compact Differencing Technique," *Journal of Computational Physics*, Vol. 19, 1975, pp. 90–109.

[79] Fujii, K., *Numerical Methods for Computational Fluid Dynamics*, University of Tokyo Press, Tokyo, 1994, in Japanese.

[80] Tannehill, J. C., Anderson, D. A., and Pletcher, R. H., *Computational Fluid Mechanics and Heat Transfer*, Taylor & Francis, Washington, D.C., 2nd ed., 1997.

[81] Liepmann, H. W. and Roshko, A., *Elements of Gasdynamics*, Dover Publications, Inc., Mineola, New York, 2001.

[82] Masatsuka, K., *I do like CFD Volume 1, second edition*, Lulu Press, 2013.

[83] White, F. M., *Visous fluid flows*, 1991.

[84] Beam, R. M. and Warming, R. F., "An Implicit Factored Scheme for the Compressible Navier-Stokes Equations," *AIAA Journal*, Vol. 16, No. 4, April 1978, pp. 393–402.

[85] Chakravarthy, S. R., "Relaxation Methods for Unfactored Implicit Upwind Schemes," *AIAA-1984-165*, January 1984.

[86] Matsuno, K., "A Time-accurate Iterative Scheme for Solving the Unsteady Compressible Flow Equations," *AIAA-1989-1992*, 1989.

[87] Visbal, M. R. and Gaitonde, D. V., "High-Order Accurate Methods for Unsteady Vortical Flows on Curviliner Meshes," *AIAA-1998-131*, 1998.

[88] Gaitonde, D. V. and Visbal, M. R., "Further development of a Navier-Stokes solution procedure based on higher-order formulas," *AIAA-1999-557*, 1999.

[89] Arasawa, T., Fujii, K., and Miyaji, K., "Application of High-Order Compact Difference Scheme to Vortical Flow Computation over a Delta and Double-Delta Wings," *AIAA-2003-3537*, June 2003.

[90] Arasawa, T., Fujii, K., and Miyaji, K., "High-Order Compact Difference Scheme Applied to Double-Delta Wing Vortical Flows," *Journal of Aircraft*, Vol. 41, No. 4, 2004, pp. 953–957.

[91] Gordnier, R. E. and Visbal, M. R., "Compact Difference Scheme Applied to Simulation of Low-Sweep DeltaWing Flow," *AIAA Journal*, Vol. 43, No. 8, August 2005, pp. 1744–1752.

[92] Gordnier, R. E., Visbal, M. R., Gursul, I., and Wang, Z., "Computational and Experimental Investigation of a Nonslender Delta Wing," *AIAA-2007-894*, 2007.

[93] Sherer, S. E., Visbal, M. R., and Gordnier, R. E., "Computational Study of Reynolds Number and Angle-of-Attack Effects on a 1303 UCAV Configuration with a High-Order Overset-Grid Algorithm," *AIAA-2009-751*, 2009.

[94] Morgan, P. E. and Visbal, M. R., "Large-Eddy Simulation Modeling Issues for Flow Around Wing Sections," *AIAA-2003-4152*, 2003.

[95] Morgan, P. E. and Visbal, M. R., "Large-Eddy Simulation of Airfoil Flows," *AIAA-2003-777*, 2003.

[96] Kawai, S. and Fujii, K., "Prediction of a Thin-Airfoil Stall Phenomenon Using LES/RANS Hybrid Methodology with Compact Difference Scheme," *AIAA-2004-2714*, 2004.

[97] Kawai, S. and Fujii, K., "Analysis and Prediction of Thin-Airfoil Stall Phenomena Using Hybrid Turbulent Methodology," *AIAA Journal*, Vol. 43, No. 5, May 2005, pp. 953–961.

[98] Kawai, S. and Fujii, K., "Compact Scheme with Filtering for Large-Eddy Simulation of Transitional Boundary Layer," *AIAA Journal*, Vol. 46, No. 3, March 2008, pp. 690–700.

[99] Kawai, S. and Fujii, K., "Compact Differencing and Filtering Schemes for Large-Eddy Simulation of Compressible Transitional Boundary Layer," *AIAA-2007-3842*, 2007.

[100] Kawai, S. and Fujii, K., "Large-Eddy Simulation of Compressible Transitional Boundary Layer," *AIAA-2006-7941*, 2006.

[101] Okamoto, K., Nonomura, T., and Fujii, K., "Computational Analysis of Noise Sources inside the High Speed Flow over a Bump," *ASME FEDSM-2007-37536*, 2007.

[102] Okamoto, K., Nonomura, T., and Fujii, K., "Computational Analysis of Noise Sources inside the High Speed Flow over a Generalized Bump," *AIAA-2008-64*, 2008.

[103] Shima, E. and Jounouchi, T., "Role of CFD in Aeronautical Engineering (No.14) - AUSM type Upwind Schemes-," *Proceedings of the 14th NAL Symposium on Aircraft Computational Aerodynamics*, NAL, 1997, pp. 7–12.

[104] Roe, P. L., "Approximate Riemann Solvers, Parameter Vectors, and Difference Scheme," *Journal of Computational Physics*, Vol. 43, No. 2, 1981, pp. 357–372.

[105] Liou, M. S., "Towards an Improved CFD Method: AUSM+," *AIAA-1995-1701*, 1995.

[106] van Leer, B., "Towards the Ultimate Conservation Difference Scheme. IV. A New Approach to Numerical Convection," *Journal of Computational Physics*, Vol. 23, No. 3, 1977, pp. 276–299.

[107] van Leer, B., "Towards the Ultimate Conservation Difference Scheme. V. A Second-Order Sequel to Godunov's Method," *Journal of Computational Physics*, Vol. 32, 1979, pp. 101–136.

[108] Visbal, M. R. and Gaitonde, D. V., "Computation of aeroacoustic fields on general geometries using compact differencing and filtering schemes," *AIAA-1999-3706*, 1999.

[109] Koutsavdis, E. K., Blaisdell, G. A., and A. S. Lyrintzis, A. S., "A Numerical Investigation of Two-dimensional Jets Using Saptial Filtering," *AIAA-1999-1875*, 1999.

[110] Gaitonde, D. V. and Visbal, M. R., "Padé-Type Higher-Order Boundary Filters for the Navier-Stokes Equations," *AIAA Journal*, Vol. 38, No. 11, 2000, pp. 2103–2112.

[111] Nagarajan, S., Lele, S. K., and Ferziger, J. H., "A Robust High-order Compact Method for Large Eddy Simulation," *Journal of Computational Physics*, Vol. 191, 2003, pp. 392–419.

[112] Fyfe, D. J., "Economical Evaluation of Runge-Kutta Formulae," *Mathematics of Computation*, Vol. 20, No. 95, 1966, pp. 392–398.

[113] Courant, R., Friedrichs, K., and Lewyt, H., "On the Partial Difference Equations of Mathematical Physics," *IBM Journal of Research and Development*, Vol. 11, No. 2, 1967, pp. 215–234.

[114] Choi, H. and Moin, P., "Effects of the Computational Time Step on Numerical Solutions of Turbulent Flow," *Journal of Computational Physics*, Vol. 113, 1994, pp. 1–4.

[115] Iizuka, N., *Study of Mach Number Effect on the Dynamic Stability of a Blunt Re-entry Capsule*, Ph.D. thesis, University of Tokyo, 2006.

[116] Iizuka, N. and Fujii, K., "Evaluation of Dynamic Base Pitching Moment of a Blunt ReEntry Capsule in Transonic Region," *Proceedings of 57th International Astronautical Congress IAC06-D2P.1.9*, 2006.

[117] Nishida, H. and Nonomura, T., "ADI-SGS Scheme on Ideal Magnetohydrodynamics," *Journal of Computational Physics*, Vol. 228, 2009, pp. 3182–3188.

[118] Fujii, K., "Efficiency Improvement of Unified Implicit Relaxation/Time Integration Algorithms," *AIAA Journal*, Vol. 37, No. 1, 1999, pp. 125–128.

[119] Yoon, S. and Jameson, A., "An LU-SSOR Scheme for the Euler and Navier-Stokes Equations," *AIAA-1987-600*, January 1987.

[120] Yoon, S. and Jameson, A., "Lower-Upper Symmetric-Gauss-Seidel Method for the Euler and Navier-Stokes Equations," *AIAA Journal*, Vol. 26, No. 9, September 1988, pp. 1025–1026.

[121] Yee, H., "Construction of explicit and implicit symmetric TVD schemes and their applications," *Journal of Computational Physics*, Vol. 68, No. 1, 1987, pp. 151–179.

[122] Yee, H. and Shinn, J., "Semi-Implicit and Fully Implicit Shock-Capturing Methods for Hyperbolic Conservation Laws with Stiff Source Terms," *AIAA-1987-1116*, June 1987.

[123] Jameson, A. and Turkel, E., "Implicit schemes and LU Decompositions," *Mathematics of Computation*, Vol. 37, 1981, pp. 385–397.

[124] Lombard, C. K., Bardina, J., Venkatapathy, E., and Oliger, J., "Multi-Dimensional Formulation of CSCM - An Upwind Flux Difference Eigenvector Split Method for the Compressible Navier-Stokes Equations," *AIAA-1983-1895*, July 1983.

[125] Steger, J. L. and Warming, R. F., "Flux Vector Splitting of the Inviscid Gasdynamic Equations with Application to Finit-Difference Methods," *Journal of Computational Physics*, Vol. 40, 1981, pp. 263–293.

[126] Hirsch, C., *Numerical Computation of Internal and External Flows, Volume 2*, John Wiley & Sons, 1988.

[127] Pulliam, T. H. and Chaussee, D. S., "A Diagonal Form of an Implicit Approximate-Factorization Algorithm," *Journal of Computational Physics*, Vol. 39, 1981, pp. 347–363.

[128] Pulliam, T. H. and Steger, J. L., "Implicit Finite-Difference Simulations of Three-Dimensional Compressible Flow," *AIAA Journal*, Vol. 18, No. 2, February 1980, pp. 159–167.

[129] Steger, J. L., "Implicit Finite-Difference Simulation of Flow about Arbitrary Two-Dimensional Geometries," *AIAA Journal*, Vol. 16, No. 7, July 1978, pp. 679–686.

[130] Obayashi, S. and Kuwahara, K., "An Approximate LU Factorization Method for the Compressible Navier-Stokes Equations," *Journal of Computational Physics*, Vol. 63, No. 1, 1986, pp. 157–167.

[131] MacCormack, R. W., "A Numerical Method for Solving the Equations of Compressible Viscous Flow," *AIAA Journal*, Vol. 20, No. 9, September 1982, pp. 1275–1281.

[132] Smagorinsky, J., "General Circulation Experiments with the Primitive Equations, Part1: The Basic Experiment," *Monthly Weather Review*, Vol. 91, No. 3, March 1963, pp. 99–152.

[133] Gristein, F. F. and Fureby, C., "Recent Progress on MILES for High Reynolds Number Flows," *Journal of Fluids Engineering, Transactions of the ASME*, Vol. 124, 2002, pp. 848–861.

[134] Fujii, K., "Unified Zonal Method Based on the Fortified Solution Algorithm," *Journal of Computational Physics*, Vol. 118, 1995, pp. 92–108.

[135] Berenger, J.-P., "A Perfectly Matched Layer for the Absorption of Electromagnetic Waves," *Journal of Computational Physics*, Vol. 114, 1994, pp. 185–200.

[136] Hu, F., "On Absorbing Boundary Condition for Linear Euler Equations by a Perfectly Matched Layer," *Journal of Computational Physics*, Vol. 129, 1996, pp. 201–219.

[137] Freund, J. B., "A Simple Method for Computing Far-field Sound in Aeroacoustic Computations," *Journal of Computational Physics*, Vol. 157, 2000, pp. 796–800.

[138] Colonius, T., "Modeling Artificial Boundary Conditions for Compressible Flow," *Annual Review of Fluid Mechanics*, Vol. 36, 2004, pp. 315–345.

[139] Hirsch, C., *Numerical Computation of Internal and External Flows*, John Willy and Sons, Inc., 1988.

[140] Rizzi, A., "Damped Euler-Equation Methods to Compute Transonic Flow Around Wing-Body Combinations," *AIAA Journal*, Vol. 20, No. 10, October 1982, pp. 1321–1328.

[141] Shyy, W., Jayaraman, B., and Andersson, A., "Modeling of glow discharge-induced fluid dynamics," *Journal of Applied Physics*, Vol. 92, No. 11, 2002, pp. 6434–6443.

[142] Mertz, B. E. and Corke, T. C., "Time-Dependent Dielectric Barrier Dishcharge Plasma Actuator Modeling," *AIAA-2009-1083*, 2009.

[143] Orlov, D. M., Corke, T. C., and Patel, M. P., "Electric Circuit Model for Aerodynamic Plasma Actuator," *AIAA-2006-1206*, 2006.

[144] Ibrahim, I. H. and Skote, M., "Simulations of the linear plasma synthetic jet actuator utilizing a modified Suzen-Huang model," *Physics of Fluids*, Vol. 24, 2012, pp. 113602.

[145] Suzen, Y. B., Huang, P. G., Jacob, J. D., and Ashpis, D. E., "Numerical Simulations of Plasma Based Flow Control Application," *AIAA-2005-4633*, 2005.

[146] Suzen, Y. B. and Huang, P. G., "Simulations of Flow Separation Contorl using Plasma Actuator," *AIAA-2006-877*, 2006.

[147] Suzen, Y. B., Huang, P. G., and Ashpis, D. E., "Numerical Simulations of Flow Separation Control in Low-Pressure Turbines using Plasma Actuators," *AIAA-2007-937*, January 2007.

[148] Tanahashi, T., "The Relation between Vorticity and Shear Stress on a Curved Wall," *Transactions of the JSME*, Vol. 44, 1978, pp. 657–658, in Japanese.

[149] Sekimoto, S., Asada, K., Anyoji, M., Nonomura, T., and Fujii, K., "Comparative Study of Co-flow and Counter Blowing DBD Plasma Actuators for Separated Flow over an Airfoil," *AIAA 2012-1137*, 2012.

[150] Nonomura, T., Aono, H., Sato, M., Yakeno, A., Okada, K., Abe, Y., and Fujii, K., "Control Mechanism of Plasma Actuator for Separated Flow around NACA0015 at Reynolds Number 63,000 -Separation Bubble Related Mechanisms-," *AIAA 2013-0853*, 2013.

[151] Goksel, B., Greenblatt, D., Rechenberg, I., Nayeri, C. N., and Paschereit, C. O., "Steady and Unsteady Plasma Wall Jets for Separation and Circulation Control," *AIAA-2006-3686*, 2006.